UC San Diego

UC San Diego Electronic Theses and Dissertations

Title

Astrocyte BMP Signaling in Fragile X Syndrome and Cortical Development

Permalink

https://escholarship.org/uc/item/12z5w5n7

Author

Deng, James

Publication Date

2024

Supplemental Material

https://escholarship.org/uc/item/12z5w5n7#supplemental

Peer reviewed|Thesis/dissertation

eScholarship.org Powered by the California Digital Library
University of California

UNIVERSITY OF CALIFORNIA SAN DIEGO

Astrocyte BMP Signaling in Fragile X Syndrome and Cortical Development

A dissertation submitted in partial satisfaction of the requirements for the degree

Doctor of Philosophy

in

Neurosciences

by

James D. Deng

Committee in Charge:

Professor Nicola Allen, Chair
Professor Joseph Gleeson, Co-Chair
Professor Susan Ackerman
Professor Yimin Zou

2024

Copyright

James D. Deng, 2024

All rights reserved.

The dissertation of James Derong Deng is approved, and it is acceptable in quality and form for publication on microfilm and electronically.

University of California San Diego

2024

TABLE OF CONTENTS

Dissertation Approval Page iii
Table of Contents.....iv
List of Abbreviations v
List of Supplemental Tables vii
List of Figures viii
Acknowledgments x
Vita xi
Abstract of the Dissertation xii
Chapter 1. Introduction 1
Chapter 2. Improving Fmr1 KO phenotypes by suppressing of astrocyte BMP signaling 29
Chapter 3. Nuclear transcriptomics of Fmr1 KO with and without Smad4 cKO 57
Chapter 4. Proteomic analysis of Fmr1 KO with and without Smad4 cKO 78
Chapter 5. BMP signaling in astrocyte cortical heterogeneity and maturation 110
Chapter 6. Conclusions 134
Chapter 7. Methods 142

LIST OF ABBREVIATIONS

AC	Auditory cortex
ASD	Autism spectrum disorder
B6	C57BL/6J genetic background
BMP	Bone morphogenetic protein
cKO	Conditional knock out
CNS	Central nervous system
CSF	Cerebrospinal fluid
DEG	Differentially expressed gene
DEP	Differentially expressed protein
ECM	Extracellular matrix
ER	Endoplasmic reticulum
FACS	Fluorescence-activated cell sorting
Fmr1	Fragile X messenger ribonucleoprotein 1 (gene)
FMRP	Fragile X messenger ribonucleoprotein (protein)
FXS	Fragile X syndrome
GABA	Gamma-aminobutyric acid
GSEA	Gene set enrichment analysis
IC	Inferior colliculus
IHC	Immunohistochemistry
KO	Knock out
L	Layer
L2FC	Log2 fold change
MACS	Magnetic-activated cell sorting
mGluR	Metabotropic glutamate receptor
mm10	*M. musculus* genome version 10
mTOR	Mammalian target of rapamycin
nRNAseq	Nuclear RNA sequencing

OPC	Oligodendrocyte precursor cell
P	Postnatal
PNN	Perineuronal net
smFISH	Single molecule fluorescence *in situ* hybridization
smFP	Spaghetti monster fluorescent protein
TGFβ	Transforming growth factor beta
TMT	Tandem mass tagging
TPM	Transcript per million
VC	Visual cortex
WT	Wild type

LIST OF SUPPLEMENTAL FILES

Supplemental Data Table 1. Data from RNA sequencing experiments. Displaying TPM values for each gene for each sample.
Supplemental Data Table 2. Differentially-expressed genes (DEGs) from RNA sequencing, based on criteria: average TPM > 1 in WT samples, Benjamini-Hochberg (BH) adjusted p-value < 0.05, |fold change (FC)| > 1.5.
Supplemental Data Table 3. Gene-set enrichment analysis (GSEA) data on RNA sequencing. Enrichment of gene sets and pathways MSigDB, Gene Ontology (GO), Reactome, KEGG, Wikipathway, and BioCarta. Genes with TPM > 1 in every sample were used for GSEA, with ranking based on sign(log2 fold change)*-log10(p-value), for each comparison.
Supplemental Data Table 4. Gene lists and associated RNA-seq z-score averaged by genotype of the glycolysis/gluconeogenesis set (KEGG M11521) and the oxidative phosphorylation set (MSigDB MM3893).
Supplemental Data Table 5. Gene list and pairwise comparisons in RNA sequencing data for BMP pathway components.
Supplemental Data Table 6. Data from proteomics experiment. Displaying TMT raw signal values for each protein for each sample, average TMT signal per genotype, and enrichment of experimental over control samples.
Supplemental Data Table 7. Differentially-expressed proteins (DEPs) from proteomics, based on |FC| > 1.25 and p-value < 0.05, unpaired t-test
Supplemental Data Table 8. Gene-set enrichment analysis (GSEA) data on proteomics. Enrichment of sets and pathways MSigDB, Gene Ontology (GO), Reactome, KEGG, Wikipathway, and BioCarta. Proteins with Turbo/smFP enrichment ratio > 1.75 were used for GSEA, with ranking based on sign(log2 fold change)*-log10(p-value), for each comparison.
Supplemental Data Table 9. Gene sets with cortical layer-enriched genes used for gene-set enrichment analysis (GSEA).

LIST OF FIGURES

Figure 1.1. Overview of cell types in the brain, the synapse, and the neuron 13

Figure 1.2. Complexity of astrocyte morphology 14

Figure 1.3. Overview of anatomy of the brain cortex and astrocyte and neuron development ..15

Figure 1.4. The canonical BMP signaling pathway 16

Figure 1.5. Inhibition of BMP signaling in cultured Fmr1 KO astrocytes rescues Fmr1 KO neurite outgrowth deficit 17

Figure 2.1. Smad4 cKO suppresses astrocyte BMP signaling 41

Figure 2.2. Additional immunohistochemical validation and characterization of astrocyte Smad4 cKO at P28 42

Figure 2.3. Additional validation and characterization of astrocyte Smad4 cKO at P14 44

Figure 2.4. Characterization of astrocyte Smad4 cKO cell density and cortical area 45

Figure 2.5. Smad4 cKO reduces severity of Fmr1 KO audiogenic seizures 47

Figure 2.6. Smad4 cKO does not improve Fmr1 KO visual acuity or ocular dominance plasticity deficits 48

Figure 2.7. Smad4 cKO rescues Fmr1 KO auditory cortex inhibitory synapse density deficit 49

Figure 3.1. Fresh and frozen tissue comparison for glyoxal-fixed nuclear isolation 66

Figure 3.2. Nuclear transcriptomics identifies Fmr1 KO and Smad4 cKO astrocyte *in vivo* transcriptomic dysregulation 67

Figure 3.3. Gating strategy and validation of nuclear transcriptomic experiment 68

Figure 3.4. Smad4 cKO moderates Fmr1 KO astrocyte transcriptomic activation of metabolic pathways 69

Figure 3.5. Full gene sets for glycolysis/gluconeogenesis and oxidative phosphorylation 70

Figure 3.6. Comparison of *in vivo* RNA-seq transcriptomics with other datasets 71

Figure 3.7. Astrocyte reactivity genes in nRNA-seq 73

Figure 4.1. Development of ER-TurboID for studying astrocyte secreted and membrane proteins 90

Figure 4.2. Protocol and validation of ER-targeted TurboID for *in vivo* astrocyte proximity labeling proteomics 92

Figure 4.3. Additional validation of ER-TurboID for studying astrocyte proteins *in vivo* 93

Figure 4.4. Optimization of TurboID protocol for *in vivo* labeling of secreted proteins 95

Figure 4.5. ER-TurboID labels astrocyte secreted and membrane proteins 96

Figure 4.6. ER-TurboID identifies dysregulated Fmr1 KO astrocyte secreted and membrane proteins 97

Figure 4.7. Minimal to slight correlations between *in vivo* transcriptomics and ER-TurboID proteomics 98

Figure 4.8. Comparison of ER-TurboID proteomics with other datasets 99

Figure 4.9. Western blot validation of ER-TurboID-identified differentially expressed astrocyte-secreted proteins, Brevican and HepaCAM 101

Figure 4.10. Smad4 cKO restores Fmr1 KO astrocyte deficit in secretory machinery 103

Figure 4.11. Full protein list for secretory machinery gene set.....104

Figure 5.1. Transcriptomic and proteomic analysis of Smad4 cKO astrocytes 119

Figure 5.2. BMP signaling present in developing astrocytes varies across cortical layers 120

Figure 5.3. Smad4 cKO astrocytes have altered expression of astrocyte layer-enriched gene programs 122

Figure 5.4. Pial expression of *Myoc* is abolished in Smad4 cKO 123

Figure 5.5. L1 and L6 expression of *Tnc* is reduced in Smad4 cKO 124

Figure 5.6. Expression of Chrdl1 is not changed in Smad4 cKO 125

Figure 5.7. Sparc is upregulated in L1, L2, and L6 in Smad4 cKO 126

Figure 5.8. AQP4 is downregulated in Smad4 cKO cortical parenchyma 127

Figure 5.9. BMP-related gene expression is not changed in Chrdl1 KO visual cortex at P28 ..128

ACKNOWLEDGMENTS

I owe an immeasurable debt to my advisor Dr. Nicola Allen for her constant support, advice, patience, and careful mentorship. I am lucky to get scientific training from the very best.

I would like to acknowledge all members of the Allen lab past and present for their help and support, and in particular, Drs. Ashley Brandebura and Lara Labarta-Bajo for their expertise, training, and guidance.

The work in this dissertation was made possible by the collaborative scientific ecosystem of the Salk Institute and UCSD, in particular the dedicated staff of core facilities such as Drs. Jolene Diedrich and Antonio Pinto, who performed crucial experiments in this dissertation.

This work would not have been possible without the unconditional support of my family, friends, and communities, for which I will be always appreciative. In particular I am grateful to my partner Aaron Gozum for helping me to find the meaning in my work, being there to support through the best and the worst, and always gently pushing me to be more thoughtful.

I am grateful to funding sources including the National Institute of Child Health and Human Development and the FRAXA Research Foundation.

Chapters 1-7, in part, have been submitted for publication. Deng J**,** Labarta-Bajo L, Brandebura AN, Kahn SB, Pinto AFM, Diedrich JK, Allen NJ (2024). Suppression of astrocyte BMP signaling improves fragile X syndrome molecular signatures and functional deficits. The dissertation author will be the first author of this publication, and Dr. Nicola Allen will be the senior author and principal investigator.

VITA

2026 Doctor of Medicine (anticipated)
University of California San Diego

2024 Doctor of Philosophy in Neurosciences
University of California San Diego

2017 Bachelor of Science in Chemistry
Massachusetts Institute of Technology

PUBLICATIONS

Deng J, Labarta-Bajo L, Brandebura AN, Kahn SB, Pinto AFM, Diedrich JK, Allen NJ (2024) Suppression of astrocyte BMP signaling improves fragile X syndrome molecular signatures and functional deficits.
Submitted.

Deng J, Brandebura AN, Labarta-Bajo L, Kahn SB, Pinto AFM, Diedrich JK, Allen NJ (2024) Astrocyte BMP signaling in cortical heterogeneity and development.
In preparation for submission

Labarta-Bajo, **Deng J**, Contreras M, and Allen NJ (2023) Protocol for the purification and transcriptomic analysis of mouse astrocytes using GFAT. *STAR Protocols*, 4: 102599.

Caldwell A, Sancho L, **Deng J**, Bosworth A, Miglietta A, Diedrich J, Shokhirev M, and Allen N (2022) Aberrant astrocyte protein secretion contributes to altered neuronal development in diverse disorders. *Nature Neurosci*ence, 25: 1163-1178.

Mennie KM, Reutershan MH, White C, Adams B, Becker B, **Deng J**, Katz JD, LaBlue E, Margrey K, and Saurí J. (2021) Divergent and Regioselective Synthesis of Pyrazolo[1,5-*a*]pyridines and Imidazo[1,5-*a*]pyridines. *Organic Letters,* 23(12): 4694–4698.

Bartko S, **Deng J**, and Danheiser RL (2016). Synthesis of 1-Iodopropyne. *Organic Syntheses,* 93: 245-262.

Deng J, Wang YP, and Danheiser RL (2015) Synthesis of 4,4-Dimethoxybut-1-yne. *Organic Syntheses,* 92: 13-25.

FIELDS OF STUDY

Major Field: Neuroscience

Studies in astrocyte biology
Professor Nicola Allen

ABSTRACT OF THE DISSERTATION

Astrocyte BMP Signaling in Fragile X Syndrome and Cortical Development

by

James D. Deng

Doctor of Philosophy in Neurosciences

University of California San Diego, 2024

Professor Nicola Allen, Chair
Professor Joseph Gleeson, Co-Chair

Astrocytes are glial cells with critical roles in brain development, maturation, homeostasis, and plasticity, and dysregulations in astrocytes contribute to neurodevelopmental and neurologic disorders. This dissertation investigates the role of astrocytes in the neurodevelopmental disorder fragile X syndrome (FXS) as well as in the heterogeneity and development of the cortex. I used mouse genetic tools to suppress astrocyte bone morphogenetic protein (BMP) signaling *in vivo*, and ask how this suppression affected fragile X syndrome molecular, functional, and behavioral phenotypes as well as cortical astrocyte heterogeneity and development. Chapter 2 describes

generation and validation of the model to suppress astrocyte BMP signaling with astrocyte-specific conditional knock out (cKO) of Smad4, and asks whether Smad4 cKO can rescue FXS functional phenotypes. I find that Smad4 cKO lessens severity of audiogenic seizures in FXS mice, does not affect FXS visual acuity or ocular dominance plasticity, and restores deficits in inhibitory synapses present in FXS auditory cortex. Chapter 3 identifies transcriptomic changes in both typical and FXS-affected cortical astrocytes with or without BMP signaling. I find that FXS-affected astrocytes have an overall hypermetabolic transcriptomic signature that is moderated by Smad4 cKO. Chapter 4 describes development of a method to profile astrocyte secreted and membrane proteins *in vivo*, and identifies proteomic changes in both typical and FXS-affected cortical astrocytes with or without BMP signaling. I find that FXS-affected astrocytes have downregulated secretory machinery and secreted proteins, with these alterations minimized by Smad4 cKO. Chapter 5 investigates the role of astrocyte BMP signaling in typical development, applying transcriptomic and proteomic data from previous chapters. I find that Smad4-dependent BMP signaling is necessary for spatially-segregated astrocyte transcriptomic variability and in particular pial astrocyte gene signatures, and that BMP signaling mediates aspects of astrocyte and cortical maturation. These data demonstrate that astrocytes contribute to FXS molecular and functional phenotypes, that targeting astrocyte BMP signaling can mitigate FXS symptoms, and that BMP signaling affects astrocyte cortical heterogeneity and development. Overall, this dissertation demonstrates that an astrocyte signaling pathway mediates both aspects of typical development as well as molecular and functional changes in a genetic neurodevelopmental disorder.

Chapter 1. Introduction

Cell types in the brain

The field of neuroscience has traditionally centered the electrically excitable neuron as its core subject. Indeed other cell types in the brain were referred to as “neuroglia” (Greek: “brain glue”), a name reflecting the historical misconception of these cells as homogeneous, passive, and secondary. With the advent of tools enabling research focusing on glia, “neuroglia” were separated into astrocytes, oligodendrocytes and their precursors, microglia, and ependymal cells, among others, each playing a crucial role in brain function (**Figure 1.1A**).

Neurons or nerve cells are the signaling units of the nervous system. Neurons typically contain (1) a cell body with the nucleus and core metabolic machinery, (2) branching dendrites, where neurons receive incoming signals, (3) an axon that extends from the cell body to carry the output signal a specified distance and often has fine branching, and (4) synaptic terminals, specialized protrusions for communication with other neurons (**Figure 1.1C**).[1] Synapses are the sites of communication between neurons and are formed from the presynaptic terminals of one neuron, a narrow synaptic cleft, and postsynaptic areas on another neuron’s dendrites (or less commonly, cell body or axon) (**Figure 1.1B**). To transmit signals, presynaptic neurons can release neurotransmitters into the synaptic cleft that then bind to receptors on the postsynaptic neuron and activate downstream signaling pathways.

Astrocytes (Greek: astro “star” + cyte “cell”) are star-shaped cells constituting ~15% of all brain cells,[2] and their branching processes tile the central nervous systems (CNS) of organisms from the mouse and rat to marmoset and human. The elaborate structure (**Figure 1.2**) of astrocytes parallels and enables their many diverse functions. Astrocytes have a cell body (soma), major processes emanating from the soma (~6+ branches), distal extensions contacting blood

vessels (1+ endfeet),[3] and small branches contacting synapses, the connections between neurons (~100,000s leaflets/perisynaptic processes) and thereby forming the tripartite synapse (**Figure 1.1B**).[4,5] These intricate processes allow astrocytes to contribute to brain metabolic support and ion and neurotransmitter homeostasis;[6] to communicate bidirectionally with other astrocytes via gap junctions as well as with neurons, oligodendrocytes, oligodendrocyte precursor cells, and microglia (**Figure 1.1A**);[7] and to regulate synapse formation, function, and elimination.[8] Notably, across mammalian species, astrocytes increase in size, morphological complexity, and diversity as brain size increases,[5] suggesting astrocytes are critical for higher order cognitive functions.

Oligodendrocytes (Schwann cells in the peripheral nervous system) generate lipid-filled myelin sheaths that enwrap neuronal axons and thereby speed up signal propagation as well as provide metabolic support (**Figure 1.1A**).[9] Oligodendrocyte precursor cells (OPCs) proliferate throughout life, generate myelinating oligodendrocytes, receive synaptic inputs from neurons, and likely perform still-unidentified roles in brain function (**Figure 1.1A**).[10,11] Microglia are myeloid cells that as the brain's resident macrophages, patrol the brain, presenting antigens and phagocytosing other cells and cell parts such as synapses during both health and injury, infection, or other disease (**Figure 1.1A**).[12] Ependymal cells line the ventricles, cavities within the brain, and produce and regulate cerebrospinal fluid (CSF), which circulates in the spaces around the brain and spinal cord.[13] Endothelial cells line the interior of blood vessels in the brain—from capillaries to arteries—and help form the blood-brain barrier that protects the brain from external insults.[14] Other cell types include vascular and leptomeningeal cells such as fibroblasts that form the meninges that surround the brain,[15] pericytes and smooth muscle cells that surround capillaries and arteries respectively and regulate blood flow,[16,17] and various immune system cells.[18]

Neurodevelopment and the role of astrocytes

Brain development is an exquisitely complex and highly regulated process that includes the formation of the neural tube as a precursor to the brain and spinal cord, early embryonic patterning, the birth of neurons and glial cells, the outgrowth of neuronal processes, and the formation and maturation of synapses that constitute connections between neurons in functional circuits (**Figure 1.3C**). Below I will describe key aspects of this process and highlight the role of astrocytes in typical as well as dysregulated neurodevelopment.

Neurogenesis and gliogenesis. After the establishment of the neural tube by inductive factors early in embryonic development, as well as its regional subdivision into spinal cord, hindbrain, midbrain, and forebrain, the rapid birth of neurons occurs.[19] Progenitor cells located in the ventricular zone (interior lumen) of the neural tube proliferate rapidly.[20,21] Among these progenitors are radial glial cells, whose cell bodies are located in the ventricular zone but extend processes to the pial (external) surface.[21] These processes scaffold the developing brain and guide newly born neurons migrating from the ventricular zone to their terminal locations.[20,21] In the cerebral cortex (**Figure 1.3A**)—the largest region in the human brain and the physical substrate for higher-order sensory and cognitive processing—this migration occurs from inside-out, with earliest-born neurons residing in deeper layers and later-born neurons located in upper layers.[22] Mammalian cortex has six stereotyped layers, each with characteristic cell types and circuitry (**Figure 1.3B**).[20] Inhibitory interneurons, a subtype of neurons that release inhibitory neurotransmitter gamma-aminobutyric acid (GABA) and comprise 10-20% of neurons, originate in a different proliferative zone (medial ganglionic eminence) but then migrate to the cortex.[23] Up to half of newly born neurons do not survive; survival and suppression of a latent cell death pathway requires environmentally-determined neurotrophic factors such as neurotrophins, glial-derived neurotrophic factor (GDNF), and nerve growth factor (NGF).[24–26] Neural progenitors then undergo a precisely timed fate specification switch after which daughter cells are in the glial

(astrocyte and oligodendrocyte) lineage; this switch is regulated by intrinsic and extrinsic cellular processes including suppression of proneural pathways and transcription factors such as notch, N-CoR, and neurogenin, as well as induction of proglial pathways and transcriptions factors such as Sox9 and NFIA/NFIB (astrocytes), and Olig1/2 (oligodendrocytes).[27–32]

Neurite outgrowth. Prior to forming synapses with one another to build functioning neural circuits, neurons must correctly identify their partners. This occurs through the process of axonal pathfinding and is regulated by axonal growth cones, which are highly motile and receptor-containing specialized structures at axons tip that incorporate external cues to navigate.[33] Gradients of extracellular matrix components (e.g. laminin), cell surface adhesion molecules (e.g. cadherins, immunoglobulins, ephrins), and secreted repulsive (e.g. slits, semaphorins, BMPs) and attractive cues (e.g. nerve growth factor, netrin, Wnt) all serve to instruct growth cones' journeys.[34–42] Dendritic pathfinding, guidance, and branching occurs in parallel, uses some of the same sets of molecules as axons[43] as well as dendrite-specific organelles (e.g. Golgi outposts) and transcription factors (e.g. NeuroD1), among many other factors.[44]

Synapse formation and maturation. Formation and refinement of synapses allows neurons to form circuits and communicate with one another. Synaptogenesis is an interactive process that broadly requires apposition of pre- and postsynaptic neuron branches as well as spatial clustering of synapse-associated components and machinery (neurotransmitter vesicle/release machinery in the presynapse, neurotransmitter receptors and associated protein complexes in the postsynapse). Some examples of molecular effectors of synapse formation that have been characterized include neuron-intrinsic presynaptic neurexins and postsynaptic neuroligins, adhesion molecules that enable apposition of pre- and postsynaptic components,[45,46] and brain-derived neurotrophic factor (BDNF), which can enhance synaptic vesicle docking and protein production.[47]

Astrocytes in typical neurodevelopment. Astrocytes mature in concert with maturing synapses and circuits (**Figure 1.3C**), and astrocytes are increasingly recognized to play active roles in neurodevelopment from dendrite growth to synapse formation, maturation, and pruning.[48] Neurons cultured with either astrocytes or with astrocyte-conditioned media (ACM) containing secreted factors survive longer, form more elaborate dendritic/axonal structures, and develop several times more synapses than neurons cultured alone.[49–51]

Astrocytes secrete many growth factors and extracellular matrix proteins involved in early neuronal survival and neurite outgrowth, such as brain-derived neurotrophic factor (BDNF), insulin-like growth factor 1 (IGF1), glial-derived neurotrophic factor (GDNF), ciliary neurotrophic factor (CNTF), laminin, and fibronectin.[52–58] They also express membrane proteins and secreted proteins involved in growth cone guidance and repulsion such as ephrins, semaphorins, tenascin, chondroitin sulfate proteoglycans (CSPGs), and heparan sulfate proteoglycans (HSPGs).[59–61]

Several different astrocyte-secreted and astrocyte membrane proteins have been characterized to effect different stages of synaptic development and maturation. Astrocyte-secreted thrombospondins (Tsps) and hevin (Sparcl1) induce the formation of structurally mature but silent and inactive synapses.[62,63] Astrocyte-secreted glypicans 4 and 6 (Gpc4, Gpc6) are sufficient to induce functional synapses, and Gpc4 recruits postsynaptic AMPA receptors (AMPARs) to dendritic surfaces.[64,65] Astrocyte transforming growth factor beta (TGFβ), BDNF, and gamma protocadherins can also induce excitatory synapse formation,[66–69] astrocyte neurocan, HepaCAM, and gamma protocadherins can mediate inhibitory synapse formation,[69–71] and astrocyte CSPGs and tumor necrosis factor alpha (TNFa) can regulate surface AMPARs.[72–74] In contrast, astrocyte-secreted SPARC (secreted protein acidic and rich in cysteine) blocks synapse formation and decreases synaptic AMPAR levels by antagonizing hevin.[63] Astrocyte-secreted chordin-like 1 (Chrdl1) recruits calcium-impermeable AMPAR subunits to mediate maturation of synapses.[75] The *in vivo* expression timeline of these astrocyte-secreted proteins

parallels their effect: Tsps and Gpc4/6 are expressed highly from mouse postnatal day (P)0 to P7, when synapses are beginning to form, while Chrdl1 reaches peak expression at P14, when the AMPAR subunit switch is known to occur.[75,76]

Astrocytes in neurodevelopmental disorders. Both cell-intrinsic and non-cell-autonomous astrocyte dysfunction is increasingly recognized to play a role in neurodevelopmental disorders.[77,48,76,78] Astrocyte dysregulations implicated in different forms of neurodevelopmental disorders include changes in their gene expression profiles—including changed membrane receptors and ion channels, increased reactivity, and altered signaling—as well as impairments in support of neuronal maturation.[78] Synaptic dysfunction is prominent in many neurological disorders, and dysregulated astrocyte-synapse contacts and astrocyte-secreted proteins play a role. Indeed, recent studies have shown a role for astrocyte-secreted proteins in mouse models of the three genetic neurodevelopmental disorders fragile X syndrome (FXS),[79,80] Rett syndrome (RTT),[81–83] and Down syndrome (DS).[84,85] In both FXS and RTT, wild type (WT) astrocytes or simply the conditioned media containing astrocyte-secreted compounds (ACM) can rescue mutant neuron phenotypes,[79,81,86,87] and in DS, astrocyte-secreted thrombospondin 1 regulates spine density and synapse formation.[84]

Fragile X syndrome

Fragile X syndrome and autism spectrum disorder. Fragile X syndrome (FXS) is the most common single-gene cause and most common inherited form of intellectual disability (ID) and autism spectrum disorder (ASD), and it causes lifelong morbidity in around 1 in 5,000.[88,89] FXS is caused by loss of fragile X messenger ribonucleoprotein (FMRP), most commonly through CGG trinucleotide repeat expansion in the FMR1 promoter on the X chromosome. Despite being the most prevalent inherited form of intellectual disability, FXS is predominantly treated by symptom

only.[90] The causal gene of FXS, FMR1, is located on the X chromosome, and so affected males are homozygous and affected females are heterozygous and mosaic for *FMR1* expression due to random inactivation of the X chromosome. Clinical severity of FXS and prevalence of comorbid conditions (ASD, seizures) correlates with the percentage of cells with abnormal *FMR1* expression,[88] and thus females typically have less severe and more variable manifestations of FXS than males.[91,92] FXS presents with a constellation of characteristic clinical features that may or may not be present in every diagnosed individual: intellectual disability (85% in males, 30% in females), autism spectrum disorder symptoms (50-60% in males, 20% in females), attention-deficit/hyperactivity disorder (80% in males, 40% in females), childhood seizures (8-16% in males, 3-7% in females), anxiety (86% in males, 77% in females), and sensory hyperreactivity across modalities (visual, tactile, auditory; 87% of males and 68% of females with at least one symptom[93,94]) are common neurologic and neuropsychiatric symptoms; other manifestations include characteristic physical features including hyperextensible joints relating to connective tissue changes, macroorchidism, motor delays and coordination deficits.[88] Characterization of FXS in gender-non-conforming individuals and those with differences in sexual development is understudied and merits further direct attention.

Molecular biology of fragile X syndrome. FMRP is a central regulator of gene expression, and one of its key roles is to act as a translational repressor and regulator of hundreds of mRNAs.[95] FMRP historically has been established to inhibit translation initiation and stall polyribosomes,[95–97] though recent reports suggest it can also activate translation of specific mRNAs,[96,97] bind to and modulate activity of other proteins including ion channels or target them for proteosomal degradation,[97] and even regulate RNA editing, transcription, and chromatin both indirectly through its other roles as well as through direct binding and nuclear localization.[96] Experimental research in FXS primarily uses the Fmr1 KO mouse model.[98] While this model does not capture the transcriptional silencing of the FMR1 gene seen in most human FXS,[88,99] it does

recapitulate phenotypes observed in human FXS such as immature dendritic spines,[100–102] altered cortical volume,[103,104] hypersensitivity,[105] macroorchidism,[105] and seizures. Research with Fmr1 KO has implicated many pathways mediating the effects of FMRP deficiency.[88,105–107] Established pathways and phenotypes include excessive metabotropic glutamate receptor signaling (mGluR) associated with downstream phosphoinositide 3-kinase/mammalian target of rapamycin (PI3K/mTOR) pathway activation and altered neuronal plasticity in many brain regions, reduction in the inhibitory gamma-aminobutyric acid (GABAergic) system across brain regions and associated excitatory-inhibitory imbalances, ion channel dysfunction, dysregulated endocannabinoid signaling, increased bulk level of translation, and decreased cyclic AMP metabolism, among others.[88,97] However, understanding of how these mechanisms interact and lead to neuropathological, electrophysiologic (hyperexcitability),[107] and behavioral phenotypes remains incomplete. Moreover, while targeting these pathways can rescue Fmr1 KO deficits in mice,[108–117] results in clinical trials are often equivocal.[118–120] This may reflect an incomplete understanding of this complex disorder. Moreover, as many of the pathways affected by FXS overlap with those in the more prevalent sporadic ASD,[97,106,121,122] knowledge of FXS pathophysiology may also translate to ASD.

Astrocytes in fragile X syndrome. Most research in FXS has focused on intrinsic changes within neurons. However, emerging research has identified that astrocytes play a role.[77,123] Beside their established role in maintaining homeostasis in the brain, astrocytes are increasingly recognized as active participants in the development and plasticity of dendritic spines and synapses.[48,76] As astrocytes mature in concert with neurons, they release temporally regulated proteins to promote stages of neural development from dendrite growth and synapse formation, to maturation and pruning.[76,124] *In vivo*, mouse postnatal day (P)7 astrocytes express FMRP at double the levels of neurons,[125] and astrocyte-specific KO of FMRP precipitates FXS-like dendritic spine, electrophysiologic, and behavioral deficits, while astrocyte-specific re-expression of FMRP

rescues the same deficits.[126–128] One possible mechanism of astrocyte involvement in FXS is via disinhibition of astrocyte mGluR5, leading to downregulation of glutamate transporter 1 (GLT1), increased synaptic cleft glutamate, and enhanced neuronal excitability.[126,129] Another possible underlying mechanism is via alteration of secreted proteins by FXS astrocytes. *In vitro*, co-culture of WT neurons with FXS astrocytes results in abnormal dendritic morphology and impaired synaptic protein clustering at 7 but not 21 days, while co-culture of FXS neurons with WT astrocytes shows normal development, suggesting a causal role for astrocytes in FXS pathology.[79,80] Work in our lab and others has shown astrocyte conditioned media (ACM) from FXS astrocytes is sufficient to induce neurite outgrowth and electrophysiologic defects, suggesting a role for astrocyte-secreted proteins.[87,130,131] Recent work has separately implicated astrocyte choleterol[132,133] as well as several astrocyte-secreted proteins such as neurotrophin-3,[131] thrombospondin-1,[134] hevin,[135] and SPARC[135] in FXS pathogenesis. However, the mechanistic link from FMRP to these proteins remains uncertain. Moreover, no FXS studies have selectively perturbed astrocyte-secreted proteins *in vivo*.

BMP Signaling

The BMP pathway. Bone Morphogenetic Proteins (BMPs) are members of the transforming growth factor β (TGFβ) protein superfamily (**Figure 1.4**).[136] Originally described as cytokines that induce bone formation, BMPs are now appreciated for roles spanning multiple organ systems, and across stages of life from embryonic development to homeostasis and tissue repair.[137,138] BMPs are ligands that transduce their signals through serine/threonine kinase receptors (BMPR1A, BMPR1B, and BMPR2) on the plasma membrane.[137,138] Downstream BMP signaling occurs both via SMAD-dependent (canonical) pathways and SMAD-independent (noncanonical) pathways. In the canonical pathway, secreted BMPs—typically homo- or heterodimers—bind to and promote the colocalization of a heterotetrameric complex of two

BMPR1 and two BMPR2 receptors.[136–138] The constitutively active kinase domain of BMPR2 then phosphorylates the glycine-serine-rich (GS) domain of BMPR1, activating its kinase activity and promoting phosphorylation of the carboxyl-terminal S-S-X-S motif of receptor-regulated SMADs (R-SMADs) SMAD1, SMAD5, and/or SMAD8.[137,138] This C-terminal phosphorylation in turn promotes formation of trimeric complexes with transcriptional mediator SMAD4 (R-SMAD-R-SMAD-SMAD4), which translocate into the nucleus and coordinate with other transcriptional machinery to target hundreds of genomic loci including the *Id* genes.[136,139] Notably, non-BMP TGFβ ligands activate transcriptional responses via a similar canonical pathway, via TGFBR1/TGBR2, R-SMADs SMAD2 and SMAD3, and trimeric complexes of these R-SMADs with SMAD4.[136] Despite both employing SMAD4, the BMP and TGFβ cascades generate pathway-specific responses through differential complex binding in the nucleus, as well as through other context-, developmental state-, and cell type-specific factors.[136] Apart from the canonical pathway above, many variations and cross-pathway interactions have been reported.[136–138] The cytoplasmic C-terminal domain of BMPR2 can mediate activation of LIM domain kinase 1 (LIMK1), which then phosphorylates cofilin to inhibit actin polymerization and regulate neurite outgrowth.[140]

BMPs in the nervous system. BMP signaling is implicated in many early neurodevelopmental processes such as gastrulation, dorsoventral neural tube patterning via a gradient with Sonic Hedgehog (SHH), neuronal axonal guidance, forebrain development, and cerebellar granule neuron development.[137,141–143] BMPs also promote astrogliogenesis from glial progenitors,[142] inhibit oligodendroglial and neuronal cell fate in precursors,[144] as well as regulate synapse formation,[66,145–147] dendritic outgrowth,[148–151] and blood-brain barrier formation.[152] BMPs lead to maturation of astrocytes *in vitro* with involvement of canonical signaling.[153] However, the role of BMP signaling in and on astrocytes *in vivo* during postnatal development into adulthood remains poorly understood. Apart from their many required roles in neurodevelopment, BMPs and

dysregulated BMP signaling have been implicated in many neurologic disorders spanning from neurodevelopmental disorders such as fragile X syndrome, Williams syndrome, Angelman syndrome, Mowat-Wilson syndrome, and Troyer syndrome to neurodegenerative disorders such as Alzheimer's disease, Parkinson's disease, Huntington's disease, amyotrophic lateral sclerosis (ALS), and multiple sclerosis.[137]

BMPs, fragile X syndrome, and a role for astrocytes? Recent work by Kashima and colleagues demonstrated that a global heterozygous BMPR2 loss of function could rescue FXS spine phenotypes (morphological immaturity of dentate gyrus spines at P7), and that this rescue was phenocopied by intracerebroventricular injection of LIMK inhibitor, suggesting noncanonical BMP signaling as a mediator of FXS pathology.[140] Given the reported causal role of astrocytes in FXS phenotypes *in vitro*, previous graduate student Alison Caldwell explored whether BMP signaling in or by astrocytes could be mediating FXS phenotypes (**Figure 1.5**). In unbiased transcriptional and secretomic profiling of astrocytes cultured in serum-free media from P7 WT or Fmr1 KO mice, canonical BMP transcriptional signatures were increased in Fmr1 KO astrocytes, and BMP6 was increased both at the level of Fmr1 KO astrocyte RNA and secreted proteins.[86] Interestingly, incubating WT astrocytes with BMP6 led to over the third of the same 130 protein secretion changes as in Fmr1 KO astrocytes.[86] These results suggest that autocrine or paracrine astrocyte BMP signaling may be upstream of Fmr1 KO astrocyte protein secretion dysregulation. Moreover, Fmr1 KO astrocyte-conditioned media (ACM) led to decreased neurite outgrowth in cultured WT neurons, and inhibiting BMP signaling in FXS astrocytes with noggin led to astrocyte-conditioned media that rescued neurite outgrowth deficits.[86] This rescue effect was not due to residual noggin in the conditioned media, as WT neurons growth with Fmr1 KO ACM supplemented with noggin did not have rescued outgrowth.[86] Together, these results suggest canonical BMP signaling in astrocytes as a mediator of FXS pathology. Could this be a mechanism of FXS pathophysiology *in vivo* as well? Alison found that astrocytes in P7 Fmr1 KO

mouse visual cortex had increased pSMAD1/5/8 and thus canonical BMP signaling,[86] suggesting the *in vitro* mechanism may apply *in vivo* as well.

BMP signaling in astrocyte heterogeneity? Astrocytes are increasingly recognized as being diverse both across and within brain regions.[154–157] Across the brain, astrocytes specialize to their physiologic context: "bushy" irregularly-shaped protoplasmic astrocytes in grey matter,[154] "star-like" regularly-contoured fibrous astrocytes in white matter,[154] elaborately-branched Bergman glia spanning the molecular layer of the cerebellum,[155] and Müller glia spanning the stereotyped retinal layers are prototypical examplars.[156] Recent studies have established that this morphological diversity correlates to a transcriptomic diversity of astrocytes across regions.[158] In recent years multiple groups have demonstrated that astrocyte morphological heterogeneity, like that of neurons, correlates with both their functional and transcriptional diversity.[154,155,159] This is evident between brain regions such as cortex, hippocampus, thalamus and cerebellum,[158,160–163] as well as within brain regions such as for astrocytes in different cortical layers or regions of the hippocampus.[76,159,164–168] Progress has been made in understanding what underlies some of this heterogeneity, indicating a role for interactions with neighboring neurons and extrinsic cues including secreted morphogens.[164–166] However, a complete understanding of the factors that shape astrocyte intraregional heterogeneity is still lacking.

This dissertation seeks to ask the following questions: can suppressing astrocyte BMP signaling improve FXS phenotypes *in vivo*? What are mechanisms through which BMP signaling may mediate FXS phenotypes in the complex cellular milieu of the *in vivo* brain parenchyma? Asked more broadly, can modulation of a pathway intrinsic to non-neuronal cells improve FXS deficits? Moreover, what is the function of BMP signaling in astrocyte heterogeneity and development in its entirety?

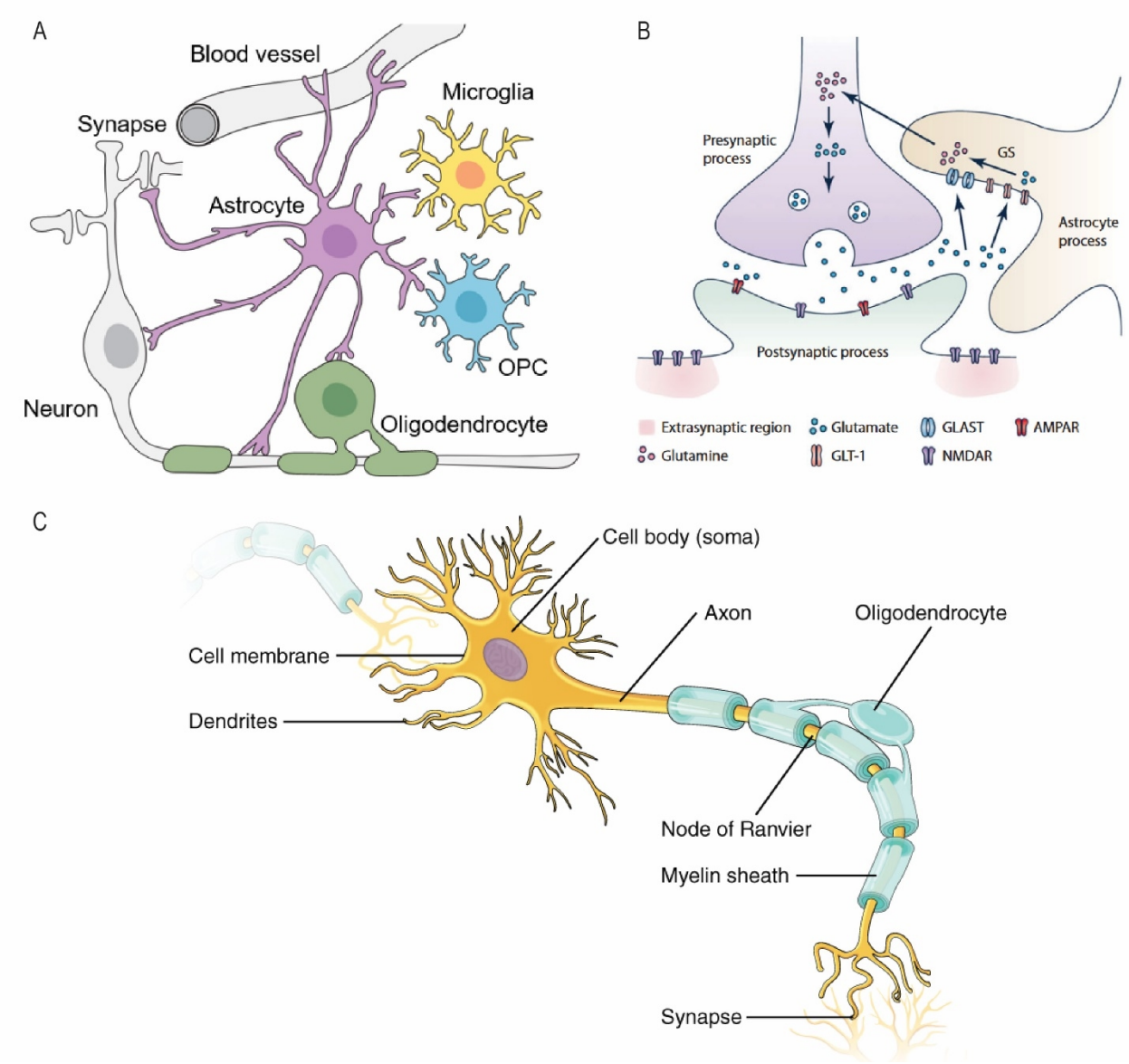

Figure 1.1. Overview of cell types in the brain, the synapse, and the neuron.

A. Major cell types in the brain include neurons, astrocytes (purple), oligodendrocytes (green), microglia (yellow), and oligodendrocyte precursor cells (OPCs) (blue). Adapted from Allen and Lyons, 2018.[7]
B. Overview of the synapse, where neuron presynaptic processes (purple) appose postsynaptic processes (green), separated by a synaptic cleft. Astrocyte processes (orange) play key functions at the synapse. AMPAR = alpha-amino-3-hydroxy-5-methyl-4-isoxazolepropionic acid receptor, a common neurotransmitter receptor. NMDAR = N-methyl-D-aspartic acid receptor, another common neurotransmitter receptor. GLAST = glutamate aspartate transporter. GLT-1 = glutamate transporter 1. Graphic from Blanco-Suárez et al., 2018.[48]
C. Schematization of the anatomy of a neuronal cell, including dendrites, soma or cell body, as well as axon and synapses. Image from Wikimedia (https://commons.wikimedia.org/wiki/File:1206_The_Neuron.jpg).

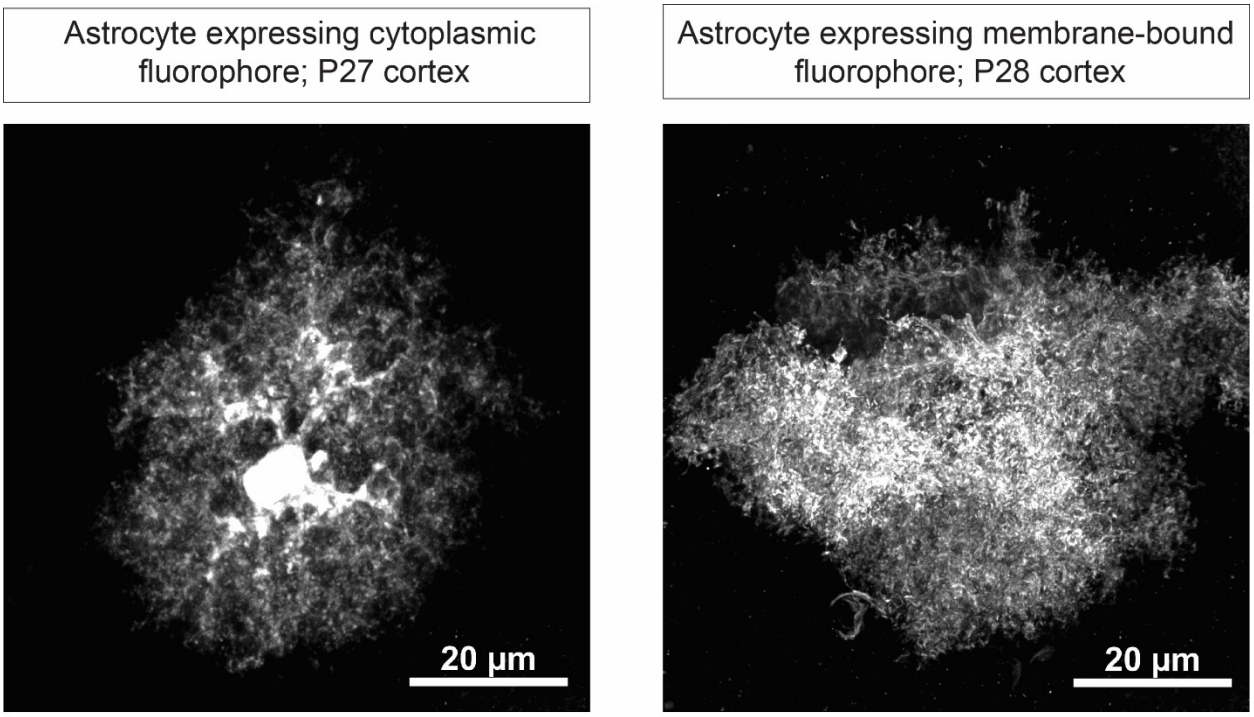

Figure 1.2. Complexity of astrocyte morphology. Showing two cortical astrocytes (see Figure 1.3), one labeled with cytoplasmic fluorophore, and one labeled with membrane-bound fluorophore. P = postnatal day (age of mouse).

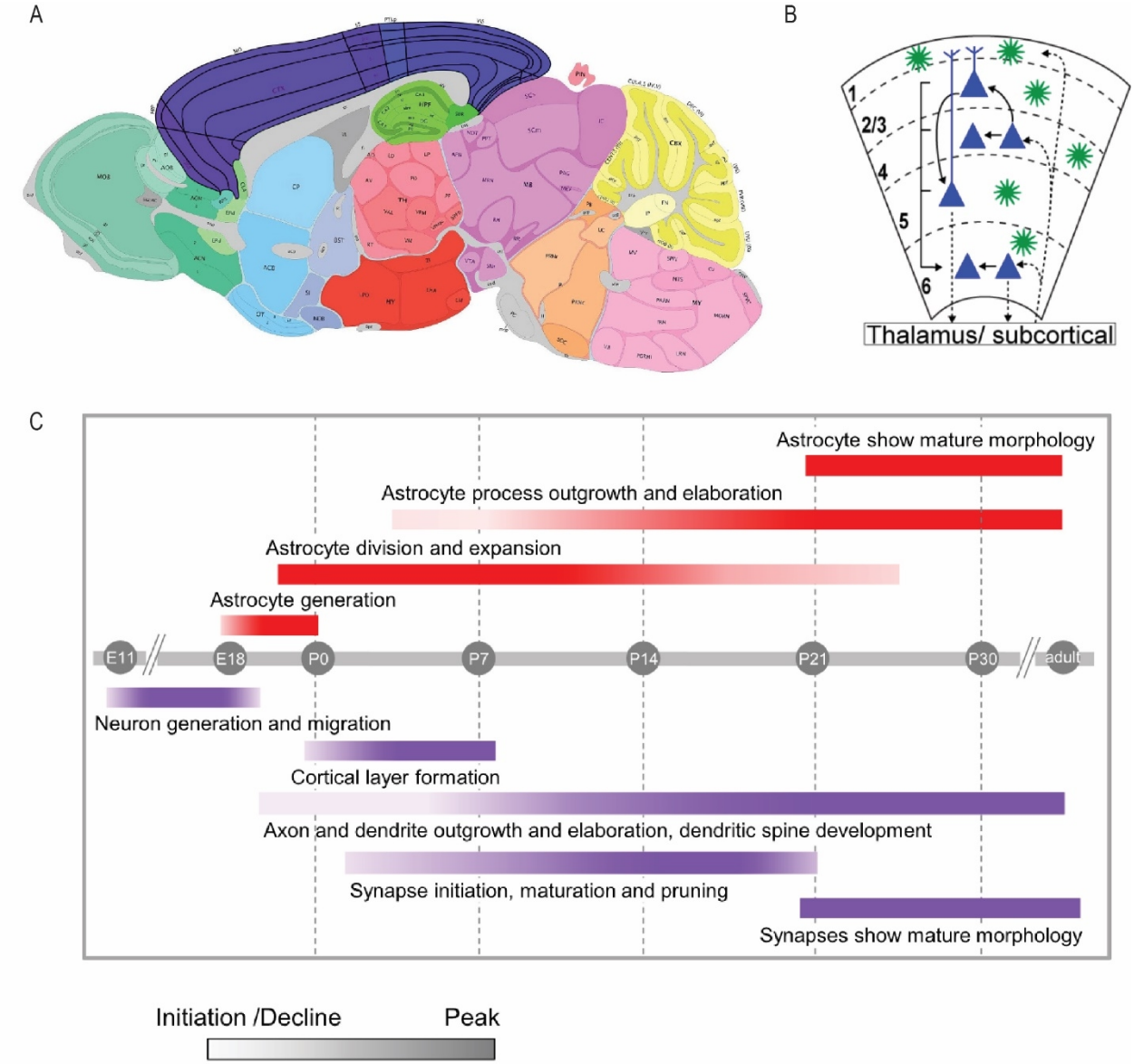

Figure 1.3. Overview of anatomy of the brain cortex and astrocyte and neuron development.

A. Sagittal section of mouse brain, viewed in the Allen Brain Atlas (mouse.brain-map.org). The region highlighted in purple is the cortex.
B. Schematic of the six cortical layers. Neurons schematized with blue triangles and astrocytes with green circles. Canonical cortical circuits with inputs and outputs are illustrated with arrows. Graphic from Farhy-Tselnicker et al., 2021.[169]
C. Overview of synchrony of astrocyte and neuronal development in the mouse brain. Graphic from Farhy-Tselnicker et al., 2017.[76] P = postnatal day (age of mouse).

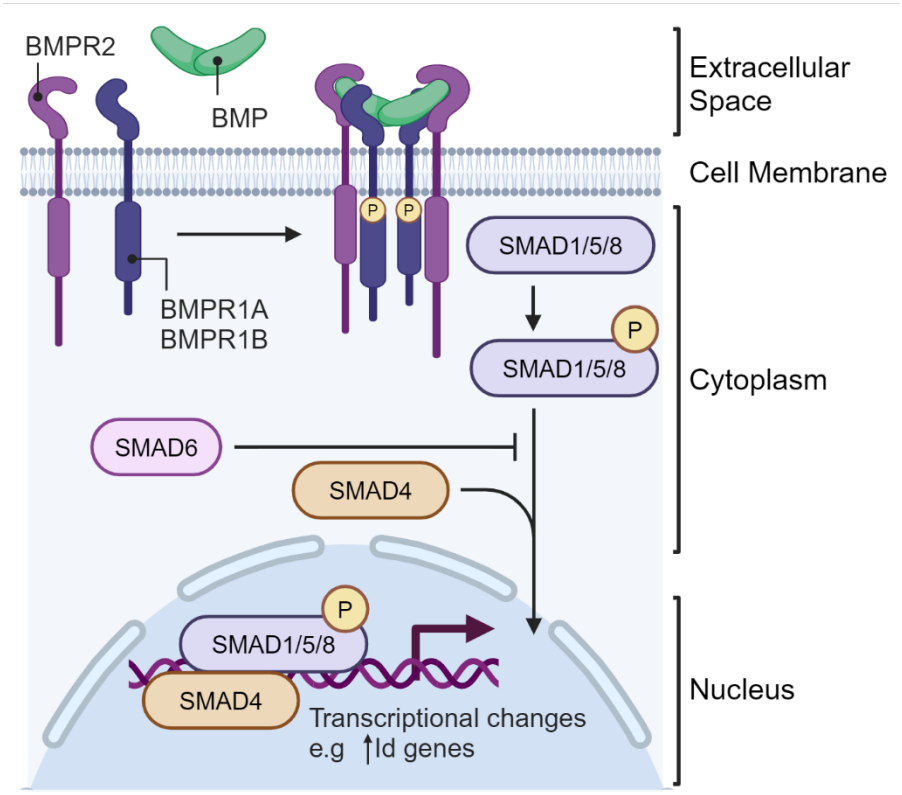

Figure 1.4. The canonical bone morphogenetic protein (BMP) signaling pathway. Signals from extracellular BMPs are mediated by receptors and SMAD proteins, and transcriptional changes are effected by protein complexes including SMAD4.

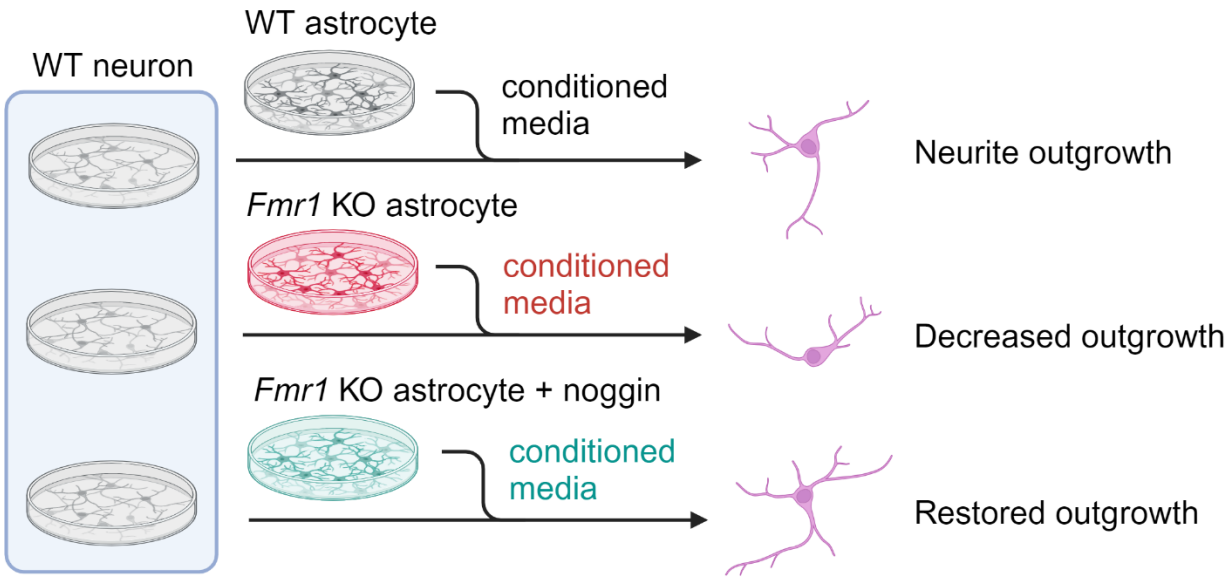

Figure 1.5. Inhibition of BMP signaling in cultured Fmr1 KO astrocytes rescues Fmr1 KO neurite outgrowth deficits. Created based on Caldwell et al., 2022.[86]

References

1. *Principles of Neural Science, 5th edition.* Edited by Kandel, ER, Schwartz JH, Jessell TM, Siegelbaum SA, and Hudspeth AJ. McGraw-Hill, New York (2013).

2. Allen, N. J. Star Power: Astrocytes Regulate Behavior. *Cell* **177**, 1091–1093 (2019).

3. Hösli, L. *et al.* Direct vascular contact is a hallmark of cerebral astrocytes. *Cell Reports* **39**, 110599 (2022).

4. Baldwin, K. T., Murai, K. K. & Khakh, B. S. Astrocyte morphology. *Trends in Cell Biology* S0962892423002040 (2023) doi:10.1016/j.tcb.2023.09.006.

5. Allen, N. J. & Eroglu, C. Cell Biology of Astrocyte-Synapse Interactions. *Neuron* **96**, 697–708 (2017).

6. Barros, L. F., Schirmeier, S. & Weber, B. The Astrocyte: Metabolic Hub of the Brain. *Cold Spring Harb Perspect Biol* a041355 (2024) doi:10.1101/cshperspect.a041355.

7. Allen, N. J. & Lyons, D. A. Glia as architects of central nervous system formation and function. *Science* **362**, 181–185 (2018).

8. Chung, W.-S., Baldwin, K. T. & Allen, N. J. Astrocyte Regulation of Synapse Formation, Maturation, and Elimination. *Cold Spring Harb Perspect Biol* a041352 (2024) doi:10.1101/cshperspect.a041352.

9. Simons, M. & Nave, K.-A. Oligodendrocytes: Myelination and Axonal Support. *Cold Spring Harb Perspect Biol* **8**, a020479 (2016).

10. Bergles, D. E. & Richardson, W. D. Oligodendrocyte Development and Plasticity. *Cold Spring Harb Perspect Biol* **8**, a020453 (2016).

11. Akay, L. A., Effenberger, A. H. & Tsai, L.-H. Cell of all trades: oligodendrocyte precursor cells in synaptic, vascular, and immune function. *Genes Dev.* **35**, 180–198 (2021).

12. Li, Q. & Barres, B. A. Microglia and macrophages in brain homeostasis and disease. *Nat Rev Immunol* **18**, 225–242 (2018).

13. Del Bigio, M. R. Ependymal cells: biology and pathology. *Acta Neuropathol* **119**, 55–73 (2010).

14. Wolburg, H., Noell, S., Mack, A., Wolburg-Buchholz, K. & Fallier-Becker, P. Brain endothelial cells and the glio-vascular complex. *Cell Tissue Res* **335**, 75–96 (2009).

15. Pietilä, R. *et al.* Molecular anatomy of adult mouse leptomeninges. *Neuron* S0896627323006669 (2023) doi:10.1016/j.neuron.2023.09.002.

16. Hall, C. N. *et al.* Capillary pericytes regulate cerebral blood flow in health and disease. *Nature* **508**, 55–60 (2014).

17. Frösen, J. & Joutel, A. Smooth muscle cells of intracranial vessels: from development to disease. *Cardiovascular Research* **114**, 501–512 (2018).

18. Castellani, G., Croese, T., Peralta Ramos, J. M. & Schwartz, M. Transforming the understanding of brain immunity. *Science* **380**, eabo7649 (2023).

19. Götz, M. & Huttner, W. B. The cell biology of neurogenesis. *Nat Rev Mol Cell Biol* **6**, 777–788 (2005).

20. Rakic, P. Evolution of the neocortex: a perspective from developmental biology. *Nat Rev Neurosci* **10**, 724–735 (2009).

21. Lui, J. H., Hansen, D. V. & Kriegstein, A. R. Development and Evolution of the Human Neocortex. *Cell* **146**, 18–36 (2011).

22. Olson, E. C. & Walsh, C. A. Smooth, rough and upside-down neocortical development. *Current Opinion in Genetics & Development* **12**, 320–327 (2002).

23. Corbin, J. G., Nery, S. & Fishell, G. Telencephalic cells take a tangent: non-radial migration in the mammalian forebrain. *Nat Neurosci* **4**, 1177–1182 (2001).

24. Hamburger, V. & Levi-Montalcini, R. Proliferation, differentiation and degeneration in the spinal ganglia of the chick embryo under normal and experimental conditions. *J. Exp. Zool.* **111**, 457–501 (1949).

25. Yuan, J. & Yankner, B. A. Apoptosis in the nervous system. *Nature* **407**, 802–809 (2000).

26. Oppenheim, R. W. Naturally occurring cell death during neural development. *Trends in Neurosciences* **8**, 487–493 (1985).

27. Gaiano, N. & Fishell, G. The Role of Notch in Promoting Glial and Neural Stem Cell Fates. *Annu. Rev. Neurosci.* **25**, 471–490 (2002).

28. Hermanson, O., Jepsen, K. & Rosenfeld, M. G. N-CoR controls differentiation of neural stem cells into astrocytes. *Nature* **419**, 934–939 (2002).

29. Sun, Y. *et al.* Neurogenin Promotes Neurogenesis and Inhibits Glial Differentiation by Independent Mechanisms. *Cell* **104**, 365–376 (2001).

30. Deneen, B. *et al.* The Transcription Factor NFIA Controls the Onset of Gliogenesis in the Developing Spinal Cord. *Neuron* **52**, 953–968 (2006).

31. Kang, P. *et al.* Sox9 and NFIA Coordinate a Transcriptional Regulatory Cascade during the Initiation of Gliogenesis. *Neuron* **74**, 79–94 (2012).

32. Zhou, Q. & Anderson, D. J. The bHLH Transcription Factors OLIG2 and OLIG1 Couple Neuronal and Glial Subtype Specification. *Cell* **109**, 61–73 (2002).

33. Tessier-Lavigne, M. & Goodman, C. S. The Molecular Biology of Axon Guidance. *Science* **274**, 1123–1133 (1996).

34. Zou, Y. & Lyuksyutova, A. I. Morphogens as conserved axon guidance cues. *Current Opinion in Neurobiology* **17**, 22–28 (2007).

35. Zou, Y., Stoeckli, E., Chen, H. & Tessier-Lavigne, M. Squeezing Axons Out of the Gray Matter. *Cell* **102**, 363–375 (2000).

36. Charron, F., Stein, E., Jeong, J., McMahon, A. P. & Tessier-Lavigne, M. The Morphogen Sonic Hedgehog Is an Axonal Chemoattractant that Collaborates with Netrin-1 in Midline Axon Guidance. *Cell* **113**, 11–23 (2003).

37. Augsburger, A., Schuchardt, A., Hoskins, S., Dodd, J. & Butler, S. BMPs as Mediators of Roof Plate Repulsion of Commissural Neurons. *Neuron* **24**, 127–141 (1999).

38. Serafini, T. *et al.* The netrins define a family of axon outgrowth-promoting proteins homologous to C. elegans UNC-6. *Cell* **78**, 409–424 (1994).

39. Hattori, D., Millard, S. S., Wojtowicz, W. M. & Zipursky, S. L. Dscam-Mediated Cell Recognition Regulates Neural Circuit Formation. *Annu. Rev. Cell Dev. Biol.* **24**, 597–620 (2008).

40. Frisén, J. *et al.* Ephrin-A5 (AL-1/RAGS) Is Essential for Proper Retinal Axon Guidance and Topographic Mapping in the Mammalian Visual System. *Neuron* **20**, 235–243 (1998).

41. Kidd, T. *et al.* Roundabout Controls Axon Crossing of the CNS Midline and Defines a Novel Subfamily of Evolutionarily Conserved Guidance Receptors. *Cell* **92**, 205–215 (1998).

42. Kolodkin, A. L. *et al.* Neuropilin Is a Semaphorin III Receptor. *Cell* **90**, 753–762 (1997).

43. Kim, S. & Chiba, A. Dendritic guidance. *Trends in Neurosciences* **27**, 194–202 (2004).

44. Jan, Y.-N. & Jan, L. Y. Branching out: mechanisms of dendritic arborization. *Nat Rev Neurosci* **11**, 316–328 (2010).

45. Graf, E. R., Zhang, X., Jin, S.-X., Linhoff, M. W. & Craig, A. M. Neurexins Induce Differentiation of GABA and Glutamate Postsynaptic Specializations via Neuroligins. *Cell* **119**, 1013–1026 (2004).

46. Baudouin, S. & Scheiffele, P. SnapShot: Neuroligin-Neurexin Complexes. *Cell* **141**, 908-908.e1 (2010).

47. Suzuki, S. *et al.* Brain-Derived Neurotrophic Factor Regulates Cholesterol Metabolism for Synapse Development. *Journal of Neuroscience* **27**, 6417–6427 (2007).

48. Blanco-Suárez, E., Caldwell, A. L. M. & Allen, N. J. Role of astrocyte-synapse interactions in CNS disorders: Astrocyte-synapse disease. *The Journal of Physiology* **595**, 1903–1916 (2017).

49. Banker, G. A. Trophic Interactions Between Astroglial Cells and Hippocampal Neurons in Culture. *Science* **209**, 809–810 (1980).

50. Pfrieger, F. W. & Barres, B. A. Synaptic Efficacy Enhanced by Glial Cells in Vitro. *Science* **277**, 1684–1687 (1997).

51. Ullian, E. M., Sapperstein, S. K., Christopherson, K. S. & Barres, B. A. Control of Synapse Number by Glia. *Science* **291**, 657–661 (2001).

52. Dougherty, K. D., Dreyfus, C. F. & Black, I. B. Brain-Derived Neurotrophic Factor in Astrocytes, Oligodendrocytes, and Microglia/Macrophages after Spinal Cord Injury. *Neurobiology of Disease* **7**, 574–585 (2000).

53. Liesi, P. & Silver, J. Is astrocyte laminin involved in axon guidance in the mammalian CNS? *Developmental Biology* **130**, 774–785 (1988).

54. Müller, A., Hauk, T. G. & Fischer, D. Astrocyte-derived CNTF switches mature RGCs to a regenerative state following inflammatory stimulation. *Brain* **130**, 3308–3320 (2007).

55. Ang, L. C., Bhaumick, B., Munoz, D. G., Sass, J. & Juurlink, B. H. J. Effects of astrocytes, insulin and insulin-like growth factor I on the survival of motoneurons in vitro. *Journal of the Neurological Sciences* **109**, 168–172 (1992).

56. Tom, V. J., Doller, C. M., Malouf, A. T. & Silver, J. Astrocyte-Associated Fibronectin Is Critical for Axonal Regeneration in Adult White Matter. *J. Neurosci.* **24**, 9282–9290 (2004).

57. Rocha, S. M., Cristovão, A. C., Campos, F. L., Fonseca, C. P. & Baltazar, G. Astrocyte-derived GDNF is a potent inhibitor of microglial activation. *Neurobiology of Disease* **47**, 407–415 (2012).

58. Cahoy, J. D. *et al.* A Transcriptome Database for Astrocytes, Neurons, and Oligodendrocytes: A New Resource for Understanding Brain Development and Function. *Journal of Neuroscience* **28**, 264–278 (2008).

59. Molofsky, A. V. *et al.* Astrocyte-encoded positional cues maintain sensorimotor circuit integrity. *Nature* **509**, 189–194 (2014).

60. Meiners, S., Powell, E. & Geller, H. A distinct subset of tenascin/CS-6-PG-rich astrocytes restricts neuronal growth in vitro. *J. Neurosci.* **15**, 8096–8108 (1995).

61. Powell, E. M., Meiners, S., DiProspero, N. A. & Geller, H. M. Mechanisms of astrocyte-directed neurite guidance. *Cell and Tissue Research* **290**, 385–393 (1997).

62. Christopherson, K. S. *et al.* Thrombospondins Are Astrocyte-Secreted Proteins that Promote CNS Synaptogenesis. *Cell* **120**, 421–433 (2005).

63. Kucukdereli, H. *et al.* Control of excitatory CNS synaptogenesis by astrocyte-secreted proteins Hevin and SPARC. *Proc. Natl. Acad. Sci. U.S.A.* **108**, (2011).

64. Allen, N. J. *et al.* Astrocyte glypicans 4 and 6 promote formation of excitatory synapses via GluA1 AMPA receptors. *Nature* **486**, 410–414 (2012).

65. Farhy-Tselnicker, I. *et al.* Astrocyte-Secreted Glypican 4 Regulates Release of Neuronal Pentraxin 1 from Axons to Induce Functional Synapse Formation. *Neuron* **96**, 428-445.e13 (2017).

66. Fuentes-Medel, Y. *et al.* Integration of a Retrograde Signal during Synapse Formation by Glia-Secreted TGF-β Ligand. *Current Biology* **22**, 1831–1838 (2012).

67. Diniz, L. P. *et al.* Astrocyte-induced Synaptogenesis Is Mediated by Transforming Growth Factor β Signaling through Modulation of d-Serine Levels in Cerebral Cortex Neurons. *Journal of Biological Chemistry* **287**, 41432–41445 (2012).

68. Gómez-Casati, M. E. *et al.* Nonneuronal cells regulate synapse formation in the vestibular sensory epithelium via erbB-dependent BDNF expression. *Proc. Natl. Acad. Sci. U.S.A.* **107**, 17005–17010 (2010).

69. Garrett, A. M. & Weiner, J. A. Control of CNS Synapse Development by γ-Protocadherin-Mediated Astrocyte–Neuron Contact. *J. Neurosci.* **29**, 11723–11731 (2009).

70. Baldwin, K. T. *et al.* HepaCAM controls astrocyte self-organization and coupling. *Neuron* **109**, 2427-2442.e10 (2021).

71. Irala, D. *et al.* Astrocyte-secreted neurocan controls inhibitory synapse formation and function. *Neuron* S0896627324001612 (2024) doi:10.1016/j.neuron.2024.03.007.

72. Pyka, M. *et al.* Chondroitin sulfate proteoglycans regulate astrocyte-dependent synaptogenesis and modulate synaptic activity in primary embryonic hippocampal neurons. *Eur J of Neuroscience* **33**, 2187–2202 (2011).

73. Frischknecht, R. *et al.* Brain extracellular matrix affects AMPA receptor lateral mobility and short-term synaptic plasticity. *Nat Neurosci* **12**, 897–904 (2009).

74. Stellwagen, D. & Malenka, R. C. Synaptic scaling mediated by glial TNF-α. *Nature* **440**, 1054–1059 (2006).

75. Blanco-Suarez, E., Liu, T.-F., Kopelevich, A. & Allen, N. J. Astrocyte-Secreted Chordin-like 1 Drives Synapse Maturation and Limits Plasticity by Increasing Synaptic GluA2 AMPA Receptors. *Neuron* **100**, 1116-1132.e13 (2018).

76. Farhy-Tselnicker, I. & Allen, N. J. Astrocytes, neurons, synapses: a tripartite view on cortical circuit development. *Neural Development* **13**, (2018).

77. Molofsky, A. V. *et al.* Astrocytes and disease: a neurodevelopmental perspective. *Genes Dev.* **26**, 891–907 (2012).

78. Cresto, N., Pillet, L.-E., Billuart, P. & Rouach, N. Do Astrocytes Play a Role in Intellectual Disabilities? *Trends in Neurosciences* **42**, 518–527 (2019).

79. Jacobs, S. & Doering, L. C. Astrocytes Prevent Abnormal Neuronal Development in the Fragile X Mouse. *Journal of Neuroscience* **30**, 4508–4514 (2010).

80. Jacobs, S., Nathwani, M. & Doering, L. C. Fragile X astrocytes induce developmental delays in dendrite maturation and synaptic protein expression. *BMC Neuroscience* **11**, 132 (2010).

81. Ballas, N., Lioy, D. T., Grunseich, C. & Mandel, G. Non–cell autonomous influence of MeCP2-deficient glia on neuronal dendritic morphology. *Nat Neurosci* **12**, 311–317 (2009).

82. Okabe, Y. *et al.* Alterations of Gene Expression and Glutamate Clearance in Astrocytes Derived from an MeCP2-Null Mouse Model of Rett Syndrome. *PLoS ONE* **7**, e35354 (2012).

83. Williams, E. C. *et al.* Mutant astrocytes differentiated from Rett syndrome patients-specific iPSCs have adverse effects on wild-type neurons. *Human Molecular Genetics* **23**, 2968–2980 (2014).

84. Garcia, O., Torres, M., Helguera, P., Coskun, P. & Busciglio, J. A Role for Thrombospondin-1 Deficits in Astrocyte-Mediated Spine and Synaptic Pathology in Down's Syndrome. *PLoS ONE* **5**, e14200 (2010).

85. Chen, C. *et al.* Role of astroglia in Down's syndrome revealed by patient-derived human-induced pluripotent stem cells. *Nat Commun* **5**, 4430 (2014).

86. Caldwell, A. L. M. *et al.* Aberrant astrocyte protein secretion contributes to altered neuronal development in multiple models of neurodevelopmental disorders. *Nat Neurosci* **25**, 1163–1178 (2022).

87. Sharma, S. D. *et al.* Astrocytes mediate cell non-autonomous correction of aberrant firing in human FXS neurons. *Cell Reports* **42**, 112344 (2023).

88. Hagerman, R. J. *et al.* Fragile X syndrome. *Nature Reviews Disease Primers* **3**, (2017).

89. Genovese, A. & Butler, M. G. The Autism Spectrum: Behavioral, Psychiatric and Genetic Associations. *Genes* **14**, 677 (2023).

90. Esch, H. V., Firth, H. V. & TePas, E. Fragile X syndrome: Management in children and adolescents. *UpToDate* (2020).

91. Keysor, C. S. & Mazzocco, M. M. M. A developmental approach to understanding Fragile X syndrome in females. *Microscopy Research and Technique* **57**, 179–186 (2002).

92. Bartholomay, K., Lee, C., Bruno, J., Lightbody, A. & Reiss, A. Closing the Gender Gap in Fragile X Syndrome: Review of Females with Fragile X Syndrome and Preliminary Research Findings. *Brain Sciences* **9**, 11 (2019).

93. Lachiewicz, A. M. *et al.* Sensory Symptoms and Signs of Hyperarousal in Individuals with Fragile X Syndrome: Findings from the FORWARD Registry and Database Multisite Study. *J Autism Dev Disord* (2023) doi:10.1007/s10803-023-06135-y.

94. Rais, M., Binder, D. K., Razak, K. A. & Ethell, I. M. Sensory Processing Phenotypes in Fragile X Syndrome. *ASN Neuro* **10**, 175909141880109 (2018).

95. Darnell, J. C. *et al.* FMRP Stalls Ribosomal Translocation on mRNAs Linked to Synaptic Function and Autism. *Cell* **146**, 247–261 (2011).

96. Richter, J. D. & Zhao, X. The molecular biology of FMRP: new insights into fragile X syndrome. *Nat Rev Neurosci* (2021) doi:10.1038/s41583-021-00432-0.

97. Bagni, C. & Zukin, R. S. A Synaptic Perspective of Fragile X Syndrome and Autism Spectrum Disorders. *Neuron* **101**, 1070–1088 (2019).

98. The Dutch-Belgian Fragile X Consortium. Fmr1 knockout mice: A model to study fragile X mental retardation. *Cell* **78**, 23–33 (1994).

99. Dahlhaus, R. Of Men and Mice: Modeling the Fragile X Syndrome. *Frontiers in Molecular Neuroscience* **11**, (2018).

100. He, C. X. & Portera-Cailliau, C. The trouble with spines in fragile X syndrome: density, maturity and plasticity. *Neuroscience* **251**, 120–128 (2013).

101. Nimchinsky, E. A., Oberlander, A. M. & Svoboda, K. Abnormal Development of Dendritic Spines in *FMR1* Knock-Out Mice. *The Journal of Neuroscience* **21**, 5139–5146 (2001).

102. Comery, T. A. *et al.* Abnormal dendritic spines in fragile X knockout mice: Maturation and pruning deficits. *Proceedings of the National Academy of Sciences* **94**, 5401–5404 (1997).

103. Ellegood, J., Pacey, L. K., Hampson, D. R., Lerch, J. P. & Henkelman, R. M. Anatomical phenotyping in a mouse model of fragile X syndrome with magnetic resonance imaging. *NeuroImage* **53**, 1023–1029 (2010).

104. Lai, J. K. Y., Lerch, J. P., Doering, L. C., Foster, J. A. & Ellegood, J. Regional brain volumes changes in adult male FMR1-KO mouse on the FVB strain. *Neuroscience* **318**, 12–21 (2016).

105. Kazdoba, T. M., Leach, P. T., Silverman, J. L. & Crawley, J. N. Modeling fragile X syndrome in the Fmr1 knockout mouse. *Intractable & Rare Diseases Research* **3**, 118–133 (2014).

106. Telias, M. Molecular Mechanisms of Synaptic Dysregulation in Fragile X Syndrome and Autism Spectrum Disorders. *Frontiers in Molecular Neuroscience* **12**, (2019).

107. Yan, Q. J., Asafo-Adjei, P. K., Arnold, H. M., Brown, R. E. & Bauchwitz, R. P. A phenotypic and molecular characterization of the fmr1-tm1Cgr Fragile X mouse. *Genes, Brain and Behavior* **3**, 337–359 (2004).

108. McCamphill, P. K. *et al.* Selective inhibition of glycogen synthase kinase 3α corrects pathophysiology in a mouse model of fragile X syndrome. *Science Translational Medicine* **12**, (2020).

109. Pyronneau, A. *et al.* Aberrant Rac1-cofilin signaling mediates defects in dendritic spines, synaptic function, and sensory perception in fragile X syndrome. *Science Signaling* **10**, eaan0852 (2017).

110. Dölen, G. *et al.* Correction of Fragile X Syndrome in Mice. *Neuron* **56**, 955–962 (2007).

111. Licznerski, P. *et al.* ATP Synthase c-Subunit Leak Causes Aberrant Cellular Metabolism in Fragile X Syndrome. *Cell* **0**, (2020).

112. Gkogkas, C. G. *et al.* Pharmacogenetic Inhibition of eIF4E-Dependent Mmp9 mRNA Translation Reverses Fragile X Syndrome-like Phenotypes. *Cell Reports* **9**, 1742–1755 (2014).

113. Dolan, B. M. *et al.* Rescue of fragile X syndrome phenotypes in Fmr1 KO mice by the small-molecule PAK inhibitor FRAX486. *Proceedings of the National Academy of Sciences* **110**, 5671–5676 (2013).

114. Santini, E. *et al.* Reducing eIF4E-eIF4G interactions restores the balance between protein synthesis and actin dynamics in fragile X syndrome model mice. *Science Signaling* **10**, eaan0665 (2017).

115. Bhattacharya, A. *et al.* Targeting Translation Control with p70 S6 Kinase 1 Inhibitors to Reverse Phenotypes in Fragile X Syndrome Mice. *Neuropsychopharmacology* **41**, 1991–2000 (2016).

116. Shukla, T. *et al.* A Highly Selective MNK Inhibitor Rescues Deficits Associated with Fragile X Syndrome in Mice. *Neurotherapeutics* (2020) doi:10.1007/s13311-020-00932-4.

117. Razak, K. A., Dominick, K. C. & Erickson, C. A. Developmental studies in fragile X syndrome. *J Neurodevelop Disord* **12**, 13 (2020).

118. Berry-Kravis, E. M. *et al.* Drug development for neurodevelopmental disorders: lessons learned from fragile X syndrome. *Nature Reviews Drug Discovery* **17**, 280–299 (2018).

119. Yamasue, H., Aran, A. & Berry-Kravis, E. Emerging pharmacological therapies in fragile X syndrome and autism: *Current Opinion in Neurology* **32**, 635–640 (2019).

120. Erickson, C., Schaefer, T. & Davenport, M. Emerging pharmacologic treatment options for fragile X syndrome. *The Application of Clinical Genetics* 75 (2015) doi:10.2147/TACG.S35673.

121. Kaufmann, W. E. *et al.* Autism Spectrum Disorder in Fragile X Syndrome: Cooccurring Conditions and Current Treatment. *Pediatrics* **139**, S194–S206 (2017).

122. Willsey, H. R., Willsey, A. J., Wang, B. & State, M. W. Genomics, convergent neuroscience and progress in understanding autism spectrum disorder. *Nat Rev Neurosci* **23**, 323–341 (2022).

123. Talvio, K. & Castrén, M. L. Astrocytes in fragile X syndrome. *Front. Cell. Neurosci.* **17**, 1322541 (2024).

124. Baldwin, K. T. & Eroglu, C. Molecular mechanisms of astrocyte-induced synaptogenesis. *Current Opinion in Neurobiology* **45**, 113–120 (2017).

125. Zhang, Y. *et al.* An RNA-Sequencing Transcriptome and Splicing Database of Glia, Neurons, and Vascular Cells of the Cerebral Cortex. *Journal of Neuroscience* **34**, 11929–11947 (2014).

126. Higashimori, H. *et al.* Selective Deletion of Astroglial FMRP Dysregulates Glutamate Transporter GLT1 and Contributes to Fragile X Syndrome Phenotypes In Vivo. *Journal of Neuroscience* **36**, 7079–7094 (2016).

127. Hodges, J. L. *et al.* Astrocytic Contributions to Synaptic and Learning Abnormalities in a Mouse Model of Fragile X Syndrome. *Biological Psychiatry* **82**, 139–149 (2017).

128. Jin, S. *et al.* Astroglial FMRP modulates synaptic signaling and behavior phenotypes in FXS mouse model. *Glia* (2020) doi:10.1002/glia.23915.

129. Higashimori, H. *et al.* Astroglial FMRP-dependent translational down-regulation of mGluR5 underlies glutamate transporter GLT1 dysregulation in the fragile X mouse. *Human Molecular Genetics* **22**, 2041–2054 (2013).

130. Caldwell, A. L. M., Diedrich, J. K., Shokhirev, M. N. & Allen, N. J. Aberrant astrocyte protein secretion contributes to altered neuronal development in diverse disorders. *BioRxiv* 939991 (2020) doi:10.1101/2020.02.17.939991.

131. Yang, Q. *et al.* Excessive Astrocyte-Derived Neurotrophin-3 Contributes to the Abnormal Neuronal Dendritic Development in a Mouse Model of Fragile X Syndrome. *PLoS Genetics* **8**, e1003172 (2012).

132. Talvio, K. *et al.* An iPSC-derived astrocyte model of fragile X syndrome exhibits dysregulated cholesterol homeostasis. *Commun Biol* **6**, 789 (2023).

133. Ren, B. *et al.* Dysregulated cholesterol metabolism, aberrant excitability and altered cell cycle of astrocytes in fragile X syndrome. *Glia* **71**, 1176–1196 (2023).

134. Cheng, C., Lau, S. K. M. & Doering, L. C. Astrocyte-secreted thrombospondin-1 modulates synapse and spine defects in the fragile X mouse model. *Molecular Brain* **9**, (2016).

135. Wallingford, J., Scott, A. L., Rodrigues, K. & Doering, L. C. Altered Developmental Expression of the Astrocyte-Secreted Factors Hevin and SPARC in the Fragile X Mouse Model. *Frontiers in Molecular Neuroscience* **10**, (2017).

136. Massagué, J. & Sheppard, D. TGF-β signaling in health and disease. *Cell* **186**, 4007–4037 (2023).

137. Kashima, R. & Hata, A. The role of TGF-β superfamily signaling in neurological disorders. *ABBS* **50**, 106–120 (2018).

138. Katagiri, T. & Watabe, T. Bone Morphogenetic Proteins. *Cold Spring Harbor Perspectives in Biology* **8**, a021899 (2016).

139. Okur, Z. *et al. Control of Neuronal Excitation-Inhibition Balance by BMP-SMAD1 Signaling*. http://biorxiv.org/lookup/doi/10.1101/2023.03.11.532164 (2023) doi:10.1101/2023.03.11.532164.

140. Kashima, R. *et al.* Augmented noncanonical BMP type II receptor signaling mediates the synaptic abnormality of fragile X syndrome. *Science Signaling* **9**, ra58–ra58 (2016).

141. Le Dréau, G. & Martí, E. The multiple activities of BMPs during spinal cord development. *Cell. Mol. Life Sci.* **70**, 4293–4305 (2013).

142. Liu, A. & Niswander, L. A. Bone morphogenetic protein signalling and vertebrate nervous system development. *Nature Reviews Neuroscience* **6**, 945–954 (2005).

143. Hegarty, S. V., O'Keeffe, G. W. & Sullivan, A. M. BMP-Smad 1/5/8 signalling in the development of the nervous system. *Progress in Neurobiology* **109**, 28–41 (2013).

144. Bond, A. M., Bhalala, O. G. & Kessler, J. A. The dynamic role of bone morphogenetic proteins in neural stem cell fate and maturation. *Devel Neurobio* **72**, 1068–1084 (2012).

145. Poon, V. Y., Choi, S. & Park, M. Growth factors in synaptic function. *Front. Synaptic Neurosci.* **5**, (2013).

146. Ball, R. W., Peled, E. S., Guerrero, G. & Isacoff, E. Y. BMP signaling and microtubule organization regulate synaptic strength. *Neuroscience* **291**, 155–166 (2015).

147. Berke, B., Wittnam, J., McNeill, E., Van Vactor, D. L. & Keshishian, H. Retrograde BMP Signaling at the Synapse: A Permissive Signal for Synapse Maturation and Activity-Dependent Plasticity. *Journal of Neuroscience* **33**, 17937–17950 (2013).

148. Beck, H. N., Drahushuk, K., Jacoby, D. B., Higgins, D. & Lein, P. J. Bone morphogenetic protein-5 (BMP-5) promotes dendritic growth in cultured sympathetic neurons. *BMC Neuroscience* 11 (2001).

149. Esquenazi, S., Monnerie, H., Kaplan, P. & Le Roux, P. BMP-7 and Excess Glutamate: Opposing Effects on Dendrite Growth from Cerebral Cortical Neurons in Vitro. *Experimental Neurology* **176**, 41–54 (2002).

150. Withers, G. S., Higgins, D., Charette, M. & Banker, G. Bone morphogenetic protein-7 enhances dendritic growth and receptivity to innervation in cultured hippocampal neurons: BMP-7 enhances dendritic growth of CNS neurons. *European Journal of Neuroscience* **12**, 106–116 (2000).

151. Aihara, S., Fujimoto, S., Sakaguchi, R. & Imai, T. BMPR-2 gates activity-dependent stabilization of dendrites during mitral cell remodeling. *BioRxiv* 358861 (2020) doi:10.1101/2020.10.30.358861.

152. Araya, R. *et al.* BMP signaling through BMPRIA in astrocytes is essential for proper cerebral angiogenesis and formation of the blood–brain-barrier. *Molecular and Cellular Neuroscience* **38**, 417–430 (2008).

153. Scholze, A. R., Foo, L. C., Mulinyawe, S. & Barres, B. A. BMP Signaling in Astrocytes Downregulates EGFR to Modulate Survival and Maturation. *PLoS ONE* **9**, e110668 (2014).

154. Bayraktar, O. A., Fuentealba, L. C., Alvarez-Buylla, A. & Rowitch, D. H. Astrocyte Development and Heterogeneity. *Cold Spring Harb Perspect Biol* **7**, a020362 (2015).

155. Haim, L. B. & Rowitch, D. H. Functional diversity of astrocytes in neural circuit regulation. *Nature Reviews Neuroscience* **18**, 31–41 (2017).

156. Khakh, B. S. & Deneen, B. The Emerging Nature of Astrocyte Diversity. *Annual Review of Neuroscience* **42**, 187–207 (2019).

157. Bartels, T., Rowitch, D. H. & Bayraktar, O. A. Generation of Mammalian Astrocyte Functional Heterogeneity. *Cold Spring Harb Perspect Biol* a041351 (2024) doi:10.1101/cshperspect.a041351.

158. Endo, F. *et al.* Molecular basis of astrocyte diversity and morphology across the CNS in health and disease. *Science* **378**, eadc9020 (2022).

159. Zeisel, A. *et al.* Cell types in the mouse cortex and hippocampus revealed by single-cell RNA-seq. *Science* **347**, 1138–1142 (2015).

160. Boisvert, M. M., Erikson, G. A., Shokhirev, M. N. & Allen, N. J. The Aging Astrocyte Transcriptome from Multiple Regions of the Mouse Brain. *Cell Reports* **22**, 269–285 (2018).

161. Batiuk, M. Y. *et al.* Identification of region-specific astrocyte subtypes at single cell resolution. *Nature Communications* **11**, (2020).

162. Clarke, L. E. *et al.* Normal aging induces A1-like astrocyte reactivity. *Proc. Natl. Acad. Sci. U.S.A.* **115**, (2018).

163. Morel, L. *et al.* Molecular and Functional Properties of Regional Astrocytes in the Adult Brain. *J. Neurosci.* **37**, 8706–8717 (2017).

164. Bayraktar, O. A. *et al.* Astrocyte layers in the mammalian cerebral cortex revealed by a single-cell in situ transcriptomic map. *Nature Neuroscience* **23**, 500–509 (2020).

165. Farmer, W. T. *et al.* Neurons diversify astrocytes in the adult brain through sonic hedgehog signaling. *Science* **351**, 849–854 (2016).

166. Lanjakornsiripan, D. *et al.* Layer-specific morphological and molecular differences in neocortical astrocytes and their dependence on neuronal layers. *Nat Commun* **9**, 1623 (2018).

167. Karpf, J. *et al.* Dentate gyrus astrocytes exhibit layer-specific molecular, morphological and physiological features. *Nat Neurosci* **25**, 1626–1638 (2022).

168. Viana, J. F. *et al.* Astrocyte structural heterogeneity in the mouse hippocampus. *Glia* glia.24362 (2023) doi:10.1002/glia.24362.

169. Farhy-Tselnicker, I. *et al.* Activity-dependent modulation of synapse-regulating genes in astrocytes. *eLife* **10**, e70514 (2021).

Chapters 1-7, in part, have been submitted for publication. Deng J, Labarta-Bajo L, Brandebura AN, Kahn SB, Pinto AFM, Diedrich JK, Allen NJ (2024). Suppression of astrocyte BMP signaling improves fragile X syndrome molecular signatures and functional deficits. The dissertation author will be the first author of this publication, and Dr. Nicola Allen will be the senior author and principal investigator.

Chapter 2. Improving Fmr1 KO phenotypes by suppressing astrocyte BMP signaling

Introduction

Rationale

Our hypothesis is that upregulated BMP signaling in astrocytes contributes to alterations in FXS, so we asked if suppressing astrocyte BMP signaling can rescue FXS functional phenotypes. We focused on FXS phenotypes in the auditory and visual systems: audiogenic seizure susceptibility, visual acuity, ocular dominance plasticity, and inhibitory synaptic density in auditory cortex.

Fmr1 KO mouse phenotypes overlap with those in FXS patients

FXS has a manifestation spanning from molecular, cellular, and neuroanatomical changes to behavioral alterations.[1] While the syndrome's behavioral manifestations—impaired cognition, anxiety, hyperactivity, hypersensitivity, perseveration, among others—are most commonly noted in patients,[1] brain imaging, tissue, and cellular-level studies have consistently described other features such as early brain overgrowth including enlarge caudate, an increase in morphologically immature dendritic spines, and molecular changes including increased mGluR signaling, mTOR pathway activity, increased MMP9, and impaired induction of cAMP.[1–3] FXS in patients is most commonly caused by an elongated CGG repeat in the 5' untranslated region of the *FMR1* gene leading to DNA methylation, histone hypoacetylation, and transcriptional silencing.[4] Mosaicism in CGG repeat length can lead to mosaic methylation and variable expression, even within one patient.[1] The Fmr1 KO mouse model is the most well-characterized FXS model.[5] Even though this mouse line loses FMRP not from DNA methylation-based silencing but insertion of a neomycin cassette into Fmr1 exon 5,[6] the Fmr1 KO mouse recapitulates many of the cellular, morphological, and behavioral phenotypes of FXS patients.[2,5] Fmr1 KO also have morphologically

immature dendritic spines in several brain regions at specific timepoints,[7] increased mGluR signaling, increased ERK and mTOR pathway activity, increased MMP9, and impaired induction of cAMP.[2,8] Functionally, Fmr1 KO mice have sensory hypersensitivity across several modalities, reduced seizure threshold, impaired visuospatial discrimination, increased repetitive behaviors, and macroorchidism.[2,5,9,10] Strength of Fmr1 KO phenotypes can vary depending on mouse genetic background: cognitive testing, audiogenic seizure susceptibility, open field hyperactivity, marble-burying stereotypy, increased novel food eaten, startle response, and social behaviors were all found to vary across strain backgrounds, with the tested mice being of C57Bl/6J background and five F1 (first filial generation) hybrid lines crossing C57Bl/6J with A/J, DBA/2J, FVB/NJ, 129S1/SvImJ, and CD-1.[11] The most commonly used backgrounds in Fmr1 KO research are C57Bl/6J (B6) and FVB/NJ (FVB),[5,12,13] and the B6 background is used exclusively in experiments in this dissertation. Many phenotypes such as increased susceptibility and severity of audiogenic seizures, increased marble-burying, and increased locomotor activity, while variable between backgrounds, have been found by different groups to be consistent within a particular genetic background.[5] In particular, audiogenic seizure susceptibility appears to model FXS patient hypersensitivity.[10] Even though FXS patient seizures (prevalence: 8-16% of males, 3-7% of females)[1] are not triggered by sound and thus may be localized differently, both FXS patient seizure and Fmr1 KO audiogenic seizures are present only in a temporally constrained period during childhood.[1,5] Moreover, hyperexcitability that may underlie these seizures is present in multiple brain regions in both FXS patients and Fmr1 KO mice.[1,14,15] At a molecular level, audiogenic seizures may share a similar etiology as other FXS phenotypes, as molecular corrections such as mGluR5 signaling reduction or ERK1/2 signaling reduction that reduce audiogenic seizures also correct other FXS phenotypes.[16–19] As a result, audiogenic seizure testing has become a common benchmark to test new hypotheses in FXS pathophysiology.[10]

Auditory pathway dysregulation in Fmr1 KO and FXS

The auditory pathway—a circuit including brainstem nuclei, inferior colliculus, lateral geniculate nucleus, and auditory cortex (AC)—is dysregulated at multiple steps in both Fmr1 KO mice and FXS patients.[20] At the level of brainstem, Fmr1 KO mice and FXS patients have altered cytoarchitecture and dendritic branching,[21] and Fmr1 KO mice have hyperexcitability,[22] loss of frequency tuning precision[23] and tonotopicity,[24] larger excitatory currents,[23] and dysregulated excitation to inhibition (E/I) ratio.[20,23] Auditory brainstem responses are delayed in FXS patients but possibly confounded by conditions such as otitis media and anesthesia,[20,25] while responses in Fmr1 KO mice are altered and dependent on strain (FVB vs. B6).[22,26,27] At the level of the inferior colliculus, cell type specific Fmr1 deletion in subcortical regions causes audiogenic seizures, and restoration of FMRP in neurons in inferior colliculus in a global Fmr1 KO prevents audiogenic seizures, showing the inferior colliculus is critical in audiogenic seizure pathophysiology.[28] At the level of auditory cortex, both Fmr1 KO mice and FXS patients have electrophysiological differences from control: FXS patients have increased left hemispheric activation during auditory discrimination tasks,[29] and both FXS patients and Fmr1 KO mice have increased gamma frequency band power in resting state EEG as well as elevated amplitude of some event-related potentials, indicating overall reduced habituation to repeated sound and a noisy resting state.[30–32] Moreover, developmental studies demonstrate an impaired critical period plasticity in Fmr1 KO primary auditory cortex rescuable by mGluR5 blockage.[26]

Visual dysregulation in Fmr1 KO and FXS

The visual system is also dysregulated across different brain regions in both Fmr1 KO and FXS. In the Fmr1 KO retina, neurons have altered dendritic structure, mice have decreased light sensitivity, and decreased excitation to inhibition ratio.[33] In visual cortex, Fmr1 KO mice have increased evoked action potentials in L5 pyramidal neurons upon white matter stimulation as well as enhanced spontaneous firing.[34] Behaviorally, both Fmr1 KO mice and FXS patients have decreased visual discriminatory learning capacity in a similar go/no-go task.[9] Additionally, Fmr1

KO mice have impaired contrast discrimination, depth perception, and light senstivity,[33,35] as well as abnormally increased ocular dominance plasticity during the visual critical period,[17] as assayed by changes in visually-evoked potentials after visual deprivation, suggesting delayed closing of the critical period in visual cortex, similar to changes reported in other cortical areas.[26,36]

Inhibitory system dysregulation in Fmr1 KO and FXS

Multiple components of the inhibitory or GABAergic (GABA = gamma-aminobutyric acid, the principal inhibitory neurotransmitter of the brain) system have been implicated in FXS pathophysiology.[1,8,37–39] At a macroscopic level, inhibitory interneuron subtypes such as parvalbumin-positive interneurons are decreased in both Fmr1 KO mice and FXS patients.[40–43] Interneurons are also developmentally hypoactive,[40] GABA-A and GABA-B receptors are also decreased in expression in Fmr1 KO and FXS patients,[44–46] and overall postsynaptic scaffolding protein gephyrin levels as well as spontaneous inhibitory postsynaptic currents in amygdala are reduced,[47] all suggesting a weakened inhibitory drive. Moreover, the developmentally regulated switch in GABA-A receptors from being excitatory (depolarizing) to inhibitory (hyperpolarizing) is delayed,[48,49] contributing to a imbalance in the excitatory-to-inhibitory ratio in FXS,[39] similar to effects observed in other forms of autism spectrum disorder.[14,50,51] Given that synapses overall are a prominent site of dysregulation in FXS,[52–56] it is therefore not surprising that inhibitory synapses are dysregulated in Fmr1 KO with an observed decrease in GABAergic synapses in upper layers and increase in lower layers of adult somatosensory cortex.[57–59] Importantly, correcting inhibition appears to restore some Fmr1 KO deficits in mice,[60,61] suggesting a promising therapeutic role for inhibitory modulation in FXS.

Astrocyte-dependent phenotypes in Fmr1 KO and FXS

Astrocytes express FMRP and have been causally implicated in some FXS deficits.[62] Initial studies employed *in vitro* systems to dissect out cell type-specific effects of the Fmr1 KO genotype, and found that wild-type hippocampal neurons cultured with astrocytes from FXS mice had altered dendritic morphology and impaired synaptic protein clustering at 7 but not 21 days *in*

vitro, suggesting delayed neuronal development.[63] Additionally, astrocyte-conditioned media (ACM) containing secreted factors from FXS astrocytes led to decreased neurite outgrowth related to wild-type ACM when applied to wild-type neurons,[64] suggesting a role for secreted proteins. Astrocytes also complicate the mGluR theory of FXS, in which elevated mGluR signaling is thought to be linked to abnormal dendritic spine morphology, electrophysiologic and metabolic alterations, as well as functional phenotypes.[17,65] Astrocytes express mGluR5 but it is decreased in Fmr1 KO, which leads to decreased expression of glutamate transporter 1 (GLT-1), in turn causing decreased glutamate reuptake.[66] Astrocyte FMRP has also been linked to Fmr1 KO phenotypes in vivo: astrocyte-specific Fmr1 KO contributes to cortical hyperexcitability, locomotor hyperactivity, motor learning deficit, and cognitive deficits, whereas astrocyte-specific Fmr1 reexpression rescues cortical hyperexcitability, locomotor hyperactivity, and social novelty preference.[67,68] Deficits in the astrocyte potassium channel Kir4.1 were shown to underlie neuronal hyperexcitability and some behavioral deficits in Fmr1 KO.[69] An astrocyte-specific Fmr1 KO led to decrease in auditory cortex GABAergic synapse density, suggesting astrocyte involvement in FXS inhibitory deficits.[59] These studies highlight a role for astrocytes in FXS.

Targeting the astrocyte BMP pathway

To define the role of astrocyte BMP signaling in FXS, we elected to suppress astrocyte BMP signaling *in vivo* and determine whether that might improve Fmr1 KO phenotypes. Given that there are many individual BMP ligands, and that their expression and distribution vary with time and location,[70] we chose to focus on inhibiting the BMP signaling machinery within astrocytes. Another advantage of this strategy over a BMP ligand KO is that astrocytes would have suppressed BMP signaling regardless of the BMP source, whether it is autocrine or paracrine from other astrocytes as we saw in culture,[64] or from other cell types such as vascular leptomeningeal cells or oligodendroglial lineage cells, which can express various BMP isoforms in vivo.[71]

To suppress BMP signaling, we chose to KO BMP downstream transcriptional mediator SMAD4 (**Figure 2.1A**). SMAD4 is the downstream point of convergence for all canonical BMP and TGFβ signaling,[70] and thus a SMAD4 KO will capture the effect of all BMP isoforms, as well as potential compensatory use of the TGFβ signaling pathway. Moreover, targeting this point of convergence allows maximum impact for a single gene KO, in a pathway with multiple points of redundance and duplication (receptors are heterotetramers of BMPR1A, BMPR1B, BMPR2; receptor-SMADs are SMAD1, SMAD5, and SMAD8).[70,72] Additionally, previous *in vitro* data showed genes such as the *Id* family, known SMAD4-mediated transcripts, were elevated in Fmr1 KO astrocytes *in vitro*.[64]

To achieve an astrocyte-specific KO, we used a mouse genetics strategy to express Cre recombinase selectively in astrocytes with Gfap-Cre73.12 (**Figure 2.1B**).[73] This line has been characterized to be active and enable recombination in astrocytes by early postnatal timepoints (P1-P7).[74] We crossed this line to a Smad4 floxed mouse[75] so that offspring would be homozygous floxed to maximize the effect of the Smad4 conditional KO (cKO). To enable comparison of littermates with and without Smad4 cKO, we set up breedings both with (1) Fmr1 -/- females, yielding littermate Fmr1 KO males with and without Smad4 cKO, and with (2) Fmr1 +/+ females, yielding littermate Fmr1 WT males with and without Smad4 cKO.

Results

Smad4 cKO suppresses *in vivo* astrocyte BMP signaling

To suppress *in vivo* BMP signaling specifically in astrocytes, we utilized an astrocyte-specific Smad4 conditional knockout (Smad4 cKO) by crossing Smad4 floxed mice[75] to the astrocyte-specific Gfap-Cre73.12 line[73,74] all in the B6 background (**Figure 2.1B**). Given the presence of visual and auditory manifestations in FXS patients,[1,9] and the use of visual (acuity,[35]

plasticity[17]) and auditory (audiogenic seizure[10]) phenotypes in Fmr1 KO research, we focused our validation on the visual and auditory pathways. Immunohistochemistry for SMAD4, astrocyte nuclear marker SOX9, and neuron nuclear marker NEUN in P28 auditory cortex showed 72±7% decrease in astrocyte nuclei immunopositive for SMAD4 with no change in neuronal nuclei SMAD4 immunopositivity (**Figure 2.1C,2.2B**). Moreover, the Smad4 cKO was effective across cortex, with each layer of auditory and visual cortex having >65% reduction of SMAD4 positive SOX9+ cells (**Figure 2.2A,C**), and moderately effective in the inferior and superior colliculi, visual and auditory recipient zones with 26-36% decrease overall and 46-61% decrease in superficial areas (**Figure 2.2F,G**). To ensure that SMAD4 was removed from astrocytes during early development, we analyzed whole cortex at P14, identifying the recombined Smad4 locus in DNA isolated from cortical astrocytes, and a decrease in SMAD4 by western blot on acutely isolated cortical astrocytes (**Figure 2.3**).

To validate that the Smad4 cKO effectively suppressed BMP signaling in astrocytes, we performed immunohistochemistry for the known BMP-induced protein ID3.[70] ID3 expression in SOX9+ astrocyte nuclei in P28 cortex was significantly downregulated (**Figure 2.2G,H**). Given the known role for BMP signaling in astrocyte cell fate and neurogenesis inhibition,[76,77] and a recent report of Smad4 involvement in astrocyte proliferation,[78] we also quantified cortical layer thickness, astrocyte number, and total cell number in P28 cortex. We found no difference in astrocyte and total cell numbers in Smad4 cKO mice relative to littermate controls, and a small decrease in cell density (**Figures 2.4B,F**) driven by a small increase in cortical thickness (**Figure 2.4D,H**), indicating no gross alteration in cell fate. Overall, we generated and validated astrocyte Smad4 cKO, a mouse model with specific suppression of BMP signaling in astrocytes.

Smad4 cKO improves Fmr1 KO audiogenic seizure severity

Our hypothesis is that upregulated BMP signaling in astrocytes contributes to alterations in FXS, so we first asked if suppressing astrocyte BMP signaling can rescue FXS functional

phenotypes. We tested for improvement in audiogenic seizures (AGS), a prevalent assay in Fmr1 KO research that models FXS patient hypersensitivity and seizures.[10] In this assay, P20-23 mice in the four genotypes (1) WT, (2) WT;Smad4 cKO, (3) FXS, and (4) FXS;Smad4 cKO were tested for susceptibility to and severity of audiogenic seizures (**Figure 2.5A,B**). Seizures were scored on a 0-2 scale of increasing severity: (0) no reaction, (1) convulsions, and (2) respiratory failure. We used male mice because female FXS patients (and mice) are heterozygous and mosaic for the FMR1 gene, leading to less severe and more variable manifestiations.[79] We found that FXS mice had more severe seizures than WT mice, and that FXS;Smad4cKO mice had less severe seizures than FXS mice (**Figure 2.5B**). Importantly, FXS;Smad4 cKO mice also had a significantly lower proportion of mice with score 2 (1 of 16) than FXS mice (8 of 15) (**Figure 2.5C**). Smad4 cKO thus reduces Fmr1 KO audiogenic seizure severity.

We next asked if Smad4 deletion in astrocytes could similarly rescue visual Fmr1 KO phenotypes. Visual phenotypes of Fmr1 KO mice include delayed learning in a visual discrimination task that models FXS patient visual discrimination deficits[9] and increased ocular dominance plasticity (ODP).[17] We elected to probe Fmr1 KO mouse vision with the optomotor task for visual acuity,[80,81] and found that at P26, Fmr1 KO mice have decreased visual acuity relative to WT littermates (WT: 0.376±0.002 cyc/deg, Fmr1 KO: 0.349±0.007 cyc/deg) (**Figure 2.6A**). However, Smad4 cKO did not improve Fmr1 KO decreased visual acuity (FXS: 0.354±0.005 cyc/deg; FXS;Smad4 cKO: 0.349±0.007 cyc/deg) (**Figure 2.6B**). To test for ocular dominance plasticity, we assayed for binocular zone enlargement during the visual critical period after monocular enucleation (ME) via single molecule FISH for immediate early gene *Arc*, as described previously[82] (**Figure 2.6C**). Paralleling the known Fmr1 KO ocular dominance hyperplasticity phenotype[17] and delayed critical period phenotype across Fmr1 KO sensory systems,[36] we found that in Fmr1 KO, the size of the activation zone after 4 days visual deprivation was significantly larger than in WT littermate pairs (FXS: 1390±51μm; WT: 1180±55μm) (**Figure**

2.6D,E). However, Smad4 cKO did not significantly change activation zone width (**Figure 2.6F**), indicating no improvement in Fmr1 KO hyperplastic ocular dominance plasticity. Overall, we validated three functional Fmr1 KO phenotypes, and found that Smad4 cKO in astrocytes does not change visual acuity or ocular dominance plasticity, but significantly reduces audiogenic seizure severity.

Smad4 cKO rescues Fmr1 KO decrease in auditory cortex inhibitory synapse density

Astrocytes can regulate synapse formation, function, and elimination through their secreted proteins.[83] In Fmr1 KO, GABAergic system dysfunction including decreases in inhibitory synaptic density in brain regions[47] such as auditory cortex[59] is thought to underlie Fmr1 KO circuit deficits.[14,51] Reduced inhibition can underlie seizures; given we saw reduction in Fmr1 KO audiogenic seizure severity with Smad4 cKO, we asked whether this improvement might be mediated by changes to inhibition. We hypothesized Smad4 cKO might improve Fmr1 KO pathology at the level of synapses and decided to focus on inhibitory synapses.

To probe synaptic density, we performed immunohistochemistry to label inhibitory presynaptic marker Vgat along with postsynaptic marker Gephyrin at P28. Given our finding that Smad4 cKO can reduce Fmr1 KO audiogenic seizure severity (**Figure 2.5B**), we focused on auditory cortex and analyzed inhibitory synapses in L2/3. In Fmr1 KO we found a decrease in colocalized Vgat-Gephyrin (59±6.3% of WT; **Figures 2.7A,B**) driven by a decrease in Gephyrin (65±17% of WT) and a trend towards decreased Vgat (83±6.0% of WT). Strikingly, in Fmr1 KO with Smad4 cKO, average Vgat, Gephyrin, and colocalized Vgat-Gephyrin density were restored to WT levels (Vgat: 100±9.7% of WT; Gephyrin 97±42% of WT; colocalized Vgat-Gephyrin 101±18% of WT; **Figures 2.7B**). In conclusion, we find that Smad4 cKO improves an Fmr1 KO deficit in inhibitory synaptic density in auditory cortex.

Discussion

In this chapter, I validate a model to suppress BMP signaling in astrocytes *in vivo* with Smad4 cKO, then show that Smad4 cKO can reduce Fmr1 KO audiogenic seizure severity and rescue the Fmr1 KO auditory cortex inhibitory synapse deficit, while it does not affect Fmr1 KO visual acuity or ocular dominance plasticity phenotypes.

Suppression of astrocyte BMP signaling with Smad4 cKO

We used mouse genetics to generate a mouse model for *in vivo* suppression of BMP signaling within astrocytes by knocking out Smad4 conditionally. As measured by immunohistochemistry in astrocytes and neurons at P28, the cKO was effective in cortical astrocytes (70-90%) with no observed effect in neurons, moderately effective in the collicular astrocytes (20-60% by region), and ineffective in astrocytes of the medial geniculate nucleus of the thalamus. This variable effectiveness across brain regions is consistent with others' reports and with variable expression of the Gfap-Cre73.12 promoter across brain regions.[74,84] Additionally, experiments at P14 showed genomic DNA recombination had occurred and that SMAD4 protein was ~50% reduced in cortical astrocytes as a whole, in time for developmental phenotypes important to FXS such as audiogenic seizures (typically assayed at P20-25). The discrepancy between the ~50% by western blot at P14 and 70-90% at P28 may be due to SMAD4 protein produced by astrocytes prior to DNA genomic recombination; to substantiate this hypothesis, further investigation would be required, e.g. into the half-life of SMAD4, or quantifying the level of SMAD4 fluorescence intensity at earlier timepoints. Importantly, the decrease in ID3 intensity by immunostaining in the majority (>90%) of SOX9+ cortical astrocytes where ID3 signal is ordinarily present (L1, L6, white matter) (**Figure 2.2G,H**, **5.2D,E,F**) demonstrated that Smad4 cKO could effectively reduce BMP downstream signaling mediators. Thus Smad4 cKO produces a selective inhibition of BMP signaling in astrocytes.

Mechanisms underlying Smad4 cKO rescue of Fmr1 KO phenotypes

We found that suppressing canonical astrocyte BMP signaling with Smad4 cKO lessens Fmr1 KO audiogenic seizure severity and rescues Fmr1 KO inhibitory synapse deficits in auditory cortex. The decrease in Fmr1 KO auditory cortex inhibitory synapses we see is similar in size to that observed by others,[59] and in line with cortical hyperexcitability observed across multiple Fmr1 KO cortical regions.[14] The restoration of inhibitory synapses in auditory cortex by Smad4 cKO is one mechanism that may reduce auditory hypersensitivity. Importantly, the Smad4 cKO reduction in Fmr1 KO seizure severity was not a complete rescue to the WT level. This moderating effect may reflect the partial KO (~36±3% overall, 61±4% superficially) of astrocyte Smad4 in inferior colliculus (**Figure 2.2F,G**), a region linked to audiogenic seizure etiology.[28]

Importantly, Smad4 cKO did not improve either of the two visual phenotypes tested. Fragile X visual acuity may not be purely a cortical effect; indeed, growing reports suggest Fmr1 KO retinal dysfunction can underlie deficits in contrast responsiveness.[33,85] Additionally, the optomotor reflex used to probe visual acuity relies on pathways including not only cortex but also pontine and midbrain nuclei, where Smad4 cKO effectiveness was not quantified. However, ocular dominance plasticity (ODP) is a measure of cortical experience-dependent plasticity, and the effectiveness of Smad4 cKO in visual cortex by P28, when we measured ODP, suggests that mechanisms independent of astrocyte BMP signaling may underlie the Fmr1 KO ocular dominance plasticity phenotypes. While it is possible that an incomplete astrocyte Smad4 cKO at earlier timepoints, when the visual circuits are being set up, could underlie the lack of rescue, it would be unsurprising for effects independent of astrocytes to drive Fmr1 KO OD hyperplasticity, as many studies have shown neuron-intrinsic effects driving FXS pathophysiology. Additionally, we did not assay for inhibitory synapses in visual cortex; it is possible there are Fmr1 KO changes to inhibition in visual cortex that are not improved by Smad4 cKO, indeed, preliminary western blotting on whole cortical lysates from the four genotype groups suggests no significant changes

in Vgat or Gephyrin on a whole-cortex level. Therefore, future experiments such as quantifying synapses in visual cortex at P28 could enhance mechanistic understanding of the Smad4 cKO improvements in Fmr1 KO phenotypes. Additional experiments could include validating Smad4 cKO in different cortical regions at different timepoints, quantification of excitatory synapses in auditory or visual cortex (preliminary study of Vglut1-PSD95 and Vglut2-PSD95 synapses in auditory cortex show no significant changes in Fmr1 KO or Smad4 cKO), and electrophysiology interrogation of auditory and visual circuits both in excitatory neurons and inhibitory interneurons, which could be immature in Fmr1 KO auditory cortex.

Altogether, we found that suppressing astrocyte BMP signaling improves Fmr1 KO functional deficits *in vivo*. These studies thus add to the literature on astrocyte contribution to FXS pathophysiology[62] and moreover represent the first example of an astrocyte-specific pathway intervention (apart from re-expressing FMRP) reported to improve Fmr1 KO deficits *in vivo*. From a translational perspective, could the BMP pathway be targeted for pharmacological rescue in FXS? Machinery (Bmpr1b) and downstream signaling (Id3) is enriched in astrocytes relative to other cell types at P14 (see Chapter 5),[71] but other cell types do have the capacity to respond to BMPs and are affected by them during development.[76] Thus, pharmacologic inhibition of BMP signaling would likely affect multiple cell types and could possibly yield results different from those observed in the studies of this chapter. However, more broadly, these experiments as well as other astrocyte-focused FXS studies are significant in that they highlight the importance of paying attention to multiple different cell types and their interactions. With a deeper understanding of FXS pathophysiology across cell types, it may be possible to more accurately appraise the clinical potential of preclinical drugs for FXS, increasing chances for clinical trial success and decreasing negative effects on patients during the drug development process.

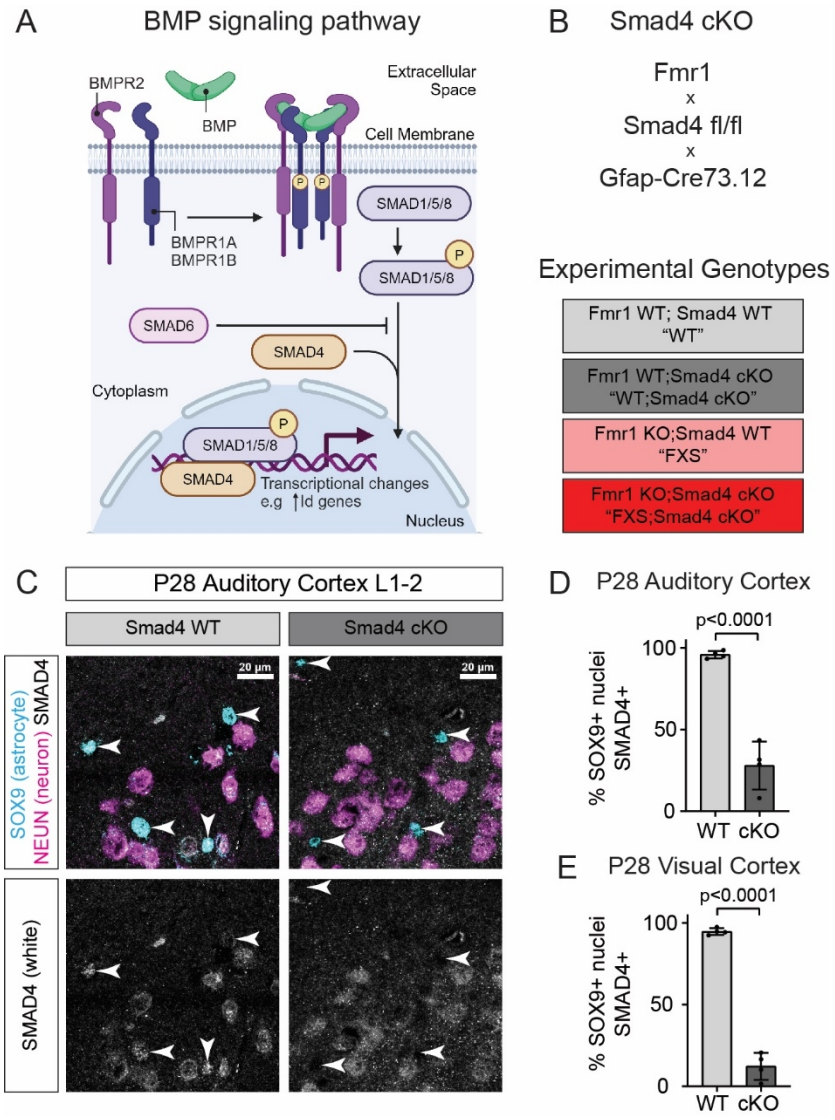

Figure 2.1. Smad4 cKO suppresses astrocyte BMP signaling.

A. Schematic of the canonical BMP pathway, as in Figure 1.4. BMPs bind to BMPR, leading to phosphorylation of SMAD1/5/8; pSMAD forms a heteromeric complex with SMAD4, which translocates to the nucleus and regulates transcription.
B. Outline of mouse genetics strategy to achieve Smad4 conditional knock-out in astrocytes.
C. Smad4 cKO deletes Smad4 from astrocytes. Example images of L1 to L2 auditory cortex, immunohistochemistry for SMAD4, SOX9 (astrocyte nuclei), and NEUN (neuronal nuclei). White arrowheads indicate SOX9+ astrocyte nuclei.
D. Quantification across P28 auditory cortex, percentage of SOX9+ nuclei that expressed SMAD4 higher than the parenchymal background. N = 4 mice/condition. Statistics by t-test.
E. P28 visual cortex data, analyzed as in 2.1D. N = 4 mice/condition. Statistics by t-test.

Figure 2.2. Additional immunohistochemical validation and characterization of astrocyte Smad4 cKO.

A. Smad4 cKO effectiveness in P28 auditory cortex. N = 4 mice per genotype. Statistics for layers by 2-way ANOVA with Sidak's test for multiple comparisons. Statistics for overall by t-test.
B. Smad4 cKO has no detectable effect on neurons in P28 auditory cortex. N = 4 mice per genotype. Statistics for layers by 2-way ANOVA with Sidak's test for multiple comparisons. Statistics for overall by t-test.
C. Smad4 cKO effectiveness in P28 visual cortex. N = 4 mice per genotype. Statistics as in S2.2A.
D. Smad4 cKO effectiveness in P14 visual cortex. N = 3 mice per genotype. Statistics as in S2.2A.
E. Smad4 cKO achieves KO in P28 inferior colliculus. Immunohistochemistry for astrocyte nuclear marker SOX9, neuronal nuclear marker NEUN, and SMAD4 shows removal of SMAD4 specifically in some astrocytes. White arrowheads indicate Sox9+ astrocyte nuclei.
F. Quantification of Smad4 cKO at P28 in superior colliculus, inferior colliculus, and medial geniculate nucleus of the thalamus. For the colliculi, SOX9+ cells were quantified both separated by superficial ("sup") vs. deep, as well as altogether ("all"). Superficially located SOX9+ cells were defined as located within 100um of the dorsal pial surface, and deep SOX9+ were defined as located greater than 100um from the dorsal pial surface. N = 3-4 mice per genotype per age. Statistics by t-test.
G. Smad4 cKO downregulates ID3 in astrocytes. Example images of L1-2 auditory cortex, immunohistochemistry for ID3 and SOX9 (astrocyte nuclei).
H. Quantification of ID3 intensity within SOX9 nuclei across P28 auditory cortex. Black dots denote average for one mouse, grey dots denote individual SOX9+ nuclei. Four independent experiments, each quantifying one littermate pair. Statistics by t-test on mice.

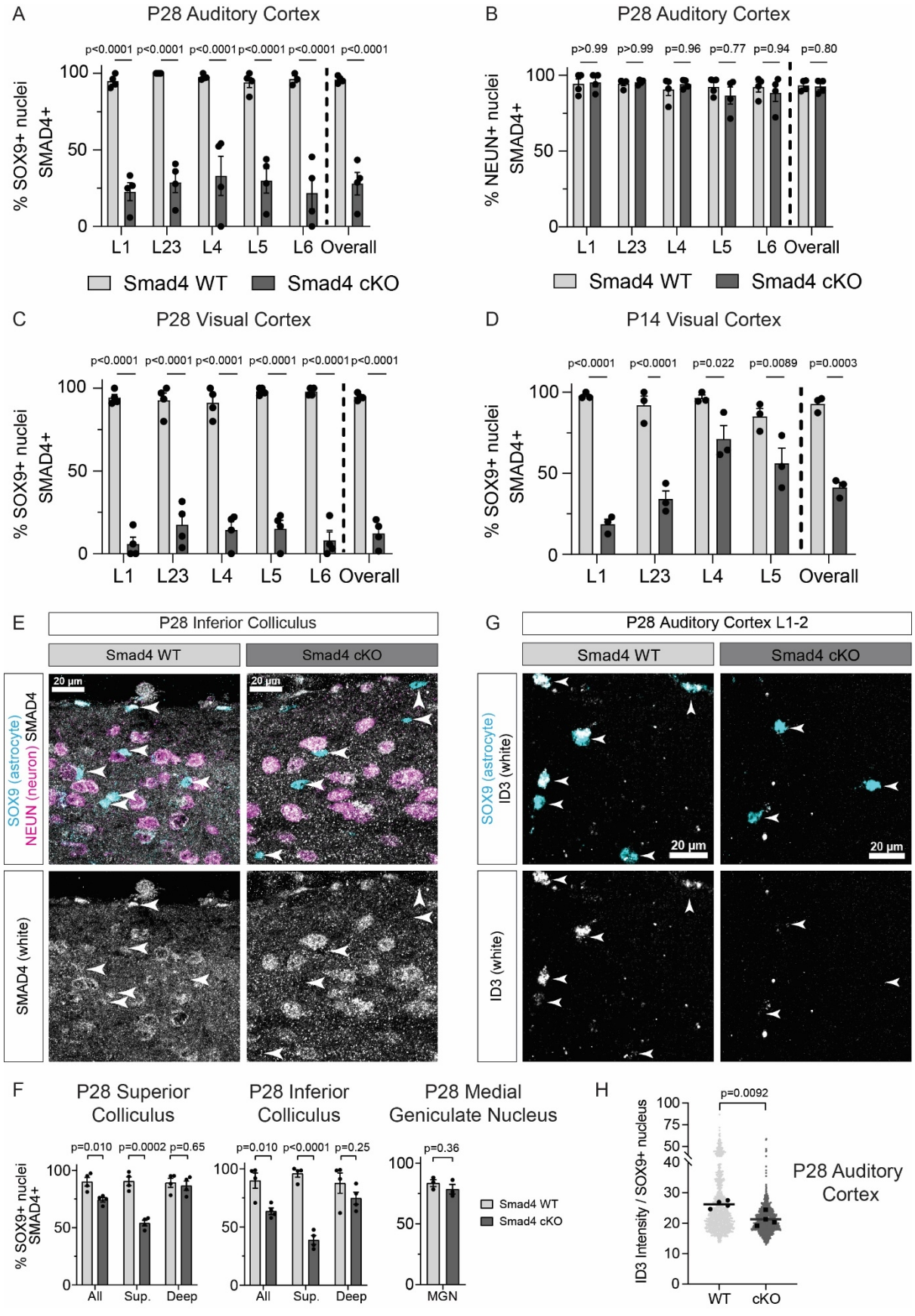
A
P28 Auditory Cortex
p<0.0001 p<0.0001 p<0.0001 p<0.0001 p<0.0001 p<0.0001
% SOX9+ nuclei SMAD4+
100
50
0
L1 L23 L4 L5 L6 Overall
Smad4 WT
Smad4 cKO
B
P28 Auditory Cortex
p>0.99 p>0.99 p=0.96 p=0.77 p=0.94 p=0.80
% NEUN+ nuclei SMAD4+
L1 L23 L4 L5 L6 Overall
Smad4 WT
Smad4 cKO
C
P28 Visual Cortex
p<0.0001 p<0.0001 p<0.0001 p<0.0001 p<0.0001 p<0.0001
% SOX9+ nuclei SMAD4+
L1 L23 L4 L5 L6 Overall
D
P14 Visual Cortex
p<0.0001 p<0.0001 p=0.022 p=0.0089 p=0.0003
% SOX9+ nuclei SMAD4+
L1 L23 L4 L5 Overall
E
P28 Inferior Colliculus
Smad4 WT
Smad4 cKO
20 µm
SOX9 (astrocyte)
NEUN (neuron)
SMAD4
SMAD4 (white)
G
P28 Auditory Cortex L1-2
Smad4 WT
Smad4 cKO
SOX9 (astrocyte)
ID3 (white)
20 µm
ID3 (white)
F
P28 Superior Colliculus
P28 Inferior Colliculus
P28 Medial Geniculate Nucleus
p=0.010 p=0.0002 p=0.65
p=0.010 p<0.0001 p=0.25
p=0.36
% SOX9+ nuclei SMAD4+
All Sup. Deep
All Sup. Deep
MGN
Smad4 WT
Smad4 cKO
H
p=0.0092
ID3 Intensity / SOX9+ nucleus
100
75
50
40
30
20
10
0
WT cKO
P28 Auditory Cortex

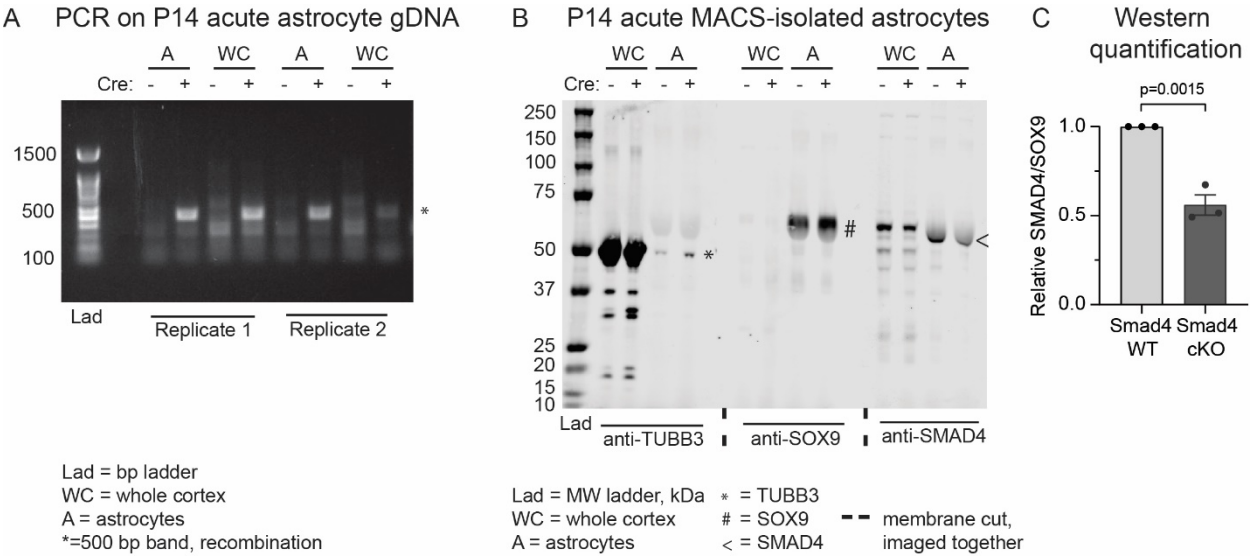

Figure 2.3. Additional validation and characterization of astrocyte Smad4 cKO at P14.

A. PCR for recombined Smad4 sequence (see primer in methods) in genomic DNA isolated from whole cortex (WC) and magnetic-activated cell sorting (MACS)-purified acute whole cortical astrocytes with and without Smad4 cKO at P14.
B. Whole cortex (WC) and MACS-purified acute whole cortical astrocytes (A) with and without Smad4 cKO isolated at P14 and probed by western blot for neuronal marker TUBB3, astrocyte marker SOX9, and SMAD4. Cortices from 2-3 mice were combined in one MACS experiment for each sample.
C. Quantification of Figure 2.3B. N = 3 independent experiments. Statistics by t-test.

Figure 2.4. Characterization of astrocyte Smad4 cKO cell density and cortical area.

A. Immunohistochemistry for astrocyte cytosolic marker S100B in P28 visual cortex.
B. B to D: Astrocyte marker S100B density (B), absolute S100B+ cell count (C), and imaged cortical area (D) by layer (N = 8 mice pairs). Statistics for cortical layers by 2-way ANOVA with Sidak's test for multiple comparisons, statistics for overall by unpaired t-test.
E. Nuclear marker DAPI in P28 visual cortex
F. F to H: Nuclear marker DAPI density (F), absolute DAPI+ nuclei count (G), and imaged cortical area (H) by layer (N = 5 mice pairs). Statistics for cortical layers by 2-way ANOVA with Sidak's test for multiple comparisons, statistics overall by unpaired t-test.

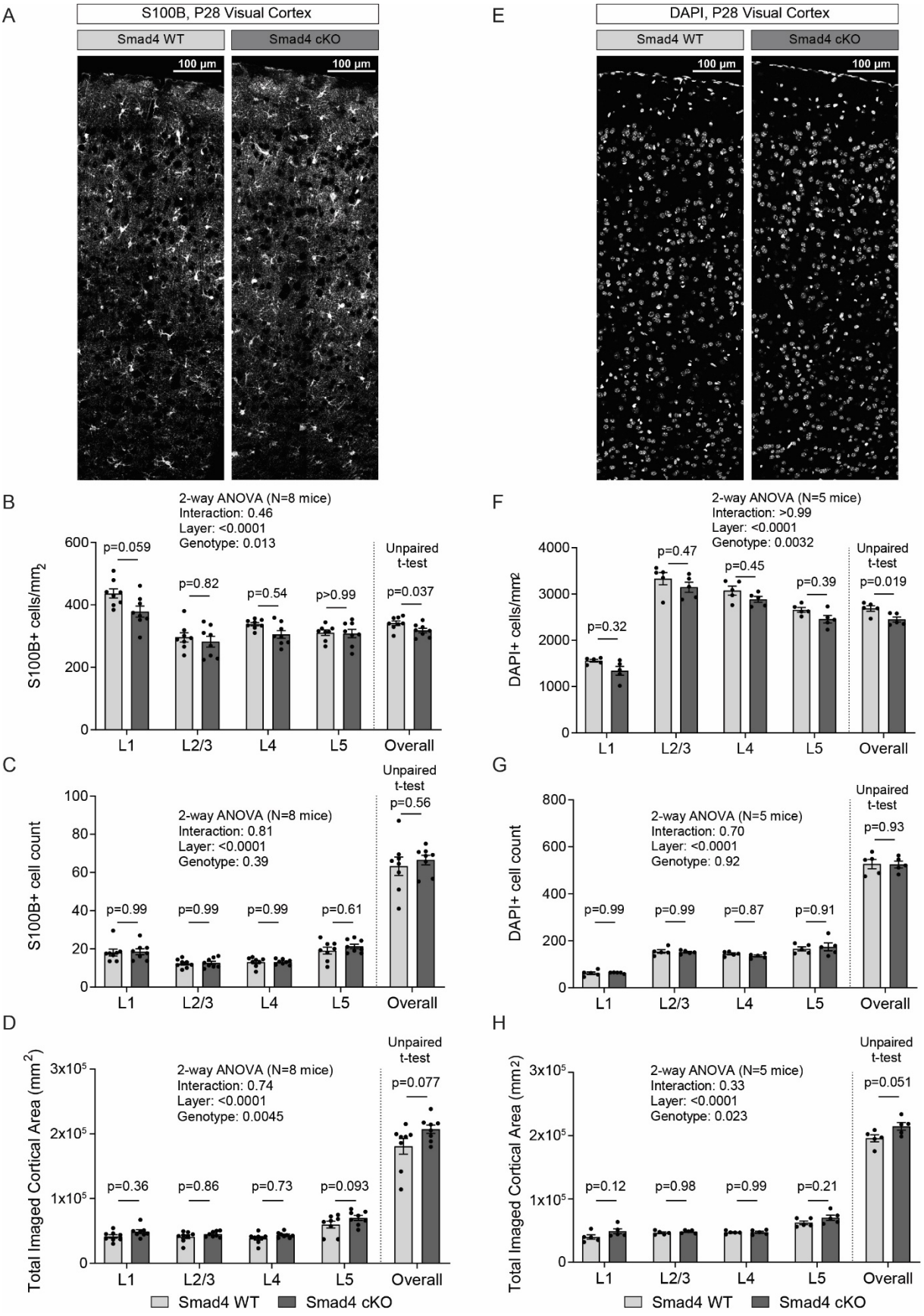
A
S100B, P28 Visual Cortex
Smad4 WT
Smad4 cKO
100 µm
100 µm
E
DAPI, P28 Visual Cortex
Smad4 WT
Smad4 cKO
100 µm
100 µm
B
2-way ANOVA (N=8 mice)
Interaction: 0.46
Layer: <0.0001
Genotype: 0.013
S100B+ cells/mm2
p=0.059
p=0.82
p=0.54
p>0.99
Unpaired t-test
p=0.037
L1
L2/3
L4
L5
Overall
F
2-way ANOVA (N=5 mice)
Interaction: >0.99
Layer: <0.0001
Genotype: 0.0032
DAPI+ cells/mm2
p=0.32
p=0.47
p=0.45
p=0.39
Unpaired t-test
p=0.019
C
S100B+ cell count
2-way ANOVA (N=8 mice)
Interaction: 0.81
Layer: <0.0001
Genotype: 0.39
p=0.99
p=0.99
p=0.99
p=0.61
Unpaired t-test
p=0.56
G
DAPI+ cell count
2-way ANOVA (N=5 mice)
Interaction: 0.70
Layer: <0.0001
Genotype: 0.92
p=0.99
p=0.99
p=0.87
p=0.91
Unpaired t-test
p=0.93
D
Total Imaged Cortical Area (mm2)
2-way ANOVA (N=8 mice)
Interaction: 0.74
Layer: <0.0001
Genotype: 0.0045
p=0.36
p=0.86
p=0.73
p=0.093
Unpaired t-test
p=0.077
H
Total Imaged Cortical Area (mm2)
2-way ANOVA (N=5 mice)
Interaction: 0.33
Layer: <0.0001
Genotype: 0.023
p=0.12
p=0.98
p=0.99
p=0.21
Unpaired t-test
p=0.051
Smad4 WT
Smad4 cKO

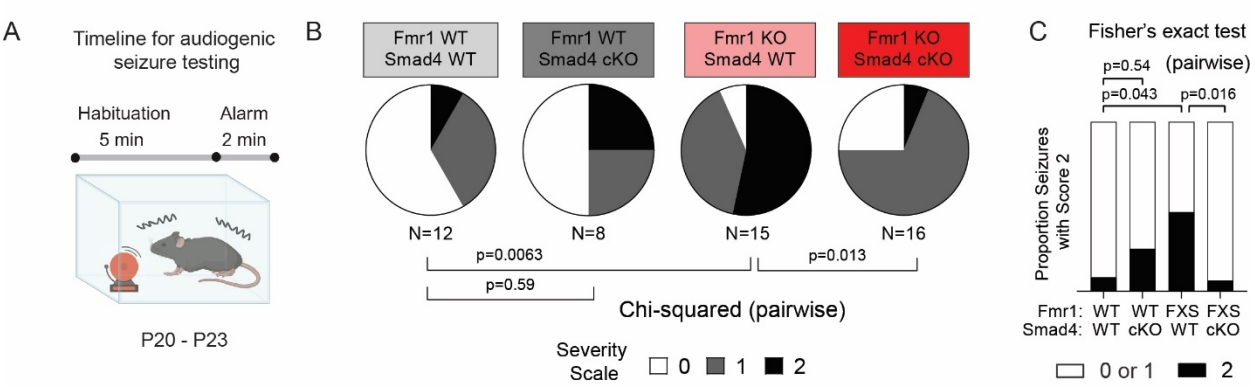

Figure 2.5. Smad4 cKO reduces severity of Fmr1 KO audiogenic seizures.

A. Timeline for audiogenic seizure testing at P20-23.
B. Quantification of the audiogenic seizure severity as follows: 0 = no observed seizure activity, 1 = progression to convulsions, 2 = progression to respiratory failure. N = 12 WT, 8 WT;Smad4 cKO, 15 FXS, 16 FXS;Smad4 cKO. Statistics by Chi-squared pairwise between groups, using counts in each of the three categories. Chi-squared for 4 groups p = 0.0045.
C. Smad4 cKO reduces respiratory failure from audiogenic seizures, same data as Fig 2.5B replotted. N = 12 WT, 8 WT;Smad4 cKO, 15 FXS, 16 FXS;Smad4 cKO. Statistics for pairwise comparisons by Fisher's exact test, using counts. Chi-squred test for 4 groups: p = 0.0279.

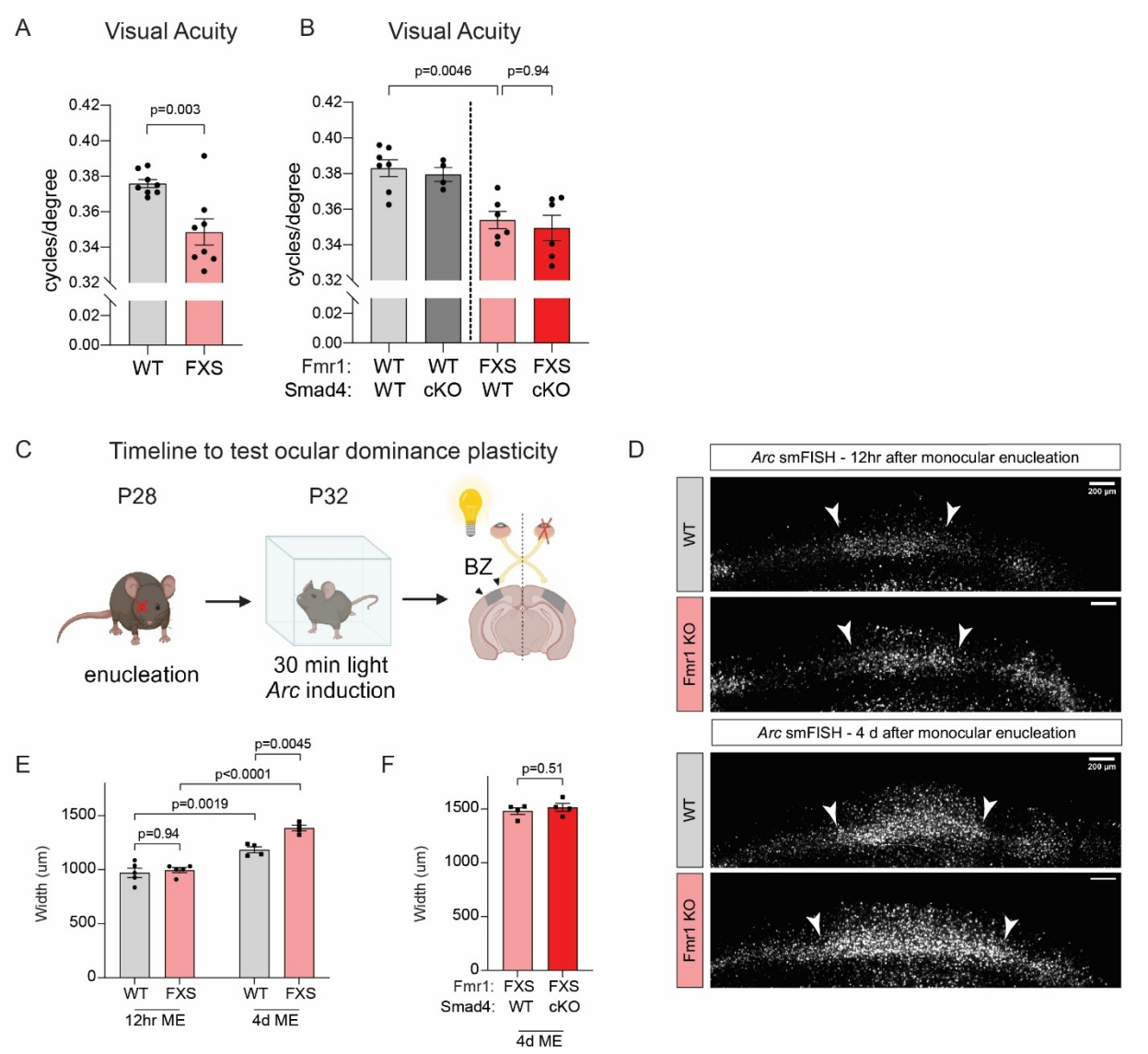

Figure 2.6. Smad4 cKO does not improve Fmr1 KO visual acuity or ocular dominance plasticity deficits.

A. Visual acuity in the Fmr1 KO line. N = 8 Fmr1 WT, 8 Fmr1 KO. Statistics by unpaired t-test.
B. Visual acuity in the Fmr1 KO;Smad4 cKO line. N = 7 WT, 4 WT;Smad4 cKO, 6 FXS, 6 FXS;Smad4 cKO. Statistics by two-way ANOVA with Tukey's test for multiple comparisons.
C. Timeline for Arc assay.
D. Example images of Arc smFISH in binocular zone (BZ) of visual cortex from experiments on the Fmr1 KO line. White arrowheads denote edges of the BZ, used to assess BZ width.
E. Quantification of 2.6D, N = 5 WT 12hr, 5 Fmr1 KO 12hr, 4 WT 4d, 4 Fmr1 KO 4d. Statistics by two-way ANOVA with Tukey's test for multiple comparisons.
F. Quantification of experiments on the Fmr1 KO;Smad4 cKO line. N = 4 FXS, 4 FXS;Smad4 cKO. Statistics by unpaired t-test.

Figure 2.7. Smad4 cKO rescues Fmr1 KO auditory cortex inhibitory synapse density deficit.

A. Example inhibitory synaptic immunohistochemistry images from L2/3 auditory cortex. Example colocalized Vgat-Gephyrin puncta indicated by yellow arrowheads.
B. Quantification of Figure 2.7A, N = 8 mice per genotype. Statistics by two-way ANOVA with Tukey's test for multiple comparisons.

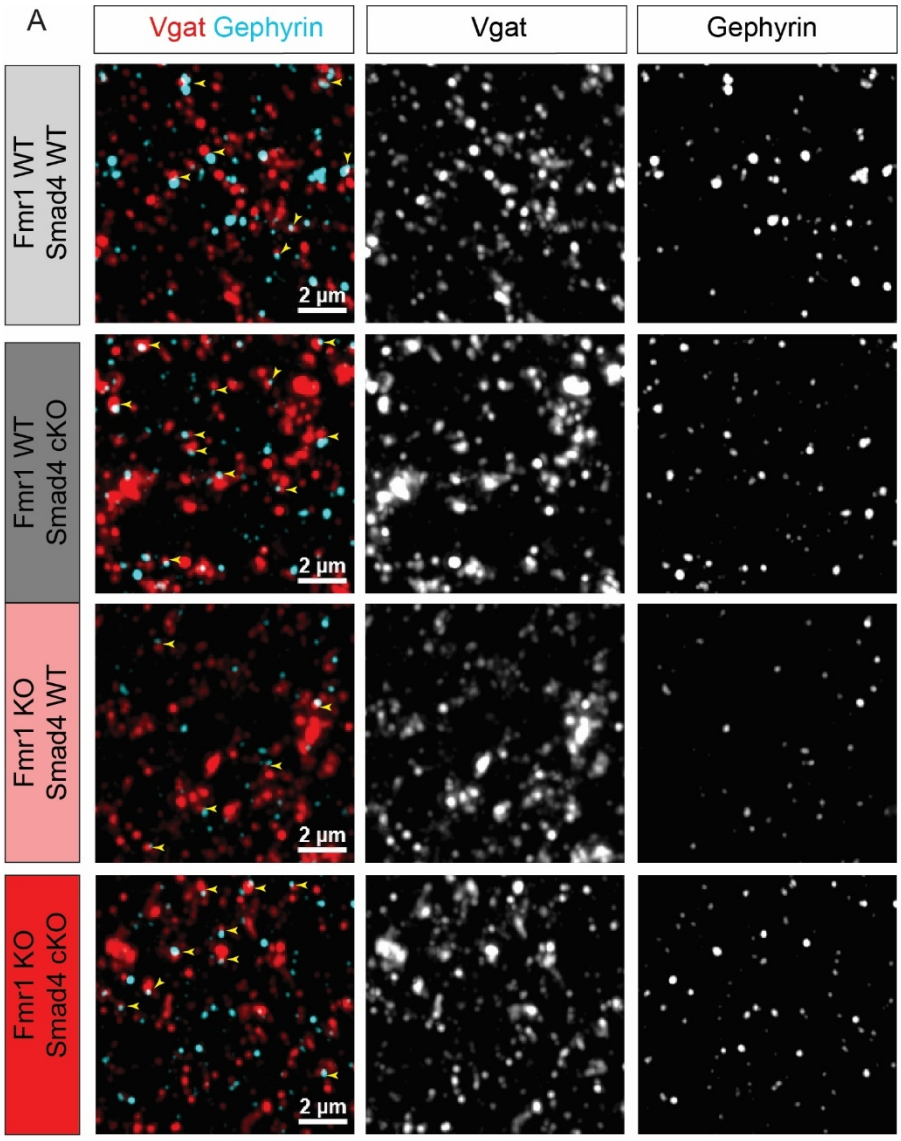
A
Vgat Gephyrin
Vgat
Gephyrin
Fmr1 WT Smad4 WT
Fmr1 WT Smad4 cKO
Fmr1 KO Smad4 WT
Fmr1 KO Smad4 cKO
2 µm

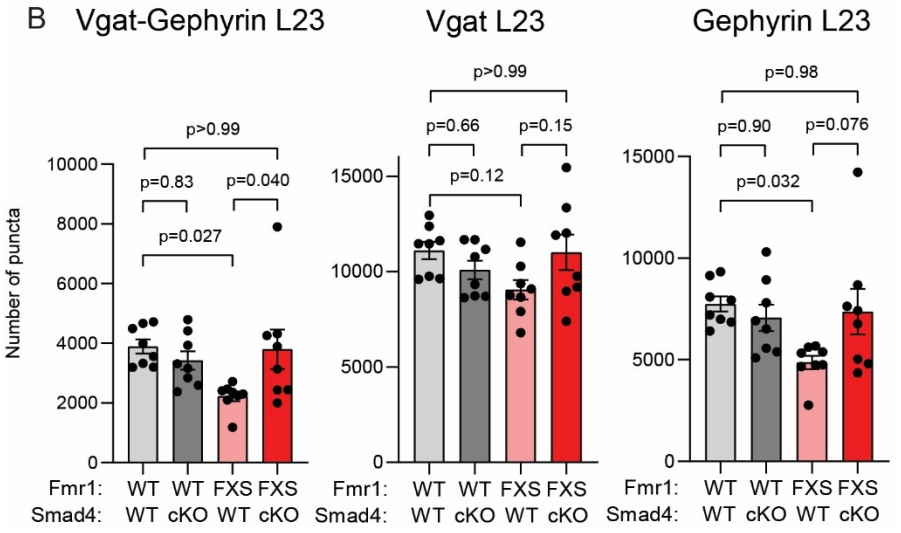
B
Vgat-Gephyrin L23
Vgat L23
Gephyrin L23
Number of puncta
p>0.99
p=0.83
p=0.040
p=0.027
p=0.66
p=0.15
p=0.12
p=0.98
p=0.90
p=0.076
p=0.032
Fmr1: WT WT FXS FXS
Smad4: WT cKO WT cKO

References

1. Hagerman, R. J. *et al.* Fragile X syndrome. *Nature Reviews Disease Primers* **3**, (2017).

2. Dahlhaus, R. Of Men and Mice: Modeling the Fragile X Syndrome. *Frontiers in Molecular Neuroscience* **11**, (2018).

3. Lai, J. K. Y., Lerch, J. P., Doering, L. C., Foster, J. A. & Ellegood, J. Regional brain volumes changes in adult male FMR1-KO mouse on the FVB strain. *Neuroscience* **318**, 12–21 (2016).

4. Richter, J. D. & Zhao, X. The molecular biology of FMRP: new insights into fragile X syndrome. *Nat Rev Neurosci* (2021) doi:10.1038/s41583-021-00432-0.

5. Kazdoba, T. M., Leach, P. T., Silverman, J. L. & Crawley, J. N. Modeling fragile X syndrome in the Fmr1 knockout mouse. *Intractable & Rare Diseases Research* **3**, 118–133 (2014).

6. The Dutch-Belgian Fragile X Consortium. Fmr1 knockout mice: A model to study fragile X mental retardation. *Cell* **78**, 23–33 (1994).

7. He, C. X. & Portera-Cailliau, C. The trouble with spines in fragile X syndrome: density, maturity and plasticity. *Neuroscience* **251**, 120–128 (2013).

8. Bagni, C. & Zukin, R. S. A Synaptic Perspective of Fragile X Syndrome and Autism Spectrum Disorders. *Neuron* **101**, 1070–1088 (2019).

9. Goel, A. *et al.* Impaired perceptual learning in a mouse model of Fragile X syndrome is mediated by parvalbumin neuron dysfunction and is reversible. *Nature Neuroscience* **21**, 1404–1411 (2018).

10. Osterweil, E. K. Seizing control of fragile X syndrome. *Sci. Transl. Med.* **12**, eaba2902 (2020).

11. Spencer, C. M. *et al.* Modifying behavioral phenotypes in Fmr1KO mice: genetic background differences reveal autistic-like responses. *Autism Res* **4**, 40–56 (2011).

12. Ding, Q., Sethna, F. & Wang, H. Behavioral analysis of male and female Fmr1 knockout mice on C57BL/6 background. *Behavioural Brain Research* **271**, 72–78 (2014).

13. Yan, Q. J., Asafo-Adjei, P. K., Arnold, H. M., Brown, R. E. & Bauchwitz, R. P. A phenotypic and molecular characterization of the fmr1-tm1Cgr Fragile X mouse. *Genes, Brain and Behavior* **3**, 337–359 (2004).

14. Contractor, A., Klyachko, V. A. & Portera-Cailliau, C. Altered Neuronal and Circuit Excitability in Fragile X Syndrome. *Neuron* **87**, 699–715 (2015).

15. Gibson, J. R., Bartley, A. F., Hays, S. A. & Huber, K. M. Imbalance of Neocortical Excitation and Inhibition and Altered UP States Reflect Network Hyperexcitability in the Mouse Model of Fragile X Syndrome. *Journal of Neurophysiology* **100**, 2615–2626 (2008).

16. Michalon, A. *et al.* Chronic Pharmacological mGlu5 Inhibition Corrects Fragile X in Adult Mice. *Neuron* **74**, 49–56 (2012).

17. Dölen, G. *et al.* Correction of Fragile X Syndrome in Mice. *Neuron* **56**, 955–962 (2007).

18. Osterweil, E. K., Krueger, D. D., Reinhold, K. & Bear, M. F. Hypersensitivity to mGluR5 and ERK1/2 Leads to Excessive Protein Synthesis in the Hippocampus of a Mouse Model of Fragile X Syndrome. *Journal of Neuroscience* **30**, 15616–15627 (2010).

19. Sawicka, K., Pyronneau, A., Chao, M., Bennett, M. V. L. & Zukin, R. S. Elevated ERK/p90 ribosomal S6 kinase activity underlies audiogenic seizure susceptibility in fragile X mice. *Proc. Natl. Acad. Sci. U.S.A.* **113**, (2016).

20. McCullagh, E. A. *et al.* Mechanisms underlying auditory processing deficits in Fragile X syndrome. *FASEB j.* **34**, 3501–3518 (2020).

21. Kulesza, R. J. & Mangunay, K. Morphological features of the medial superior olive in autism. *Brain Research* **1200**, 132–137 (2008).

22. El-Hassar, L. *et al.* Modulators of Kv3 Potassium Channels Rescue the Auditory Function of Fragile X Mice. *J. Neurosci.* **39**, 4797–4813 (2019).

23. Garcia-Pino, E., Gessele, N. & Koch, U. Enhanced Excitatory Connectivity and Disturbed Sound Processing in the Auditory Brainstem of Fragile X Mice. *J. Neurosci.* **37**, 7403–7419 (2017).

24. Strumbos, J. G., Brown, M. R., Kronengold, J., Polley, D. B. & Kaczmarek, L. K. Fragile X Mental Retardation Protein Is Required for Rapid Experience-Dependent Regulation of the Potassium Channel Kv3.1b. *J. Neurosci.* **30**, 10263–10271 (2010).

25. Miezejeski, C. M. *et al.* Longer brainstem auditory evoked response latencies of individuals with fragile X syndrome related to sedation. *Am. J. Med. Genet.* **74**, 167–171 (1997).

26. Kim, H., Gibboni, R., Kirkhart, C. & Bao, S. Impaired Critical Period Plasticity in Primary Auditory Cortex of Fragile X Model Mice. *J. Neurosci.* **33**, 15686–15692 (2013).

27. Rotschafer, S. E., Marshak, S. & Cramer, K. S. Deletion of Fmr1 Alters Function and Synaptic Inputs in the Auditory Brainstem. *PLoS ONE* **10**, e0117266 (2015).

28. Gonzalez, D. *et al.* Audiogenic Seizures in the *Fmr1* Knock-Out Mouse Are Induced by *Fmr1* Deletion in Subcortical, VGlut2-Expressing Excitatory Neurons and Require Deletion in the Inferior Colliculus. *J. Neurosci.* **39**, 9852–9863 (2019).

29. Hall, S. S., Walter, E., Sherman, E., Hoeft, F. & Reiss, A. L. The neural basis of auditory temporal discrimination in girls with fragile X syndrome. *J Neurodevelop Disord* **1**, 91–99 (2009).

30. Wang, J. *et al.* A resting EEG study of neocortical hyperexcitability and altered functional connectivity in fragile X syndrome. *J Neurodevelop Disord* **9**, 11 (2017).

31. Lovelace, J. W., Ethell, I. M., Binder, D. K. & Razak, K. A. Translation-relevant EEG phenotypes in a mouse model of Fragile X Syndrome. *Neurobiology of Disease* **115**, 39–48 (2018).

32. Rotschafer, S. & Razak, K. Altered auditory processing in a mouse model of fragile X syndrome. *Brain Research* **1506**, 12–24 (2013).

33. Vlasits, A. L., Syeda, M., Wickman, A., Guzman, P. & Schmidt, T. M. *Atypical Retinal Function in a Mouse Model of Fragile X Syndrome*. http://biorxiv.org/lookup/doi/10.1101/2024.03.15.585283 (2024) doi:10.1101/2024.03.15.585283.

34. McCamphill, P. K. *et al.* Selective inhibition of glycogen synthase kinase 3α corrects pathophysiology in a mouse model of fragile X syndrome. *Science Translational Medicine* **12**, (2020).

35. Felgerolle, C. *et al.* Visual Behavior Impairments as an Aberrant Sensory Processing in the Mouse Model of Fragile X Syndrome. *Front. Behav. Neurosci.* **13**, 228 (2019).

36. Martin, B. S. & Huntsman, M. M. Pathological Plasticity in Fragile X Syndrome. *Neural Plasticity* **2012**, 1–12 (2012).

37. Tempio, A., Boulksibat, A., Bardoni, B. & Delhaye, S. Fragile X Syndrome as an interneuronopathy: a lesson for future studies and treatments. *Front. Neurosci.* **17**, 1171895 (2023).

38. Nomura, T. Interneuron Dysfunction and Inhibitory Deficits in Autism and Fragile X Syndrome. *Cells* **10**, 2610 (2021).

39. Morin-Parent, F., Champigny, C., Lacroix, A., Corbin, F. & Lepage, J.-F. Hyperexcitability and impaired intracortical inhibition in patients with fragile-X syndrome. *Transl Psychiatry* **9**, 312 (2019).

40. Kourdougli, N. *et al.* Improvement of sensory deficits in fragile X mice by increasing cortical interneuron activity after the critical period. *Neuron* S0896627323004683 (2023) doi:10.1016/j.neuron.2023.06.009.

41. Selby, L., Zhang, C. & Sun, Q.-Q. Major defects in neocortical GABAergic inhibitory circuits in mice lacking the fragile X mental retardation protein. *Neuroscience Letters* **412**, 227–232 (2007).

42. Lee, F. H. F., Lai, T. K. Y., Su, P. & Liu, F. Altered cortical Cytoarchitecture in the Fmr1 knockout mouse. *Molecular Brain* **12**, (2019).

43. Juarez, P., Salcedo-Arellano, M. J., Dufour, B. & Martinez-Cerdeño, V. Fragile X cortex is characterized by decreased parvalbumin-expressing interneurons. *Cerebral Cortex* **34**, bhae103 (2024).

44. Braat, S. *et al.* The $GABA_A$ receptor is an FMRP target with therapeutic potential in fragile X syndrome. *Cell Cycle* **14**, 2985–2995 (2015).

45. Kang, J.-Y. *et al.* Deficits in the activity of presynaptic γ-aminobutyric acid type B receptors contribute to altered neuronal excitability in fragile X syndrome. *Journal of Biological Chemistry* **292**, 6621–6632 (2017).

46. Gantois, I. *et al.* Expression profiling suggests underexpression of the GABAA receptor subunit δ in the fragile X knockout mouse model. *Neurobiology of Disease* **21**, 346–357 (2006).

47. Olmos-Serrano, J. L. *et al.* Defective GABAergic Neurotransmission and Pharmacological Rescue of Neuronal Hyperexcitability in the Amygdala in a Mouse Model of Fragile X Syndrome. *Journal of Neuroscience* **30**, 9929–9938 (2010).

48. He, Q., Nomura, T., Xu, J. & Contractor, A. The Developmental Switch in GABA Polarity Is Delayed in Fragile X Mice. *J. Neurosci.* **34**, 446–450 (2014).

49. Nomura, T. *et al.* Delayed Maturation of Fast-Spiking Interneurons Is Rectified by Activation of the TrkB Receptor in the Mouse Model of Fragile X Syndrome. *J. Neurosci.* **37**, 11298–11310 (2017).

50. Nelson, S. B. & Valakh, V. Excitatory/Inhibitory Balance and Circuit Homeostasis in Autism Spectrum Disorders. *Neuron* **87**, 684–698 (2015).

51. Contractor, A., Ethell, I. M. & Portera-Cailliau, C. Cortical interneurons in autism. *Nat Neurosci* **24**, 1648–1659 (2021).

52. Pfeiffer, B. E. & Huber, K. M. The State of Synapses in Fragile X Syndrome. *Neuroscientist* **15**, 549–567 (2009).

53. Telias, M. Molecular Mechanisms of Synaptic Dysregulation in Fragile X Syndrome and Autism Spectrum Disorders. *Frontiers in Molecular Neuroscience* **12**, (2019).

54. Hu, H. *et al.* Ras Signaling Mechanisms Underlying Impaired GluR1-Dependent Plasticity Associated with Fragile X Syndrome. *J. Neurosci.* **28**, 7847–7862 (2008).

55. Guo, W. *et al.* Fragile X Proteins FMRP and FXR2P Control Synaptic GluA1 Expression and Neuronal Maturation via Distinct Mechanisms. *Cell Reports* **11**, 1651–1666 (2015).

56. Chojnacka, M. *et al.* Impaired synaptic incorporation of AMPA receptors in a mouse model of fragile X syndrome. *Front. Mol. Neurosci.* **16**, 1258615 (2023).

57. Simhal, A. K. *et al.* Multifaceted Changes in Synaptic Composition and Astrocytic Involvement in a Mouse Model of Fragile X Syndrome. *Sci Rep* **9**, 13855 (2019).

58. Wang, G. X., Smith, S. J. & Mourrain, P. Fmr1 KO and Fenobam Treatment Differentially Impact Distinct Synapse Populations of Mouse Neocortex. *Neuron* **84**, 1273–1286 (2014).

59. Rais, M. *et al. Astrocytes Regulate Inhibition in Fragile X Syndrome*. http://biorxiv.org/lookup/doi/10.1101/2022.02.08.479618 (2022) doi:10.1101/2022.02.08.479618.

60. Heulens, I., D'Hulst, C., Van Dam, D., De Deyn, P. P. & Kooy, R. F. Pharmacological treatment of fragile X syndrome with GABAergic drugs in a knockout mouse model. *Behavioural Brain Research* **229**, 244–249 (2012).

61. Olmos-Serrano, J. L., Corbin, J. G. & Burns, M. P. The $GABA_A$ Receptor Agonist THIP Ameliorates Specific Behavioral Deficits in the Mouse Model of Fragile X Syndrome. *Dev Neurosci* **33**, 395–403 (2011).

62. Talvio, K. & Castrén, M. L. Astrocytes in fragile X syndrome. *Front. Cell. Neurosci.* **17**, 1322541 (2024).

63. Jacobs, S. & Doering, L. C. Astrocytes Prevent Abnormal Neuronal Development in the Fragile X Mouse. *Journal of Neuroscience* **30**, 4508–4514 (2010).

64. Caldwell, A. L. M. *et al.* Aberrant astrocyte protein secretion contributes to altered neuronal development in multiple models of neurodevelopmental disorders. *Nat Neurosci* **25**, 1163–1178 (2022).

65. Berry-Kravis, E. Mechanism-Based Treatments in Neurodevelopmental Disorders: Fragile X Syndrome. *Pediatric Neurology* **50**, 297–302 (2014).

66. Higashimori, H. *et al.* Astroglial FMRP-dependent translational down-regulation of mGluR5 underlies glutamate transporter GLT1 dysregulation in the fragile X mouse. *Human Molecular Genetics* **22**, 2041–2054 (2013).

67. Jin, S. *et al.* Astroglial FMRP modulates synaptic signaling and behavior phenotypes in FXS mouse model. *Glia* **69**, 594–608 (2021).

68. Hodges, J. L. *et al.* Astrocytic Contributions to Synaptic and Learning Abnormalities in a Mouse Model of Fragile X Syndrome. *Biological Psychiatry* **82**, 139–149 (2017).

69. Bataveljic, D. *et al.* Astroglial Kir4.1 potassium channel deficit drives neuronal hyperexcitability and behavioral defects in Fragile X syndrome mouse model. *Nat Commun* **15**, 3583 (2024).

70. Katagiri, T. & Watabe, T. Bone Morphogenetic Proteins. *Cold Spring Harbor Perspectives in Biology* **8**, a021899 (2016).

71. Farhy-Tselnicker, I. *et al.* Activity-dependent modulation of synapse-regulating genes in astrocytes. *eLife* **10**, e70514 (2021).

72. Massagué, J. & Sheppard, D. TGF-β signaling in health and disease. *Cell* **186**, 4007–4037 (2023).

73. Garcia, A. D. R., Doan, N. B., Imura, T., Bush, T. G. & Sofroniew, M. V. GFAP-expressing progenitors are the principal source of constitutive neurogenesis in adult mouse forebrain. *Nat Neurosci* **7**, 1233–1241 (2004).

74. Farhy-Tselnicker, I. *et al.* Astrocyte-Secreted Glypican 4 Regulates Release of Neuronal Pentraxin 1 from Axons to Induce Functional Synapse Formation. *Neuron* **96**, 428-445.e13 (2017).

75. Yang, X., Li, C., Herrera, P.-L. & Deng, C.-X. Generation of Smad4/Dpc4 conditional knockout mice. *genesis* **32**, 80–81 (2002).

76. Kashima, R. & Hata, A. The role of TGF-β superfamily signaling in neurological disorders. *ABBS* **50**, 106–120 (2018).

77. Gross, R. E. *et al.* Bone Morphogenetic Proteins Promote Astroglial Lineage Commitment by Mammalian Subventricular Zone Progenitor Cells. *Neuron* **17**, 595–606 (1996).

78. Ohlig, S. *et al.* Molecular diversity of diencephalic astrocytes reveals adult astrogenesis regulated by Smad4. *EMBO J* (2021) doi:10.15252/embj.2020107532.

79. Keysor, C. S. & Mazzocco, M. M. M. A developmental approach to understanding Fragile X syndrome in females. *Microscopy Research and Technique* **57**, 179–186 (2002).

80. Prusky, G. T., Alam, N. M., Beekman, S. & Douglas, R. M. Rapid Quantification of Adult and Developing Mouse Spatial Vision Using a Virtual Optomotor System. *Invest. Ophthalmol. Vis. Sci.* **45**, 4611 (2004).

81. Durand, S. *et al.* NMDA Receptor Regulation Prevents Regression of Visual Cortical Function in the Absence of Mecp2. *Neuron* **76**, 1078–1090 (2012).

82. Blanco-Suarez, E., Liu, T.-F., Kopelevich, A. & Allen, N. J. Astrocyte-Secreted Chordin-like 1 Drives Synapse Maturation and Limits Plasticity by Increasing Synaptic GluA2 AMPA Receptors. *Neuron* **100**, 1116-1132.e13 (2018).

83. Chung, W.-S., Baldwin, K. T. & Allen, N. J. Astrocyte Regulation of Synapse Formation, Maturation, and Elimination. *Cold Spring Harb Perspect Biol* a041352 (2024) doi:10.1101/cshperspect.a041352.

84. Garcia, A. D. R., Doan, N. B., Imura, T., Bush, T. G. & Sofroniew, M. V. GFAP-expressing progenitors are the principal source of constitutive neurogenesis in adult mouse forebrain. *Nat Neurosci* **7**, 1233–1241 (2004).

85. Rossignol, R. *et al.* Visual Sensorial Impairments in Neurodevelopmental Disorders: Evidence for a Retinal Phenotype in Fragile X Syndrome. *PLoS ONE* **9**, e105996 (2014).

Chapters 1-7, in part, have been submitted for publication. Deng J, Labarta-Bajo L, Brandebura AN, Kahn SB, Pinto AFM, Diedrich JK, Allen NJ (2024). Suppression of astrocyte BMP signaling improves fragile X syndrome molecular signatures and functional deficits. The dissertation author will be the first author of this publication, and Dr. Nicola Allen will be the senior author and principal investigator.

Chapter 3. Nuclear transcriptomics of Fmr1 KO with and without Smad4 cKO

Introduction

Rationale

Given that suppressing astrocyte BMP signaling can reduce some FXS functional deficits, we sought to identify how this occurs on a molecular level. To do this, we first turned to RNA sequencing to unbiasedly identify which specific astrocyte gene programs are altered in Fmr1 KO, and if suppression of astrocyte BMP signaling with Smad4 cKO improves them.

Transcriptomic changes in FXS

Despite being a monogenic disorder, FXS has complex manifestations at the neuroanatomical, circuit, and behavioral levels.[1–3] Underlying these characteristic phenotypes is an altered physiological state at the molecular level within individual cells.[4–6] With the advent of genomic technologies allowing unbiased characterization at the level of the entire transcriptome and proteome, the molecular changes caused by loss of FMRP have begun to be detailed, both across the brain and in astrocytes.

Fragile X messenger ribonucleoprotein (FMRP), the deficiency of which causes FXS, is known to regulate translation and ribosomal stalling by binding directly to mRNAs.[7,8] Using cross-linking immunoprecipitation and sequencing (CLIP-seq) to crosslink proteins to RNA, purify FMRP, and assay FMRP-bound transcripts, several groups have established that FMRP can directly bind to hundreds to thousands of distinct mRNAs.[7–9] The exact transcripts bound by FMRP vary by brain region but have significant overlap; moreover, the genes significantly overlapped with genes dysregulated in other forms of autism spectrum disorder and were enriched for synapse-related genes.[7,9] Specific FMRP mRNA targets have been validated to be

de-repressed upon Fmr1 KO, leading to the notion of FMRP as a translational repressor. Indeed, excessive protein synthesis has been shown in multiple brain regions of the Fmr1 KO mouse[10–12] and in some human studies.[13]

Which mRNAs are dysregulated in FXS brain tissue? Bulk RNAseq transcriptomic studies have probed this question in different systems, from primary mouse neuronal cortical/hippocampal cultures,[4] mouse cortex or hippocampal tissue,[4,14,15] human FXS fetal tissue,[16] FXS iPSC-neurons[17] and organoids,[16] among others. Commonly reported dysregulated pathways and gene sets include ribosomal and translation initiation genes, biosynthetic and metabolic processes (mTOR, oxidative phosphorylation), and synaptic genes.[4,14–17] However, FXS bulk RNAseq studies combining all cell types in a tissue often show only subtle transcriptomic changes; this may reflect potential masking by cell type-specific responses to FMRP loss.[18] Single-cell RNAseq across cortical cell types in developing Fmr1 KO mice (P5) showed upregulated translation, mitochondrial processes, and mTOR signaling and downregulated vesicle transport and ion homeostasis across cell types, along with dysregulated astrocyte-neuron communication and astrocyte synapse-related genes.[18] In contrast, a recent translating ribosome affinity purification RNAseq dataset from astrocytes in postnatal (P) 40 Fmr1 KO mice showed only modest changes relative to Fmr1 WT, with 54 differentially expressed genes ($p < 0.05$).[19]

Results

Transcriptomics of Fmr1 KO and Smad4 cKO mice with nuclear RNAseq

To gain a detailed and unbiased profile of dysregulated pathways in astrocytes in Fmr1 KO, and how they might be improved by Smad4 cKO *in vivo*, we employed astrocyte nuclear RNA sequencing (nRNAseq). We used a protocol optimized in Labarta-Bajo et al. that includes glyoxal

fixation, homogenization of brain tissue to single nuclei, antibody immunostaining for astrocyte nuclear marker SOX9 and neuronal nuclear marker NEUN, and fluorescence-activated cell sorting (FACS) for SOX9+NEUN- nuclei (**Figure 3.2A**).[20,21] This protocol allows for cell-type enrichment for astrocytes for an *in vivo* transcriptome, without relying on techniques such as the RiboTag (ribosomal tagging)[22] that require an astrocyte-enriched Cre recombinase and would be incompatible with the above strategy to achieve Smad4 cKO using Cre (Smad4 WT controls with no Cre would lack RiboTag expression). Moreover, sequencing nuclei specifically may better capture the transcriptional dysregulation caused by KO of the transcriptional regulator SMAD4.[23]

The protocol for astrocyte nRNAseq can be used both for freshly dissected and frozen tissue specimens. We performed a pilot test on P28 cortical tissue to determine whether freshly dissected tissue might give a higher proportion of SOX9+NEUN- cells isolated by FACS. After processing in parallel two cortices—one freshly dissected, and one flash frozen in liquid nitrogen and rethawed—we found during FACS that SOX9+NEUN- nuclei separated further in fluorescence intensity from other nuclei in the fresh sample compared to the frozen sample (**Figure 3.1**). Applying the same FACS gate (fluorescence intensity criteria for selection of the SOX9+NEUN- cell population) to the two samples resulted in 11.0% of all sorted single nuclei in the fresh sample being captured but only 3.59% of sorted single nuclei in the frozen sample being captured, reflecting a population-level decrease in SOX9 immunostaining fluorescence intensity in SOX9+ nuclei (**Figure 3.1**). This was similar to the result at P120 reported in Labarta-Bajo et al., 2023,[20] and the figure of 11.0% is similar to the expected percentage of astrocytes among cortical cells.[24] As better population separation enables higher purity, we thus elected to perform FACS sorting only on freshly-collected tissue for this experiment.

<u>Fmr1 KO astrocytes have a hypermetabolic transcriptional state *in vivo*</u>

Given that suppressing astrocyte BMP signaling can reduce some FXS functional deficits, we sought to identify how this occurs on a molecular level, first using RNA sequencing to

unbiasedly identify which specific astrocyte gene programs are altered in Fmr1 KO, and if suppression of astrocyte BMP signaling improves them. We profiled cortical astrocytes at P26-28 in mice of the four genotypes (1) WT, (2) WT;Smad4 cKO, (3) FXS, and (4) FXS;Smad4 cKO in the C57Bl6/J background (N=4-6 mice/genotype) (**Fig 3.2B**). We used whole cortex in order to obtain enough astrocytes to perform bulk RNA sequencing, and isolated astrocyte nuclei using glyoxal fixation combined with antibody staining for SOX9 and FACS purification (**Figure 3.2A, 3.3A**).[20,21] To validate astrocyte specificity of purified nuclei, we averaged the transcript per million (TPM) for a series of known cell type-specific genes,[25] and found enrichment for astrocytes over other cell types (**Figure 3.3B**). Inspection of aligned sequencing reads to the *Smad4* exon 9 and *Fmr1* exon 5 loci showed reads were consistent with Smad4 recombination and Fmr1 KO respectively (**Figure 3.3C**). As further confirmation for the data in Chapter 2 showing suppression of BMP signaling, we saw a decrease in *Id3* expression in Smad4 cKO (adj-p = 3.1e-20, log2 fold change (L2FC) = -2.28; **Table S2**).

We compared FXS to WT to determine genes dysregulated by Fmr1 KO in astrocytes, finding 149 differentially expressed genes (DEGs) (**Figure 3.2C,D, Table S2**; threshold p-adj < 0.05, fold change (FC) > 1.5, TPM in WT > 1). Interestingly, genes encoding for astrocyte-secreted proteins were among the top upregulated (*Chil1*, *Ptn*, *Chrdl1*) and downregulated (*Sema3c*) when ranked by Benjamini-Hochberg (B-H) adjusted p-value.[26–29] Gene set enrichment analysis (GSEA) revealed top Fmr1 KO upregulated gene sets to be “oxidative phosphorylation,” “cholesterol homeostasis,” and “mTorc1 signaling,” while top downregulated gene sets were related to “interferon response” (**Figure 3.4E**, **Table S3**). Several groups have reported metabolic hyperactivity in bulk brain tissue and other cell types in Fmr1 KO[2,30–32] as well as cholesterol dysregulation in Fmr1 KO astrocytes;[33–35] our data also finds this hypermetabolic transcriptional signature in Fmr1 KO astrocytes *in vivo*.

Additionally, we compared these Fmr1 KO DEGs to a list of 842 genes known to be bound to and thus likely regulated by Fragile X Messenger Ribonucleoprotein (FMRP), the protein product of *Fmr1*.[7] While only 4 DEGs (*Kcnt1, Plxnd1, Rn45s, Shank3*) are known FMRP targets (p = 0.76), overall, the set of FMRP targets filtered to those enriched in astrocytes at an mRNA level[36] (141 genes) had an average log2 fold change (FXS vs. WT) greater than the set of all genes (p = 6.6e-16, **Figure 3.2E**), implying FMRP directly regulates gene expression in astrocytes. We also compared this *in vivo* nuclear RNA transcriptomic dataset to an *in vivo* P40 Fmr1 KO (FVB line) astrocyte translating RNAseq dataset,[19] and a cultured P7 Fmr1 KO astrocyte transcriptome,[26] and surprisingly found low overlap and minimal correlation in log2 fold change of DEGs (**Figure 3.6A,C,D,E**), highlighting the roles that cellular context, genetic background, and timepoint may play in identifying transcriptomic alterations in a disease model.

Smad4 cKO moderates Fmr1 KO astrocyte transcriptomic activation of metabolic pathways

Our primary goal is to determine if Smad4 cKO can rescue Fmr1 KO astrocyte dysregulation and elucidate molecular pathways underlying any functional improvement. We thus performed the additional pairwise comparisons: WT;Smad4cKO to WT (Comparison 3), FXS;Smad4cKO to FXS (Comparison 2), and FXS;Smad4cKO to WT (Comparison 4) (**Figure 3.4A**). First, examining the effect of Smad4 cKO in WT, we found 150 DEGs (**Figure 3.2C, Table S2**). Interestingly, log2 fold changes (L2FC) of Smad4 cKO DEGs correlated negatively to L2FC of the same genes in astrocytes cultured with BMP4 (r = -0.41) or BMP6 (r = -0.60) and not TGFβ1 (r = +0.39) (**Figure 3.4B**),[37] suggesting preferential suppression of the astrocyte BMP and not TGFβ transcriptional signature. Moreover, at the level of individual DEGs, 44% of downregulated DEGs in Smad4 cKO *in vivo* were upregulated DEGs in astrocytes cultured with BMP6 (**Figure 3.6B**), showing similarity in astrocyte transcriptomic response to BMP signaling *in vitro* and *in vivo*.

Comparing FXS;Smad4cKO to WT (Comparison 4), we found 284 DEGs (**Figure 3.2C, Table S2**). Notably, the majority (89 of 149) of DEGs found when comparing FXS to WT (Comparison 1) were no longer significantly changed when comparing the FXS;Smad4cKO to WT (Comparison 4) (**Figure 3.4C, Table S2**). These 89 genes thus represent FXS astrocyte transcriptional dysregulations moderated by Smad4cKO. To directly assess the impact of Smad4 cKO in the FXS background, we also compared FXS;Smad4cKO to FXS (Comparison 2). We found 106 DEGs, and again, genes encoding astrocyte-secreted proteins among top upregulated (*Sdc3 Smoc1*) and downregulated (*Myoc*, *Tnc*) genes (**Figure 3.4D, Table S2**).

At the pathway level, strikingly, GSEA showed “oxidative phosphorylation” is a top suppressed pathway comparing FXS;Smad4 cKO to FXS, and is not significantly changed comparing FXS;Smad4 cKO to WT, showing Smad4 cKO has rescued this FXS alteration (**Figure 3.4E**). This is in contrast to the “mTORC1 signaling” and “cholesterol homeostasis” pathways, which are upregulated in Fmr1 KO and not impacted by Smad4 cKO, and the “interferon A response” pathway, which is downregulated in Fmr1 KO and not impacted by Smad4 cKO. GSEA analysis on a broader set of gene sets showed “glycolysis/gluconeogenesis” also followed the same trend as “oxidative phosphorylation”, with upregulation of this pathway in FXS moderated by Smad4 cKO (**Figures 3.4F,G, 3.5**, **Table S3,4**). The effect we see in Smad4 cKO correlates with reports in other cell types showing positive regulation of glycolysis and oxidative phosphorylation by BMP signaling.[38] In summary, our RNAseq data demonstrates dysregulation of the astrocyte transcriptome in Fmr1 KO, and determines a number of genes and pathways that are partially rescued by Smad4 cKO including the hypermetabolic phenotype present in FXS astrocytes.

Discussion

Fmr1 KO astrocytes have hypermetabolic gene signatures *in vivo* lessened by Smad4 cKO

Genomic datasets have begun to detail molecular changes caused by loss of FMRP, across the brain and in astrocytes.[39,40] Our cortical astrocyte transcriptomic profiling showed upregulation of multiple metabolism-related gene sets in Fmr1 KO astrocytes. Interestingly, the top downregulated gene in Fmr1 KO was *Inpp5j*, a negative regulator of the PI3K/Akt pathway;[41] the Fmr1 KO downregulation of *Inpp5j* could therefore increase pAkt signaling and downstream metabolic (glucose metabolism, mTOR) pathways. Astrocytes are highly metabolically active and are known to support neuronal energy balance;[42,43] conversely, astrocyte metabolic dysfunction is increasingly associated with neurodevelopmental disorders,[31] with astrocyte cholesterol dysregulation[33,34] and overproduction of reactive oxidative species (ROS)[44] tied to FXS. Our finding that Smad4 cKO reduced Fmr1 KO transcriptional upregulation of oxidative phosphorylation and glycolysis and our hypothesis that this may underlie rescue of Fmr1 KO phenotypes such as audiogenic seizure susceptibility correlates with other reports that normalizing metabolic dysregulation (mTOR signaling,[45] mitochondrial health,[32,46] GSK3[12]) can normalize Fmr1 KO deficits. Alternatively, the Smad4 cKO rescue of astrocyte metabolic dysregulation in Fmr1 KO could be downstream of improved neuronal hyperexcitability, suggested by the reduced audiogenic seizures and recovered inhibitory synapse levels. This would explain why a previous *in vitro* transcriptomic study of Fmr1 KO astrocytes cultured in isolation did not show a hypermetabolic signature,[26] and emphasizes the importance of the cellular environment for phenotypes such as metabolism shaped by intercellular interaction. Indeed astrocytes are known to adapt metabolic flux in response to neuronal activity, both in physiological and pathological contexts.[43] Further functional studies of *in vivo* astrocyte metabolism in FXS, including with tools beyond transcriptomics employed here, will be crucial to determine if the metabolic effect we observe is primary or secondary in FXS pathophysiology.

Are astrocytes reactive in Fmr1 KO?

A previous report found that adult (8-week) Fmr1 KO mice have increased GFAP expression in corpus callosum, and that P1-3 serum-cultured Fmr1 KO cortical astrocytes had increased GFAP expression.[47] A hypothesis is thus that increased astrocyte reactivity in Fmr1 KO could underlie astrocyte contributions to FXS pathophysiology.[18,47] In contrast, transcriptomic analysis of P7 Fmr1 KO cortical astrocytes, cultured without serum to more closely reproduce *in vivo* conditions, showed no reactive signature in Fmr1 KO, and in fact lower expression of some reactive genes.[26] Examining expression of astrocyte reactive genes[48] in the current nRNAseq dataset from P26-28 cortical astrocytes *in vivo*, we also see no heightened reactivity in FXS relative to WT, and if anything, a trend towards reduced expression of astrocyte pan-reactive and inflammation-induced genes (**Figure 3.7**). The data from this chapter thus does not appear to contribute to the hypothesis that astrocyte reactivity underlies Fmr1 KO pathophysiology.

Does the mGluR theory of FXS apply to astrocytes?

A longstanding theory in FXS literature is that increased mGluR signaling is a central pathway mediating the effects of FMRP loss;[2] indeed, inhibiting mGluR genetically or pharmacologically could rescue many FXS phenotypes in the Fmr1 KO mouse,[10,49] though human clinical trials have been equivocal.[50–52] In contrast to the upregulation observed in neurons, mGluR5 mRNA and protein was observed to be decreased in Fmr1 KO cultured P0-3 cortical astrocytes.[53] Moreover, both mGluR3 and mGluR5, the primary mGluR family members expressed in astrocytes, were downregulated at the mRNA level in P7 cultured cortical astrocytes.[53] By P26-28, the timepoint of the nuclear RNAseq dataset described in this chapter, astrocytes have nearly completed the developmental downregulation of mGluR5,[54] and primarily express mGluR3 (TPM in WT: *Grm3* = 174.3, *Grm5* = 7.1, *Grm1,2,4,6,7,8* < 5). Interestingly, we find that mGluR3 is upregulated at P26-28 in Fmr1 KO (TPM in FXS: *Grm3* = 245.9, L2FC = 0.42, p-adj = 0.027). This contrast with other studies of mGluRs in astrocytes could be due to the fact

we measured nuclear RNA, which could be changed in the opposite direction as protein levels, as the cell attempts to compensate for a changed protein level. Alternatively, our finding could indicate that astrocytes undergo a developmental switch from early downregulation of mGluRs to later upregulation. The implications of this, and whether mGluR3/5 activity in astrocytes affects FXS phenotypes (for example through calcium store release, as documented in inferior colliculus astrocytes[55]) remain to be seen, and confirmation of mGluR changes in Fmr1 KO astrocytes will require a detailed transcriptomic timecourse.

Overall, our transcriptomic dataset provides a detailed examination of astrocyte state changes due to Fmr1 KO and Smad4 cKO. While the astrocyte Fmr1 KO transcriptomic changes we observe differ from those seen in the ribosome profiling P40 dataset in FVB-background Fmr1 KO mouse cortical astrocyte from Men et al.,[40] the lack of overlap may be due to mouse background (C57Bl6/J vs. FVB), timepoint (P26-28 vs. P40), or cellular compartment (nuclear vs. ribosomal RNA) differences. Our finding that Fmr1 KO astrocytes are hypermetabolic at P26-28 is consistent with a general hypermetabolic state observed in other cell types and bulk tissue in FXS brain,[2,30,31] and the Smad4 cKO downregulation of oxidative phosphorylation and glycolysis/gluconeogenesis pathways represents a possible mechanistic pathway underlying Smad4 cKO rescue of FXS deficits we observed in Chapter 2.

A

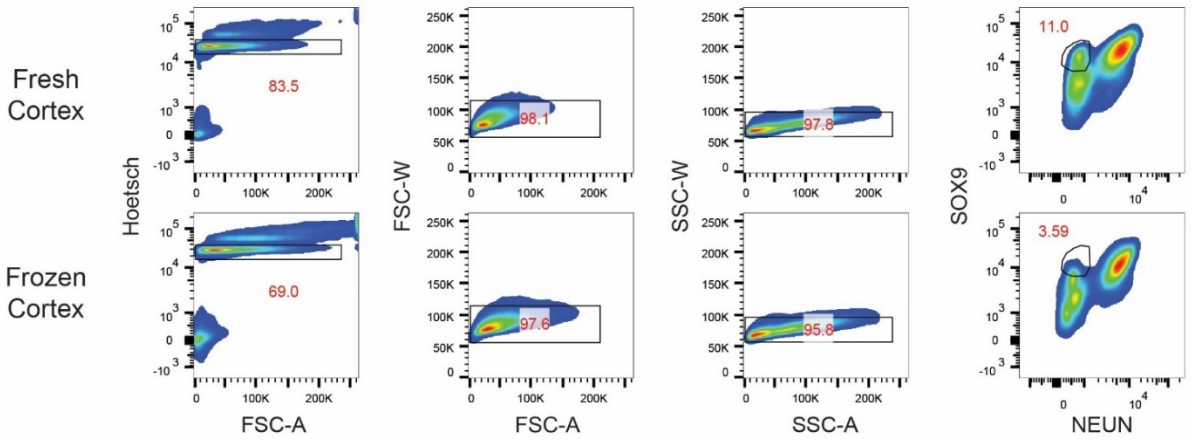

B

	Weight Cortex (mg)	Nuclei pre-FACS (million)	Sorted SOX9+NEUN- cells	Tapestation RNA (ng)
Fresh	170.1	8	150k	39
Frozen	153.9	7.1	150k	63

Figure 3.1. Fresh and frozen tissue comparison for glyoxal-fixed nuclear isolation.

A. Fluorescence-activated cell sorting (FACS) gating strategy for astrocyte (SOX9+NEUN-) nuclei. Identical gates were applied to fresh cortex and frozen cortex, and all steps for preparation for FACS were performed in parallel.
B. Experimental parameters measured for fresh and frozen tissue comparison experiment.

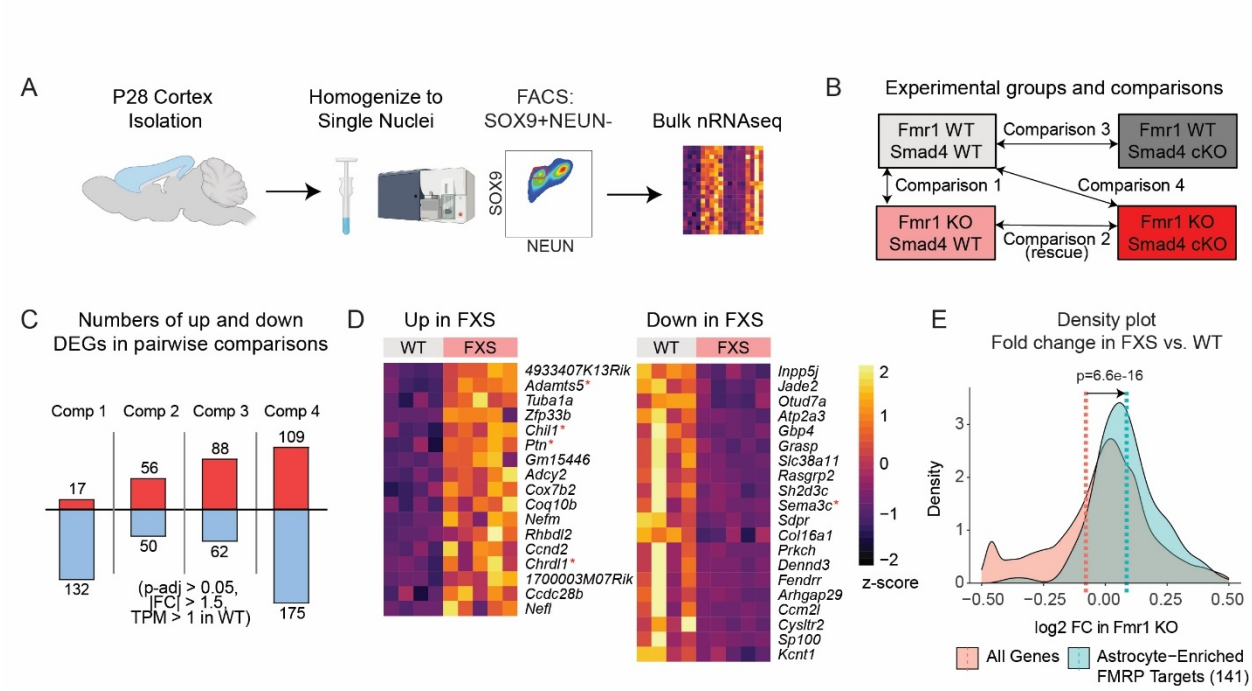

Figure 3.2. Nuclear transcriptomics identifies Fmr1 KO and Smad4 cKO astrocyte *in vivo* transcriptomic dysregulation.

A. Protocol for glyoxal-fixed astrocyte nuclei transcriptomics via FACS sorting for SOX9+NEUN- nuclei followed by bulk nRNAseq.
B. Experimental groups and pairwise comparisons.
C. Numbers of up- and down-DEGs for the transcriptomic experiment. N = 4 WT, 6 WT;Smad4 cKO, 5 FXS, 4 FXS;Smad4 cKO. Cutoffs p-adj < 0.05, FC > 1.5, TPM in WT > 1 calculated with DESeq2 with Benjamini-Hochberg (BH) correction. See also supplementary tables 1,2.
D. Top up- and downregulated genes in Fmr1 KO (Comparison 1). Genes filtered by FC > 1.5 and TPM in WT > 1, sorted by p-adj. Red asterisks indicate genes encoding known astrocyte-secreted proteins.
E. Density plot of log2 fold change in Fmr1 KO (Comparison 1) for two gene sets: (1) all genes detected in nRNAseq, (2) FMRP targets (842 genes, Darnell et al. 2011),[7] filtered to those enriched at an mRNA level in astrocytes (141 genes, Zhang et al. 2014).[36] The average log2 fold changes for these gene sets are denoted with dashed lines. The two distributions are significant different, statistics by z-test.

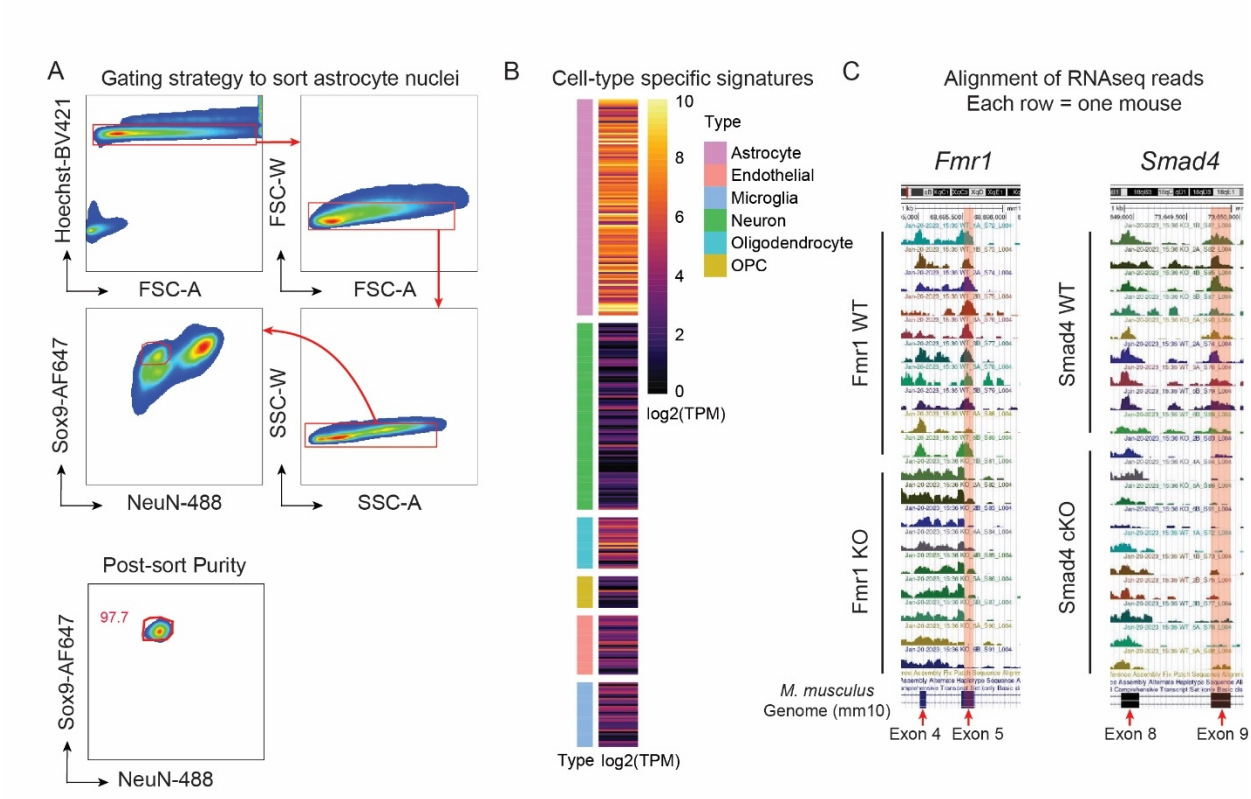

Figure 3.3. Gating strategy and validation of nuclear transcriptomic experiment.

A. Above, FACS gating strategy to obtain SOX9+NEUN- nuclei for sequencing. Below, example purity plot.
B. Heatmap of average abundance in nRNAseq for known cell-type specific genes. OPC = oligodendrocyte precursor cell.
C. Bigwig plots aligning RNAseq reads to the *M. Musculus* genome (mm10). Each sample (one mouse) is one row. Fmr1 KO samples have depletion of reads to the latter half of *Fmr1* exon 5, corresponding to the locus where a neomycin resistance cassette was inserted to create the KO. Smad4 cKO samples have depletion of reads to *Smad4* exon 9, the locus where loxP sites were inserted to create the floxed mouse. The red rectangles denote these loci.

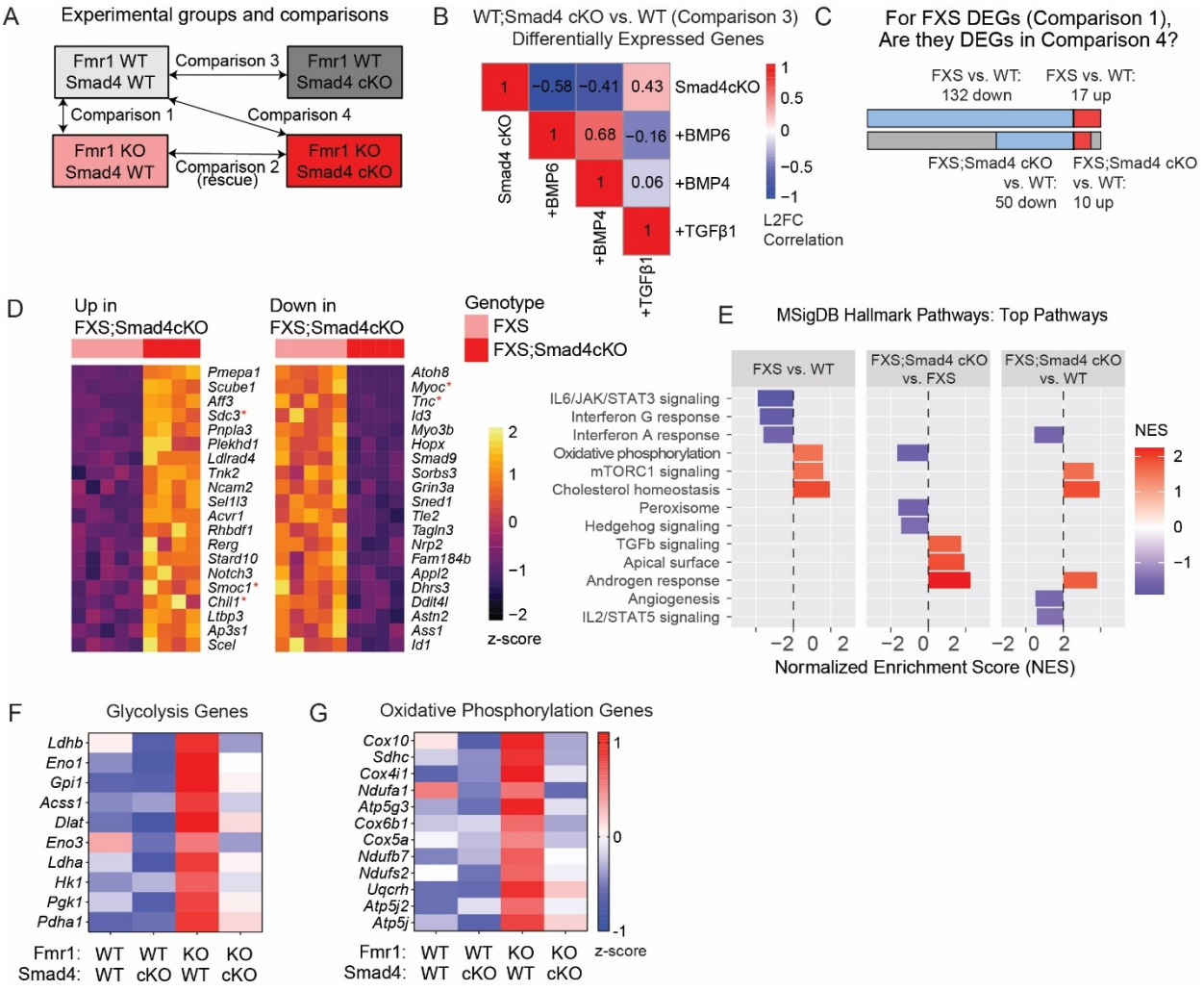

Figure 3.4. Smad4 cKO moderates Fmr1 KO astrocyte transcriptomic activation of metabolic pathways.

A. Pairwise comparisons and groups for RNAseq experiment.
B. Correlation matrix for L2FC of 150 *in vivo* RNAseq Smad4 cKO DEGs, between *in vivo* RNAseq Smad4cKO, WT astrocytes incubated with BMP6 (Caldwell et al., 2022),[26] and cultured astrocytes incubated with BMP4 or TGFβ1 (Divolis et al., 2017).[37]
C. For the 149 FXS DEGs (Comparison 1), the majority are no longer significantly changed in Comparison 4 (FXS;Smad4cKO vs. WT) (See Table S2 for list).
D. Top up- and downregulated genes in FXS;Smad4cKO compared to FXS (Comparison 2). Genes filtered by FC > 1.5 and TPM in WT > 1, sorted by p-adj. Red asterisks indicate genes encoding known astrocyte-secreted proteins.
E. Top 3 significantly up- and down-regulated pathways by normalized enrichment score (NES), for each of the comparisons 1, 2, and 4; via gene set enrichment analysis on the MSigDB Hallmark Gene Sets with all genes TPM>1 ranked by –log10(p-value) * sign(L2FC).
F. and G. Z-scores of genes in (F) “glycolysis” (KEGG M11521) and (G) “oxidative phosphorylation” (MSigDB MM3893) gene sets, averaged for each genotype; displaying genes up in Fmr1 KO and lowered by Smad4 cKO. See Figure 3.5 for full gene sets.

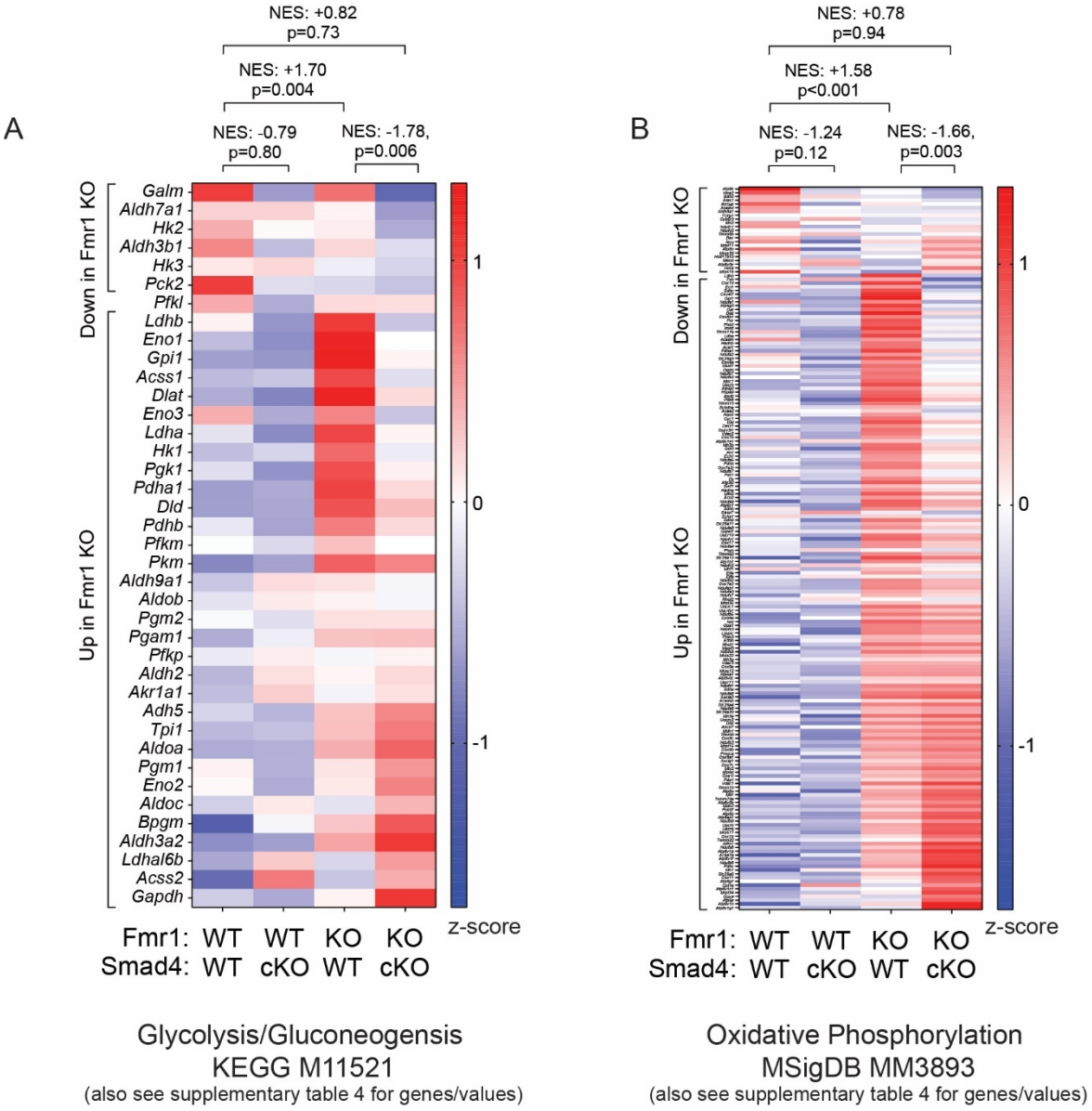

Figure 3.5. Full gene sets for glycolysis/gluconeogenesis and oxidative phosphorylation.

A. Z-scores of all genes in “glycolysis” gene set (KEGG M11521), averaged within each genotype, displaying all 39 genes in the set with average TPM > 1 for each genotype group.
B. Z-scores of all genes in “oxidative phosphorylation” gene set (MSigDB 3893), averaged within each genotype, displaying all 193 genes in the set with average TPM > 1 for each genotype group.

Figure 3.6. Comparison of *in vivo* RNAseq transcriptomics with other datasets.

A. Overlap of Fmr1 KO up- and downregulated genes from *in vivo* RNAseq with up- and downregulated genes from RNAseq of cultured P7 Fmr1 KO astrocytes (Caldwell et al., 2022).[26]
B. Overlap of Smad4 cKO up- and downregulated genes from *in vivo* RNAseq with up- and downregulated genes from RNAseq of cultured P7 astrocytes incubated with BMP6 (Caldwell et al., 2022).[26]
C. Overlap of Fmr1 KO up- and downregulated genes from *in vivo* RNAseq with translating RNAseq profiling of P40 Fmr1 KO astrocytes in FVB line (Men et al., 2020).[40]
D. Scatterplot of L2FCs for all 15682 genes detected, between *in vivo* RNAseq and cultured Fmr1 KO astrocytes (Caldwell et al., 2022).[26]
E. Scatterplot as in 3.6D, limited to the set of 103 *in vivo* RNAseq Fmr1 KO DEGs also detected *in vitro*.
F. Scatterplot of L2FCs for the set of all 18300 genes between *in vivo* RNAseq Smad4cKO and cultured WT astrocytes incubated with BMP6 (Caldwell et al., 2022).[26]
G. Scatterplot as in 3.6F, limited to the set of 149 *in vivo* RNAseq Smad4cKO DEGs also detected *in vitro*.

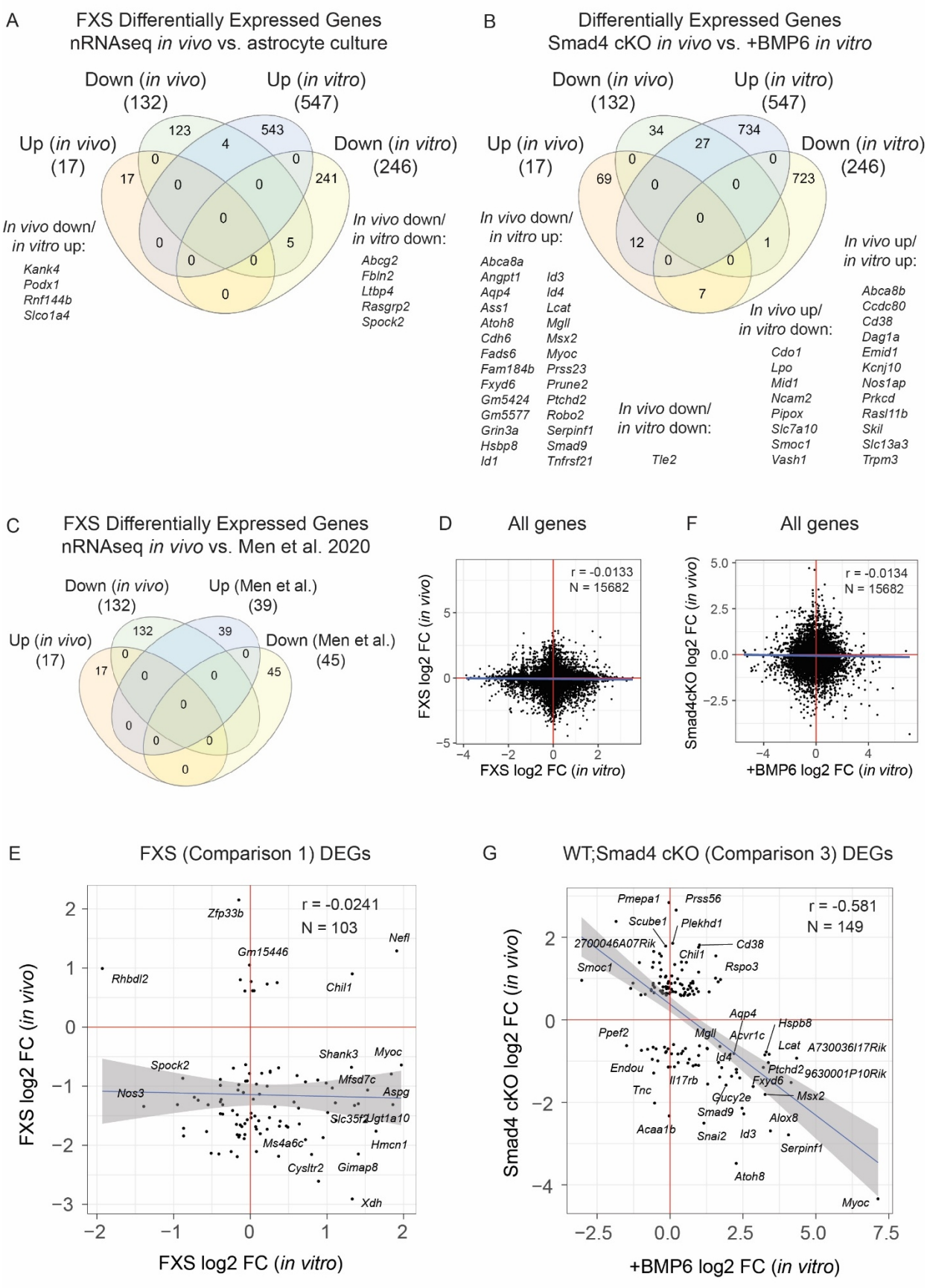
A
FXS Differentially Expressed Genes
nRNAseq in vivo vs. astrocyte culture
Down (in vivo) (132)
Up (in vitro) (547)
Up (in vivo) (17)
Down (in vitro) (246)
123
543
4
0
0
17
0
0
241
0
0
0
0
5
0
0
0
In vivo down/ in vitro up:
Kank4
Podx1
Rnf144b
Slco1a4
In vivo down/ in vitro down:
Abcg2
Fbln2
Ltbp4
Rasgrp2
Spock2
B
Differentially Expressed Genes
Smad4 cKO in vivo vs. +BMP6 in vitro
Down (in vivo) (132)
Up (in vitro) (547)
Up (in vivo) (17)
Down (in vitro) (246)
34
734
27
0
0
69
0
0
723
0
12
1
0
0
7
In vivo down/ in vitro up:
Abca8a
Angpt1
Aqp4
Ass1
Atoh8
Cdh6
Fads6
Fam184b
Fxyd6
Gm5424
Gm5577
Grin3a
Hsbp8
Id1
Id3
Id4
Lcat
Mgll
Msx2
Myoc
Prss23
Prune2
Ptchd2
Robo2
Serpinf1
Smad9
Tnfrsf21
In vivo down/ in vitro down:
Tle2
In vivo up/ in vitro down:
Cdo1
Lpo
Mid1
Ncam2
Pipox
Slc7a10
Smoc1
Vash1
In vivo up/ in vitro up:
Abca8b
Ccdc80
Cd38
Dag1a
Emid1
Kcnj10
Nos1ap
Prkcd
Rasl11b
Skil
Slc13a3
Trpm3
C
FXS Differentially Expressed Genes
nRNAseq in vivo vs. Men et al. 2020
Down (in vivo) (132)
Up (Men et al.) (39)
Up (in vivo) (17)
Down (Men et al.) (45)
132
39
0
0
17
0
0
45
0
0
0
0
0
D
All genes
r = -0.0133
N = 15682
FXS log2 FC (in vivo)
FXS log2 FC (in vitro)
F
All genes
r = -0.0134
N = 15682
Smad4cKO log2 FC (in vivo)
+BMP6 log2 FC (in vitro)
E
FXS (Comparison 1) DEGs
r = -0.0241
N = 103
Zfp33b
Nefl
Gm15446
Rhbdl2
Chil1
Shank3
Myoc
Spock2
Mfsd7c
Nos3
Aspg
Slc35f2
Ugt1a10
Ms4a6c
Hmcn1
Cysltr2
Gimap8
Xdh
FXS log2 FC (in vivo)
FXS log2 FC (in vitro)
G
WT;Smad4 cKO (Comparison 3) DEGs
r = -0.581
N = 149
Pmepa1
Prss56
Scube1
Plekhd1
2700046A07Rik
Cd38
Chil1
Smoc1
Rspo3
Aqp4
Hspb8
Ppef2
Mgll
Acvr1c
Lcat
A730036I17Rik
Id4
Endou
Ptchd2
9630001P10Rik
Il17rb
Fxyd6
Tnc
Msx2
Gucy2e
Smad9
Alox8
Acaa1b
Snai2
Id3
Serpinf1
Atoh8
Myoc
Smad4 cKO log2 FC (in vivo)
+BMP6 log2 FC (in vitro)

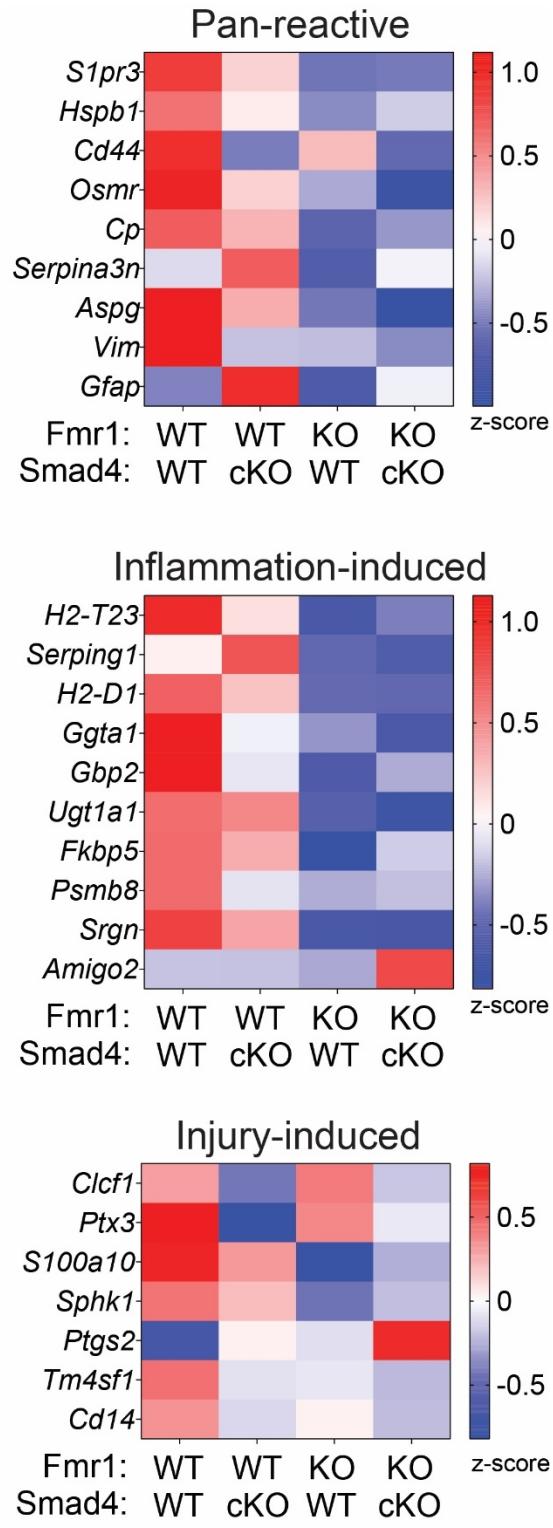

Figure 3.7. Astrocyte reactivity genes in nRNAseq. Average z-scores by genotype for expression of astrocyte pan-reactive, inflammation-induced, and injury-induced genes, list taken from Liddelow et al. 2017,[48] filtering for genes expressed in nRNAseq with average TPM > 1 in at least one genotype group.

References

1. Contractor, A., Klyachko, V. A. & Portera-Cailliau, C. Altered Neuronal and Circuit Excitability in Fragile X Syndrome. *Neuron* **87**, 699–715 (2015).

2. Hagerman, R. J. *et al.* Fragile X syndrome. *Nature Reviews Disease Primers* **3**, (2017).

3. Irwin, S. A. *et al.* Dendritic spine and dendritic field characteristics of layer V pyramidal neurons in the visual cortex of fragile-X knockout mice. *American Journal of Medical Genetics* **111**, 140–146 (2002).

4. Prilutsky, D. *et al.* Gene expression analysis in Fmr1KO mice identifies an immunological signature in brain tissue and mGluR5-related signaling in primary neuronal cultures. *Molecular Autism* **6**, 66 (2015).

5. Bagni, C. & Zukin, R. S. A Synaptic Perspective of Fragile X Syndrome and Autism Spectrum Disorders. *Neuron* **101**, 1070–1088 (2019).

6. Richter, J. D. & Zhao, X. The molecular biology of FMRP: new insights into fragile X syndrome. *Nat Rev Neurosci* (2021) doi:10.1038/s41583-021-00432-0.

7. Darnell, J. C. *et al.* FMRP Stalls Ribosomal Translocation on mRNAs Linked to Synaptic Function and Autism. *Cell* **146**, 247–261 (2011).

8. Ascano, M. *et al.* FMRP targets distinct mRNA sequence elements to regulate protein expression. *Nature* **492**, 382–386 (2012).

9. Maurin, T. *et al.* HITS-CLIP in various brain areas reveals new targets and new modalities of RNA binding by fragile X mental retardation protein. *Nucleic Acids Research* **46**, 6344–6355 (2018).

10. Dölen, G. *et al.* Correction of Fragile X Syndrome in Mice. *Neuron* **56**, 955–962 (2007).

11. Louros, S. R. *et al.* Excessive proteostasis contributes to pathology in fragile X syndrome. *Neuron* **111**, 508-525.e7 (2023).

12. McCamphill, P. K. *et al.* Selective inhibition of glycogen synthase kinase 3α corrects pathophysiology in a mouse model of fragile X syndrome. *Science Translational Medicine* **12**, (2020).

13. Qin, M. *et al.* Altered Cerebral Protein Synthesis in Fragile X Syndrome: Studies in Human Subjects and Knockout Mice. *J Cereb Blood Flow Metab* **33**, 499–507 (2013).

14. Wang, Z. *et al.* Effects of Fmr1 Gene Mutations on Sex Differences in Autism-Like Behavior and Dendritic Spine Development in Mice and Transcriptomic Studies. *Neuroscience* **534**, 16–28 (2023).

15. Hale, C. R. *et al.* FMRP regulates mRNAs encoding distinct functions in the cell body and dendrites of CA1 pyramidal neurons. *eLife* **10**, e71892 (2021).

16. Kang, Y. *et al.* A human forebrain organoid model of fragile X syndrome exhibits altered neurogenesis and highlights new treatment strategies. *Nat Neurosci* **24**, 1377–1391 (2021).

17. Lu, P. *et al.* Integrated transcriptome analysis of human iPS cells derived from a fragile X syndrome patient during neuronal differentiation. *Science China Life Sciences* **59**, 1093–1105 (2016).

18. Donnard, E., Shu, H. & Garber, M. Single cell transcriptomics reveals dysregulated cellular and molecular networks in a fragile X syndrome model. *PLoS Genet* **18**, e1010221 (2022).

19. Men, Y. *et al.* Astroglial FMRP deficiency cell-autonomously up-regulates miR-128 and disrupts developmental astroglial mGluR5 signaling. *Proceedings of the National Academy of Sciences* **117**, 25092–25103 (2020).

20. Labarta-Bajo, L., Deng, J., Contreras, M. & Allen, N. J. Protocol for the purification and transcriptomic analysis of mouse astrocytes using GFAT. *STAR Protocols* **4**, 102599 (2023).

21. Sun, W. *et al.* SOX9 Is an Astrocyte-Specific Nuclear Marker in the Adult Brain Outside the Neurogenic Regions. *J. Neurosci.* **37**, 4493–4507 (2017).

22. Sanz, E. *et al.* Cell-type-specific isolation of ribosome-associated mRNA from complex tissues. *Proc. Natl. Acad. Sci. U.S.A.* **106**, 13939–13944 (2009).

23. Dhaliwal, N. K. & Mitchell, J. A. Nuclear RNA Isolation and Sequencing. in *Long Non-Coding RNAs* (eds. Feng, Y. & Zhang, L.) vol. 1402 63–71 (Springer New York, New York, NY, 2016).

24. Allen, N. J. & Eroglu, C. Cell Biology of Astrocyte-Synapse Interactions. *Neuron* **96**, 697–708 (2017).

25. Boisvert, M. M., Erikson, G. A., Shokhirev, M. N. & Allen, N. J. The Aging Astrocyte Transcriptome from Multiple Regions of the Mouse Brain. *Cell Reports* **22**, 269–285 (2018).

26. Caldwell, A. L. M. *et al.* Aberrant astrocyte protein secretion contributes to altered neuronal development in multiple models of neurodevelopmental disorders. *Nat Neurosci* **25**, 1163–1178 (2022).

27. Jiang, W. *et al.* CHI3L1 signaling impairs hippocampal neurogenesis and cognitive function in autoimmune-mediated neuroinflammation. *Sci. Adv.* **9**, eadg8148 (2023).

28. Brandebura, A. N., Asbell, Q. N., Micael, M. K. B. & Allen, N. J. *Dysregulation of Astrocyte-Secreted Pleiotrophin Contributes to Neuronal Structural and Functional Deficits in Down Syndrome*. http://biorxiv.org/lookup/doi/10.1101/2023.09.26.559633 (2023) doi:10.1101/2023.09.26.559633.

29. Blanco-Suarez, E., Liu, T.-F., Kopelevich, A. & Allen, N. J. Astrocyte-Secreted Chordin-like 1 Drives Synapse Maturation and Limits Plasticity by Increasing Synaptic GluA2 AMPA Receptors. *Neuron* **100**, 1116-1132.e13 (2018).

30. Sharma, A. *et al.* Dysregulation of mTOR Signaling in Fragile X Syndrome. *Journal of Neuroscience* **30**, 694–702 (2010).

31. Kotchetkov, P., Blakeley, N. & Lacoste, B. Involvement of brain metabolism in neurodevelopmental disorders. in *International Review of Neurobiology* vol. 173 67–113 (Elsevier, 2023).

32. Licznerski, P. *et al.* ATP Synthase c-Subunit Leak Causes Aberrant Cellular Metabolism in Fragile X Syndrome. *Cell* **0**, (2020).

33. Benachenhou, S. *et al.* Cholesterol alterations in fragile X syndrome, autism spectrum disorders and other neurodevelopmental disorders. in *International Review of Neurobiology* vol. 173 115–139 (Elsevier, 2023).

34. Talvio, K. *et al.* An iPSC-derived astrocyte model of fragile X syndrome exhibits dysregulated cholesterol homeostasis. *Commun Biol* **6**, 789 (2023).

35. Ren, B. *et al.* Dysregulated cholesterol metabolism, aberrant excitability and altered cell cycle of astrocytes in fragile X syndrome. *Glia* **71**, 1176–1196 (2023).

36. Zhang, Y. *et al.* An RNA-Sequencing Transcriptome and Splicing Database of Glia, Neurons, and Vascular Cells of the Cerebral Cortex. *Journal of Neuroscience* **34**, 11929–11947 (2014).

37. Divolis, G. *et al.* Activation of both transforming growth factor-β and bone morphogenetic protein signalling pathways upon traumatic brain injury restrains pro-inflammatory and boosts tissue reparatory responses of reactive astrocytes and microglia. *Brain Communications* **1**, fcz028 (2019).

38. Yang, J., Ueharu, H. & Mishina, Y. Energy metabolism: A newly emerging target of BMP signaling in bone homeostasis. *Bone* **138**, 115467 (2020).

39. Dionne, O. & Corbin, F. An “Omic” Overview of Fragile X Syndrome. *Biology* **10**, 433 (2021).

40. Men, Y. *et al.* Astroglial FMRP deficiency cell-autonomously up-regulates miR-128 and disrupts developmental astroglial mGluR5 signaling. *Proc. Natl. Acad. Sci. U.S.A.* **117**, 25092–25103 (2020).

41. Ye, Y. *et al.* PI(4,5)P2 5-phosphatase A regulates PI3K/Akt signalling and has a tumour suppressive role in human melanoma. *Nat Commun* **4**, 1508 (2013).

42. Bonvento, G. & Bolaños, J. P. Astrocyte-neuron metabolic cooperation shapes brain activity. *Cell Metabolism* **33**, 1546–1564 (2021).

43. Barros, L. F., Schirmeier, S. & Weber, B. The Astrocyte: Metabolic Hub of the Brain. *Cold Spring Harb Perspect Biol* a041355 (2024) doi:10.1101/cshperspect.a041355.

44. Vandenberg, G. G., Dawson, N. J., Head, A., Scott, G. R. & Scott, A. L. Astrocyte-mediated disruption of ROS homeostasis in Fragile X mouse model. *Neurochemistry International* **146**, 105036 (2021).

45. Sawicka, K., Pyronneau, A., Chao, M., Bennett, M. V. L. & Zukin, R. S. Elevated ERK/p90 ribosomal S6 kinase activity underlies audiogenic seizure susceptibility in fragile X mice. *Proc. Natl. Acad. Sci. U.S.A.* **113**, (2016).

46. Shen, M. *et al.* Species-specific FMRP regulation of RACK1 is critical for prenatal cortical development. *Neuron* S089662732300702X (2023) doi:10.1016/j.neuron.2023.09.014.

47. Lee, F. H. F., Lai, T. K. Y., Su, P. & Liu, F. Altered cortical Cytoarchitecture in the Fmr1 knockout mouse. *Molecular Brain* **12**, (2019).

48. Liddelow, S. A. *et al.* Neurotoxic reactive astrocytes are induced by activated microglia. *Nature* **541**, 481–487 (2017).

49. Michalon, A. *et al.* Chronic Pharmacological mGlu5 Inhibition Corrects Fragile X in Adult Mice. *Neuron* **74**, 49–56 (2012).

50. Berry-Kravis, E. *et al.* Effects of AFQ056 on language learning in fragile X syndrome. *Journal of Clinical Investigation* **134**, e171723 (2024).

51. Neul, J. L. Challenges in developing therapies in fragile X syndrome: how the FXLEARN trial can guide research. *Journal of Clinical Investigation* **134**, e175036 (2024).

52. Hagerman, R. J. & Hagerman, P. J. Fragile X Syndrome: Lessons Learned and What New Treatment Avenues Are on the Horizon. *Annu. Rev. Pharmacol. Toxicol.* **62**, annurev-pharmtox-052120-090147 (2022).

53. Higashimori, H. *et al.* Astroglial FMRP-dependent translational down-regulation of mGluR5 underlies glutamate transporter GLT1 dysregulation in the fragile X mouse. *Human Molecular Genetics* **22**, 2041–2054 (2013).

54. Sun, W. *et al.* Glutamate-Dependent Neuroglial Calcium Signaling Differs Between Young and Adult Brain. *Science* **339**, 197–200 (2013).

55. Kellner, V. *et al.* Dual metabotropic glutamate receptor signaling enables coordination of astrocyte and neuron activity in developing sensory domains. *Neuron* **109**, 2545-2555.e7 (2021).

Chapters 1-7, in part, have been submitted for publication. Deng J, Labarta-Bajo L, Brandebura AN, Kahn SB, Pinto AFM, Diedrich JK, Allen NJ (2024). Suppression of astrocyte BMP signaling improves fragile X syndrome molecular signatures and functional deficits. The dissertation author will be the first author of this publication, and Dr. Nicola Allen will be the senior author and principal investigator.

Chapter 4. Proteomic analysis of Fmr1 KO astrocytes with and without Smad4 cKO

Introduction

Rationale

Astrocyte-secreted proteins are known to contribute to *in vitro* Fmr1 KO phenotypes, as well as mediate Fmr1 KO phenotypic rescue when astrocyte BMP signaling is inhibited.[1] Additionally, from the RNAseq experiment in Chapter 3, genes encoding known astrocyte-secreted proteins[1–5] were among the top Fmr1 KO upregulated (*Adamts5*, *Chil1, Ptn*, *Chrdl1*) and downregulated (*Sema3c*) genes (**Figure 3.2D**), as well as Smad4 cKO upregulated (*Sdc3*, *Sparc, C4b*) and downregulated (*Myoc*, *Tnc*, *Serpinf1*) genes (**Figure 3.4D, Table S2**). However, correlation between astrocyte transcriptional changes and protein secretion changes is limited: in a study of cultured P7 astrocytes probing both cell lysate transcriptome as well as secreted media proteome in FXS, only 4 of 131 upregulated secreted proteins ($p < 0.05$) were upregulated in RNA (547 total upregulated genes at FC > 1.5, adj-$p < 0.05$), and only 4 of 108 downregulated secreted proteins ($p < 0.05$) were downregulated in RNA (246 total downregulated genes).[1] This low level of overlap may reflect the general inability of transcriptional information to capture protein levels, which are also governed by alternative splicing, transcript degradation, post-translational modifications, protein-protein interactions and protein degradation.[6] Moreover, specific to FXS, FMRP further disassociates RNA and protein levels, given its complex molecular effects including translation repression as well as activation.[7] To assess how Smad4 cKO might improve Fmr1 KO astrocyte-secreted proteins *in vivo*, we thus sought to quantify changes in astrocyte secretion at the protein level.

Fragile X syndrome proteomics

Given the established role of FMRP as a protein translational repressor, and the bulk increase in protein translation others have observed across brain regions,[8–10] many studies have incorporated unbiased proteomic profiling to study changes in protein levels in Fmr1 KO and FXS. Various analyses including multiple *in vivo* brain regions in Fmr1 KO mouse and patient, *ex vivo* Fmr1 KO brain slice, different Fmr1 KO primary culture systems, as well as human induced pluripotent stem cell (hiPSC)-based neuron and astrocyte cultures have been characterized.[6,11–17] Common dysregulated proteins span cellular functions including synaptic plasticity, RNA translation, and mitochondrial function.[6] Studies of Fmr1 KO synaptosomes have shown increased expression of proteins involved in synaptic pruning, formation, and maturation[17,18] as well as neurite outgrowth, synaptic vesicles, and synaptic transmission.[19,20] Study of the *de novo* translation profile of Fmr1 KO mouse hippocampal slices shows increased expression of biosynthetic, protein-folding, and synaptic proteins such as mGluR5.[11] Bulk profiling of Fmr1 KO cortical tissue has shown dysregulation of ribosomal proteins, complement, and coagulation pathways among other changes.[12,15,16] While there are fewer astrocyte-specific proteomic studies, a recent report of FACS-sorted P40 cortical astrocytes showed dysregulation of phagosome maturation, axon guidance, gap junction, and gluconeogenesis/glycolysis proteins,[21] and cultured hiPSC-astrocyte proteomics shows upregulated translation, citric acid cycle, and fatty acid oxidation pathways and downregulated cholesterol biosynthesis and nucleocytoplasmic transport.[14] However, the above studies do not yet include coverage of astrocyte-secreted proteins in Fmr1 KO *in vivo*.

Proximity labeling proteomics

Technologies to probe *in vivo* proteomes in a cell type-specific or subcompartment-specific manner broadly fall into two categories: metabolic/isotopic labeling and proximity labeling. In metabolic labeling, radioisotope-labeled or biorthogonal amino acids are incorporated via supplementation and can be subsequently analyzed via radiography or click chemistry on

biorthogonal amino acids (e.g. click chemistry).[22] tRNA synthetases engineered to incorporate biologically inert biorthogonal amino acids can then generate specificity when genetically targeted to specific cell types or organelles.[23] In proximity labeling, an enzyme is introduced into the system and nonspecifically labels nearby proteins with a tag that enables subsequent purification.[24] Proximity labeling enzymes often require higher-than-biological concentrations of tag and/or catalyst, which can be supplemented at specific times to enable temporal control of protein labeling.[24] Prominent examples include peroxidases to label nearby tyrosines with biotin (e.g. ascorbate acid peroxidase or APEX[25]) and biotin ligases to label nearby lysines with biotin (e.g. BioID,[26] TurboID[27]). The former requires supplementation with biotin-phenol tag and hydrogen peroxide catalyst, the toxicity of which makes APEX suitable primarily for shorter labeling periods for *in vitro* or *ex vivo* settings.[28] The latter requires ATP at biological levels as well as supplemented biotin; the low toxicity of biotin makes BioID and TurboID ideal for *in vivo* experiments.[28] To label astrocyte-secreted proteins *in vivo* while avoiding hydrogen peroxide and the need for an additional click chemistry step, we chose to use a biotin-based proximity labeling approach.

Astrocyte-specific *in vivo* proteomics

Recent advancements in cell type-specific *in vivo* proteomics enabled by metabolic labeling and proximity labeling approaches[23,27,29] have led to profiling of astrocytes *in vivo*. Rayaprolu et al. characterized the astrocyte cytosolic proteome and its variations between brain regions with TurboID.[30] Takano et al. characterized the astrocyte synaptic cleft proteome with a Split-TurboID approach, in which two catalytically inactive halves of the TurboID enzyme were expressed at astrocyte and neuron membranes and regain catalytic activity only when physically apposed in close proximity, i.e. at astrocyte-neuron membrane contacts.[31] Prabhakar et al. characterized the astrocyte cytosolic proteome between various brain regions with metabolic labeling using MetRS.[32] Finally, Soto et al. characterized various astrocyte subcompartments (cytosol, plasma membrane, endfeet, fine processes, gap junctions, K channels) with TurboID

fusion proteins.[33] However, these published approaches do not focus on astroctye secreted proteins and as a result have little to no coverage of this subcompartment.

In this chapter, we adapt a proximity labeling approach to quantify astrocyte secreted and membrane proteins *in vivo*. We use this approach to quantify proteins and pathways dysregulated in Fmr1 KO and Smad4 cKO and ask if Smad4 cKO might reverse protein dysregulations in Fmr1 KO astrocytes.

Results

Development of proximity labeling constructs to label astrocyte secreted proteins

To profile the full complement of astrocyte-secreted proteins *in vivo*, we took a proximity labeling proteomic approach with the enzyme TurboID,[27] which labels nearby proteins with biotin. Expressing TurboID in a cell-type and compartment-specific manner enables *in vivo* biotin tagging and subsequent streptavidin enrichment of proteins within a specific cellular compartment. We subcloned and tested three constructs based on subcellular TurboID localizations known to target secreted proteins: endoplasmic reticulum membrane (ERM) facing cytosol (via cytochrome P450 (C1(1-29)) targeting sequence),[27] ERM facing ER lumen (via fusion protein with Sec61b),[34] and ER lumen (via KDEL ER retention signal) (**Figure 4.1A**).[34,35] We also subcloned a construct with TurboID expressed throughout cytosol (cyto-TurboID with nuclear exclusion sequence) as comparison. All three ER constructs were expressed in cultured astrocytes in a net-like morphology characteristic of ER, in contrast to the diffuse expression of cyto-TurboID, and exhibited active biotinylation (**Figure 4.1B,C**). Pilot mass spectrometry on both astrocyte conditioned media and lysates suggested highest labeling of secreted proteins in the ER lumen construct (ER-TurboID) (**Figure 4.1D**). To test ER-TurboID *in vivo*, we packaged the construct

into AAV-PHP.eB (an adeno-associated virus with serotype allowing crossing of the blood-brain barrier to transduce the CNS),[36] injected virus retroorbitally at P12, labeled with exogenous biotin by subcutaneous injection from P21 to P26, and collected mice at P27 (**Figure 4.2A**). ER-TurboID was highly expressed by P20 (**Figure 4.3A**) and incorporated biotin efficiently and specifically in astrocytes by P27 (**Figures 4.2B,C**). Thus we adapted and optimized a protocol to label astrocyte-secreted proteins *in vivo*.

Optimization of protocol to isolate biotin-tagged secreted proteins

To optimally enrich for secreted proteins while isolating biotin-tagged proteins, we optimized several parameters of the streptavidin pulldown described by others.[29] Specifically, we performed pilot testing to optimize the biotin binding reagent (magnetic streptavidin beads vs. neutravidin agarose), the ratio of tissue to biotin binding reagent, the tissue lysis buffer, and the immunoaffinity depletion of endogenous biotinylated enzymes. As a result of these optimizations (**Figure 4.4**), we determined that streptavidin magnetic beads resulted in more specific enrichment than neutravidin agarose, that a ratio of one ul streptavidin beads to 20ug biotin-labeled tissue could optimally enrich for biotinylated proteins, that a lysis buffer based on detergent NP40 was most suitable for enriching for astrocyte secreted and membrane proteins, and that immunodepletion with anti-pyruvate carboxylase antibody conjugated to magnetic protein G beads resulted in >80% depletion of this highly prevalent endogenously biotinylated background protein.

Interrogating *in vivo* astrocyte endoplasmic reticulum-passaged proteins

To identify astrocyte-secreted proteins changed in Fmr1 KO and Smad4 cKO, three mice each of the four genotypes (1) WT, (2) WT;Smad4 cKO, (3) FXS, and (4) FXS;Smad4 cKO in the C57Bl6/J background were injected with ER-TurboID virus (**Figure 4.5A**). One mouse of each genotype was injected with virus expressing control protein spaghetti monster fluorescent protein

(smFP-HA, **Figures 4.2A, 4.3B,C**). All mice were given exogenous biotin, cortices were lysed, depleted for endogenously biotinylated pyruvate carboxylase as in [37], and biotinylated proteins were purified by streptavidin pulldown, pooled for 16-plex tandem mass tagging (TMT) to enable quantification using isotopic labeling, and analyzed by high-resolution liquid chromatography-mass spectroscopy (LC-MS) (**Figure 4.5A**). In total MS identified 22609 peptides corresponding to 2138 distinct proteins (**Table S6**). To validate enrichment of astrocyte labeling, we took detected proteins from a list of cell type-specific markers,[38] then calculated for each protein the ratio of (1) the average TMT signal across the 12 ER-TurboID samples, compared to (2) the average TMT signal across the 4 control samples. Astrocyte-specific markers showed highest enrichment compared to other cell type markers (log2 Turbo/Control ratio = 2.00), validating this approach (**Figure 4.2D, 4.3E**).

To better understand the proteins labeled by ER-TurboID, we took the 200 proteins with highest enrichment (corresponding to log2[Turbo/Control] > 2.38) to characterize the astrocyte ER-TurboID proteome (**Figure 4.5A**). This list includes known astrocyte-secreted proteins (e.g. APOE, GPC5, CLU, SPARCL1) as well as known astrocyte membrane proteins (e.g. ITGB5, GRM3, AQP4) and many perineuronal net (PNN) components (e.g. ACAN, BCAN, NCAN, VCAN, HAPLN1, HAPLN4). Cross-referencing a cell type-specific gene expression database shows a substantial number of proteins have known mRNA-level enrichment in astrocytes relative to other CNS cell types (95/200, 48%) (**Figure 4.5A**). Bioinformatics analysis showed that this proteome contains proteins localizing to the extracellular region (55 of 200, 28%), plasma membrane (67 of 200, 34%), or both (16/200, 8%); proteins predicted to have a signal peptide (111/200, 56%); and proteins encoded by genes implicated in neurologic disorders (57/200, 29%) (**Figure 4.5A**). Moreover, gene ontology for cellular compartment showed these 200 proteins are significantly enriched for the endoplasmic reticulum, membrane, and extracellular compartments (**Figure**

4.5B). In summary, we adapted and validated a proximity labeling approach to quantify astrocyte-secreted and membrane proteins *in vivo*.

Fmr1 KO astrocytes downregulate extracellular matrix proteins and secretory machinery

To determine proteins dysregulated in Fmr1 KO astrocytes, we compared FXS to WT, finding 95 differentially expressed proteins (DEPs) (**Figure 4.6A, Table S7**; threshold $p < 0.05$, $|FC| > 1.25$), 97% of which are enriched in TurboID over control. Among the Fmr1 KO DEPs (**Figures 4.6B,D**), we found downregulation of many perineuronal net components (ACAN, BCAN, NCAN, HAPLN1, HAPLN4, TNR), in concordance with Fmr1 KO literature documenting immature perineuronal nets in brain regions including auditory cortex.[39–41] Additionally, many cell membrane proteins with known genetic association to autism spectrum disorder were downregulated in Fmr1 KO (e.g. NRXN2,[42] NRXN3,[43] PLXNB1,[44] LRP1,[44] NRCAM[45]). Moreover, Fmr1 KO downregulated DEPs overlap significantly with known FMRP targets[46] (17/89 = 19% of downregulated DEPs, p = 9.6e-9) (**Figure 4.6C**), demonstrating that FMRP regulates protein expression in astrocytes. Cellular compartment analysis of the Fmr1 KO DEPs highlights that many detected DEPs localize to the ER, vesicles, membrane, and extracellular compartments, and have signal peptides (**Figure 4.6E,F**), as expected for this ER-TurboID proteomic method. At the pathway level, GSEA for the Fmr1 KO comparison showed downregulation of gene sets "protein secretion" and "apical junction" and upregulation of "mitotic spindle" (**Figure 4.10D**; **Table S8**).

We asked to what extent the changes we found in gene expression (RNAseq) were recapitulated at the protein level (ER-TurboID). We found no overlap between DEGs and DEPs, and Fmr1 KO vs WT fold changes for TPM (RNA) and TMT signal (protein) showed low correlation (**Figures 4.7A,B,C**). At the level of absolute abundance, there was a low, slightly positive, correlation (**Figures 4.7D,E,F**). This low degree of overlap between RNA and protein findings may be due to the different cellular compartments assayed (nuclear RNA vs. ER-transited

proteins)[47] as well as uncoupling of transcription from translation in the absence of translational regulator FMRP,[6] but also illustrates the importance of transcriptomics and proteomics as independent readouts of cellular state and function. Finally, we compared this *in vivo* proteomic dataset to an *in vivo* P40 Fmr1 KO astrocyte whole-cell proteomics dataset[21] and a cultured P7 Fmr1 KO astrocyte secreted protein dataset[1] and surprisingly found low overlap between the DEPs, and minimal correlations in log2 fold change of DEPs (**Figure 4.8A,C,D,E**), highlighting the roles that cellular context, subcellular compartment, and timepoint may play in proteomic variability.

Smad4 cKO restores Fmr1 KO astrocyte deficit in secretory machinery

We next asked if Smad4 cKO could rescue Fmr1 KO astrocyte proteomic dysregulation by performing pairwise comparisons across the four genotypes (1) WT, (2) WT;Smad4 cKO, (3) FXS, and (4) FXS;Smad4 cKO. First, to validate our proteomics results, we performed western blotting on cortical lysates from all four genotype groups for brevican (BCAN), a protein downregulated in the ER-TurboID data in FXS and Smad4 cKO (**Tables S6,7**) that is known to be astrocyte-enriched,[48] BMP-induced,[49,50] and a component of perineuronal nets. We found the same changes in BCAN expression across genotypes in western blot and ER-TurboID proteomics: a decrease in both Smad4 cKO and Fmr1 KO (**Figure 4.9A,B,C**). We also performed western blotting on cortical lysates for the astrocyte membrane protein hepaCAM, which was upregulated in our proteomic dataset in Smad4 cKO in both WT and FXS (**Figure 4.9F**). HepaCAM, which is known to be sufficient to induce inhibitory synaptogenesis,[51] was trending towards an increase in cortical lysates from FXS;Smad4 cKO compared to FXS (**Figure 4.9D,E**).

We then examined differentially expressed proteins and pathways in the pairwise comparisons FXS;Smad4cKO to FXS (Comparison 2) and FXS;Smad4cKO to WT (Comparison 4) (**Figure 4.10A**). Comparing FXS;Smad4cKO to WT (Comparison 4), we observed 134 DEPs (**Table S7**). Notably, the majority (57 of 95) of DEPs found when comparing FXS to WT

(Comparison 1) were no longer significantly changed when comparing the FXS;Smad4cKO to WT (Comparison 4) (**Figure 4.10B, Table S6**). These 57 proteins thus represent FXS proteomic dysregulations moderated by Smad4 cKO.

To directly assess the impact of Smad4 cKO in the FXS background, we also compared FXS;Smad4cKO to FXS (Comparison 2). We found 88 DEPs, and saw perineuronal net components as well as astrocyte-secreted Glypican 5 as top downregulated proteins (**Figure 4.10C**). In this comparison, top upregulated DEPs in FXS;Smad4cKO from FXS included both proteins restored to near WT levels (e.g. AP2A2, ALDOC, BIN1) and FXS-independent effects (e.g. MAPRE1, EIF3A) (**Figure 4.10C**). In contrast, top downregulated DEPs in FXS;Smad4 cKO augmented FXS changes (**Figure 4.10C**).

At the pathway level, GSEA showed “protein secretion” was a top activated pathway comparing FXS;Smad4 cKO to FXS, and not significantly changed when comparing FXS;Smad4 cKO to WT (**Figure 4.10D**). This reflects a rescue of the FXS downregulation of the “protein secretion” pathway and was driven by several proteins in secretory/vesicular trafficking/endocytosis pathway machinery downregulated in Fmr1 KO (e.g. CLTA, CLTC, AP2S1, AP2B1, AP2M1) and restored to near WT levels by Smad4 cKO (**Figure 4.10E, 4.11**). Additionally, vesicular trafficking proteins were decreased in conditioned media of astrocytes cultured with BMP6 (**Figure 4.10F**), strengthening the negative association between astrocyte BMP signaling and secretory machinery. However, Fmr1 KO upregulation of the mitotic spindle protein set and downregulation of the apical junction protein set were not affected by Smad4 cKO. In summary, our *in vivo* astrocyte proteomic dataset identifies a downregulation of secreted, membrane, and perineuronal net proteins in Fmr1 KO, with an Fmr1 KO deficit in vesicular trafficking machinery improved by Smad4 cKO.

Discussion

ER-TurboID to study astrocyte secreted and membrane proteins *in vivo*

Proteomics studies in Fmr1 KO have shown upregulated translation machinery and RNA-binding proteins in bulk tissue and neurons, as well as upregulated complement and coagulation pathways both in bulk tissue and in astrocytes.[1,16] However, until recently there has been an absence of tools to quantify astrocyte-secreted proteins *in vivo*. We developed a new approach to profile astrocyte ER-passaged proteins and quantify secreted and membrane proteins across different conditions during a specified timeframe. Our use of a construct targeted to the endoplasmic reticulum allows enriched labeling of proteins transited through the canonical secretion and membrane protein pathway, and the 16-plex tandem mass tag technology allows comparison across multiple conditions with both the statistical power to identify changed proteins as well as the incorporation of control non-TurboID background samples. Validation of our TurboID proteomic results by western blotting on cortical lysates (**Figure 4.9**) demonstrates the strength and reliability of this approach.

Smad4 cKO improves Fmr1 KO astrocyte downregulation of secretory machinery

We identified that many FMRP targets are dysregulated at a protein level in Fmr1 KO astrocytes (**Figure 4.6C**), and that secretory machinery including clathrins and Golgi adaptor proteins are downregulated in Fmr1 KO and improved by Smad4 cKO. BMP signaling thus could control bulk level of astrocyte-secreted proteins in Fmr1 KO. Indeed, the majority of changed secreted proteins in Fmr1 KO were downregulated (**Figure 4.6A**), and nearly half of the Fmr1 KO downregulated proteins had signal peptides, while none of the Fmr1 KO upregulated proteins did (**Figure 4.6F**). Other notable proteins that were downregulated in FXS (Comparison 1) and improved in FXS;Smad4 cKO (Comparison 2) include GABRA4 (GABA-A receptor alpha-4, down in Comparison 1 [FXS vs. WT], FC = 0.69, p = 0.017; trending up in Comparison 2 [FXS;Smad4

cKO vs. FXS], FC = 1.19, p = 0.25), FGG (fibrinogen, in the coagulation pathway, down in Comparison 1 [FXS vs. WT], FC = 0.48, p = 0.030, not significantly different in Comparison 2 [FXS;Smad4 cKO vs. FXS], FC = 1.57, p = 0.34), and HEPH (hephaestin, an iron transporter, BMPs are known to affect iron metabolism,[52] down in Comparison 1 [FXS vs. WT], FC = 0.48, p = 0.0099, not significantly different in Comparison 2 [FXS;Smad4 cKO vs. FXS], FC = 1.43, p = 0.27) (**Table S6,S7**). Importantly, several downregulated proteins in Fmr1 KO were further downregulated with Smad4 cKO, including GPC5, extracellular matrix components (ACAN, BCAN, HAPLN1, HAPLN4, NCAN, TNR), and membrane proteins (NCAM1, NRXN2, VCAM1) (**Figure 4.10C**). It is possible some of these proteins represent astrocyte homeostatic secretion and membrane function, which may be impaired by any alteration, e.g. either absence of FMRP or suppression of BMP signaling.

Mechanistic ties from ER-TurboID proteomic data to Smad4 cKO-improved Fmr1 KO phenotypes

By controlling secretory machinery protein levels, Smad4 cKO could control bulk level of astrocyte-secreted proteins in Fmr1 KO. Astrocytes can regulate synapse formation, function, and elimination through their secreted proteins,[53] and one hypothesis underlying Smad4 cKO rescue of Fmr1 KO inhibitory synapses (Chapter 2) is that improvements to bulk secretion in Smad4 cKO could improve Fmr1 KO synapses. Additionally, astrocyte hepaCAM, a protein sufficient to induce inhibitory synaptogenesis,[51] is upregulated from in FXS;Smad4 cKO (**Figure 4.9D,E,F**) and could drive increased inhibitory synapses in the context of FXS. BMP signaling's effect on vesicular machinery could also affect secretion of other compounds not detectable by ER-TurboID, such as peptides, lipids, and proteins without external lysine residues to enable proximity labeling.[27,54] Thus, given the Smad4 cKO improvement of the Fmr1 KO astrocyte protein secretion machinery deficit, other potential compounds not included in the ER-TurboID proteomics dataset could also mediate the Smad4 cKO improvement of Fmr1 KO phenotypes.

Overall, our proteomic dataset provides a thorough examination of astrocyte state changes due to Fmr1 KO and Smad4 cKO that complements the transcriptomic analysis in Chapter 3. While the astrocyte Fmr1 KO proteomic changes we observe differ from those seen in a FACS-sorted P40 dataset in FVB-background Fmr1 KO mouse cortical astrocytes from Men et al. (**Figure 4.8**), the lack of overlap may again be due to mouse background (B6 vs. FVB), timepoint (P27 vs. P40), or cellular compartment (ER vs. whole cell) differences. Our finding that Fmr1 KO astrocytes have a deficit in secretory machinery that is improved by Smad4 cKO represents a possible mechanistic pathway underlying Smad4 cKO rescue of FXS deficits we observed in Chapter 2. Additionally, applying this ER-passaged astrocyte proteomic approach to other genetic neurodevelopmental disorder models will allow investigation of whether there are convergent mechanisms of *in vivo* astrocyte secretome dysregulation across disorders, as we observed *in vitro*[1] and would be predicted by a convergent neuroscience approach to autism-spectrum disorder.[55]

Figure 4.1. Development of ER-TurboID for studying astrocyte secreted and membrane proteins.

A. Schematics of constructs used: GfaABC1D-HA-TurboID-NES (cytosolic control), GfaABC1D-C1(1-29)-TurboID (ERM facing cytosol), GfaABC1D-HA-TurboID-V5-KDEL (ER lumen), GfaABC1D-sec61b-V5-TurboID-HA (ERM facing lumen), and GfaABC1D-smFP (control protein).
B. Immunocytochemistry for HA tag on TurboID construct transfected into cultured astrocytes shows diffuse staining for the cytosolic construct compared to net-like staining for the three ER-based constructs.
C. Streptavidin 680 signal on western blot of lysates of cultured astrocytes transfected with the five constructs from Figure 4.1A. TurboID functionally incorporates biotin nonspecifically when biotin is added to culture media. * = pyruvate carboxylase, known endogenous biotinylated protein; ** = proprionyl-CoA carboxylase alpha chain, known endogenous biotinylated protein.
D. Spectral counts from label-free mass spectrometry pilot experiment on streptavidin-pulldown enriched labeled proteins in cultured astrocyte lysates. ER lumen construct shows highest spectral counts of known astrocyte-secreted proteins.

A

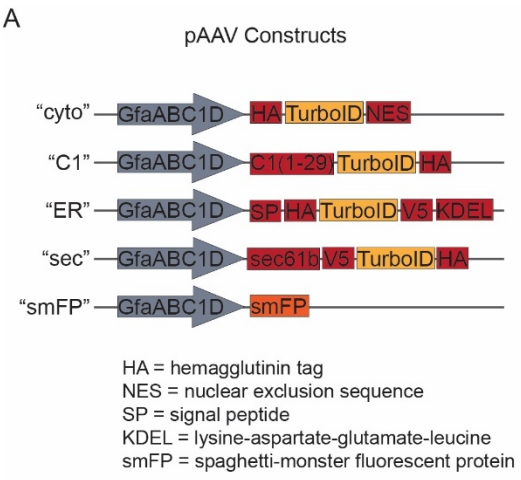

HA = hemagglutinin tag
NES = nuclear exclusion sequence
SP = signal peptide
KDEL = lysine-aspartate-glutamate-leucine
smFP = spaghetti-monster fluorescent protein

B

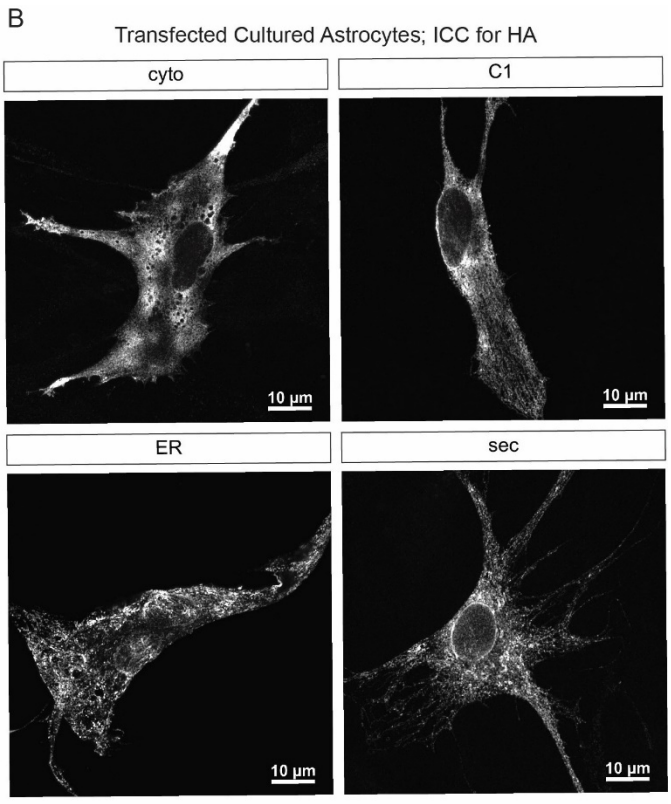

C

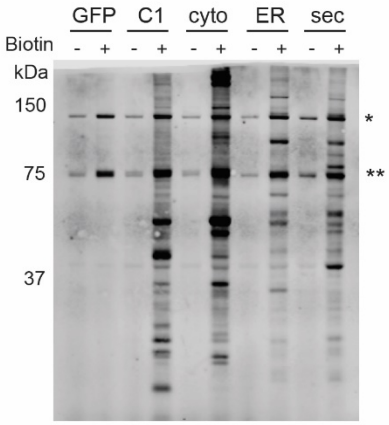

Streptavidin 680
Western blot

Lysates of transfected cultured astrocytes

C1 = C1(1-29)
cyto = cytosolic
ER = ER lumen
sec = sec61b

D

MS: lysates (cultured astrocytes, spec counts)	GFP	C1-Turbo	Cyto-Turbo	ER-Turbo (lumen)	sec61b-Turbo
Complement C3	0	0	0	13	4
Glypican-4	0	2	0	8	5
SPARC	0	1	0	1	0
Thrombospondin-1	4	3	4	9	4
Apolipoprotein E	9	9	6	22	11
Clusterin	12	11	17	19	15
Tenascin	0	1	0	6	9

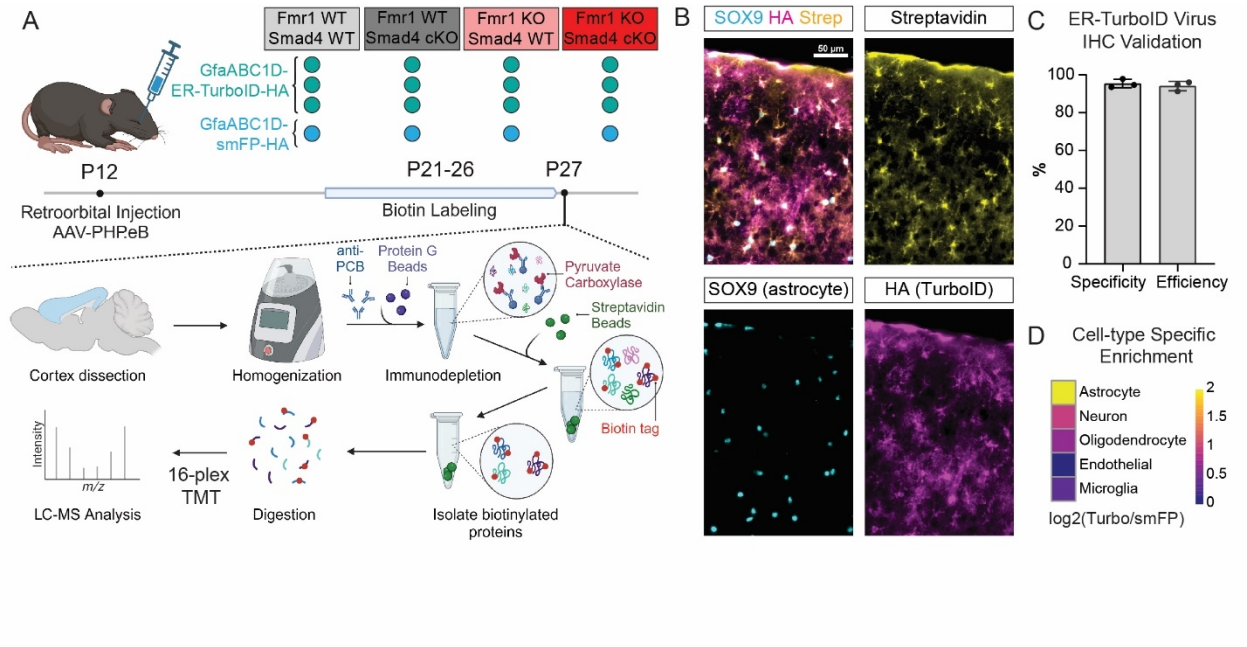

Figure 4.2. Protocol and validation of ER-targeted TurboID for *in vivo* astrocyte proximity labeling proteomics.

A. Protocol for ER-TurboID proteomics.
B. ER-TurboID biotinylates proteins in SOX9+ astrocytes. Immunohistochemistry imaged in visual cortex, for a mouse subjected to the protocol in 4.2A with fixation instead of dissection for proteomics. HA tag on ER-TurboID construct colocalizes with streptavidin (biotinylation) in cells with SOX9+ nuclei.
C. Quantification of 4.2B. Specificity quantified as (# SOX9+HA+ cells)/(# HA+ cells), efficiency quantified as (# SOX9+HA+ cells)/(# SOX9+ cells) for N = 3 mice.
D. ER-TurboID enriches for known astrocyte proteins. Plotting log2 of average Turbo to average control TMT signal, averaged across known cell type-specific proteins (see Figure 4.3E for all proteins).

Figure 4.3. Additional validation of ER-TurboID for studying astrocyte proteins *in vivo*.

A. ER-TurboID (HA tagged) is highly expressed in astrocytes by P20 after P12 retroorbital injection packaged in AAV-PHP.eB. Immunohistochemistry on visual cortex for astrocyte nuclear marker SOX9 and HA.
B. smFP is expressed specifically in astrocytes by P26 after P12 retroorbital injection packaged in AAV-PHP.eB. Immunohistochemistry on visual cortex for astrocyte nuclear marker SOX9 and HA.
C. Quantification of 4.3B. Specificity quantified as (# SOX9+HA+ cells)/(# HA+ cells), efficiency quantified as (# SOX9+HA+ cells)/(# SOX9+ cells) for N = 3 mice.
D. ER-TurboID biotinylates cortical proteins. Streptavidin 680 signal on cortical lysates collected at P27 from mice injected at P12 with ER-TurboID or control protein (smFP) and receiving subcutaneous biotin from P21-26. * = pyruvate carboxylase, known endogenous biotinylated protein; ** = proprionyl-CoA carboxylase alpha chain, known endogenous biotinylated protein.
E. ER-TurboID TMT signal is enriched for astrocyte proteins over other cell type proteins. Heatmap represents enrichment as log2 of average TurboID TMT signal divided by average control TMT signal.

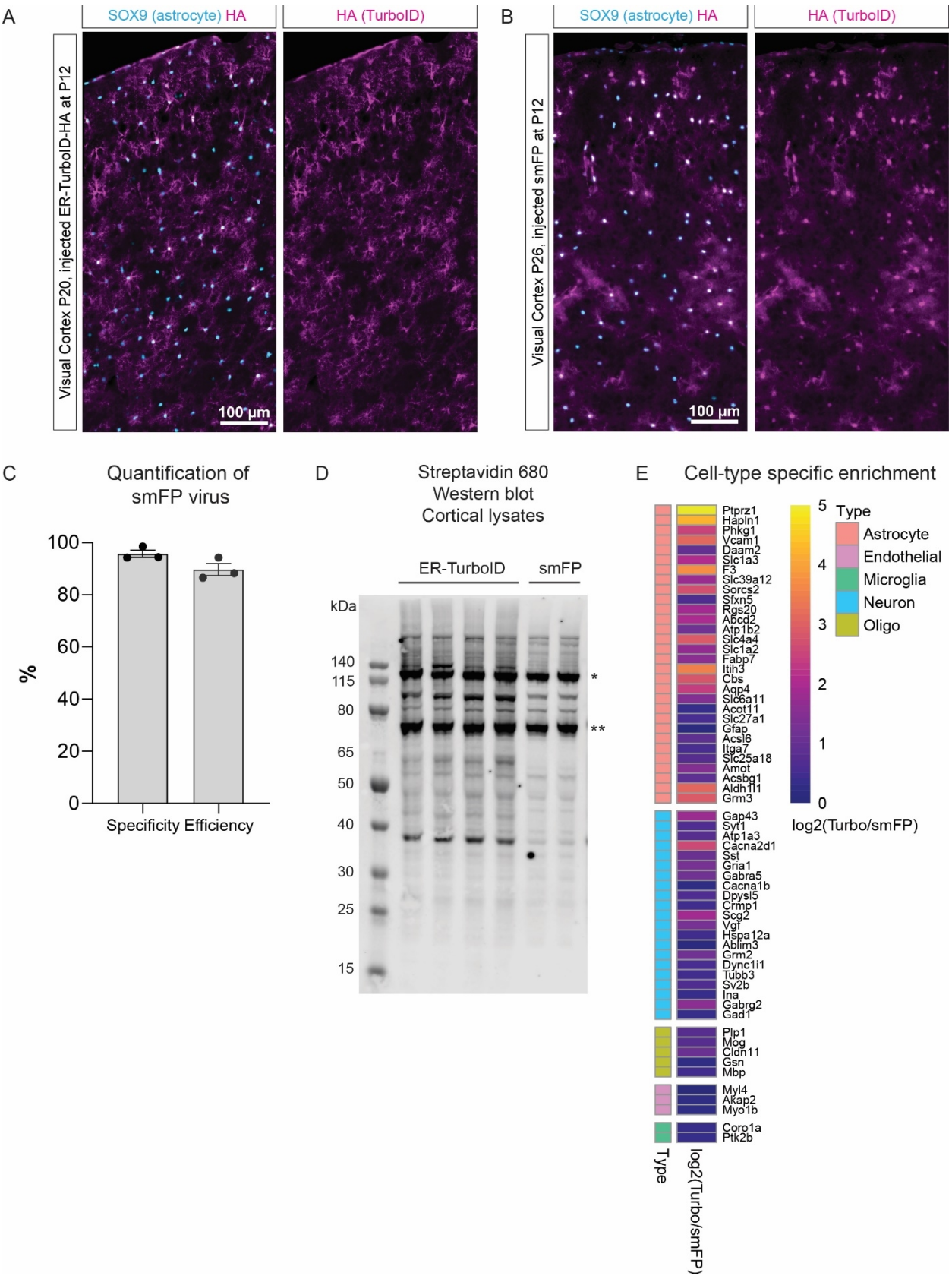
A
SOX9 (astrocyte) HA
HA (TurboID)
Visual Cortex P20, injected ER-TurboID-HA at P12
100 µm
B
SOX9 (astrocyte) HA
HA (TurboID)
Visual Cortex P26, injected smFP at P12
100 µm
C
Quantification of smFP virus
%
100
80
60
40
20
0
Specificity Efficiency
D
Streptavidin 680 Western blot Cortical lysates
ER-TurboID
smFP
kDa
140
115
80
65
50
40
30
25
15
*
**
E
Cell-type specific enrichment
Ptprz1
Hapln1
Phkg1
Vcam1
Daam2
Slc1a3
F3
Slc39a12
Sorcs2
Sfxn5
Rgs20
Abcd2
Atp1b2
Slc4a4
Slc1a2
Fabp7
Itih3
Cbs
Aqp4
Slc6a11
Acot11
Slc27a1
Gfap
Acsl6
Itga7
Slc25a18
Amot
Acsbg1
Aldh1l1
Grm3
Gap43
Syt1
Atp1a3
Cacna2d1
Sst
Gria1
Gabra5
Cacna1b
Dpysl5
Crmp1
Scg2
Vgf
Hspa12a
Ablim3
Grm2
Dync1i1
Tubb3
Sv2b
Ina
Gabrg2
Gad1
Plp1
Mog
Cldn11
Gsn
Mbp
Myl4
Akap2
Myo1b
Coro1a
Ptk2b
Type
log2(Turbo/smFP)
5
4
3
2
1
0
Type
Astrocyte
Endothelial
Microglia
Neuron
Oligo
log2(Turbo/smFP)

A

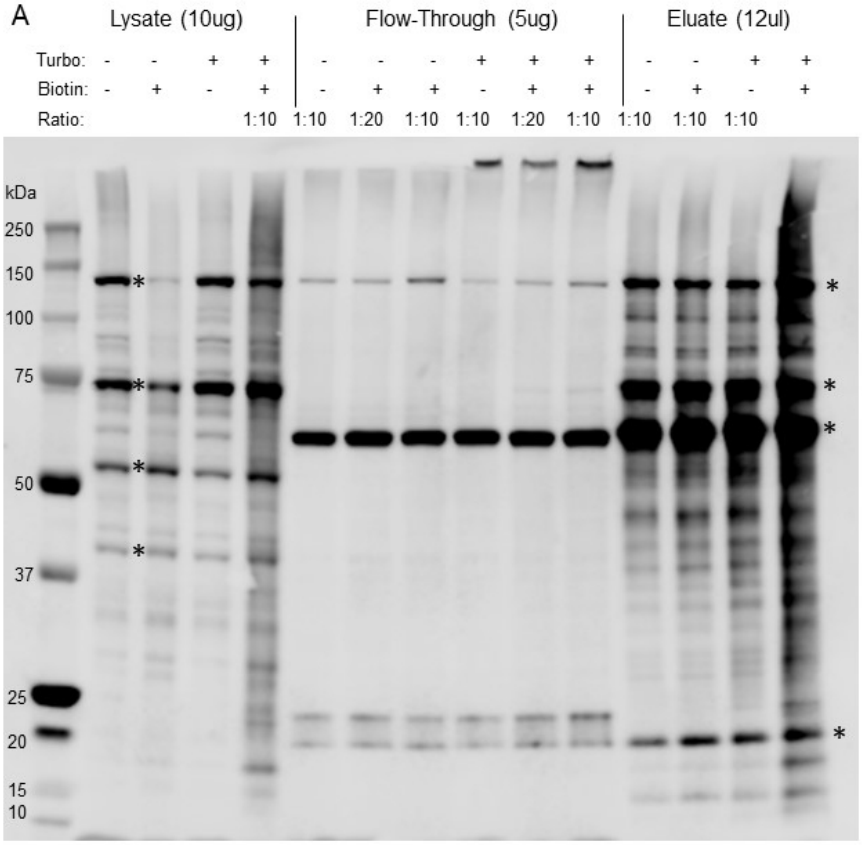

B Summary of Optimization Experiments

Optimization	Result
Both Turbo + exogenous biotin required?	Yes; expression of Turbo and exogenous biotin are both required for labeling
Magnetic streptavidin beads vs. neutravidin agarose	Both enrich well; streptavidin magnetic beads easier to handle
Ratio of streptavidin beads to biotinylated cortical tissue	1ul bead to 20ug tissue optimizes biotinylated protein signal-to-noise
Lysis buffer	NP40 buffer exceeds Triton- and Sucrose-based buffers in isolation of ApoE. NP40 buffer exceeds RIPA lysis buffer in isolation of monomeric Glt1.
Endogenous protein immunodepletion	PCB optimally depleted at ratio of 5mg cortical protein to 10ul antibody. PCCA and ACC no significant depletion at any ratio. 50ul protein G beads optimal on-target depletion while minimizing off-target depletion.

Figure 4.4. Optimization of TurboID protocol for *in vivo* labeling of secreted proteins.

A. Streptavidin western blot on *in vivo* cortex lysate samples, showing that both Turbo enzyme and exogenous biotin are required for extensive labeling. Eluate = bound to streptavidin beads, flow-through = unbound fraction. Ratio = streptavidin bead ul to lysate ug.
B. Summary of optimization experiments.

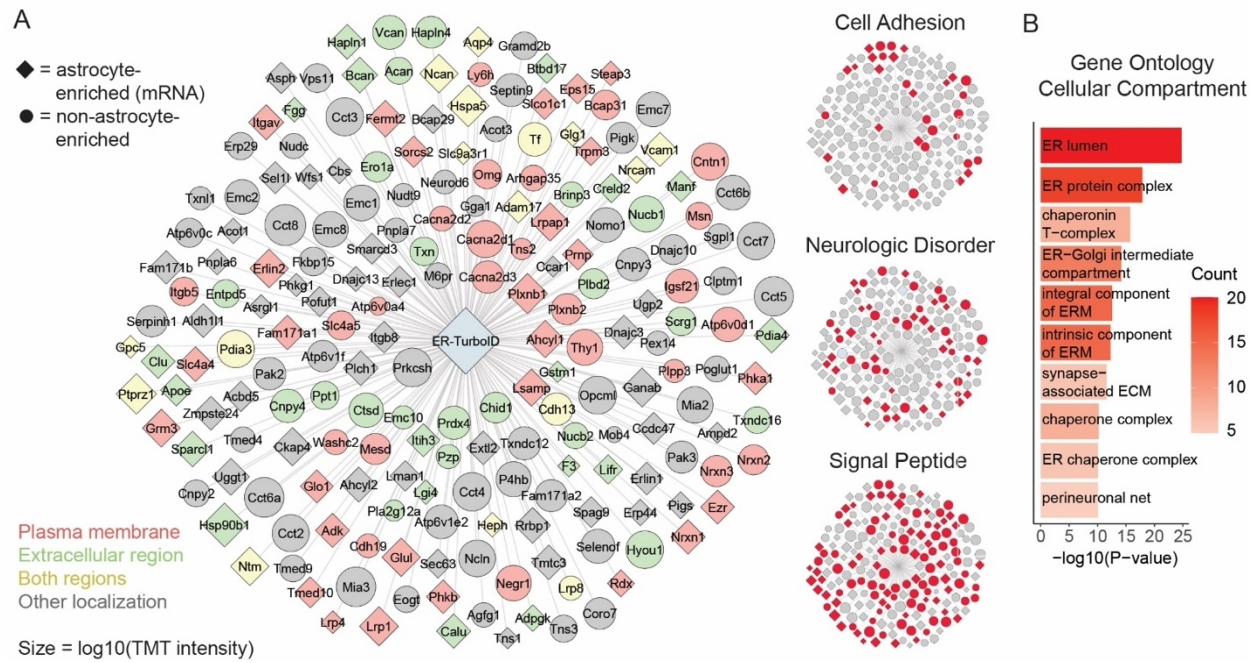

Figure 4.5. ER-TurboID labels astrocyte secreted and membrane proteins.

A. Most highly enriched proteins in the ER-TurboID proteome (log2[Turbo/Control] > 2.38, 200 proteins). Node tile size represents log10 of average TMT signal for the protein. Tile shape represents cell type: diamond = astrocyte (mRNA level higher in astrocytes compared to the average expression in other cell types [Zhang et al., 2014][48]), circle = other cell type or unknown. Tile color represents cellular compartment gene ontology annotation: green = extracellular region, red = plasma membrane, yellow = both extracellular region and plasma membrane, grey = other. Right, highlighting proteins in the functional category of cell adhesion (GO: 7155), with causative mutation linked to neurologic disorder, and with predicted signal peptide.
B. Gene ontology overrepresentation analysis based on the 200 most-enriched proteins in 4.5A, listing top 10 cellular compartment categories by p-value.

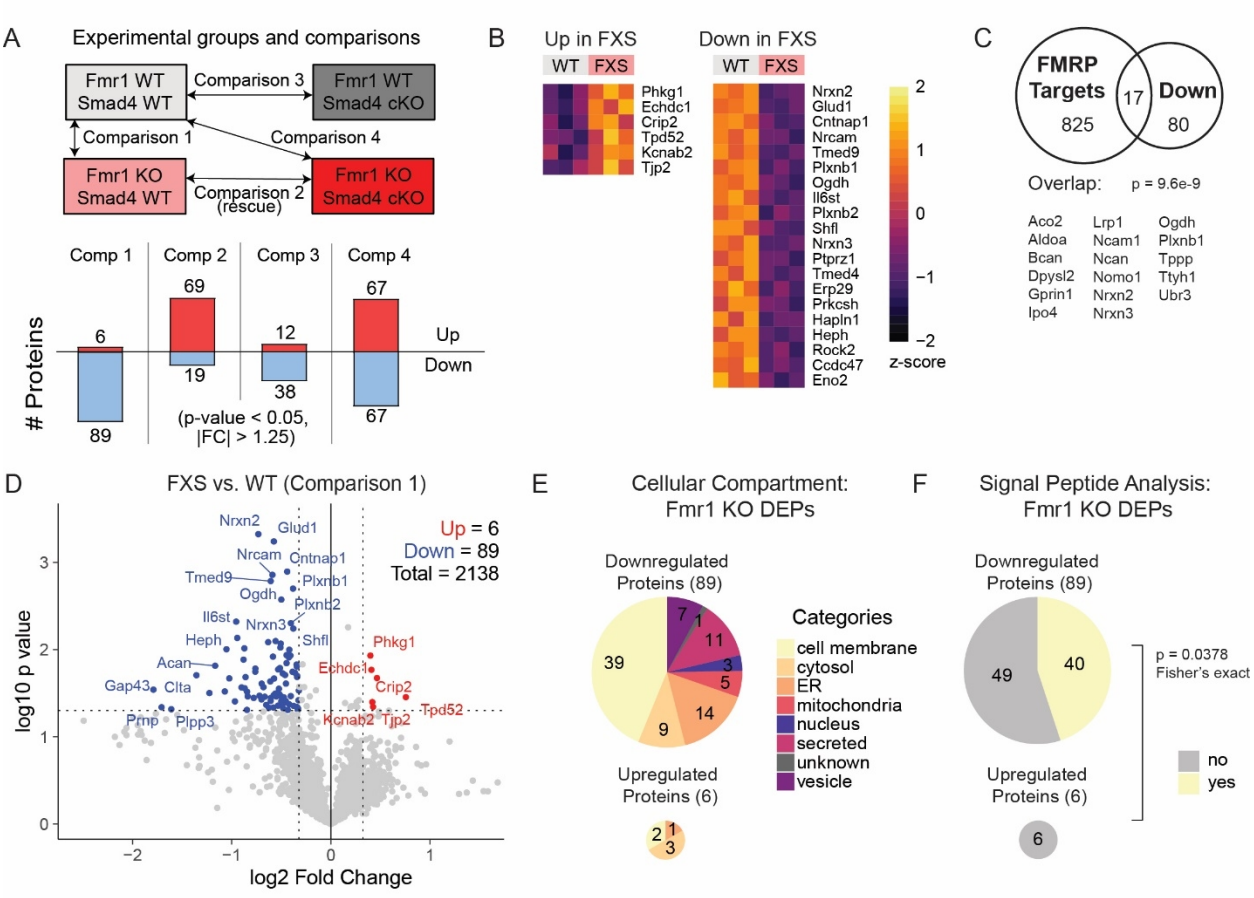

Figure 4.6. ER-TurboID identifies dysregulated Fmr1 KO astrocyte secreted and membrane proteins.

A. Groups and comparisons for the proteomic experiment. N = 3 WT, 3 WT;Smad4 cKO, 3 FXS, 3 FXS;Smad4 cKO. Proteomics processed with 16-plex TMT, including one mouse per genotype injected with virus with plasmid expressing control protein. Number of up- and downregulated proteins for each of the 4 comparisons, cutoff $p < 0.05$, $|FC| > 1.25$.
B. Top up- and downregulated proteins in Fmr1 KO (Comparison 1). Proteins sorted by p-value.
C. Overlap of known FMRP targets (Darnell et al. 2011)[46] with up- and down-regulated proteins in Fmr1 KO (Comparison 1). Statistics by Fisher's exact test with genome size 24,252 protein-coding *M. Musculus* genes.
D. Volcano plots for the Fmr1 KO vs WT comparison showing significantly up- and downregulated proteins. Dashed black line at p = 0.05.
E. Cellular compartment and F. signal peptide analysis of DEPs from Fig 4.6D, based on UniProt annotations.

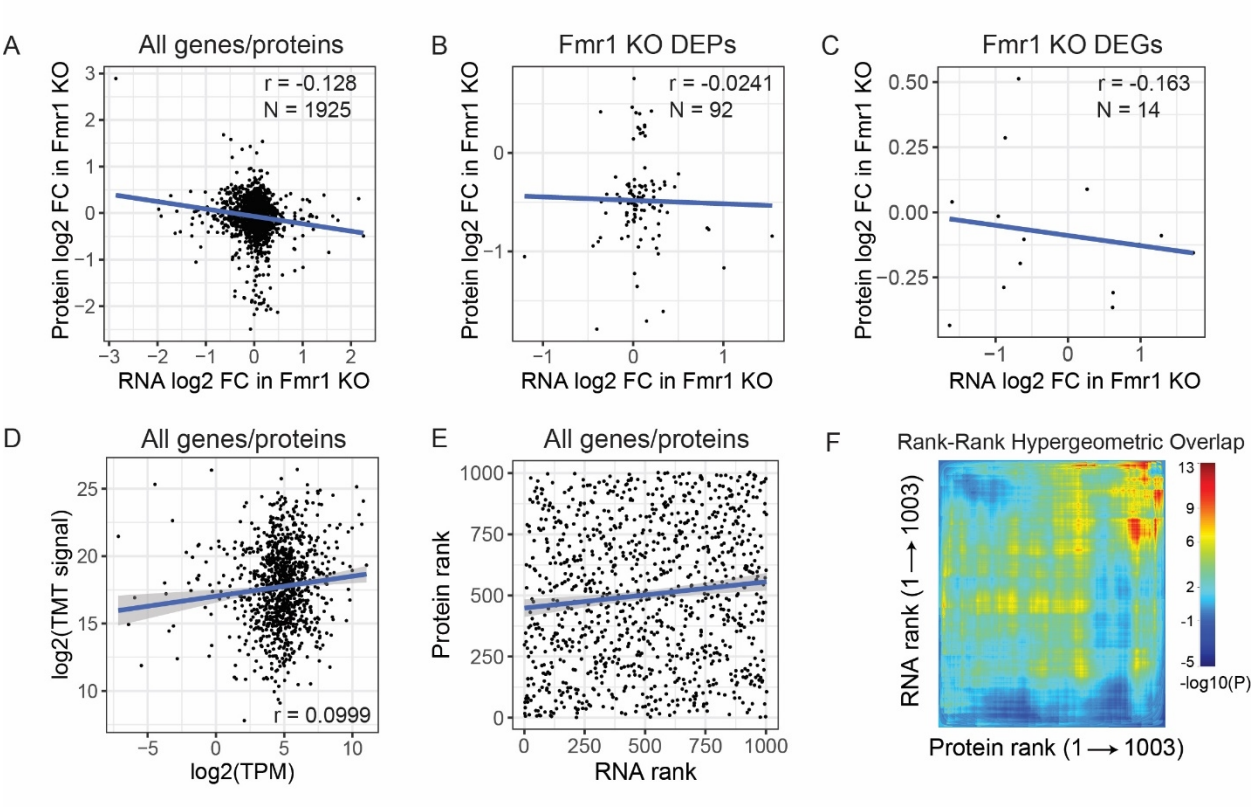

Figure 4.7. Minimal to slight correlations between *in vivo* transcriptomics and ER-TurboID proteomics.

A. Plotting log2FC in the Fmr1 KO comparison, in protein (ER-TurboID) vs. RNA, for all 1925 genes assayed by both methods.
B. Plotting log2FC in protein (ER-TurboID) vs. RNA, for all 92 proteomics Fmr1 KO DEPs ($p < 0.05$, $|FC| > 1.25$) assayed by both methods.
C. Plotting log2FC in protein (ER-TurboID) vs. RNA, for all 14 RNAseq Fmr1 KO DEGs (adj-$p < 0.05$, $FC > 1.5$, $TPM > 1$ in WT) assayed by both methods.
D. Plotting absolute proteomics TMT signal vs. log2 of TPM from RNAseq, for all 1003 genes assayed by both methods, filtering proteins for only those with average Turbo/Control TMT ratio of over 1.5.
E. Plotting protein prevalence rank by absolute TMT signal vs. RNA rank by TPM, for all 1003 genes assayed by both methods, filtering proteins for only those with average Turbo/Control TMT ratio of over 1.5. Pearson's r = 0.108.
F. Rank-rank hypergeometric overlap map using data from Figure 4.7E.

Figure 4.8. Comparison of ER-TurboID proteomics with other datasets

A. Overlap of Fmr1 KO up- and downregulated proteins from ER-TurboID proteomics with up- and downregulated proteins from conditioned media of cultured Fmr1 KO astrocytes (Caldwell et al., 2022).[1]
B. Overlap of Smad4 cKO up- and downregulated proteins from ER-TurboID proteomics with up- and downregulated proteins from conditioned media of cultured WT astrocytes incubated with BMP6 (Caldwell et al., 2022).[1]
C. Overlap of Fmr1 KO up- and downregulated proteins from ER-TurboID proteomics with up- and downregulated proteins from FACS-sorted P40 Fmr1 KO astrocytes in FVB line (Men et al., 2020).[21]
D. Correlations of Fmr1 KO L2FCs for all 451 proteins detected in both between ER-TurboID proteomics and cultured Fmr1 KO astrocytes (Caldwell et al., 2022).[1]
E. Correlations as in 4.8D, limited to the set of 31 ER-TurboID proteomics Fmr1 KO DEPs detected in Caldwell et al., 2022.[1]
F. Correlations for all 451 proteins detected in both datasets, between L2FC in Smad4 cKO in ER-TurboID proteomics vs. WT astrocytes incubated with BMP6 (Caldwell et al., 2022).[1]
G. Correlations as in 4.8F, limited to the set of 19 ER-TurboID proteomics Smad4 *c*KO DEPs detected in Caldwell et al., 2022.[1]

A

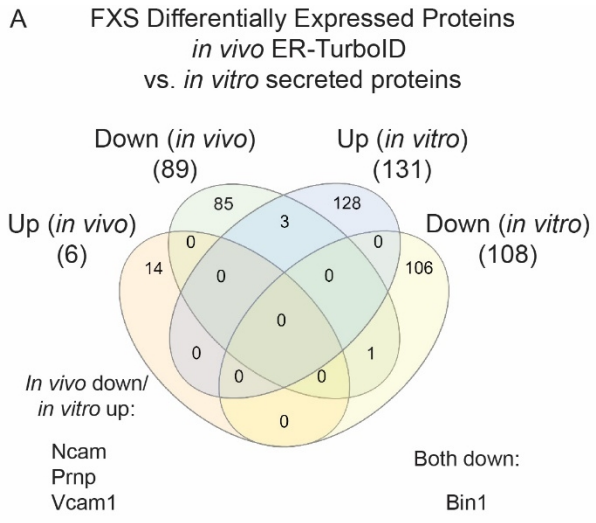
FXS Differentially Expressed Proteins
in vivo ER-TurboID
vs. in vitro secreted proteins
Down (in vivo)
(89)
Up (in vitro)
(131)
Up (in vivo)
(6)
Down (in vitro)
(108)
85
128
3
0
0
14
0
0
106
0
0
0
0
1
0
0
0
In vivo down/
in vitro up:
Ncam
Prnp
Vcam1
Both down:
Bin1

B

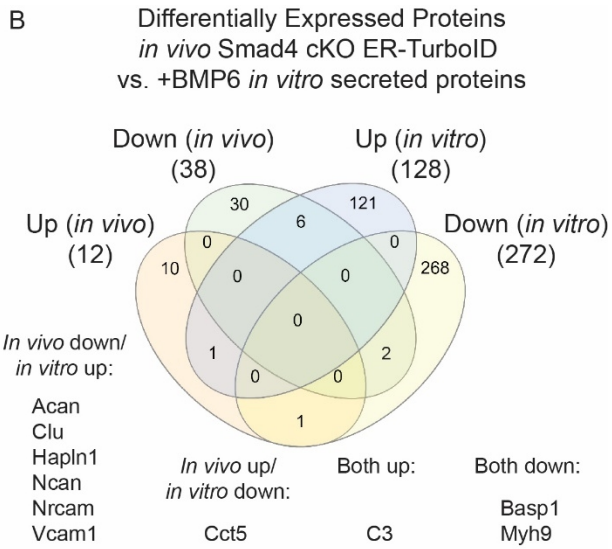
Differentially Expressed Proteins
in vivo Smad4 cKO ER-TurboID
vs. +BMP6 in vitro secreted proteins
Down (in vivo)
(38)
Up (in vitro)
(128)
Up (in vivo)
(12)
Down (in vitro)
(272)
30
121
6
0
0
10
0
0
268
0
0
1
2
0
0
1
In vivo down/
in vitro up:
Acan
Clu
Hapln1
Ncan
Nrcam
Vcam1
In vivo up/
in vitro down:
Cct5
Both up:
C3
Both down:
Basp1
Myh9

C

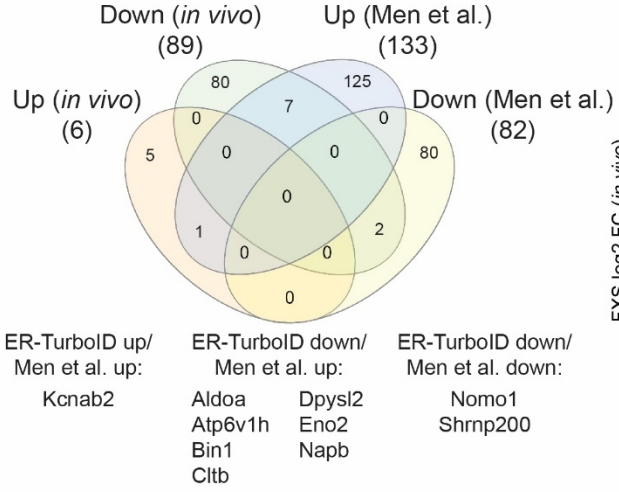
FXS Differentially Expressed Proteins
in vivo ER-TurboID vs. Men et al.
Down (in vivo)
(89)
Up (Men et al.)
(133)
Up (in vivo)
(6)
Down (Men et al.)
(82)
80
125
7
0
0
5
0
0
80
0
1
2
0
0
0
ER-TurboID up/
Men et al. up:
Kcnab2
ER-TurboID down/
Men et al. up:
Aldoa
Atp6v1h
Bin1
Cltb
Dpysl2
Eno2
Napb
ER-TurboID down/
Men et al. down:
Nomo1
Shrnp200

D

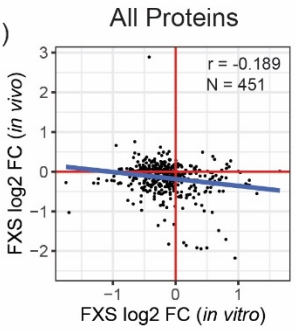
All Proteins
r = -0.189
N = 451
FXS log2 FC (in vivo)
FXS log2 FC (in vitro)

F

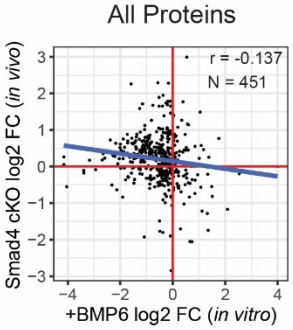
All Proteins
r = -0.137
N = 451
Smad4 cKO log2 FC (in vivo)
+BMP6 log2 FC (in vitro)

E

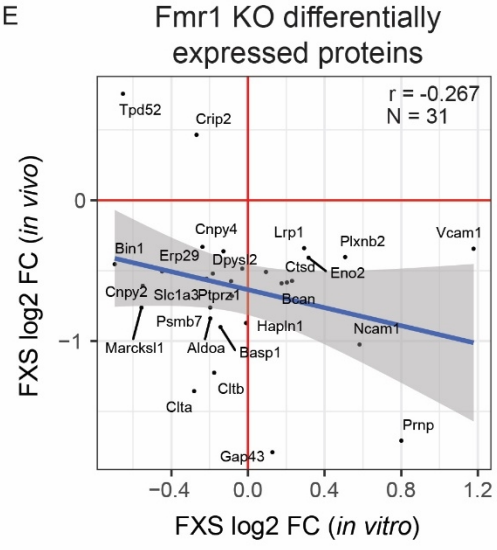
Fmr1 KO differentially
expressed proteins
r = -0.267
N = 31
Tpd52
Crip2
Cnpy4
Lrp1
Plxnb2
Vcam1
Bin1
Erp29
Dpysl2
Ctsd
Eno2
Cnpy2
Slc1a3
Ptprz1
Bcan
Psmb7
Hapln1
Ncam1
Marcksl1
Aldoa
Basp1
Cltb
Clta
Prnp
Gap43
FXS log2 FC (in vivo)
FXS log2 FC (in vitro)

G

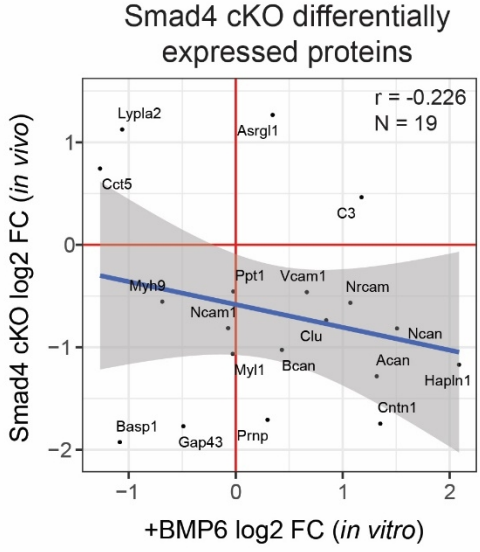
Smad4 cKO differentially
expressed proteins
r = -0.226
N = 19
Lypla2
Asrgl1
Cct5
C3
Myh9
Ppt1
Vcam1
Nrcam
Ncam1
Clu
Ncan
Myl1
Bcan
Acan
Hapln1
Cntn1
Basp1
Gap43
Prnp
Smad4 cKO log2 FC (in vivo)
+BMP6 log2 FC (in vitro)

Figure 4.9. Western blot validation of ER-TurboID-identified differentially expressed astrocyte-secreted proteins, brevican and hepaCAM

A. Western blotting on cortical lysates for brevican and actin.
B. Quantification of two brevican bands from Figure 4.9A. Statistics by two-way ANOVA with Tukey's test for multiple comparisons. Band 1 likely corresponds to the full-length brevican, while band 2 likely corresponds to a truncated cleavage product (see Hamel et al., 2005).[56] N = 6 mice per genotype.
C. Raw TMT signal from proteomics for Brevican. Statistics by two-way ANOVA with Tukey's test for multiple comparisons. N = 3 mice per genotype.
D. Western blotting on cortical lysates for hepaCAM (680 channel) and actin (800 channel).
E. Quantification of two hepaCAM bands from Figure 4.9D. Statistics by two-way ANOVA with Tukey's test for multiple comparisons. Band 1 likely corresponds to the full-length hepaCAM, while band 2 may correspond to a nonspecific band or a cleaved hepaCAM product (see Jin et al., 2023).[57] N = 5 mice per genotype.
F. Raw TMT signal from proteomics for hepaCAM. Statistics by two-way ANOVA with Tukey's test for multiple comparisons. N = 3 mice per genotype.

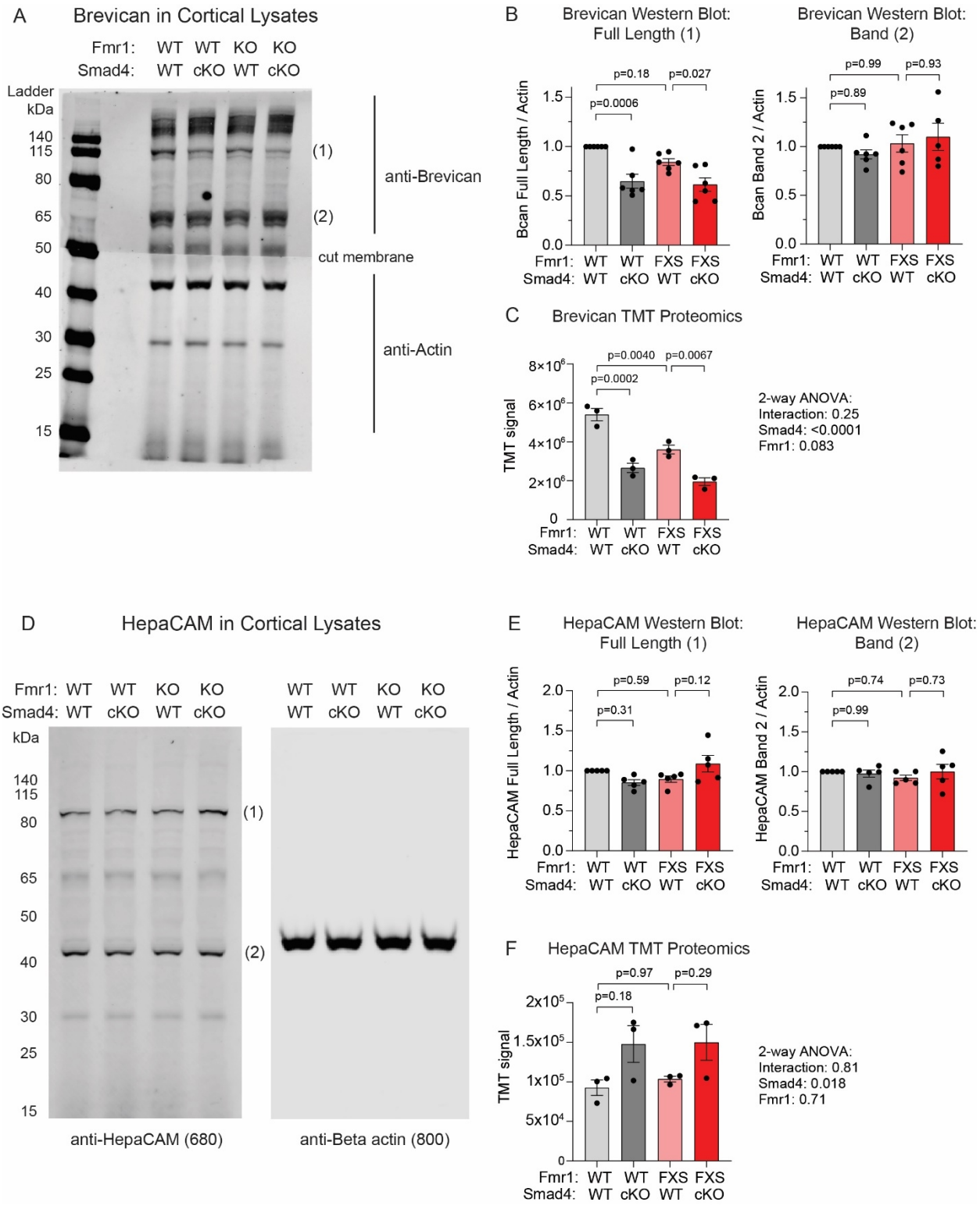
A
Brevican in Cortical Lysates
Fmr1: WT WT KO KO
Smad4: WT cKO WT cKO
Ladder kDa
140
115
80
65
50
40
30
25
15
(1)
(2)
anti-Brevican
cut membrane
anti-Actin
B
Brevican Western Blot: Full Length (1)
Bcan Full Length / Actin
p=0.18
p=0.027
p=0.0006
Brevican Western Blot: Band (2)
Bcan Band 2 / Actin
p=0.99
p=0.93
p=0.89
Fmr1: WT WT FXS FXS
Smad4: WT cKO WT cKO
C
Brevican TMT Proteomics
TMT signal
p=0.0040
p=0.0067
p=0.0002
2-way ANOVA:
Interaction: 0.25
Smad4: <0.0001
Fmr1: 0.083
D
HepaCAM in Cortical Lysates
Fmr1: WT WT KO KO
Smad4: WT cKO WT cKO
kDa
140
115
80
65
50
40
30
25
15
(1)
(2)
anti-HepaCAM (680)
anti-Beta actin (800)
E
HepaCAM Western Blot: Full Length (1)
HepaCAM Full Length / Actin
p=0.59
p=0.12
p=0.31
HepaCAM Western Blot: Band (2)
HepaCAM Band 2 / Actin
p=0.74
p=0.73
p=0.99
F
HepaCAM TMT Proteomics
TMT signal
p=0.97
p=0.29
p=0.18
2-way ANOVA:
Interaction: 0.81
Smad4: 0.018
Fmr1: 0.71

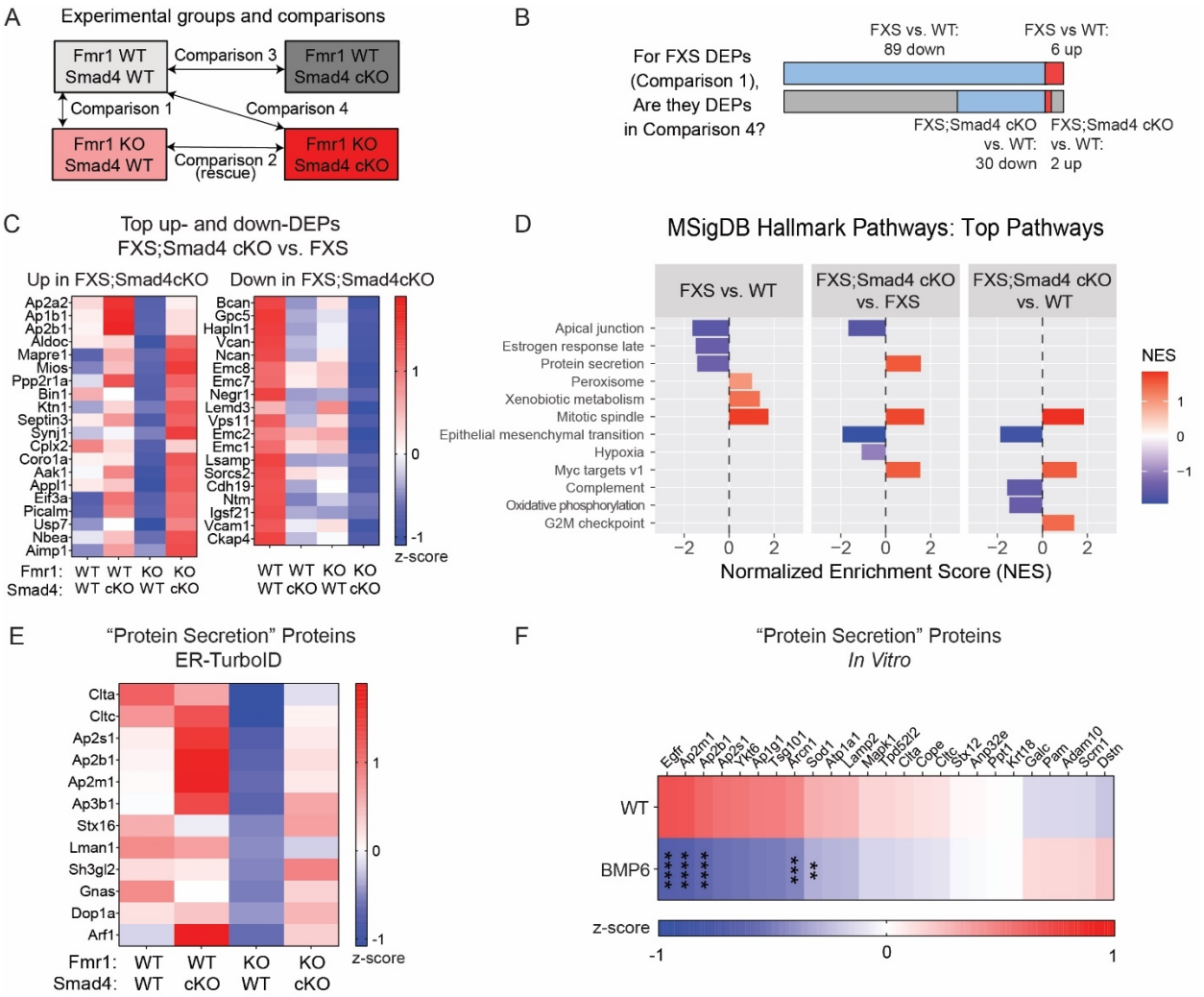

Figure 4.10. Smad4 cKO restores Fmr1 KO astrocyte deficit in secretory machinery.

A. Groups and comparisons for the proteomic experiment.
B. For the 111 FXS DEPs (Comparison 1), the majority are no longer significantly changed in Comparison 4 (FXS;Smad4 cKO vs. WT). (See Table S6 for list).
C. Average z-scores by genotype of the top up- and downregulated proteins in FXS;Smad4cKO compared to FXS (Comparison 2). Proteins sorted by p-value.
D. Top 3 up- and down-regulated pathways by normalized enrichment score (NES), for each of the comparisons 1, 2, and 4; via gene set enrichment analysis on the MSigDB Hallmark Gene Sets with all proteins Turbo/Control > 1.75 ranked by – log10(p-value) * sign(L2FC).
E. Z-scores of proteins in "protein secretion" gene set (MSigDB MM3876), averaged within each genotype; displaying proteins down in Fmr1 KO and increased by Smad4 cKO. See Figure 4.11 for full set.
F. Protein secretion machinery is downregulated in secretome of P7 WT astrocytes cultured with or without BMP6, data re-analyzed from Caldwell et al., 2022.[1] Z-scores of all detected proteins in "protein secretion" gene set (MSigDB), averaged within each genotype. Statistics as in Caldwell et al., 2022. ** denotes p < 0.01, *** denotes p < 0.001, **** denotes p < 0.0001.

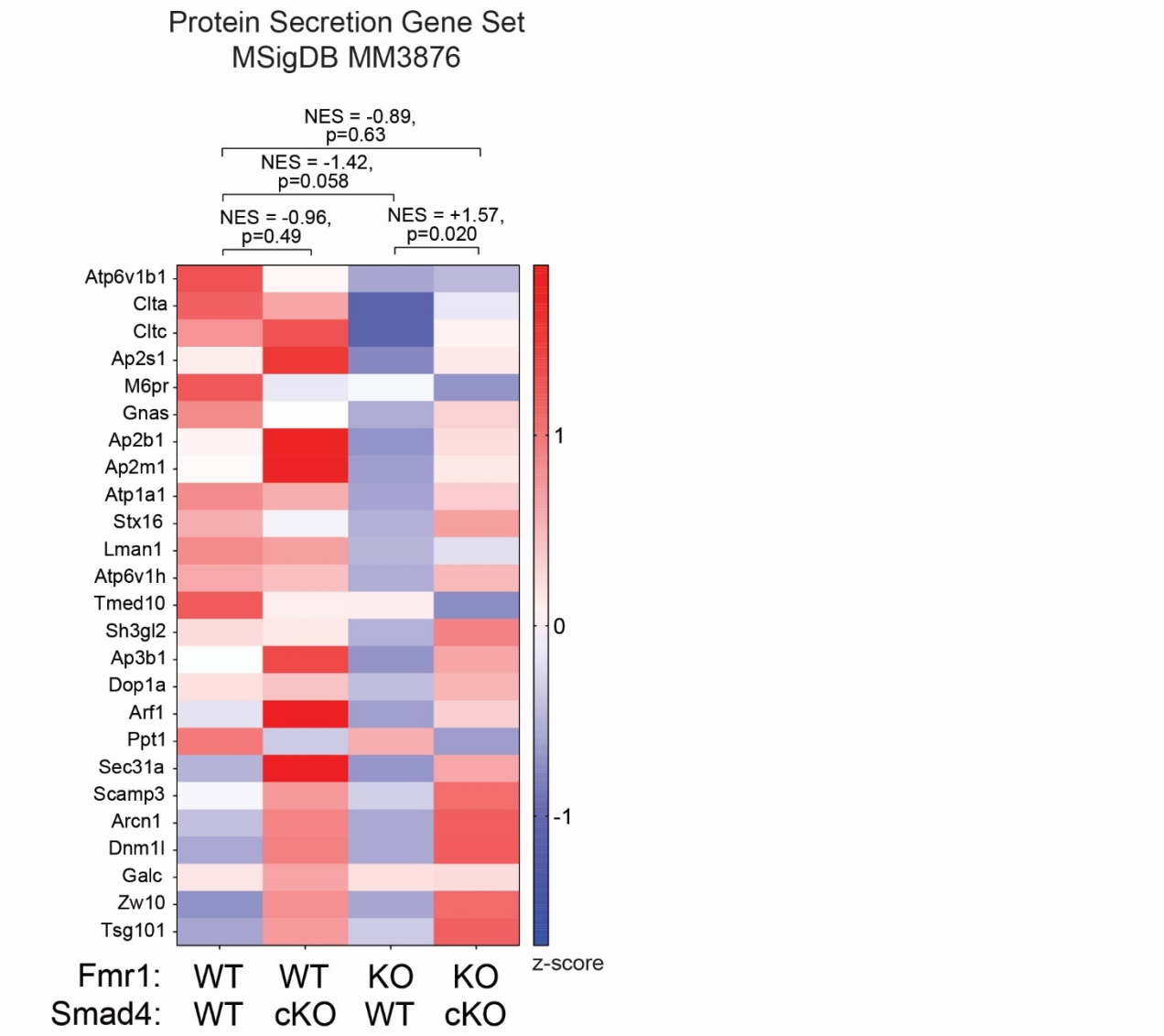

Figure 4.11. Full protein list for secretory machinery gene set.

Z-scores of all detected proteins in “protein secretion” gene set (MSigDB), averaged within each genotype.

References

1. Caldwell, A. L. M. *et al.* Aberrant astrocyte protein secretion contributes to altered neuronal development in multiple models of neurodevelopmental disorders. *Nat Neurosci* **25**, 1163–1178 (2022).

2. Blanco-Suarez, E., Liu, T.-F., Kopelevich, A. & Allen, N. J. Astrocyte-Secreted Chordin-like 1 Drives Synapse Maturation and Limits Plasticity by Increasing Synaptic GluA2 AMPA Receptors. *Neuron* **100**, 1116-1132.e13 (2018).

3. Brandebura, A. N., Asbell, Q. N., Micael, M. K. B. & Allen, N. J. *Dysregulation of Astrocyte-Secreted Pleiotrophin Contributes to Neuronal Structural and Functional Deficits in Down Syndrome*. http://biorxiv.org/lookup/doi/10.1101/2023.09.26.559633 (2023) doi:10.1101/2023.09.26.559633.

4. Kucukdereli, H. *et al.* Control of excitatory CNS synaptogenesis by astrocyte-secreted proteins Hevin and SPARC. *Proc. Natl. Acad. Sci. U.S.A.* **108**, (2011).

5. Hillen, A. E. J., Burbach, J. P. H. & Hol, E. M. Cell adhesion and matricellular support by astrocytes of the tripartite synapse. *Progress in Neurobiology* **165–167**, 66–86 (2018).

6. Abbasi, D. A., Berry-Kravis, E., Zhao, X. & Cologna, S. M. Proteomics insights into fragile X syndrome: Unraveling molecular mechanisms and therapeutic avenues. *Neurobiology of Disease* **194**, 106486 (2024).

7. Richter, J. D. & Zhao, X. The molecular biology of FMRP: new insights into fragile X syndrome. *Nat Rev Neurosci* (2021) doi:10.1038/s41583-021-00432-0.

8. McCamphill, P. K. *et al.* Selective inhibition of glycogen synthase kinase 3α corrects pathophysiology in a mouse model of fragile X syndrome. *Science Translational Medicine* **12**, (2020).

9. Qin, M. *et al.* Altered Cerebral Protein Synthesis in Fragile X Syndrome: Studies in Human Subjects and Knockout Mice. *J Cereb Blood Flow Metab* **33**, 499–507 (2013).

10. Jacquemont, S. *et al.* Protein synthesis levels are increased in a subset of individuals with fragile X syndrome. *Human Molecular Genetics* **27**, 2039–2051 (2018).

11. Bowling, H. *et al.* Altered steady state and activity-dependent de novo protein expression in fragile X syndrome. *Nat Commun* **10**, 1710 (2019).

12. Xu, B. *et al.* Proteomic Profiling of Brain and Testis Reveals the Diverse Changes in Ribosomal Proteins in fmr1 Knockout Mice. *Neuroscience* **371**, 469–483 (2018).

13. Das Sharma, S. *et al.* Widespread Alterations in Translation Elongation in the Brain of Juvenile Fmr1 Knockout Mice. *Cell Reports* **26**, 3313-3322.e5 (2019).

14. Ren, B. *et al.* Dysregulated cholesterol metabolism, aberrant excitability and altered cell cycle of astrocytes in fragile X syndrome. *Glia* **71**, 1176–1196 (2023).

15. Louros, S. R. *et al.* Excessive proteostasis contributes to pathology in fragile X syndrome. *Neuron* **111**, 508-525.e7 (2023).

16. Gao, M.-M., Shi, H., Yan, H.-J. & Long, Y.-S. Proteome profiling of the prefrontal cortex of Fmr1 knockout mouse reveals enhancement of complement and coagulation cascades. *Journal of Proteomics* **274**, 104822 (2023).

17. Liao, L., Park, S. K., Xu, T., Vanderklish, P. & Yates, J. R. Quantitative proteomic analysis of primary neurons reveals diverse changes in synaptic protein content in *fmr1* knockout mice. *Proc. Natl. Acad. Sci. U.S.A.* **105**, 15281–15286 (2008).

18. Klemmer, P. *et al.* Proteomics, Ultrastructure, and Physiology of Hippocampal Synapses in a Fragile X Syndrome Mouse Model Reveal Presynaptic Phenotype. *Journal of Biological Chemistry* **286**, 25495–25504 (2011).

19. Broek, J. A. C. *et al.* Synaptic vesicle dynamic changes in a model of fragile X. *Molecular Autism* **7**, 17 (2016).

20. Tang, B. *et al. Fmr1* deficiency promotes age-dependent alterations in the cortical synaptic proteome. *Proc. Natl. Acad. Sci. U.S.A.* **112**, (2015).

21. Men, Y. *et al.* Astroglial FMRP deficiency cell-autonomously up-regulates miR-128 and disrupts developmental astroglial mGluR5 signaling. *Proceedings of the National Academy of Sciences* **117**, 25092–25103 (2020).

22. Dieterich, D. C., Link, A. J., Graumann, J., Tirrell, D. A. & Schuman, E. M. Selective identification of newly synthesized proteins in mammalian cells using bioorthogonal noncanonical amino acid tagging (BONCAT). *Proceedings of the National Academy of Sciences* **103**, 9482–9487 (2006).

23. Mahdavi, A. *et al.* Engineered Aminoacyl-tRNA Synthetase for Cell-Selective Analysis of Mammalian Protein Synthesis. *J. Am. Chem. Soc.* **138**, 4278–4281 (2016).

24. Bosch, J. A., Chen, C. & Perrimon, N. Proximity-dependent labeling methods for proteomic profiling in living cells: An update. *WIREs Developmental Biology* **10**, e392 (2021).

25. Rhee, H.-W. *et al.* Proteomic Mapping of Mitochondria in Living Cells via Spatially Restricted Enzymatic Tagging. *Science* **339**, 1328–1331 (2013).

26. Roux, K. J., Kim, D. I., Raida, M. & Burke, B. A promiscuous biotin ligase fusion protein identifies proximal and interacting proteins in mammalian cells. *Journal of Cell Biology* **196**, 801–810 (2012).

27. Branon, T. C. *et al.* Efficient proximity labeling in living cells and organisms with TurboID. *Nature Biotechnology* **36**, 880–887 (2018).

28. Trinkle-Mulcahy, L. Recent advances in proximity-based labeling methods for interactome mapping. *F1000Res* **8**, 135 (2019).

29. Cho, K. F. *et al.* Proximity labeling in mammalian cells with TurboID and split-TurboID. *Nature Protocols* (2020) doi:10.1038/s41596-020-0399-0.

30. Rayaprolu, S. *et al.* Cell type-specific biotin labeling in vivo resolves regional neuronal and astrocyte proteomic differences in mouse brain. *Nat Commun* **13**, 2927 (2022).

31. Takano, T. *et al.* Chemico-genetic discovery of astrocytic control of inhibition in vivo. *Nature* **588**, 296–302 (2020).

32. Prabhakar, P. *et al.* Monitoring regional astrocyte diversity by cell type-specific proteomic labeling in vivo. *Glia* **71**, 682–703 (2023).

33. Soto, J. S. *et al.* Astrocyte–neuron subproteomes and obsessive–compulsive disorder mechanisms. *Nature* (2023) doi:10.1038/s41586-023-05927-7.

34. Kim, K. *et al.* Dynamic tracking and identification of tissue-specific secretory proteins in the circulation of live mice. *Nat Commun* **12**, 5204 (2021).

35. Wei, W. *et al.* Cell type-selective secretome profiling in vivo. *Nature Chemical Biology* **17**, 326–334 (2021).

36. Chan, K. Y. *et al.* Engineered AAVs for efficient noninvasive gene delivery to the central and peripheral nervous systems. *Nature Neuroscience* **20**, 1172–1179 (2017).

37. Uezu, A. *et al.* Identification of an elaborate complex mediating postsynaptic inhibition. *Science* **353**, 1123–1129 (2016).

38. Boisvert, M. M., Erikson, G. A., Shokhirev, M. N. & Allen, N. J. The Aging Astrocyte Transcriptome from Multiple Regions of the Mouse Brain. *Cell Reports* **22**, 269–285 (2018).

39. Wen, T. H. *et al.* Genetic Reduction of Matrix Metalloproteinase-9 Promotes Formation of Perineuronal Nets Around Parvalbumin-Expressing Interneurons and Normalizes Auditory Cortex Responses in Developing Fmr1 Knock-Out Mice. *Cerebral Cortex* **28**, 3951–3964 (2018).

40. Reinhard, S. M. *et al.* Reduced perineuronal net expression in Fmr1 KO mice auditory cortex and amygdala is linked to impaired fear-associated memory. *Neurobiology of Learning and Memory* **164**, 107042 (2019).

41. Van'T Spijker, H. M. & Richter, J. D. FMRP regulation of *aggrecan* mRNA translation controls perineuronal net development. *Journal of Neurochemistry* jnc.16048 (2024) doi:10.1111/jnc.16048.

42. Gauthier, J. *et al.* Truncating mutations in NRXN2 and NRXN1 in autism spectrum disorders and schizophrenia. *Hum Genet* **130**, 563–573 (2011).

43. Vaags, A. K. *et al.* Rare Deletions at the Neurexin 3 Locus in Autism Spectrum Disorder. *The American Journal of Human Genetics* **90**, 133–141 (2012).

44. The DDD Study *et al.* Synaptic, transcriptional and chromatin genes disrupted in autism. *Nature* **515**, 209–215 (2014).

45. Marui, T. *et al.* Association of the neuronal cell adhesion molecule (NRCAM) gene variants with autism. *Int. J. Neuropsychopharm.* **12**, 1 (2009).

46. Darnell, J. C. *et al.* FMRP Stalls Ribosomal Translocation on mRNAs Linked to Synaptic Function and Autism. *Cell* **146**, 247–261 (2011).

47. Hale, C. R. *et al.* FMRP regulates mRNAs encoding distinct functions in the cell body and dendrites of CA1 pyramidal neurons. *eLife* **10**, e71892 (2021).

48. Zhang, Y. *et al.* An RNA-Sequencing Transcriptome and Splicing Database of Glia, Neurons, and Vascular Cells of the Cerebral Cortex. *Journal of Neuroscience* **34**, 11929–11947 (2014).

49. Divolis, G. *et al.* Activation of both transforming growth factor-β and bone morphogenetic protein signalling pathways upon traumatic brain injury restrains pro-inflammatory and boosts tissue reparatory responses of reactive astrocytes and microglia. *Brain Communications* **1**, fcz028 (2019).

50. Okur, Z. *et al. Control of Neuronal Excitation-Inhibition Balance by BMP-SMAD1 Signaling*. http://biorxiv.org/lookup/doi/10.1101/2023.03.11.532164 (2023) doi:10.1101/2023.03.11.532164.

51. Baldwin, K. T. *et al.* HepaCAM controls astrocyte self-organization and coupling. *Neuron* **109**, 2427-2442.e10 (2021).

52. Katagiri, T. & Watabe, T. Bone Morphogenetic Proteins. *Cold Spring Harbor Perspectives in Biology* **8**, a021899 (2016).

53. Chung, W.-S., Baldwin, K. T. & Allen, N. J. Astrocyte Regulation of Synapse Formation, Maturation, and Elimination. *Cold Spring Harb Perspect Biol* a041352 (2024) doi:10.1101/cshperspect.a041352.

54. Verkhratsky, A., Matteoli, M., Parpura, V., Mothet, J. & Zorec, R. Astrocytes as secretory cells of the central nervous system: idiosyncrasies of vesicular secretion. *The EMBO Journal* **35**, 239–257 (2016).

55. Willsey, H. R., Willsey, A. J., Wang, B. & State, M. W. Genomics, convergent neuroscience and progress in understanding autism spectrum disorder. *Nat Rev Neurosci* **23**, 323–341 (2022).

56. Hamel, M. G., Mayer, J. & Gottschall, P. E. Altered production and proteolytic processing of brevican by transforming growth factor β in cultured astrocytes. *Journal of Neurochemistry* **93**, 1533–1541 (2005).

57. Jin, S. *et al.* Astroglial exosome HepaCAM signaling and ApoE antagonization coordinates early postnatal cortical pyramidal neuronal axon growth and dendritic spine formation. *Nat Commun* **14**, 5150 (2023).

Chapters 1-7, in part, have been submitted for publication. Deng J**,** Labarta-Bajo L, Brandebura AN, Kahn SB, Pinto AFM, Diedrich JK, Allen NJ (2024). Suppression of astrocyte BMP signaling improves fragile X syndrome molecular signatures and functional deficits. The

dissertation author will be the first author of this publication, and Dr. Nicola Allen will be the senior author and principal investigator.

Chapter 5. BMP signaling in astrocyte cortical heterogeneity and maturation

Introduction

Rationale

An initial survey of the P26-28 astrocyte transcriptomic dataset (Chapter 3) showed that many of the 62 DEGs downregulated in Smad4 cKO compared to WT (**Figure 5.1A,B**) are known to be genes enriched in astrocytes in specific layers of the cortex. For instance, the top downregulated gene in Smad4 cKO was *Myoc* (**Figure 5.1B**), a gene found to mark pial astrocytes[1] and also strongly upregulated in cultured astrocytes treated with either BMP4 or BMP6 (**Figure 3.6G**).[2,3] Moreover, some DEGs (e.g. *Aqp4*, Smad4 cKO nRNAseq L2FC -0.82, adj. p = 0.038, **Table S2**) are known to correlate with astrocyte maturation.[4] Additionally, examining our proteomic data (Chapter 4), many of the 38 DEPs downregulated in Smad4 cKO compared to WT are known to be involved at the synapse (GPC5, NCAN, NRCAM, among others) (**Figures 5.1C,D**). Given these leads, we sought to use both the transcriptomic (Chapter 3) and proteomic (Chapter 4) datasets as well as further experiments to ask, what is the role of astrocyte BMP signaling in cortical astrocyte heterogeneity and maturation in typically developing postnatal cortex?

Astrocyte intracortical heterogeneity

As discussed in Chapter 1, recent years have seen transcriptomic experiments confirm what was known for decades about diverse astrocyte morphology between brain regions: astrocytes' transcriptional heterogeneity parallels their morphological diversity and suggests regional specializations.[5–7] Astrocytes are increasingly recognized as heterogeneous within brain regions: in the cortex, astrocytes across different cortical layers[8–10] and in different locations on the rostral/caudal medial/lateral axes[6,8,11] have been characterized to have different characteristic transcriptional signatures. While this astrocyte intracortical heterogeneity does not approach that

of neurons,[12] and thus may not reach the threshold for separation into different cell types, many specific genes have been shown to be expressed on a gradient across cortical layers and characteristically enrich in specific layers (e.g. *Chrdl1* in cortical layers 2 to 4).[8,9,13]

What drives this heterogeneity in cortical astrocytes? Astrocytes are established to adapt their transcriptional profile and functions to the needs of neighboring neurons,[6,10] and recent studies have found drivers of astrocyte heterogeneity include interactions with neighboring neurons and extrinsic cues including layer-enriched secreted morphogens such as Sonic Hedgehog (SHH).[9,14,15] However, a full understanding of all factors that shape astrocyte intraregional heterogeneity is still incomplete.

BMP signaling in astrocyte development and function

As highlighted in Chapter 1, apart from BMP signaling's critical roles in early neurodevelopmental processes (e.g. gastrulation, dorsoventral neural tube patterning,[16] synaptogenesis,[17–19]), it also acts on astrocytes: BMPs are involved in cell fate decisions and help instruct glial progenitors to become astrocytes,[20] and BMPs lead to maturation of astrocytes *in vitro* with involvement of canonical signaling.[4]

Many members of the BMP family (Bmp1, 2, 3, 4, 5, 6, 7, 11) are expressed in postnatal developing (**Figure 5.2B**)[21] and/or adult cortex,[22] and all major cell types in cortex (neurons, astrocytes, oligodendrocytes, OPCs, microglia, endothelial cells) express BMPs.[21–23] Astrocytes are poised to be key mediators of BMP signaling in postnatal cortical development, as among cell types at P7 and P14, they express the highest levels of receptors Bmpr1a/Bmpr1b and downstream mediators Id1, Id3, and Id4 (**Figure 5.2A,C**) .[21,23] *In vitro*, BMPs are known to promote survival and maturation of astrocytes;[4] *in vivo*, BMP signaling correlates with Aqp4 expression in cortex,[24] and Smad4 cKO astrocytes had reduced proliferation in adult diencephalon.[25] However, the role of astrocyte BMP signaling in postnatal development has not yet been well characterized.

Astrocyte BMP-induced genes vary spatially

Several recent studies on cortical astrocyte heterogeneity including from our lab have found BMP-induced gene Id3 to be expressed at different levels in different single cell RNAseq (scRNAseq)-defined astrocyte subpopulations.[8,23,26] In confirmation, Id1 and Id3 expression were found via immunohistochemistry (IHC) and single molecule fluorescence *in situ* hybridization (smFISH) to be enriched in astrocytes at the pial surface as well as in the deep (L5-6) cortical layers and white matter (WM), relative to upper layers (L2-4), at multiple timepoints (P14, P30, P56) (**Figure 5.2D,E,F**).[8,9] Moreover, other BMP pathway genes (Smad6, Smad9, Bmpr1a, Bmpr1b) are enriched in the deep layer and white matter cluster astrocytes at P14.[23] This signature appears not to be limited to development or mouse cortex: in a single-cell study on adult/aged individuals (56-100yo, prefrontal cortex), Id3 emerged as an astrocyte subcluster-enriched gene;[27] this cluster mapped to L1 and WM in both human and mouse cortex, and was also enriched for BMP-induced genes Id1, Id2, Id4, and Smad9.[27] Id3-enriched astrocyte clusters are also present in other parts of the brain such as medial amygdala,[28] superior colliculus,[29] hippocampus,[30] and others.[12,31–33]

The role of BMP signaling in astrocyte heterogeneity and development

A recent report using Reelin KO mice highlighted how spatial gradation of cortical Id3 expression is inverted when neuronal layers themselves are inverted, indicative of astrocyte patterning based on neuronal layers.[8] Additionally, recent reports documented layer-specific neuron-to-astrocyte SHH signaling[34] and layer-specific neuron-to-astrocyte N-cadherin interactions.[35] Given the above studies highlighting Id3 as marking a spatially segregated astrocyte subtype, we wanted to ask, what is the impact of BMP signaling on astrocyte transcriptional heterogeneity, and how does it functionally impact astrocytes and developing neural circuits? What can our multi-omic analyses in Chapters 3 and 4 reveal about the role of BMP signaling in cortical astrocyte heterogeneity and development?

Results

Comparison of Smad4cKO nRNAseq to known astrocyte layer-enriched gene and signatures

An initial survey of the Smad4 cKO dataset showed that many DEGs were known to be astrocyte layer-enriched genes. Using the same criteria as previous (FC > 1.5, TPM > 1, p-adj < 0.05), we found 88 upregulated and 62 downregulated genes comparing Smad4 cKO to WT (**Figure 5.1A**). Gene set enrichment analysis (GSEA) on the Smad4 cKO comparison with gene sets created from bulk sequencing of upper (L2-4) vs lower (L5-6) layer cortical astrocytes[9] showed significant negative enrichment of lower-layer genes (p = 0.013; core genes *Id3*, *Serpinf1*, *Hopx*, *Slc20a1*, *Id1*, *Id2*, *Kcnq4*) and no enrichment of upper-layer genes (p = 0.25; core genes *Scel*, *Egfl6*, *Mir9-1*, *Cnr1*, *Tph2*, *Lyrm4*, *Dkk3*, *Slc16a2*, *Eogt*, *Dcc*), with many genes in both sets being significantly up- or down-regulated in Smad4 cKO, overall suggesting that BMP signaling may drive lower layer gene signatures (**Figure 5.3A**). A recent report suggested that pial astrocytes are marked by expression of *Myoc*, and among the genes enriched in *Myoc*+ astrocytes are BMP-induced genes Id1 and Id3.[1] GSEA on Smad4 cKO using a gene set of 155 *Myoc*+-enriched genes[1] showed significant negative enrichment (p<0.0001), indicating that Smad4-dependent gene expression may be a driver of the *Myoc*+ putative pial astrocyte transcriptional signature (**Figure 5.3B**).

Does expression of known layer-enriched astrocyte genes change in Smad4 cKO?

To determine if known layer-enriched genes are altered in Smad4 cKO, I performed IHC or smFISH for *Myoc*, *Tnc* , *Chrdl1*, and Sparc. Astrocyte *Myoc* is known to be expressed at the pia,[1] and was strongly downregulated in Smad4 cKO nRNAseq (nRNAseq: L2FC = -4.3, adj-p = 8.4e-31). smFISH confirmed that Smad4 cKO abolishes pial expression of *Myoc* (N = 3, p = 0.0074) (**Figure 5.4**). Astrocyte *Tnc* was also strongly downregulated in Smad4 cKO nRNAseq (nRNAseq: L2FC = -2.02, adj-p = 6.9e-17), and smFISH for *Tnc* combined IHC for astrocyte marker S100B confirmed that Smad4 cKO reduces astrocyte expression of *Tnc* where it is present in layers 1 and 6 (N=4, p < 0.0001 for L1, p = 0.038 for L6) (**Figure 5.5**). Astrocyte *Chrdl1* is

known to be enriched in cortical layers L2-L4,[8,9,13,23] and was not changed in Smad4 cKO nRNAseq. smFISH for *Chrdl1* combined with IHC for astrocyte marker S100B confirmed lack of any change in cortical astrocyte expression of *Chrdl1* across all layers (N = 4) (**Figure 5.6**). Last, astrocyte secreted protein Sparc has been found to be expressed higher in deeper cortical layers (L5-6),[9] and was upregulated in Smad4 cKO nRNAseq (L2FC = 1.34, adj-p = 2.5e-4). IHC for Sparc and astrocyte marker S100B showed upregulation of Sparc across cortical layers where it originally was expressed lower—L1 ($p < 0.0001$), L2/3 ($p = 0.0107$), and L6 ($p = 0.0499$)—with no significant change in L4 and L5 (N=4) (**Figure 5.7**). Altogether, these data show *Myoc* and *Tnc* appear to be BMP-induced genes, as their expression is lowered in Smad4 cKO where ID3 expression and thus BMP signaling is lowered in Smad4 cKO (L1 and L6), though in different distributions (pia only for *Myoc*, L1 away from pia and L6 for *Tnc*). Additionally, the data confirm that *Chrdl1*, a L2-4-enriched gene not changed in Smad4 cKO, maintained its expression pattern in Smad4 cKO. Last, Sparc expression appears to be inhibited by BMP signaling, as Smad4 cKO upregulates Sparc in the cortical layers where ID3 signaling expression is highest in WT. Thus IHC and smFISH for specific changed and unchanged genes from Smad4 cKO nRNAseq were able to validate alterations in layer-specific astrocyte gene expression.

How does Smad4 cKO affect cortical development?

Given that *in vitro*, BMPs lead to maturation of astrocytes with involvement of canonical signaling,[4] we asked whether Smad4 cKO astrocytes display immaturity. BMP signaling is known to correlate with expression and subcellular localization of water channel Aqp4,[4,24,36] which is expressed at astrocyte endfeet at blood vessels and known to regulate CNS water homeostasis. *Aqp4* is significantly downregulated in Smad4 cKO nRNAseq (adj. p = 0.038, L2FC -0.82), and IHC showed that while blood vessel-wrapping volume and AQP4 intensity around vessels did not change, parenchymal AQP4 intensity away from vessels significantly decreased in Smad4 cKO visual cortex, primarily in L1 (N=5) (**Figure 5.8**). This demonstrates that *in vivo*, canonical BMP

signaling induces increased parenchymal AQP4 localization in cortical L1. Thus BMP signaling may be functioning to induce astrocyte maturation *in vivo* through P28.

Apart from the role of astrocyte BMP signaling intrinsically in astrocyte maturation, we also asked how astrocyte BMP signaling might affect other cell types' maturation state. To assay for functional changes in astrocyte state, we turned to our proteomic data (Chapter 4). Using the same criteria as previous ($p < 0.05$), we found 12 upregulated and 39 downregulated proteins comparing Smad4 cKO to WT (**Figure 5.1C**). Of note, many of the downregulated proteins we found in our *in vivo* proteomics/secretomics dataset are proteoglycans with links to induction of synapse maturation such as GPC5,[35] and components of perineuronal nets (PNNs) associated with inhibitory interneuron maturation such as ACAN, BCAN, NCAN, VCAN, HAPLN1, and HAPLN4 (**Figure 5.1C,D**).[36] Indeed, BCAN or brevican was one of the top Smad4 cKO downregulated proteins by p-value in the proteomics dataset ($p=0.0029$, **Figure 4.9C**), and western blotting on cortical lysates validated the decrease in BCAN in Smad4 cKO (N=6, $p=0.0006$, 34±7% decrease, **Figure 4.9A,B**). Thus, in line with the known role of BMPs to induce extracellular matrix (ECM) production and remodeling in fibroblasts,[37] astrocyte BMP signaling may function to promote formation of ECM PNNs that may functionally affect other cell types.

<u>What drives cortical layer differences in astrocyte expression of BMP-induced genes?</u>

Chrdl1 is an astrocyte-secreted protein with enriched expression in cortical layers 2/3.[13] Chrdl1 has homology to the chordin family of BMP inhibitors and is known to bind BMP4, BMP6, and BMP7.[38] *Chrdl1* and *Id3* mRNA expression in astrocytes are inversely correlated across cortical layers in both WT and Reln KO mice,[8] in which superficial and deep cortical layers are inverted ("inside-out"). Increased secreted Chrdl1 in upper cortical layers could bind BMPs and potentially lower the effective BMP concentrations in upper cortical layers.

To test this hypothesis, I immunostained for BMP-induced protein ID3 in cortex of constitutive Chrdl1 KO mice developed in [13]. As a control, ID3 staining in Smad4 WT vs. cKO showed downregulation of ID3 intensity within SOX9+ astrocyte nuclei (N=3) (**Figure 5.2D,E,F**).

This effect was most prominent in L1, L6, and WM, where BMP signaling and ID3 expression is highest in astrocytes. Immunostaining in tissue from a global Chrdl1 KO, however, did not show any difference in ID3 intensity across layers (N=3) (**Figure 5.9A,B**). Furthermore, smFISH for BMP-induced gene *Tnc,* previously shown to be suppressed in Smad4 cKO, showed no change in Chrdl1 KO (**Figure 5.9C,D**). These data suggest that Chrdl1 KO does not alter layer-patterned astrocyte BMP signaling.

Discussion

In this chapter, I leverage our RNAseq (Chapter 3) and ER-TurboID proteomics (Chapter 4) datasets to interrogate the effect of SMAD4 and BMP signaling in typically developing astrocytes, and find that BMP signaling underlies transcriptional programs important for cortical astrocyte heterogeneity, and that BMP signaling may contribute to astrocyte and cortical maturation *in vivo*.

BMP signaling underlies pial astrocyte transcriptional programs

The most significantly downregulated gene in Smad4 cKO is *Myoc*, a known marker of pial astrocytes that was also found to be induced *in vitro* by BMP6. Moreover, many other genes enriched in pial astrocytes were found to be part of the BMP signature (**Figure 5.3B**). While the function of *Myoc* and more broadly the role of pial astrocytes is unknown, we speculate they may be involved in barrier formation and protection from external physical/immune insults, as the pia is the barrier between brain parenchyma and CSF. Pial astrocytes have cell bodies that lie on the plane of the pia and extend processes into the parenchyma, similar to the more elaborate interlaminar astrocytes found in humans.[1,39,40] Immature mouse cortical astrocytes transplanted into developing mouse cortex can acquire native pial signatures such as higher expression of GFAP,[41] and human pluripotent stem cell (PSC)-derived astrocyte-enriched organoids transplanted into mouse cortex can acquire interlaminar astrocyte morphology and expression

signatures,[42] suggesting that local cues can control pial astrocyte specification. Moreover, treating astrocytes *in vitro* with BMP enhances their complexity,[2,4] and astrocytes across cortical layers have different morphology and volume basally.[9]

To better understand whether BMP signaling is the cue that drives pial morphology, it will be interesting to assay astrocyte morphology, potentially through a combination of sparse viral labeling of astrocytes with fluorophore combined with thick sectioning and/or lightsheet microscopy. At P0-2 AAV2/5 expressing Lck-GFP (membrane targeted GFP) under the minimal GFAP promoter (targeting astrocytes) will be injected into the lateral ventricle at low titre to sparsely label astrocytes.[6] Preliminary experiments show this method is viable, and four Smad4 WT/cKO littermate pairs have been injected with virus. Cell volume, branching and neuropil infiltration will be quantified. We predict that astrocytes in deep and superficial layers where BMP signaling is normally high will be most impacted by Smad4 cKO, and show decreased size and complexity.

Astrocyte Smad4 cKO leads to a small increase in cortical area

Given that BMP signaling mediates cell fate from neural progenitor cells, and that Smad4 has been implicated in proliferation both in astrocytes and across cell type and body systems,[25,37,43] we performed a detailed investigation of astrocyte number and density, as well as total cell number and density, in P28 cortex. We found no changes in overall numbers across cortical layers, but density was slightly decreased, an effect driven by a slight increase in cortical area, particularly in layer 1 (**Figure 2.4**). Further studies of cell size will be necessary to determine if this increase in cortical area is driven by larger cells. Alternatively, changes to the osmotic regulation and extracellular matrix could underlie the increase in cortical volume in Smad4 cKO. A hypothesis is that the decrease in astrocyte Aqp4 in Smad4 cKO, particularly in L1 where astrocytes help form the pial barrier to CSF (**Figure 5.8**), could change homeostatic osmotic regulation such that cortical parenchyma expands. Detailed targeted experiments to assay pial

integrity such as tracer experiments and precise volumetric analyses such as via MRI would be necessary to make definitive assessments of the role of astrocyte BMP signaling in cortical volume.

Single-cell experiments will enable deeper understanding of BMP-induced astrocyte heterogeneity

Further investigation of all BMP pathway components will help answer the questions: what is the source of BMP *in vivo*? If not Chrdl1, what drives the spatial patterning of astrocyte BMP signaling? Heterogeneous expression of other BMP inhibitors (e.g. Noggin, Chordin), or else, spatially patterned secretion of BMPs may be responsible for layered astrocyte BMP signaling. Candidates for BMPs include BMP7 in CSF via secretion by choroid plexus,[44] BMP6 from astrocytes via autocrine/paracrine signaling as in [2], BMP4 from newly formed oligodendrocytes, and BMP6 or BMP7 from vascular and leptomeningeal cells (VLMCs).[45] To ask what drives cortical layer differences in astrocyte BMP signaling in an unbiased manner, we hope to perform snRNAseq on FACS-isolated cortical astrocyte nuclei and spatial transcriptomics in cortex of Smad4 WT vs cKO mice, as well as in Chrdl1 WT and Chrdl1 cKO mice. For the spatial transcriptomics, we have designed a panel to probe 300 genes that include astrocyte genes with spatial enrichment (published studies[8,10]), DEGs from Smad4 cKO astrocytes (bulk and single nucleus RNA sequencing data), cell identity genes (to determine if cell proportions are altered), neuronal layer identity genes (to determine if Smad4 cKO alters neuronal state), and BMP pathway genes (to determine source of BMP). These studies would further increase the granularity of our understanding of the role of BMP signaling in astrocyte heterogeneity.

What is the functional impact of astrocyte BMP signaling?

One hypothesis is that similar to the known role for TGFβ superfamily members in regulating fibroblast ECM production remodeling,[3,37] Smad4-dependent BMP signaling could regulate astrocyte secretion of ECM components (**Figure 4.9, 5.1C,D**) and thus parenchymal

state and maturation. To follow up on the reduction of astrocyte perineuronal net components we detected in Smad4 cKO *in vivo* proteomics (**Figure 5.1C,D**), it will be important to follow up on functional questions such as: how does Smad4 cKO affect interneuron maturation (e.g. perineuronal net formation) and function? And how does this impact circuit function and development? These questions could be answered with experiments such as electrophysiology on cortical interneurons and pyramidal neurons, as well as assays of plasticity, such as the Arc assay for ocular dominance plasticity (Chapter 2). Indeed, astrocyte-secreted factors (e.g. CHRDL1 and CCN1)[13,46] can stabilize circuits and reduce ocular dominance plasticity, so it will be interesting to see if Smad4 cKO, by reducing astrocyte expression of secreted/ECM factors, can increase ocular dominance plasticity.

Given that Smad4 cKO leads to significant changes in expression of astrocyte Sparc (**Figure 5.6**) and *Tnc* (**Figure 5.5**), both of which have literature-reported effects on synapses,[47–49] it will be important to ask, what is the effect of Smad4 cKO on synapses? Data from inhibitory synapses (Chapter 2) suggest that Smad4 cKO does not change inhibitory synapse density in P28 auditory cortex, but it will be important to also assay for excitatory synapses, as well as other cortical regions and layers.

Overall, our transcriptomic and proteomic data and analyses in this chapter highlight a role for astrocyte BMP signaling in astrocyte heterogeneity and development. Further transcriptomic studies at the single-cell level, as well as functional experiments, will allow deeper characterization of the totality of genes, spatial subgroupings, and functions enabled by astrocyte BMP signaling.

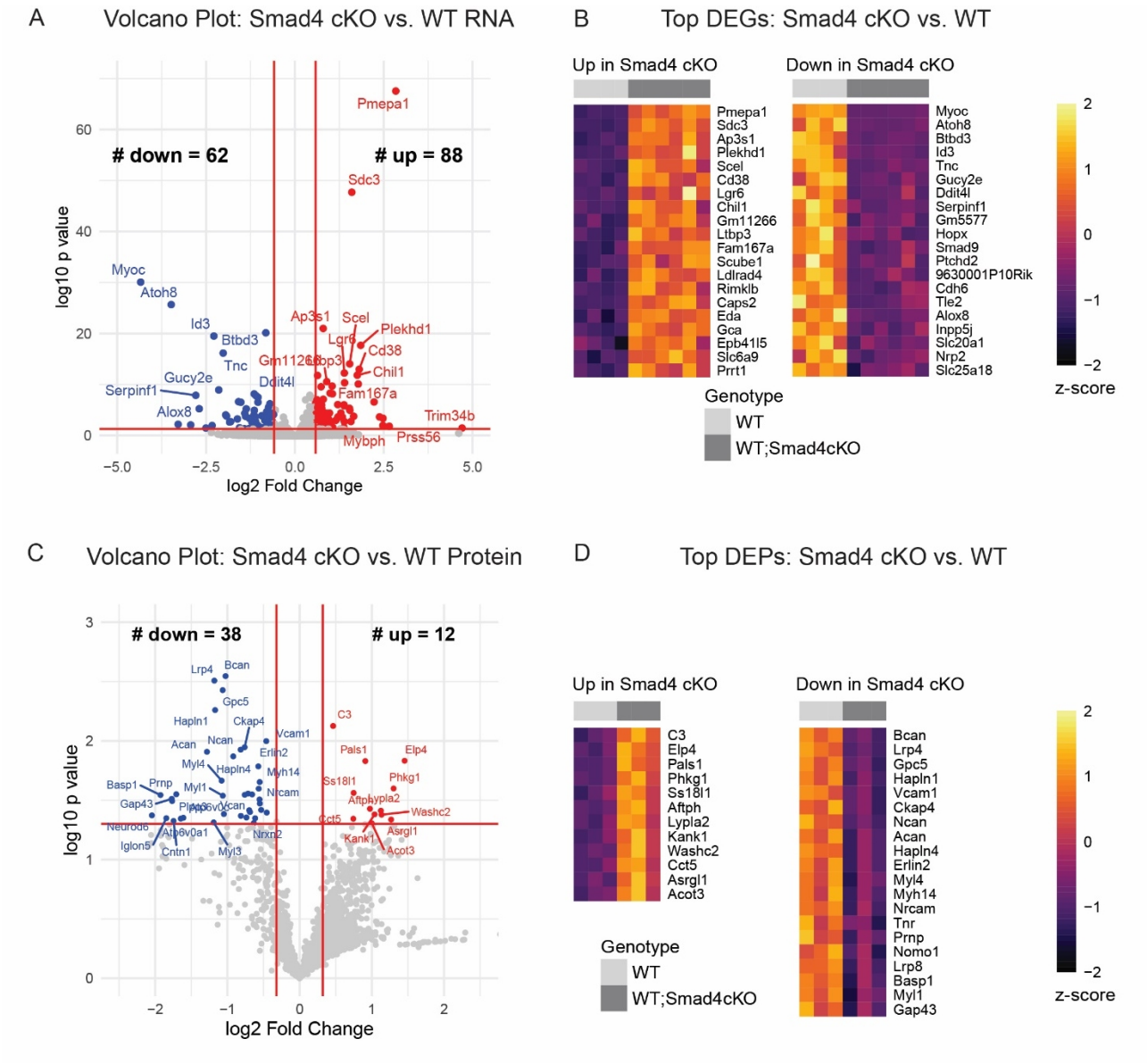

Figure 5.1. Transcriptomic and proteomic analysis of Smad4 cKO astrocytes.

A. Volcano plot of the Smad4 cKO vs. WT comparison highlighting differentially expressed genes. Data from P26-28 nRNAseq (Chapter 3). Vertical red lines at |FC| = 1.5, and horizontal red line at p-adj = 0.05.
B. Heatmaps showing top 20 significantly changed up- and down-regulated genes in Smad4 cKO, listed by adjusted p-value.
C. Volcano plot of the Smad4 cKO vs. WT comparison highlighting differentially expressed proteins. Data from P27 *in vivo* ER-targeted proteomics (Chapter 4). Vertical red lines at |FC| = 1.25, and horizontal red line at p-value = 0.05.
D. Heatmaps showing top significantly changed up- and down-regulated proteins in Smad4 cKO, listed by p-value.

Figure 5.2. BMP signaling present in developing astrocytes varies across cortical layers.

A. UMAP clustering of P14 scRNAseq dataset from Farhy-Tselnicker et al., 2021,[10] with cell types labeled as in Farhy-Tselnicker et al., 2021.
B. *Bmp4* and *Bmp6* expression overlaid on the UMAP plot.
C. *Bmpr1b* and *Id3* expression overlaid on the UMAP plot, with astrocyte cluster circled.
D. Immunohistochemistry for ID3 and astrocyte marker SOX9 in auditory cortex in Smad4 WT and Smad cKO in P28 auditory cortex. Images shown in L1-2 and L4. Data is reanalyzed from Chapter 2 (Figure 2.2G,H).
E. Quantification of ID3 immunohistochemistry in Smad4 WT shows variation across cortical layers. N = 4 mice. Black dots represent mice, and grey dots represent SOX9+ cells. Statistics by 1-way ANOVA with Tukey's test for multiple comparisons.
F. Quantification of ID3 immunohistochemistry in Smad4 WT and cKO shows reduction in ID3 intensity in Smad4 cKO in L1, L6, and white matter. N = 4 mice per genotype. Black dots represent mice, and white and grey dots represent SOX9+ cells. Statistics by 2-way ANOVA with Sidak's test for multiple comparisons

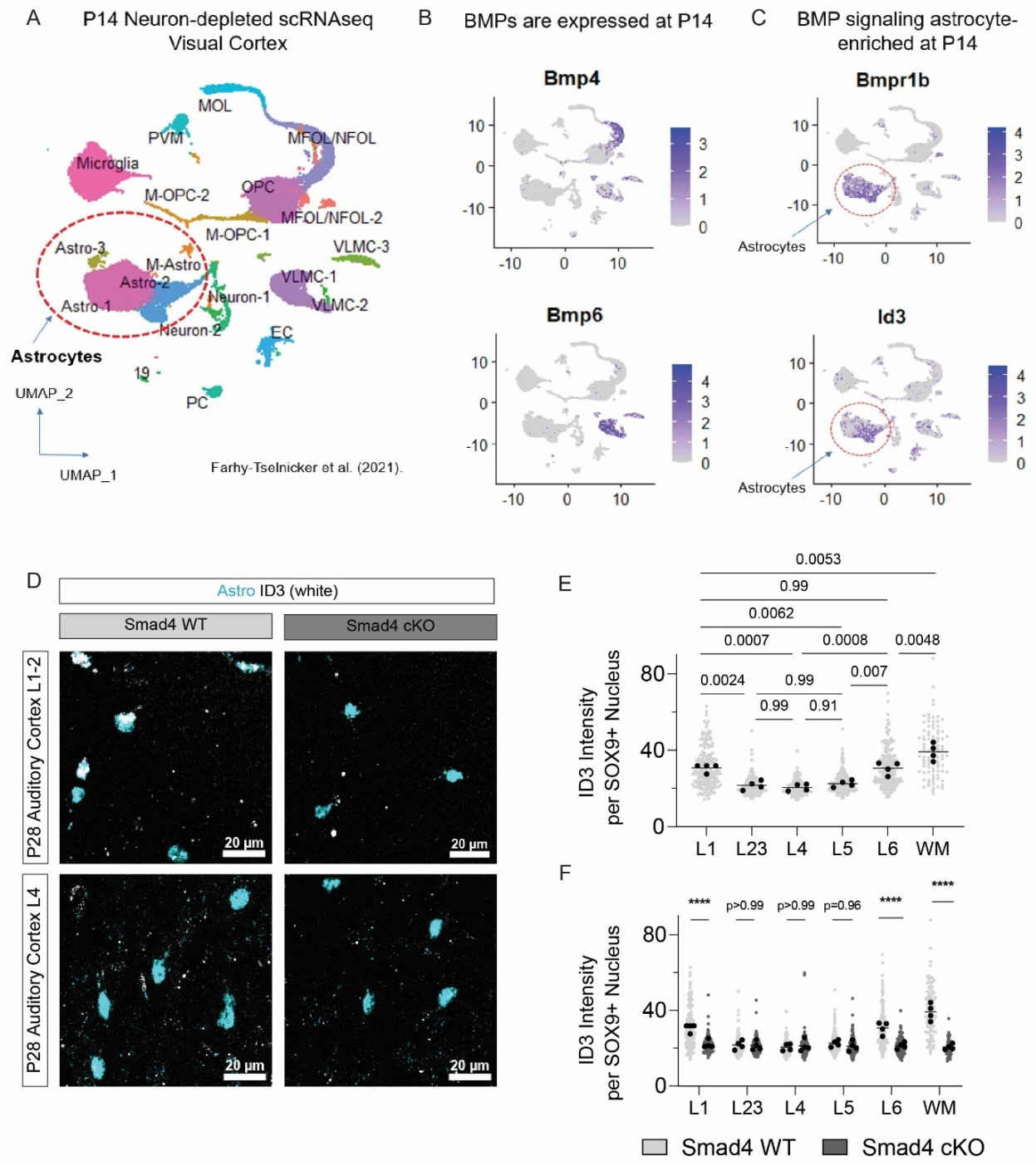
A
P14 Neuron-depleted scRNAseq
Visual Cortex
MOL
PVM
MFOL/NFOL
Microglia
M-OPC-2
OPC
MFOL/NFOL-2
M-OPC-1
Astro-3
VLMC-3
M-Astro
Astro-2
VLMC-1
Astro-1
Neuron-1
VLMC-2
Neuron-2
EC
Astrocytes
19
PC
UMAP_2
UMAP_1
Farhy-Tselnicker et al. (2021).
B
BMPs are expressed at P14
Bmp4
Bmp6
C
BMP signaling astrocyte-enriched at P14
Bmpr1b
Id3
Astrocytes
D
Astro ID3 (white)
Smad4 WT
Smad4 cKO
P28 Auditory Cortex L1-2
P28 Auditory Cortex L4
20 µm
E
ID3 Intensity per SOX9+ Nucleus
0.0053
0.99
0.0062
0.0007
0.0008
0.0048
0.0024
0.99
0.007
0.99
0.91
L1
L23
L4
L5
L6
WM
F
****
p>0.99
p>0.99
p=0.96
****
****
Smad4 WT
Smad4 cKO

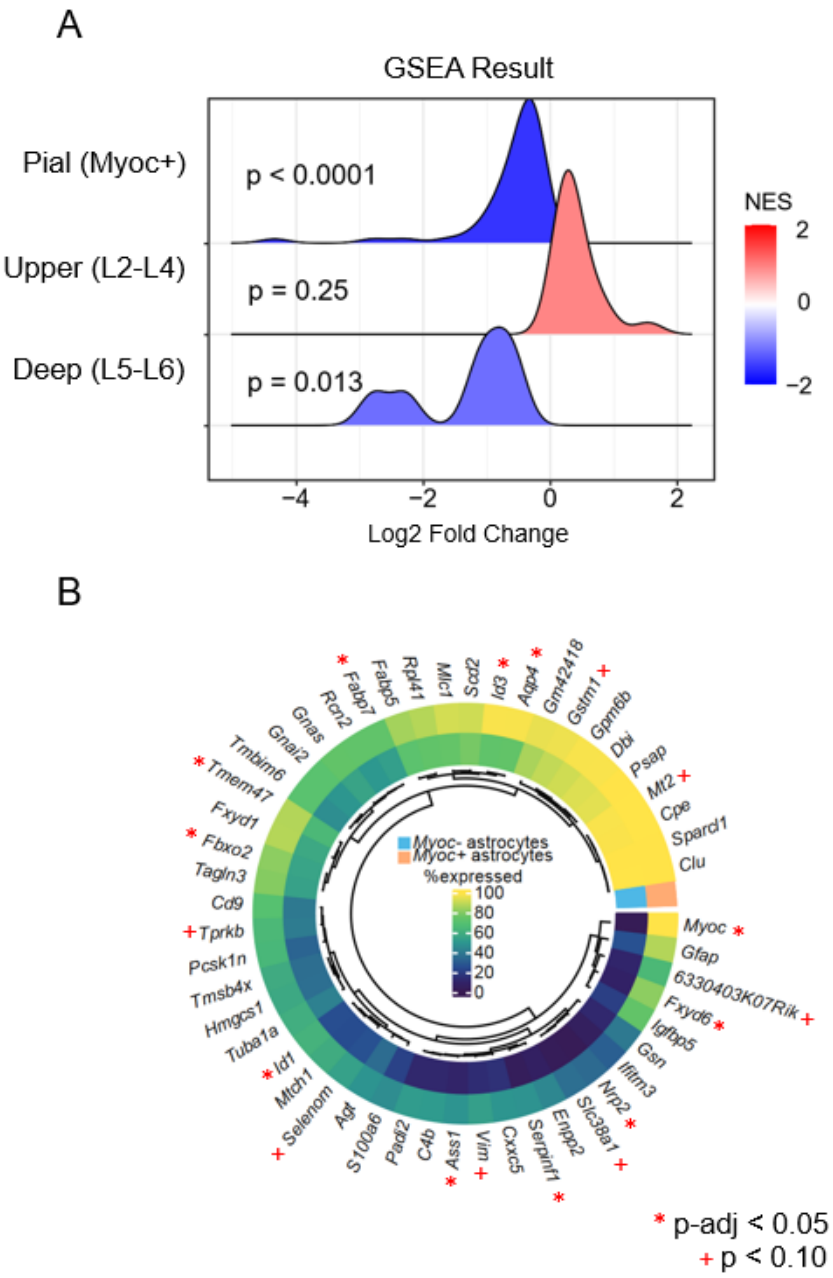

Figure 5.3. Smad4 cKO astrocytes have altered expression of astrocyte layer-enriched gene programs.

A. Gene set enrichment analysis (GSEA) of Smad4 cKO nRNAseq genes, with gene lists enriched in pial astrocytes (Hasel et al. 2023),[1] as well as upper (L2-L4) and deep (L5-L6) layer astrocytes of cortex (Lanjakornsiripan et al., 2018).[9]
B. Figure reproduced from Hasel et al. 2023,[1] showing the top 50 genes enriched in pial astrocytes (*Myoc*+) relative to other astrocytes (*Myoc*-) in a single cell RNAseq analysis combining 13 datasets from mouse cortex, hippocampus, spinal cord, and striatum. Heatmap color represents the fraction of the population expressing the gene. Of the top 50 genes enriched in *Myoc*+ astrocytes, 18 are significantly downregulated in Smad4 cKO (labeled with red asterisk to indicate p-adj < 0.05 and red cross to indicate p < 0.1).

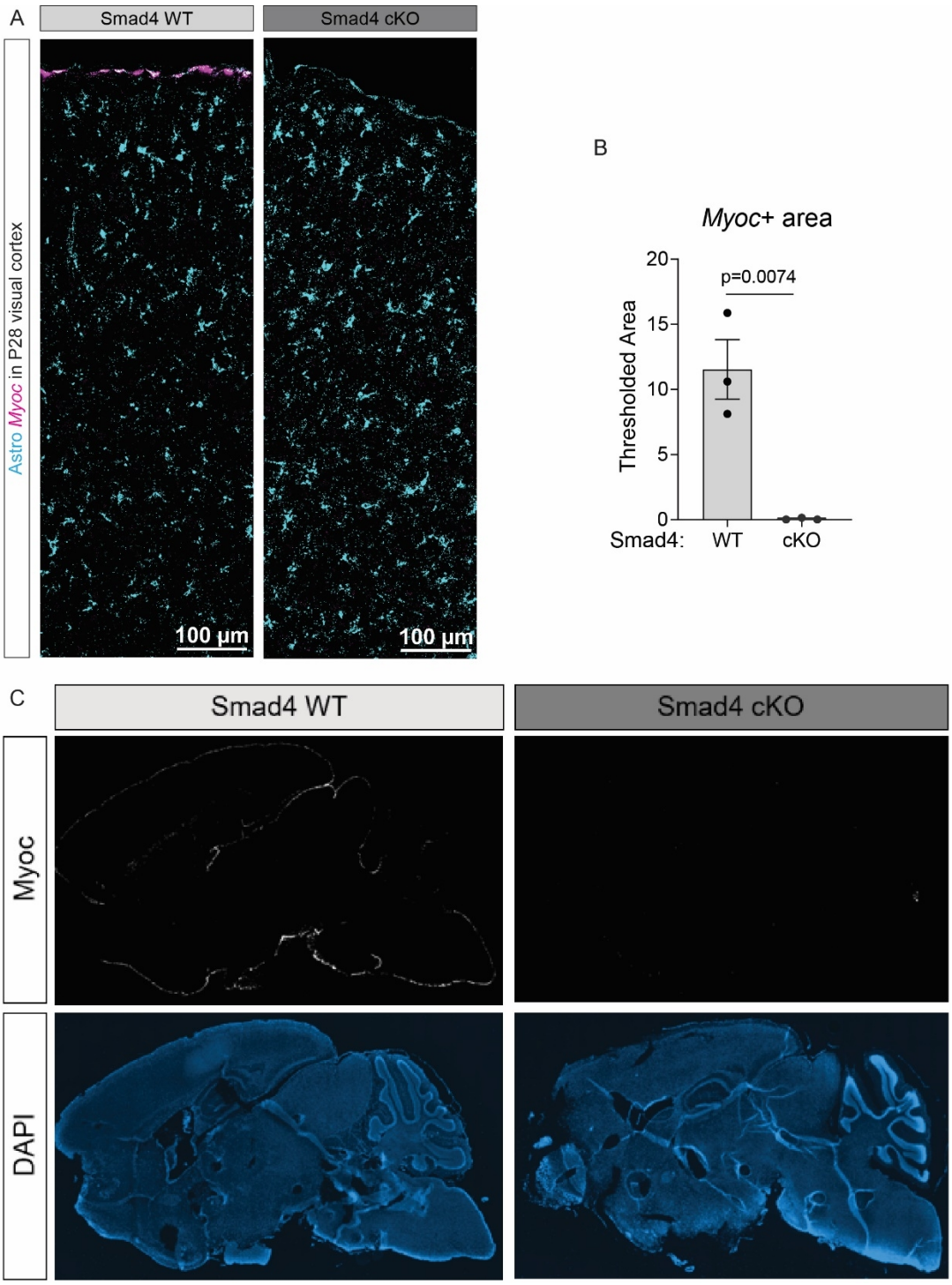

Figure 5.4. Pial expression of *Myoc* is abolished in Smad4 cKO.

A. Expression of *Myoc* and astrocyte marker *Slc1a3* (GLAST) by single molecule fluorescence *in situ* hybridization (smFISH) in P28 visual cortex.
B. Quantification of thresholded *Myoc*+ pial area. N = 3 mice per genotype, dots represent mice. Statistics by t-test.
C. Expression of *Myoc* by single molecule fluorescence *in situ* hybridization (smFISH) with DAPI counterstain in P28 sagittal sections.

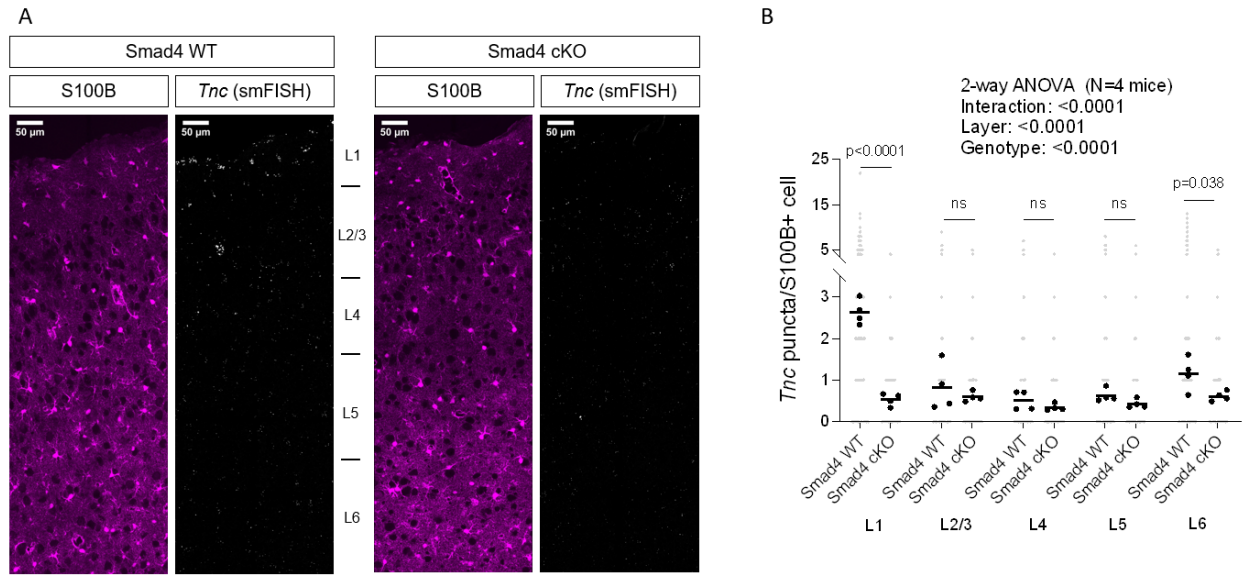

Figure 5.5. L1 and L6 expression of *Tnc* is reduced in Smad4 cKO.

A. Expression of *Myoc* and astrocyte marker S100B by single molecule fluorescence *in situ* hybridization (smFISH) combined with immunohistochemistry in P28 visual cortex.
B. Quantification of *Tnc* puncta within S100B+ astrocytes by layer. N = 4 mice per genotype. Black dots represent mice, grey dots represent S100B+ cells, and black bar is average of black dots. Statistics by 2-way ANOVA on mice with Sidak's test for multiple comparisons.

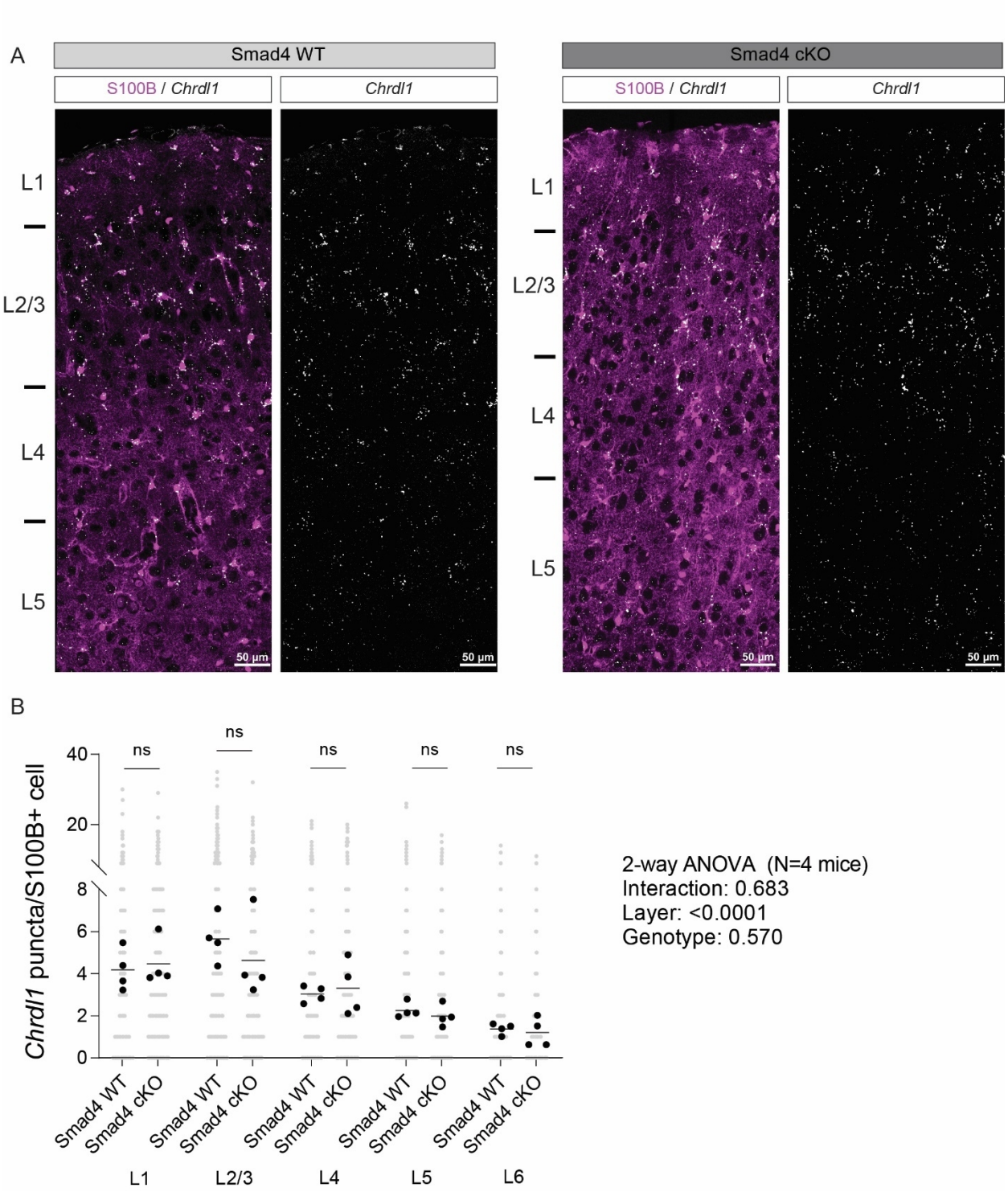

Figure 5.6. Expression of *Chrdl1* is not changed in Smad4 cKO.

A. smFISH for *Chrdl1* with immunohistochemistry for S100B in P28 visual cortex.
B. Quantification of *Chrdl1* puncta within S100B+ astrocytes by layer. N = 4 mice per genotype. Black dots represent mice, grey dots represent S100B+ cells, and black bar is average of black dots. Statistics by 2-way ANOVA on mice with Sidak's test for multiple comparisons.

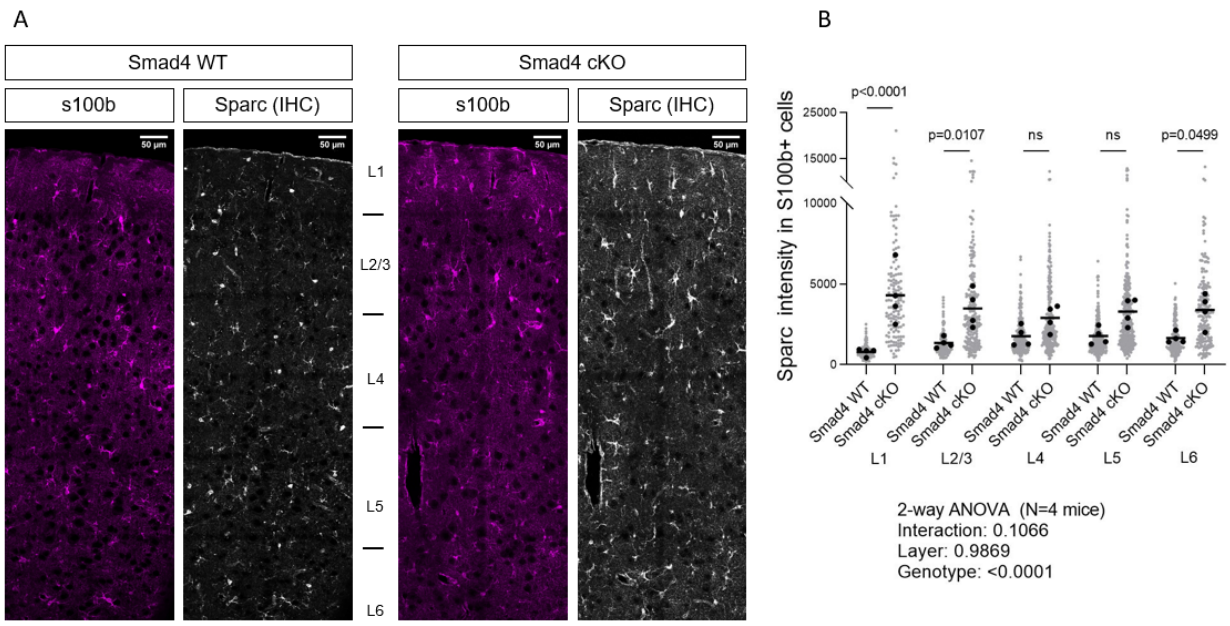

Figure 5.7. Sparc is upregulated in L1, L2, and L6 in Smad4 cKO.

A. Expression of Sparc and astrocyte marker S100B by immunohistochemistry in P28 visual cortex.
B. Quantification of Sparc fluorescence intensity within S100B+ astrocytes by layer. N = 4 mice per genotype. Black dots represent mice, grey dots represent S100B+ cells, and black bars are averages of black dots. Statistics by 2-way ANOVA on mice with Sidak's test for multiple comparisons.

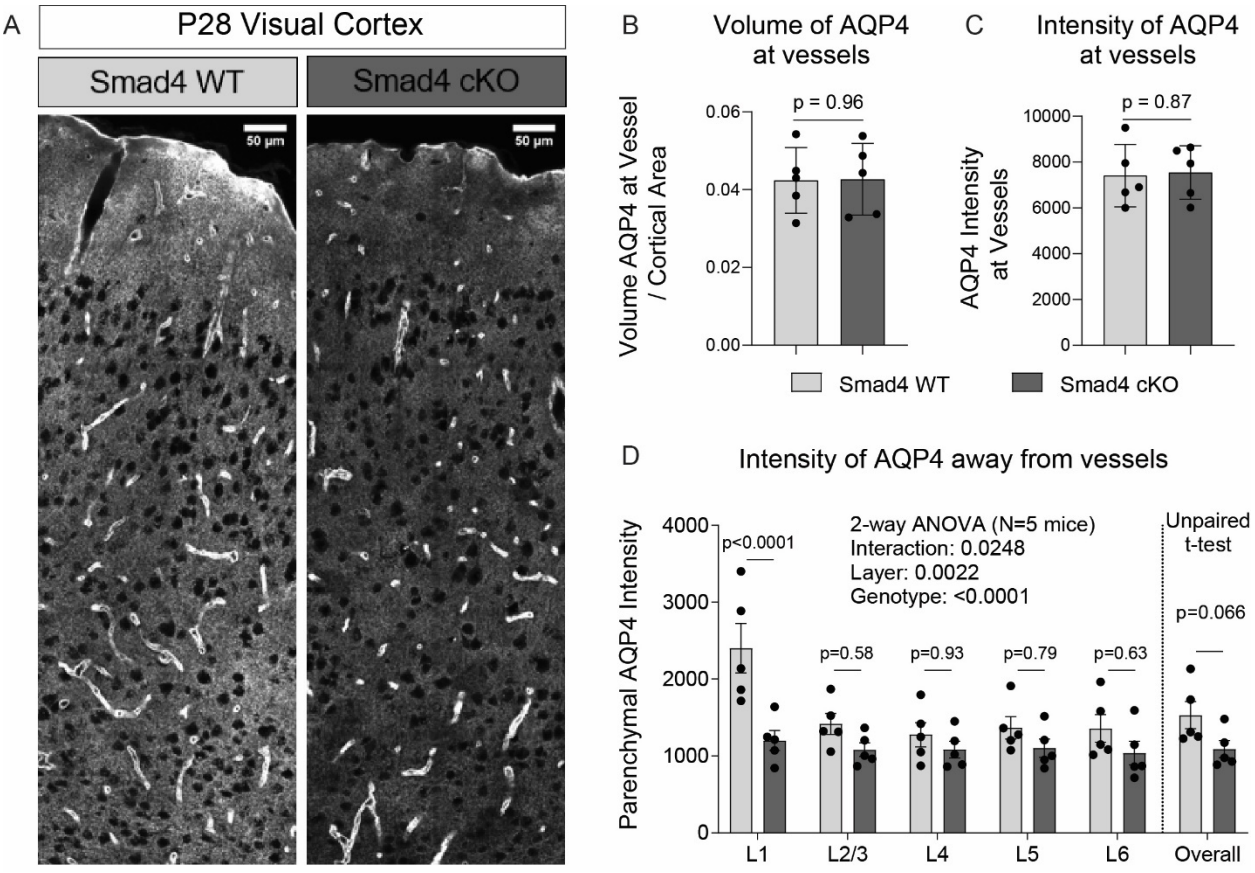

Figure 5.8. AQP4 is downregulated in Smad4 cKO cortical parenchyma.

A. Immunohistochemistry for AQP4 in P28 visual cortex.
B. Volume of AQP4 at vessels normalized to total cortical area is unchanged in Smad4 cKO. N = 5 mice per genotype. Statistics by t-test.
C. Intensity of AQP4 at vessels is unchanged in Smad4 cKO. N = 5 mice per genotype. Statistics by t-test.
D. Quantification of AQP4 intensity in parenchyma away from blood vessels. N = 5 mice per genotype. Statistics by 2-way ANOVA on mice with Sidak's test for multiple comparisons, for layers. Statistics by t-test for overall.

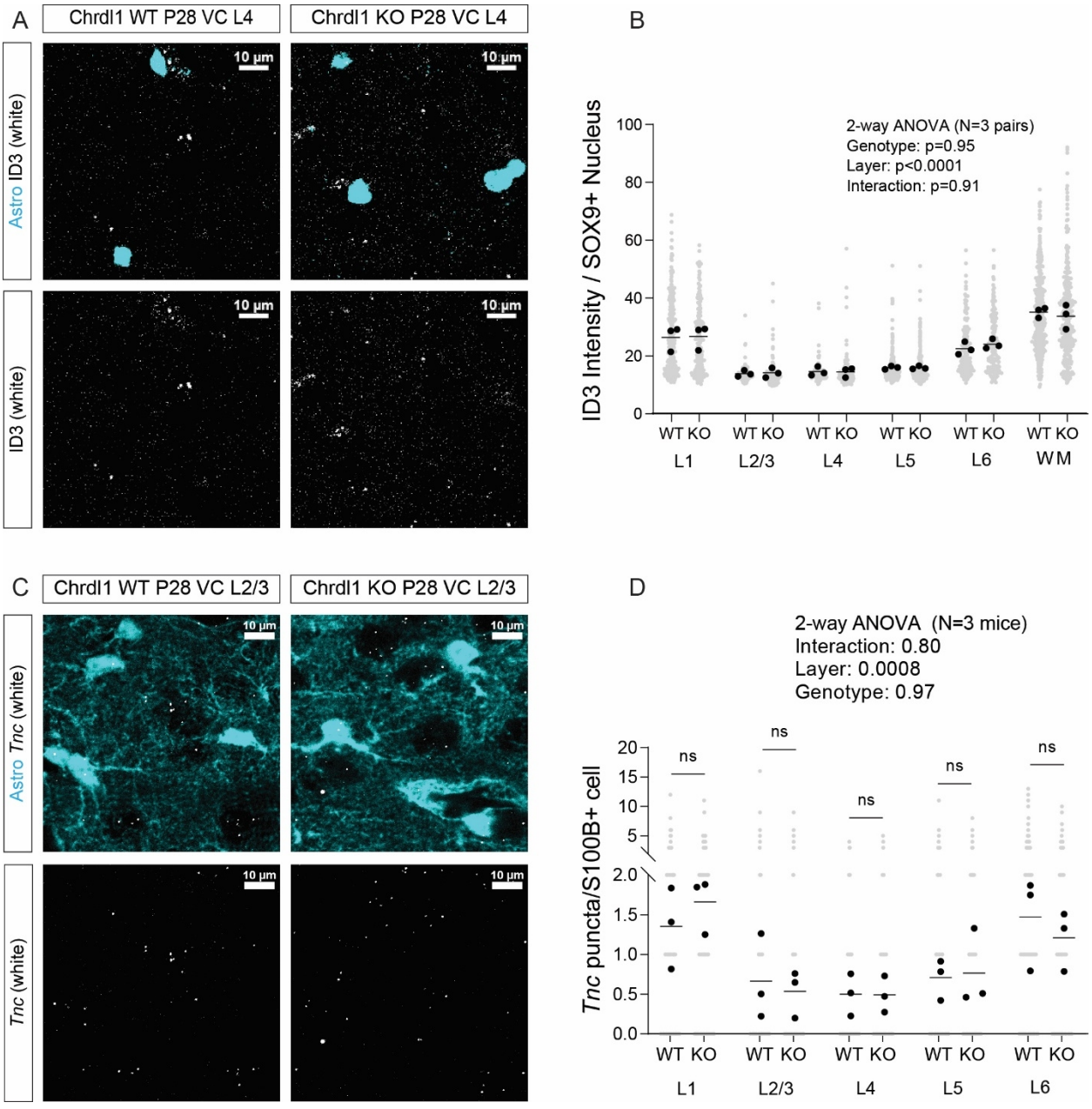

Figure 5.9. BMP-related gene expression is not changed in Chrdl1 KO visual cortex at P28.

A. Immunohistochemistry for BMP-induced protein ID3 and astrocyte nuclear marker SOX9 at P28 in visual cortex.
B. Quantification of 5.9A by 2-way ANOVA on mice with Sidak's test for multiple comparisons. N = 3 mice per genotype. Black dots represent mice, grey dots represent SOX9+ nuclei, and black bars represent averages of the black dots.
C. smFISH for BMP-induced gene *Tnc* combined with immunohistochemistry for astrocyte marker S100B at P28 in visual cortex.
D. Quantification of 5.9C by 2-way ANOVA on mice with Sidak's test for multiple comparisons. N = 3 mice per genotype. Black dots represent mice, grey dots represent SOX9+ nuclei, and black bars are averages of the black dots.

References

1. Hasel, P. *et al. Defining the Molecular Identity and Morphology of* Glia Limitans Superficialis *Astrocytes in Mouse and Human*. http://biorxiv.org/lookup/doi/10.1101/2023.04.06.535893 (2023) doi:10.1101/2023.04.06.535893.

2. Caldwell, A. L. M. *et al.* Aberrant astrocyte protein secretion contributes to altered neuronal development in multiple models of neurodevelopmental disorders. *Nat. Neurosci.* **25**, 1163–1178 (2022).

3. Divolis, G. *et al.* Activation of both transforming growth factor-β and bone morphogenetic protein signalling pathways upon traumatic brain injury restrains pro-inflammatory and boosts tissue reparatory responses of reactive astrocytes and microglia. *Brain Commun.* **1**, fcz028 (2019).

4. Scholze, A. R., Foo, L. C., Mulinyawe, S. & Barres, B. A. BMP Signaling in Astrocytes Downregulates EGFR to Modulate Survival and Maturation. *PLoS ONE* **9**, e110668 (2014).

5. Bayraktar, O. A., Fuentealba, L. C., Alvarez-Buylla, A. & Rowitch, D. H. Astrocyte Development and Heterogeneity. *Cold Spring Harb. Perspect. Biol.* **7**, a020362 (2015).

6. Endo, F. *et al.* Molecular basis of astrocyte diversity and morphology across the CNS in health and disease. *Science* **378**, eadc9020 (2022).

7. Bartels, T., Rowitch, D. H. & Bayraktar, O. A. Generation of Mammalian Astrocyte Functional Heterogeneity. *Cold Spring Harb. Perspect. Biol.* a041351 (2024) doi:10.1101/cshperspect.a041351.

8. Bayraktar, O. A. *et al.* Astrocyte layers in the mammalian cerebral cortex revealed by a single-cell in situ transcriptomic map. *Nat. Neurosci.* **23**, 500–509 (2020).

9. Lanjakornsiripan, D. *et al.* Layer-specific morphological and molecular differences in neocortical astrocytes and their dependence on neuronal layers. *Nat. Commun.* **9**, 1623 (2018).

10. Farhy-Tselnicker, I. *et al.* Activity-dependent modulation of synapse-regulating genes in astrocytes. *eLife* **10**, e70514 (2021).

11. Boisvert, M. M., Erikson, G. A., Shokhirev, M. N. & Allen, N. J. The Aging Astrocyte Transcriptome from Multiple Regions of the Mouse Brain. *Cell Rep.* **22**, 269–285 (2018).

12. Yao, Z. *et al.* A high-resolution transcriptomic and spatial atlas of cell types in the whole mouse brain. *Nature* **624**, 317–332 (2023).

13. Blanco-Suarez, E., Liu, T.-F., Kopelevich, A. & Allen, N. J. Astrocyte-Secreted Chordin-like 1 Drives Synapse Maturation and Limits Plasticity by Increasing Synaptic GluA2 AMPA Receptors. *Neuron* **100**, 1116-1132.e13 (2018).

14. Bayraktar, O. A. *et al.* Astrocyte layers in the mammalian cerebral cortex revealed by a single-cell in situ transcriptomic map. *Nat. Neurosci.* **23**, 500–509 (2020).

15. Farmer, W. T. *et al.* Neurons diversify astrocytes in the adult brain through sonic hedgehog signaling. *Science* **351**, 849–854 (2016).

16. Kashima, R. & Hata, A. The role of TGF-β superfamily signaling in neurological disorders. *Acta Biochim. Biophys. Sin.* **50**, 106–120 (2018).

17. Ball, R. W., Peled, E. S., Guerrero, G. & Isacoff, E. Y. BMP signaling and microtubule organization regulate synaptic strength. *Neuroscience* **291**, 155–166 (2015).

18. Berke, B., Wittnam, J., McNeill, E., Van Vactor, D. L. & Keshishian, H. Retrograde BMP Signaling at the Synapse: A Permissive Signal for Synapse Maturation and Activity-Dependent Plasticity. *J. Neurosci.* **33**, 17937–17950 (2013).

19. Fuentes-Medel, Y. *et al.* Integration of a Retrograde Signal during Synapse Formation by Glia-Secreted TGF-β Ligand. *Curr. Biol.* **22**, 1831–1838 (2012).

20. Liu, A. & Niswander, L. A. Bone morphogenetic protein signalling and vertebrate nervous system development. *Nat. Rev. Neurosci.* **6**, 945–954 (2005).

21. Zhang, Y. *et al.* An RNA-Sequencing Transcriptome and Splicing Database of Glia, Neurons, and Vascular Cells of the Cerebral Cortex. *J. Neurosci.* **34**, 11929–11947 (2014).

22. Hart, C. G. & Karimi-Abdolrezaee, S. Bone morphogenetic proteins: New insights into their roles and mechanisms in CNS development, pathology and repair. *Exp. Neurol.* **334**, 113455 (2020).

23. Farhy-Tselnicker, I. *et al. Activity-Dependent Modulation of Synapse-Regulating Genes in Astrocytes*. http://biorxiv.org/lookup/doi/10.1101/2020.12.30.424365 (2020) doi:10.1101/2020.12.30.424365.

24. Morita, K. *et al.* BMP signaling alters aquaporin-4 expression in the mouse cerebral cortex. *Sci. Rep.* **11**, 10540 (2021).

25. Ohlig, S. *et al.* Molecular diversity of diencephalic astrocytes reveals adult astrogenesis regulated by Smad4. *EMBO J.* (2021) doi:10.15252/embj.2020107532.

26. Batiuk, M. Y. *et al.* Identification of region-specific astrocyte subtypes at single cell resolution. *Nat. Commun.* **11**, (2020).

27. Sadick, J. S. *et al.* Astrocytes and oligodendrocytes undergo subtype-specific transcriptional changes in Alzheimer's disease. *Neuron* **110**, 1788-1805.e10 (2022).

28. Wu, Y. E., Pan, L., Zuo, Y., Li, X. & Hong, W. Detecting Activated Cell Populations Using Single-Cell RNA-Seq. *Neuron* **96**, 313-329.e6 (2017).

29. Choi, J. S. *et al.* Single-nucleus RNA sequencing of developing superior colliculus identifies neuronal diversity and candidate mediators of circuit assembly. *Cell Rep.* **42**, 113037 (2023).

30. Karpf, J. *et al.* Dentate gyrus astrocytes exhibit layer-specific molecular, morphological and physiological features. *Nat. Neurosci.* **25**, 1626–1638 (2022).

31. Langlieb, J. *et al.* The molecular cytoarchitecture of the adult mouse brain. *Nature* **624**, 333–342 (2023).

32. Zhang, M. *et al.* Molecularly defined and spatially resolved cell atlas of the whole mouse brain. *Nature* **624**, 343–354 (2023).

33. Shi, H. *et al.* Spatial atlas of the mouse central nervous system at molecular resolution. *Nature* **622**, 552–561 (2023).

34. Xie, Y. *et al.* Astrocyte-neuron crosstalk through Hedgehog signaling mediates cortical synapse development. *Cell Rep.* **38**, 110416 (2022).

35. Tan, C. X. *et al.* δ-Catenin controls astrocyte morphogenesis via layer-specific astrocyte–neuron cadherin interactions. *J. Cell Biol.* **222**, e202303138 (2023).

36. Skauli, N., Savchenko, E., Ottersen, O. P., Roybon, L. & Amiry-Moghaddam, M. Canonical Bone Morphogenetic Protein Signaling Regulates Expression of Aquaporin-4 and Its Anchoring Complex in Mouse Astrocytes. *Front. Cell. Neurosci.* **16**, 878154 (2022).

37. Massagué, J. & Sheppard, D. TGF-β signaling in health and disease. *Cell* **186**, 4007–4037 (2023).

38. Nakayama, N. *et al.* A Novel Chordin-like Protein Inhibitor for Bone Morphogenetic Proteins Expressed Preferentially in Mesenchymal Cell Lineages. *Dev. Biol.* **232**, 372–387 (2001).

39. Falcone, C. *et al.* Cortical interlaminar astrocytes across the therian mammal radiation. *J. Comp. Neurol.* **527**, 1654–1674 (2019).

40. Falcone, C. *et al.* Cortical Interlaminar Astrocytes Are Generated Prenatally, Mature Postnatally, and Express Unique Markers in Human and Nonhuman Primates. *Cereb. Cortex* **31**, 379–395 (2021).

41. Chierzi, S. *et al.* Astrocytes Transplanted during Early Postnatal Development Integrate, Mature, and Survive Long Term in Mouse Cortex. *J. Neurosci.* **43**, 1509–1529 (2023).

42. Wang, M. *et al.* Morphological diversification and functional maturation of human astrocytes in glia-enriched cortical organoid transplanted in mouse brain. *Nat. Biotechnol.* (2024) doi:10.1038/s41587-024-02157-8.

43. Zhang, Q. *et al.* EZH2/G9a interact to mediate drug resistance in non-small-cell lung cancer by regulating the SMAD4/ERK/c-Myc signaling axis. *Cell Rep.* **43**, 113714 (2024).

44. Segklia, A. *et al.* Bmp7 Regulates the Survival, Proliferation, and Neurogenic Properties of Neural Progenitor Cells during Corticogenesis in the Mouse. *PLoS ONE* **7**, e34088 (2012).

45. Choe, Y. & Pleasure, S. J. Meningeal Bmps Regulate Cortical Layer Formation. *Brain Plast.* **4**, 169–183 (2018).

46. Fernandez, L. S. Astrocyte CCN1 stabilizes neural circuits in the adult brain.

47. Kucukdereli, H. *et al.* Control of excitatory CNS synaptogenesis by astrocyte-secreted proteins Hevin and SPARC. *Proc. Natl. Acad. Sci.* **108**, (2011).

48. Jones, E. V., Bernardinelli, Y., Zarruk, J. G., Chierzi, S. & Murai, K. K. SPARC and GluA1-Containing AMPA Receptors Promote Neuronal Health Following CNS Injury. *Front. Cell. Neurosci.* **12**, 22 (2018).

49. Gottschling, C., Wegrzyn, D., Denecke, B. & Faissner, A. Elimination of the four extracellular matrix molecules tenascin-C, tenascin-R, brevican and neurocan alters the ratio of excitatory and inhibitory synapses. *Sci. Rep.* **9**, 13939 (2019).

Chapters 1-7, in part, have been submitted for publication. Deng J**,** Labarta-Bajo L, Brandebura AN, Kahn SB, Pinto AFM, Diedrich JK, Allen NJ (2024). Suppression of astrocyte BMP signaling improves fragile X syndrome molecular signatures and functional deficits. The dissertation author will be the first author of this publication, and Dr. Nicola Allen will be the senior author and principal investigator.

Chapter 6. Conclusions

In this dissertation, I investigated the role of astrocyte BMP signaling in the neurodevelopmental disorder fragile X syndrome (FXS) as well as in cortical astrocyte heterogeneity and development. I used mouse genetic tools to suppress astrocyte BMP signaling *in vivo*, and found this suppression improved several FXS molecular, functional, and behavioral phenotypes as well as affecting cortical astrocyte heterogeneity and development. I found that Smad4 cKO lessens severity of audiogenic seizures in FXS mice, did not affect FXS visual acuity or ocular dominance plasticity, and restored deficits in inhibitory synapses present in FXS auditory cortex. Using astrocyte-specific nuclear transcriptomics, I found that FXS-affected astrocytes have an overall hypermetabolic transcriptomic signature moderated by Smad4 cKO. I adapted a method to profile astrocyte secreted and membrane proteins *in vivo*, and identified that FXS-affected astrocytes have downregulated secreted proteins and secretory machinery such as clathrins and Golgi adaptor complex proteins, with these alterations minimized by Smad4 cKO. I also applied the transcriptomic and proteomic data to investigate the role of astrocyte BMP signaling in typical development and found that Smad4-dependent BMP signaling is necessary for spatially-segregated astrocyte transcriptomic variability and in particular pial astrocyte gene signatures, and that BMP signaling mediates aspects of astrocyte and cortical maturation such as aquaporin 4 expression and extracellular matrix component production. This thesis sheds light on the role of astrocyte BMP signaling in FXS phenotypes and neurotypical development, and provides leads on several astrocyte pathways that mechanistically connect BMP signaling to Fmr1 KO phenotype correction and thus represent candidates for targeted interventions. Overall, this dissertation demonstrates that an astrocyte signaling pathway mediates both aspects of typical development as well as molecular and functional changes in a genetic disorder.

Mechanisms underlying Smad4 cKO moderation of Fmr1 KO phenotypes

What pathways specifically mediate Smad4 cKO improvements to Fmr1 KO phenotypes of audiogenic seizure susceptibility and inhibitory synapse deficit (Chapter 2)? While hepaCAM, a regulator of inhibitory synaptogenesis,[1] is not changed in Fmr1 KO, Smad4 cKO leads to an increase in hepaCAM that could mitigate the Fmr1 KO baseline deficit in inhibitory synapses (**Figure 4.9D,E,F**). Alternatively, Smad4 cKO may act through the aggregated and/or interacting effects of multiple downstream actors. Indeed, secretory machinery as a whole is downregulated in Fmr1 KO (Chapter 4); by improving the Fmr1 KO deficit in secretory machinery, Smad4 cKO may help restore the levels of many secreted products. This may be analogous to what was observed *in vitro*, where BMP pathway suppression but not individual downstream protein targeting rescued Fmr1 KO neurite outgrowth.[2] Additionally, Smad4 cKO improvements to Fmr1 KO phenotypes could be secondary to Smad4 cKO moderation of Fmr1 KO astrocyte hypermetabolism (Chapter 3. Whether through specific proteins, improvements to astrocyte metabolism or secretion, or a combination of the above mechanisms, suppressing the BMP signaling pathway in astrocytes with Smad4 cKO can improve Fmr1 KO phenotypes.

Dysregulated BMP signaling in fragile X syndrome astrocytes

Previous studies have shown mice globally heterozygous for the BMP receptor Bmpr2 have a rescue in Fmr1 KO spine deficits,[3] cultured Fmr1 KO astrocytes have an elevated BMP signaling transcriptional signature,[2] and P7 cortical Fmr1 KO astrocytes have elevated canonical BMP signaling.[2] Cell-type-specific bulk and scRNAseq in P7 to P14 cortex show ongoing astrocyte BMP signaling capability (Bmpr1b enriched in astrocytes) and effect (Id3 enriched in astrocytes, vascular/leptomeningeal cell, and endothelial cells).[4,5] Surprisingly, in our astrocyte nuclear RNAseq at P26-28, we did not detect elevated expression of *Id* genes (BMP-induced) or

Smad9 (expected BMP pathway negative feedback inhibition) in Fmr1 KO.[6] However, further detailed examination of BMP-pathway related genes shows in Fmr1 KO a trending increase in the ligand *Bmp7* (L2FC +0.60, p-adj 0.11) which is restored to WT levels in FXS;Smad4cKO, as well as a significant increase in expression of Chrdl1 (WT to FXS L2FC +0.75, p-adj 0.027), which is a secreted protein that binds to and inhibits BMPs (**Tables S1,S2,S5**).[7] One hypothesis is that by P28, earlier elevations in astrocyte BMP signaling led to compensatory negative feedback such as upregulation of the inhibitor Chrdl1, resulting in normalized signaling. Within this model, earlier upregulation of astrocyte BMP signaling may still contribute to dysregulated formation of neuronal synapses and circuits. Moreover, the Smad4 cKO intervention, driven by a Cre driver line characterized to be active by P0-P7,[8] may still counteract the temporally restricted BMP signaling increase.

Future directions: astrocyte BMP signaling in fragile X syndrome

In this dissertation, I found that suppressing astrocyte BMP signaling could improve fragile X syndrome audiogenic seizures and outline potential mechanisms driving this effect. Future directions include fully parsing out mechanisms more clearly: if Smad4 cKO is increasing inhibitory synapses in FXS auditory cortex, how is it affecting interneuron maturation and function, and circuit function in FXS auditory cortex? Is hyperexcitability rescued? Smad4 cKO can affect proteins involved in both excitatory and inhibitory synapse formation and regulation (NRCAM, NCAN, HepaCAM, SPARC, and C3 among others, **Tables S2,S7**, Chapters 3 and 4). Do excitatory synapses also change in FXS;Smad4 cKO relative to FXS, and how does the excitation to inhibition ratio change overall? These exciting questions could be interrogated for example with immunohistochemsitry for the lectin wisteria floribunda agglutinin (WFA, a marker for glycosylation of perineuronal nets) and parvalbumin, as well as quantification of excitatory synapses (both Vglut1 and Vglut2) across cortical layers and regions, and electrophysiologic

recordings on inhibitory interneurons as well as excitatory pyramidal neurons in visual or auditory cortex.

Another question that arises from the differential effectiveness of Smad4 cKO in restoring Fmr1 KO auditory vs. visual phenotypes, is what underlies this differential rescue? Initial pilot experiments did not suggest a significantly different level of astrocyte BMP signaling in visual compared to auditory cortex (similar SMAD4 fluorescence intensity, similar ID3 fluorescence intensity), but previous studies found differential expression of BMP-induced genes *Tnc* and *Atoh8* between motor, somatosensory, and visual cortices (higher in visual cortex).[9] Additionally, the known BMP inhibitor Chrdl1 as well as other BMP pathway modifiers could have differential expression across brain regions.[10] To fully understand the levels of astrocyte BMP signaling at baseline across brain regions, spatial transcriptomics/proteomics experiments will be necessary.

Astrocyte metabolism (oxidative phosphorylation and glycolysis/gluconeogenesis) as well as astrocyte secretion emerged as Fmr1 KO dysregulated pathways improved by Smad4 cKO. The roles of these pathways in affecting Fmr1 KO neuronal function remain to be explored and may require specialized tools. For example, is astrocyte metabolic flux (oxidative phosphorylation, reactive oxygen species production, glucose flux) increased *in vivo*? Is this secondary to an overall increase in neuronal activity and Fmr1 KO hyperexcitability? And is the Smad4 cKO improvement also due to improvement in Fmr1 KO hyperexcitability, or is the BMP pathway acting cell-autonomously in astrocytes to control metabolism? What is the total magnitude of astrocyte secretory pathway activity and flux of secreted proteins, and is it lower in FXS and restored by Smad4 cKO? Answering these questions would require sophisticated tools for measuring metabolism/metabolic flux and secretory flux in a cell-type-specific manner *in vivo*.

Importantly, how translatable is this finding in a FXS mouse model to FXS patients? While this is ultimately a difficult question to answer without empirical evidence, Kashima et al. demonstrated that FXS patient frontal cortex had a three-fold increase in full-length BMPR2 protein by western blot, suggesting dysregulation of this pathway in FXS patients.[3] Moreover,

media taken from FXS patient iPSC-derived astrocytes produced aberrant firing in iPSC-derived neurons, highlighting a role for astrocytes in human FXS pathophysiology.[11] Further investigation of the BMP pathway in different models of FXS—for example, co-immunostaining for astrocytes and BMP-induced genes in FXS patient tissue, or probing levels of BMP pathway components and BMP-induced genes in FXS patient iPSC-derived cells or organoids—could illuminate the translatability of the findings in this dissertation. Another aspect of translatability is the relationship between FXS and other forms of autism spectrum disorder (ASD), both genetic and without known single-gene cause. Overlap at the level of both phenotypes and molecular pathways and genes/proteins disrupted in different forms of ASD[12–15] suggest a potential convergence in mechanisms including synaptic function as a key potential mediator of genetic vulnerability. Given the important role of astrocytes in synaptic formation and regulation, it will be exciting to see how astrocyte function (e.g. secreted proteins, metabolism, and other pathways found disrupted in Fmr1 KO in this dissertation) is altered in other forms of ASD.

Future directions: astrocyte BMP signaling in development

In this dissertation, I found that astrocyte BMP signaling affects expression of spatially segregating gene signatures, and that astrocyte BMP signaling may lead to cellular maturation. BMP signaling is crucial in embryonic development (BMP and SHH gradients pattern the spinal cord, disruptions to BMPs can be embryonic lethal),[16] but surprisingly little is known about BMP signaling in the CNS after birth. To better understand whether there is a gradient of BMP morphogen or signaling across postnatal cortex and other brain regions, and to fully understand all the players involved in secreting BMPs, BMP inhibitors, and receiving BMP signaling, spatial and single-cell technologies will be crucial. We hope that upcoming spatial transcriptomics (multiplexed error-robust fluorescence in situ hybridization or MERFISH) and single nuclear RNAseq experiments will help to elevate our fundamental understanding of this pathway, and the effect of Smad4 cKO and Chrdl1 cKO.

Perhaps the most striking finding in Chapter 5 is the almost complete abrogation of expression of pial astrocyte marker *Myoc* in Smad4 cKO. Based on the high degree of overlap between pial astrocyte-enriched genes and Smad4 cKO dysregulated genes (**Figure 5.3B**), BMP signaling likely is important to pial astrocyte function. What do pial astrocytes do? Again, surprisingly little is known, though simply due to their location, pial astrocytes likely play a role in barrier formation, protecting brain parenchyma from cerebrospinal fluid and external insults, whether ionic/osmotic dysregulation (pial astrocytes have enriched expression of Aqp4, Chapter 5 and Hasel et al. 2023)[17] or infectious/immune/traumatic injury. The finding that MYOC is also expressed specifically in human cortical pial astrocytes,[17] and our increasing understanding that mouse pial astrocytes have much more elaborate counterparts in human interlaminar astrocytes,[18–20] extend the relevance of BMP signaling in pial astrocytes to humans. Moreover, the fact that human iPSC derived-astrocytes transplanted into mouse cortex can adopt complex interlaminar-like morphology at the pia[21] strengthens the hypothesis that a local cue, such as BMP signaling, may trigger pial specialization. While the genetic manipulation of Smad4 cKO that we performed in mice could not be easily translated to humans, assaying for BMP pathway components and machinery in human pial tissue and/or CSF, or genetically modifying iPSC-astrocytes to be deficient in BMP signaling machinery then assaying their development and function, could help us further understand the human relevance of BMP signaling. Moreover, the molecular effects we found caused by astrocyte BMP signaling (at the synapse, in secreted proteins, etc.), could underlie the reports of astrocyte BMP effects observed in other disorders[22,23] and in response to acute injury.[24]

This dissertation represents a foray into the role of astrocyte BMP signaling. The proposed future directions, combined with new technologies and translational experiments, will hopefully allow us to better understand the many functions of the astrocytes in health and neurodevelopmental disorders, and to move towards better treatments for conditions such as FXS.

References

1. Baldwin, K. T. *et al.* HepaCAM controls astrocyte self-organization and coupling. *Neuron* **109**, 2427-2442.e10 (2021).

2. Caldwell, A. L. M. *et al.* Aberrant astrocyte protein secretion contributes to altered neuronal development in multiple models of neurodevelopmental disorders. *Nat Neurosci* **25**, 1163–1178 (2022).

3. Kashima, R. *et al.* Augmented noncanonical BMP type II receptor signaling mediates the synaptic abnormality of fragile X syndrome. *Science Signaling* **9**, ra58–ra58 (2016).

4. Zhang, Y. *et al.* An RNA-Sequencing Transcriptome and Splicing Database of Glia, Neurons, and Vascular Cells of the Cerebral Cortex. *Journal of Neuroscience* **34**, 11929–11947 (2014).

5. Farhy-Tselnicker, I. *et al.* Activity-dependent modulation of synapse-regulating genes in astrocytes. *eLife* **10**, e70514 (2021).

6. Katagiri, T. & Watabe, T. Bone Morphogenetic Proteins. *Cold Spring Harbor Perspectives in Biology* **8**, a021899 (2016).

7. Nakayama, N. *et al.* A Novel Chordin-like Protein Inhibitor for Bone Morphogenetic Proteins Expressed Preferentially in Mesenchymal Cell Lineages. *Developmental Biology* **232**, 372–387 (2001).

8. Farhy-Tselnicker, I. *et al.* Astrocyte-Secreted Glypican 4 Regulates Release of Neuronal Pentraxin 1 from Axons to Induce Functional Synapse Formation. *Neuron* **96**, 428-445.e13 (2017).

9. Boisvert, M. M., Erikson, G. A., Shokhirev, M. N. & Allen, N. J. The Aging Astrocyte Transcriptome from Multiple Regions of the Mouse Brain. *Cell Reports* **22**, 269–285 (2018).

10. Blanco-Suarez, E., Liu, T.-F., Kopelevich, A. & Allen, N. J. Astrocyte-Secreted Chordin-like 1 Drives Synapse Maturation and Limits Plasticity by Increasing Synaptic GluA2 AMPA Receptors. *Neuron* **100**, 1116-1132.e13 (2018).

11. Sharma, S. D. *et al.* Astrocytes mediate cell non-autonomous correction of aberrant firing in human FXS neurons. *Cell Reports* **42**, 112344 (2023).

12. The DDD Study *et al.* Synaptic, transcriptional and chromatin genes disrupted in autism. *Nature* **515**, 209–215 (2014).

13. Darnell, J. C. *et al.* FMRP Stalls Ribosomal Translocation on mRNAs Linked to Synaptic Function and Autism. *Cell* **146**, 247–261 (2011).

14. Willsey, H. R., Willsey, A. J., Wang, B. & State, M. W. Genomics, convergent neuroscience and progress in understanding autism spectrum disorder. *Nat Rev Neurosci* **23**, 323–341 (2022).

15. Autism Spectrum Disorder Working Group of the Psychiatric Genomics Consortium *et al.* Identification of common genetic risk variants for autism spectrum disorder. *Nature Genetics* **51**, 431–444 (2019).

16. Liu, A. & Niswander, L. A. Bone morphogenetic protein signalling and vertebrate nervous system development. *Nature Reviews Neuroscience* **6**, 945–954 (2005).

17. Hasel, P. *et al. Defining the Molecular Identity and Morphology of* Glia Limitans Superficialis *Astrocytes in Mouse and Human*. http://biorxiv.org/lookup/doi/10.1101/2023.04.06.535893 (2023) doi:10.1101/2023.04.06.535893.

18. Falcone, C. *et al.* Cortical interlaminar astrocytes across the therian mammal radiation. *J Comp Neurol* **527**, 1654–1674 (2019).

19. Falcone, C. *et al.* Cortical Interlaminar Astrocytes Are Generated Prenatally, Mature Postnatally, and Express Unique Markers in Human and Nonhuman Primates. *Cerebral Cortex* **31**, 379–395 (2021).

20. Falcone, C. *et al.* Redefining varicose projection astrocytes in primates. *Glia* **70**, 145–154 (2022).

21. Wang, M. *et al.* Morphological diversification and functional maturation of human astrocytes in glia-enriched cortical organoid transplanted in mouse brain. *Nat Biotechnol* (2024) doi:10.1038/s41587-024-02157-8.

22. Russo, K. & Wharton, K. A. BMP/TGF-B signaling as a modulator of neurodegeneration in ALS. *Developmental Dynamics* **251**, 10–25 (2022).

23. Linden, A. K., Affaneh, A., Kessler, J. A. & Peng, C. Age-Related Enhanced BMP Signaling Elicits APOE-Isoform Dependent Effects in IPSC Model of Alzheimer's Disease. *Alzheimer's & Dementia* **19**, e082494 (2023).

24. Divolis, G. *et al.* Activation of both transforming growth factor-β and bone morphogenetic protein signalling pathways upon traumatic brain injury restrains pro-inflammatory and boosts tissue reparatory responses of reactive astrocytes and microglia. *Brain Communications* **1**, fcz028 (2019).

Chapters 1-7, in part, have been submitted for publication. Deng J**,** Labarta-Bajo L, Brandebura AN, Kahn SB, Pinto AFM, Diedrich JK, Allen NJ (2024). Suppression of astrocyte BMP signaling improves fragile X syndrome molecular signatures and functional deficits. The dissertation author will be the first author of this publication, and Dr. Nicola Allen will be the senior author and principal investigator.

Chapter 7. Methods

Experimental model details

Mice

All animal work was approved by the Institutional Animal Care and Use Committee (IACUC) of the Salk Institute for Biological Studies. Mice were housed in the Salk Institute Animal Resources Department on a light cycle of 12 hours light:12 hours dark with access to food and water *ad libitum*. For experiments using developmental timepoints, littermates were used.

Fmr1 KO mice

B6.129P2-Fmr1tm1Cgr/J (Jax: 003890) line Fmr1 WT and KO male mice were used for experiments. We used male mice because female FXS patients (and mice) are heterozygous and mosaic for the *FMR1* gene due to random X inactivation, leading to less severe and more variable clinical manifestations.[1] Hemizygous male to heterozygous female crosses were used. The line was maintained on a C57Bl6/J background.

Fmr1 KO x Smad4 fl/fl x Gfap-Cre mice

The Fmr1 KO line was crossed to Smad4tm2.1Cxd/J (Smad4 fl/fl, Jax: 017462)[2] and B6.Cg-Tg(Gfap-Cre)73.12Mvs/J (Jax: 012886)[3] lines to remove Smad4 from astrocytes (Smad4 cKO). Experimental mice were obtained from three types of breeding: (1) Fmr1 WT;Smad4 fl/fl male x Fmr1 WT;Smad4 fl/fl;Gfap-Cre+ females to generate Fmr1 WT;Smad4 WT (referred to as WT) and Fmr1 WT;Smad4 cKO (referred to as WT;Smad4cKO) male littermate pairs (2) Fmr1 WT;Smad4 fl/fl male x Fmr1 KO;Smad4 fl/fl;Gfap-Cre+ females to generate Fmr1 KO;Smad4 WT (referred to as FXS) and Fmr1 KO;Smad4 cKO (referred to as FXS;Smad4cKO) male littermate pairs and (3) Fmr1 KO;Smad4 fl/fl male x Fmr1 het;Smad4 fl/fl;Gfap-Cre+ female to generate all

four of the above genotypes as well as Fmr1 KO females for line maintenance. The line was maintained on a C57Bl6/J background. For all FXS phenotype rescue experiments (in Chapters 2, 3, 4), we used male mice. For Smad4 cKO validation and other experiments in WT (Chapter 5), we used both male and female mice.

Chrdl1 KO mice

We used the Chrd1 KO germline KO mouse line generated and described in Blanco-Suarez et al., 2018.[4] The line was maintained on a C57Bl6/J background. All experiments were performed using male Chrdl1 KO (-/y) and WT (+/y) littermates.

Cell cultures

Primary astrocyte cultures

Astrocytes were obtained from the cerebral cortex of P1-2 Sprague Dawley rats (Charles River) as previously described[4–6] for the immunocytochemistry testing, or from cerebral cortex of P0-2 C57Bl6/J background mice for the proteomic experiment. Cortices of 4 mice or rats were dissociated using papain and plated on 75-cm2 tissue culture flasks coated with poly-D-lysine (Sigma P6407), then maintained in culture for 4 days in growth medium (DMEM (Thermo Fisher Scientific 11960044) supplemented with 10% heat inactivated FBS (Thermo Fisher Scientific 10437028), Penicillin-Streptomycin (Thermo Fisher Scientific 15140-122), glutamax (Thermo Fisher Scientific 35050-061), sodium pyruvate (Thermo Fisher Scientific 11360-070), hydrocortisone (Sigma H0888), and N-acetyl-L-cysteine (Sigma A8199)). Astrocytes form a monolayer adherent to the flask bottom (McCarthy and de Vellis, 1980), and after 3 days, flasks were shaken vigorously to remove non-adherent cells on overgrown layers. Two days later AraC (working concentration 10 mM; Sigma C1768) was added for 48 hr in order to inhibit proliferation and kill rapidly proliferating cells such as oligodendrocyte precursor cells and microglia. After two

more days, astrocyte-enriched cells were dissociated from the flask with trypsin, then plated on 10 or 15 cm tissue culture dishes and maintained in the growth media described above. Cells were passaged once a week and cultures were maintained for no longer than 4 weeks. Astrocyte cultures were maintained in a humidified incubator at 37C and 10% CO2.

Method Details

Tissue collection

Mice were deeply anesthetized with intraperitoneal injection of a mixture of 100 mg/kg Ketamine (Victor Medical Company 1699053) and 20 mg/kg Xylazine (Victor Medical Company 1264078). For acute astrocyte isolation and for fresh tissue collection for transcriptomics, proteomics, and western blotting experiments, cortices were dissected immediately following deep anesthesia and cervical dislocation. For fixed tissue collection for histological experiments, mice were transcardially perfused first with RT PBS followed by 4% PFA. The brains were rapidly dissected and post-fixed overnight in 4% PFA (Electron Microscopy Sciences 19210) at 4C. After 16-24 hours the brains were moved to 30% sucrose for 48-72 hours. The brains were then embedded in TFM (Electron Microscopy Sciences 72593) and frozen in a dry ice/ethanol slurry and stored at -80C until use.

Acute astrocyte isolation

Astrocytes were acutely isolated from P14 mouse cortex with a protocol modified from that described in Brandebura et al., 2023.[7] Dissected cortices were cut into ~1mm^3 pieces using a razor blade to allow for optimal enzymatic digestion. Papain digestion was performed according to kit instructions (Miltenyi MACS Neural Tissue Dissociation Kit 130-092-628). Digestion was performed using the gentleMACS Octo Dissociator with Heaters (Miltenyi 130-096-427) using the 37C_NTDK program. Cells were centrifuged at 4C 300 g for 10 minutes and then resuspended in

AstroMACS buffer and passed through a 70-um basket filter to remove clumps. Astrocytes were subsequently isolated using the Miltenyi MACS Anti-ACSA-2 Microbead kit (Miltenyi 130-097-678) according to the manufacturer's instructions, with modifications to deplete debris and microglial cells prior to positive astrocyte selection. Debris was removed with the Debris Removal Solution (Miltenyi 130-109-398), following manufacturer instructions, then the depleted solution was diluted to 15mL in cold DPBS and centrifuged at 1000g 4C 10 minutes. Microglia depletion was performed using anti-CD11b beads (Miltenyi 130-093-634) for an incubation period of 10 minutes at 4C. The flow-through from the MS magnetic column was collected and centrifuged again at 4C 300 g to remove excess beads. The supernatant was collected and subsequent positive selection for astrocytes was performed. First a 10-minute incubation with FcR blocking beads was used to minimize any nonspecific binding. ACSA2-conjugated beads were then used to positively select for astrocytes during a 15-minute incubation period at 4C (FcR and ACSA2 beads in kit, Miltenyi 130-097-678). Bound astrocytes were plunged into a new tube with AstroMACS buffer and centrifuged again at 4C 300 g 10min to remove excess beads. The astrocytes were divided and frozen at -80C either in lysis solution (for subsequent Western blotting; Pierce RIPA with 1:100 phosphatase and protease inhibitors) or as a pellet (for subsequent DNA extraction).

Western blotting

Western blotting was performed on acutely isolated astrocytes to validate Smad4 cKO, on proteomics samples to validate biotinylation, and on cortical lysates to validate brevican and hepaCAM proteomics data. Acute astrocytes frozen in lysis buffer were thawed, homogenized with pellet mixer (VWR 47747-370), and spun down (13200 rpm, 20min, 4C). For cortical lysates, one cortex was homogenized with the pellet mixer in lysis buffer (Pierce RIPA with 1:100 phosphatase and protease inhibitors), allowed to rotate for 1hr at 4C, then spun down (20000g,

15min, 4C). The concentration of the supernatant was quantified with BCA (Thermo 23227), and 25ug acute astrocyte protein or 20ug cortical lysate were used per sample.

Samples were prepared with reducing sample buffer (Thermo Fisher Scientific 39000) and boiled for 10 min at 95C (acute astrocytes and lysates for ER-TurboID validation) or 45 min at 55 C (cortical lysates). Proteins were separated on Bolt 12% Bis-Tris Plus gels (NW00120BOX) for 1 hr at constant voltage of 130V. Proteins were transferred onto Immobilion-FL PVDF membranes (Millipore IPFL00010) 100V 60min for acute astrocytes, or onto Amersham Hybond 0.2um PVDF membranes (Cytiva 10-6000-22) at 80V for 120min; in solution of Tris-Glycine Buffer (Thermo Fisher Scientific 28363). Membranes were blocked for 1 hr at room temperature in gentle shaking with blocking buffer (0.1% Casein (BioRad 1610782) in Tris Buffered Saline). Membranes were incubated overnight at 4C in gentle shaking with the primary antibody in blocking buffer, rabbit anti-SMAD4 1:1000 (Millipore ABE21), mouse anti-BCAN 1:4000 (BD Biosciences 610894), rabbit anti-HepaCAM 1:3000 (Novus NBP3-04983), mouse anti-beta-Actin 1:5000 (Millipore Sigma A1978**)**, mouse anti-TUBB3 1:5000 (BioLegend 801201), rabbit anti-Actin 1:5000 (Cell Signaling Technology 4968), or Rb anti-SOX9 1:2000 (Abcam AB185966). Membranes were washed with TBS+0.1% Tween and incubated for 1 hr at room temperature with secondary antibody goat anti-mouse Alexa 680 (1:10000, Thermo Fisher Scientific A21058), goat anti-rabbit Alexa 680 (1:10000, Thermo Fisher Scientific A21109), and goat anti-mouse DyLight 800 (1:10000, Invitrogen SA535521). For ER-TurboID validation western, no primary step was performed, and membrane blocking was followed immediately by washes and secondary (1:3000, IRDye 680RD Streptavidin). Membranes were washed with TBS+0.1% Tween, and immediately imaged on Odyssey Infrared Imager (Li-Cor) and Image Studio v5.2 software (Li-Cor). Molecular weights were visualized using Precision Plus All Blue Protein standard loading dye (BioRad 1610373) or PageRuler (Thermo 26616). Analysis of band signal intensity was done in Image Studio v5.2 software (Li-Cor). For SMAD4, signal was normalized to SOX9 intensity in different lanes the same blot (cut membrane); for BCAN, signal was normalized to Actin intensity in the

same lane of the same blot (cut membrane); for HepaCAM, signal was normalized to Actin intensity in the same lane of the same blot (HepaCAM in 680 channel, Actin in 800 channel).

DNA extraction and PCR

For validation of Smad4 cKO recombination at the Smad4 exon 9 locus, DNA was isolated from acutely isolated astrocytes and PCR for the recombined product was performed. DNA was isolated with the DNeasy blood and tissue kit (Qiagen 69504), following manufacturer instructions. PCR was performed using SYBR green PCR mastermix (Life Supply 4309155) and the below primers from those used by the creators of the Smad4 fl/fl line[2] with modifications to align with the mm10 genome:

Forward (5' to 3'): taagagccacagggtcaagc

Reverse (5' to 3'): gacccaaacgtcaccttcac

PCR products were run on a 1.5% agarose gel with expected band size of 500bp in the recombined sequence and no band expected in WT.

Immunohistochemistry and Analysis: Smad4 cKO validation

The cell type specificity of Smad4 cKO was evaluated with immunohistochemistry (IHC) for SMAD4, SOX9, and NEUN. Validation of suppression of BMP signaling in astrocytes was performed by IHC for ID3 and SOX9. Sagittal brain sections of 16 um were obtained from littermate WT and WT;Smad4 cKO mice (1.8mm lateral from midline) using a cryostat (Hacker Industries OTF5000). Sections were on Superfrost Plus micro slides (VWR 48311-703) for this as well as all other experiments involving cryosectioning. Slices were blocked and permeabilized in blocking buffer (10% donkey serum (Jackson ImmunoResearch 017-000-121) in PBS with 0.3% Triton and 100mM L-lysine) for one hour at room temperature. Primary antibodies were diluted in antibody dilution solution (5% donkey serum in PBS with 0.3% Triton and 100mM lysine) and stained overnight in a humidified chamber at 4C. Antibodies for the astrocyte marker SOX9

(1:100, Goat, R&D AF3075), neuronal marker NEUN (1:200, mouse, EMD Millipore MAB377), SMAD4 (1:250, rabbit, Millipore ABE21), and ID3 (1:200, rabbit, CST9837S) were used. The next day sections were washed three times in PBS with 0.2% Triton for 5, 10 and 15 minutes. Secondary antibody labeling was performed in antibody solution (5% donkey serum in PBS with 0.3% Triton and 100mM lysine) and for two hours at room temperature. Appropriate secondary antibodies were used (Donkey anti-goat Alexa 488, Donkey anti-rabbit Alexa 568, Donkey anti-mouse Alexa 647). Washes in PBS with 0.2% Triton were performed three times for 5, 10 and 15 minutes. DAPI was applied (1:1000) for 5 minutes followed by a PBS wash. Coverslips were mounted with SlowFADE Gold Antifade Mountant with DAPI (Invitrogen S36939).

Smad4 validation IHC was imaged on an LSM700 confocal with 40x oil-immersion objective (numerical aperture = 1.3) as 16-bit images, as a z-stack of 8 steps of 0.4um each spanning 2.8um. Images were collected as tiles (12 tiles for cortex, consisting of 6143 x 2047 pixels spanning L1 to L5-L6, 4 tiles for colliculi and medial geniculate nucleus (MGN) of the thalamus, consisting of 2047 x 2047 pixels, all with 0.16um x 0.16um pixel size). Analysis was performed using Imaris software (Bitplane) and the ImageJ LabKit plug in to automate detection of SOX9+ and NEUN+ nuclei, within which SMAD4 fluorescence intensity was quantified. Within each experiment (littermate pair), the combined distribution of nuclei SMAD4 intensities was used to assign a single threshold for SMAD4 positivity at a local minimum in the SMAD4 intensity distribution. Cells below the threshold were visually inspected and compared to surrounding parenchymal intensity to confirm lack of SMAD4 positivity.

ID3 IHC was imaged on an AxioImager Z.2 with Apotome module with 20x objective (numerical aperture = 0.8) as 14-bit images as 6 tiles spanning all layers of cortex and white matter (3887 x 1975 pixels, 0.323um x 0.323um per pixel), as a z-stack of 4 steps of 2um each with total thickness 6um. Analysis was performed using Imaris software (Bitplane) with the surfaces tool to automate detection of SOX9+ nuclei, within which ID3 intensity was quantified,

with layer stratification performed using DAPI staining. Images shown in **Figure 2.1C,2.2E,G** and **Figure 5.2D, 5.9A** are maximum intensity projections.

Immunohistochemistry and Analysis: Smad4 cKO model characterization

To quantify cortical density of S100B+ cells, immunohistochemistry was performed as above on sagittal slices from WT and WT;Smad4cKO littermate pairs, with primary antibody astrocyte marker S100B (1:500, Abcam 52642). Following imaging under the same parameters as for SMAD4 IHC above, S100B density was quantified with ImageJ using the cell counter plug-in and counting only S100B cell bodies colocalized with DAPI. Manual separation of layers was performed with visualization by DAPI. DAPI density was quantified with Imaris software (Bitplane), with automated surface creation with parameters: smoothing 0.313um, diameter 5um, threshold intensity 30, volume filtered 50 to 750 um^3, automatic seeding with predicted distance 5um. Separation by layer was performed using DAPI staining. Images shown in **Figure 2.4A,E** are maximum intensity projections.

Behavioral analysis

Behavioral testing was performed in the Salk Institute's In Vivo Scientific Services (Animal Resources Department). All behavioral tests were performed blinded to genotype.

Audiogenic Seizure Assay

The audiogenic seizure assay was performed at P20-P23, when Fmr1 KO mice are reported to have high susceptibility.[8] Mice were transported to the IVSS behavior core and allowed 30min to adapt to the low level of ambient noise (~40dB). Mice were then individually taken to a separate soundproofed room and placed in a sound-proofed chamber equipped with light, video camera, plexiglass box (7.5 x 11.5 x 5 inches), and alarm (115-125dB, Kosin Safe Sound Personal Alarm). After a 5-minute habituation period, the alarm was played for 2 minutes, with video recording throughout. Each mouse would then be scored numerically as 0 (no seizure activity), 1

(convulsive activity), and 2 (respiratory failure) for the maximum degree of severity reached during the 2-minute period. Others have reported a scale of 0-3 including a stage for wild running that precedes convulsive activity;[9] in our data, we found every mouse that had wild running progressed further to convulsive activity. Testing was always performed on all littermates in one session, blind to genotype.

Optomotor Assay

The optomotor assay was performed at age P26 with a setup from CerebralMechanics (2004) (elevated platform 5cm above top and bottom mirrors with drifting gratings at 12deg/sec created through four computer monitors encircling the platform) and software from Optomotry VR, with settings as staircase method from 0.042 cycles/deg to 0.5 cycles/deg, scoring both clockwise and counter-clockwise visual acuity. The average of these two readings was the reported visual acuity value for all data and figures in this manuscript. This setup and procedure is described in further detail by Prusky et al, 2004.[10] Mice were always tested in Fmr1 WT/KO or Cre +/- pairs, blind to genotype.

Monocular visual enucleation and Arc Analysis

Littermate WT and Fmr1 KO mice as well as littermate FXS and FXS;Smad4 cKO mice at P28 (within visual critical period) were used for these experiments, which were performed as described previously.[4,11] Mice were anesthetized with 2% isofluorane in oxygen by constant flow via nose cone. The right eye was removed by transecting the optic nerve. Gelfoam (Pfizer 031508) was placed in the empty ocular cavity. Eyelids were sutured using 6-0 silk sutures (Henry Schein 101-2636). Lidocaine 2% and erythromycin 0.5% were applied topically on the sutured eyelids. Normal rearing (NR) mice were collected 12 hr later. Mice for monocular enucleation (ME) analysis were subjected to a 12 hr light/12 hr dark cycle every day until collection 4 days later, at P32. Prior to collection, mice were exposed to light for 30 min in the alert condition to activate neurons in the visual cortex and induce expression of Arc. Mice were anesthetized with a mixture

of 100 mg/kg Ketamine (Victor Medical Company 1699053) and 20 mg/kg Xylazine (Victor Medical Company 1264078) and brains removed. Brains were coronally sectioned in half and the posterior brain collected and embedded in OCT (Scigen 4583), frozen in dry ice/ethanol, and stored at -80C.

Single molecule fluorescent *in situ* hybridization (smFISH)

Littermate WT and Fmr1 KO male mice as well as littermate FXS and FXS;Smad4 cKO male mice at P28 (within visual critical period) that underwent monocular enucleation were used to analyze *Arc* expression to characterize ocular dominance plasticity, with modifications from protocols described previously.[4,11] All sections were made using a cryostat (Hacker Industries OTF5000) at a slice thickness of 16 mm, 3.40 mm posterior to Bregma for coronal sectioning. Fluorescent (FISH) (ACDbio 320851 for V1, used for Fmr1 KO vs. WT; 323100 for V2 used for FXS vs. FXS;Smad4 cKO) *in situ* hybridizations were performed following manufacturer's instructions for fresh frozen tissue, with the following modifications. For V1, tissue was treated with Protease 4 for 12min at RT, and *Arc* probe (ACDbio 316911) was conjugated to the 550 channel with AltB, and SlowFade gold antifade mountant with DAPI was applied to every section. For V2, tissue was treated according to manufacturer instructions with the following modifications. Slides were fixed by immersing in prechilled 4% PFA in PBS for 60min at 4C, after dehydration slides were baked at 37C for 30min, Protease III was applied for 15min at RT, *Arc* probe was diluted by 50% with ACDBio probe diluent (ACDBio: 300041), and Opal fluorophore 570 (Akoya FP1488001KT) was used at 1:5000 dilution. Coverslips 22 mm X 50 mm 1.5 thickness were placed on top of the sections and sealed with nail polish. In control experiments a negative control probe was used (ACDBio 310043) to determine the level of background signal. A minimum of 4 animals were used per condition, and 2 brain sections per animal. For Arc visualization, coronal sections were imaged using fluorescence microscope Zeiss Axio Imager.Z2 at 10X magnification as 14-bit images of 100-200 tiles. Arc was imaged in channel 550. Zen blue edition software

(Zeiss) distance tool was used to measure the width of the Arc activated brain region along layer 4 of the visual cortex, contralateral to the removed eye. 2-8 brain sections were measured per mouse. Analysis was performed blind to genotype.

Immunohistochemical synaptic staining, imaging and analysis

Littermate WT and WT;Smad4 cKO pairs and littermate FXS and FXS;Smad4 cKO pairs were used for experiments, and 8 independent experiments were performed, each with one mouse of each genotype (biological replicates) processed in parallel and blind to genotype from sectioning onwards. Coronal brain sections of PFA-fixed tissue of 18 um thickness were obtained using a cryostat (Hacker Industries OTF5000) (2.7mm posterior to bregma). Slices were blocked and permeabilized in blocking buffer (10% goat serum in PBS with 0.3% Triton and 100mM L-lysine) for one hour at room temperature. Primary antibodies were diluted in antibody dilution solution (5% goat serum in PBS with 0.3% Triton and 100mM lysine) and stained overnight in a humidified chamber at 4C. The antibody used for pre-synaptic Vgat was Synaptic systems 131004 guinea pig polyclonal anti-Vgat (1:250), and for post-synaptic gephyrin was (1:500, rabbit monoclonal, synaptic systems cat #147008). The next day the slides were washed in PBS with 0.2% Triton 3 times, for 5 minutes. Appropriate secondary antibodies were used in antibody dilution solution (goat anti-guinea pig Alexa 594 and goat anti-rabbit Alexa 488). Secondary antibodies were applied for two hours at room temperature followed by three washes of 5, 10 and 15 minutes in PBS with 0.2% Triton. DAPI was applied (1:1000) for five minutes followed by a PBS wash. Coverslips were mounted with SlowFade Gold Antifade Mountant with DAPI (Invitrogen, S36939). As negative controls, the primary antibodies were omitted and the brain slices were incubated with just secondary antibodies. Images were obtained using a 63x objective (numerical aperture = 1.4) with 1.8x zoom on an LSM 880 confocal microscope with Airyscan module using super-resolution mode at 1764 x 1764 pixels, 0.04um x 0.04um pixel size, as an 8-bit image (16-bit after Airyscan processing). The laser settings and gain were maintained constant

for all experiments. Z-stacks of 0.18 um increments were obtained in Layer 2/3 with a total of 20 z-steps per image, from a depth of 2.7um to 6.3um from tissue surface. Within each experiment, each mouse was imaged and analyzed on 2-5 independent brain sections (technical replicates) that were then averaged per mouse. Quantification of colocalized puncta was performed as previously described using the Imaris software (Bitplane) spots tool and the colocalization algorithm[10,31,42]. Spot sizes were set to 0.35 um for Vgat puncta and 0.3 um for Gephyrin puncta with a center-to-center colocalization distance of 0.6 um. Thus spots from the two channels that were within 0.6 um from each other's center were quantified as a synapse. Quality threshold for puncta detection was maintained constant within each experiment. Images shown in **Figure 2.7A** are maximum orthogonal projections of the 20 z-steps.

Glyoxal-fixed astrocyte nuclei transcriptomics

Sample preparation

Samples for transcriptomics were prepared as in Labarta-Bajo et al., 2023.[12] Each sample consisted of two cortices from one mouse; mice were processed from tissue collection to fluorescence-activated nuclei sorting (FANS) in littermate Cre+/- pairs, then nuclear lysates were stored in RLT at -80C. All samples were then thawed and processed in parallel from RNA extraction to sequencing. Samples were from the four genotypes WT, WT;Smad4 cKO, FXS, FXS;Smad4 cKO, with 4 to 6 mice per genotype as biological replicates.

Nuclei preparation

Nuclei were isolated from freshly collected cortex tissue of P26-28 mice. Cortices were dissected into fragments approximately 9 mm^3 in size and placed in glyoxal acidic solution (3% w/v glyoxal [Millipore Sigma 128465], 20% ethanol [Fisher BP2818100], 0.75% acetic acid [Millipore Sigma A6283], 5mM NaOH [Millipore Sigma 72068], in ddH2O) for 15min at 4C. Tissue

was manually homogenized using a two-step Dounce homogenizer (A and B) (Sigma #D9063) in NIMT buffer (in mM: 250 sucrose, 25 KCl, 5 MgCl2, 10 Tris-Cl pH 8, 1 DTT; 1:100 dilution of 10% Triton X100 and protease inhibitor [Halt 78429]) on ice. Homogenized samples were mixed with 50% iodixanol (OptiPrep Density Gradient Medium; Sigma #D1556) and loaded onto 25% iodixanol cushion, and centrifuged at 10,000 g for 20 min at 4°C in a swinging bucket rotor (Sorval HS-4). Pellets resuspended in ice-cold DPBS with 1% w/v BSA (referred to as PBS+BSA). Nuclei were then incubated for 7 min on ice with Hoechst 33342 solution (2 mM) (Thermo #62249) (final concentration 5 μM), followed by centrifugation at 1000 g for 5 min at 4° C to pellet nuclei. Pellets were resuspended in blocking buffer containing DPBS+BSA with NEUN-Alexa488 pre-conjugated antibody (Millipore #MAB377X) at 1:1000 dilution along with SOX9 rabbit antibody (Abcam AB185966) at 1:200, and incubated for one hour. Following centrifugation at 1000 g for 5 min at 4° C to pellet nuclei, pellets were resuspended in PBS+BSA with Goat anti-Rabbit-Alexa647 at 1:200 dilution for one hour. Tubes were centrifuged at 1000g for 5 min at 4C then resuspended in 500ul PBS+BSA.

Flow cytometry and RNA extraction

FANS was performed in the Salk Institute Flow Cytometry core using a BD FACS Aria Fusion sorter with PBS for sheath fluid (a 70 μm nozzle was used for these experiments). Hoechst-positive nuclei were gated first (fluorescence measured in the BV421 channel), followed by exclusion of debris using forward and side scatter pulse area parameters (FSC-A and SSC-A), exclusion of aggregates using pulse width (FSC-W and SSC-W), before gating populations based on SOX9 and NEUN fluorescence (using the APC and FITC channels). To isolate the astrocyte population, nuclei devoid of FITC signal (NEUN-) but with APC signal (SOX9+) were collected (**Figure 3.2A**). Nuclei were purified using a one-drop single-cell sort mode (for counting accuracy); these were directly deposited into a 1.5 ml Eppendorf with 300ul PBS+BSA preloaded. Approximately 200,000 nuclei were collected per mouse (range: 115k to 276k). After sorting each

mouse, the four collected samples (SOX9+NEUN-, SOX9-NEUN-, SOX9+NEUN+, SOX9-NEUN+) were each checked for purity using the same gates. Illustrations of gating strategy and post-sort purity were created with FlowJo v10.10.0. Immediately after sorting, nuclei were centrifuged at 1000g for 5 min at 4C, then resuspended in RLT buffer with added β-mercaptoethanol (Sigma M3148), then frozen at -80C.

RNA was extracted from FANS-sorted nuclei using the RNeasy micro kit (QIAgen 74104). The homogenate was thawed at RT then RNA was extracted according to manufacturer instructions, with on-column DNase digestion and elution in 14ul water at 65C.

RNAseq

RNA sequencing libraries were generated using the Illumina Ribo-Zero Plus rRNA Depletion Kit with IDT for Illumina RNA UD Indexes (Illumina, San Diego, CA). Samples were processed following manufacturer's instructions. Average input RNA per sample as measured by TapeStation was 79ng (range: 26-203 ng). Samples with TapeStation traces indicating degraded RNA were not sequenced. Resulting libraries were multiplexed and sequenced with 100 basepair (bp) Paired End (PE100) to an average depth of 25 million reads per sample (range of 19 million to 39 million reads) on an Illumina NovaSeq 6000. Samples were demuxltiplexed using bcl2fastq v2.20 Conversion Software (Illumina, San Diego, CA).

RNAseq analysis

RNAseq sequencing data was mapped with STAR v2.5.3a to the mm10 genome, FASTQ and STAR alignment files were quality tested with MultiQC v1.0.dev0[13] (average uniquely mapped reads 87.7%, range 85.1% to 91.2%). Genes were called with Homer v4.10.4 (range 17 to 35 million mapped tags per sample).[14] Differential analysis was conducted with DESeq2 (v1.38.3),[15] with differentially expressed gene criteria as follows: average TPM>1 in WT samples, Benjamini-Hochberg (BH) adjusted p-value < 0.05, |fold change (FC)| > 1.5. Heatmaps were created using

R (v4.2.2) via RStudio (2022.12.0) using the Pheatmap package and Graphpad Prism (v8.0). Volcano plots were created with package ggplot2 (v3.4.0). Gene set enrichment analysis (GSEA) was performed to detect which pathways and gene sets were enriched in Fmr1 KO and Smad4 cKO using the package ClusterProfiler (v4.6.0).[16] The following gene sets from mouse MSigDB[17] were used: hallmark pathways, canonical pathways (including Reactome,[18] KEGG,[19] Wikipathways,[20] and BioCarta[21]), and gene ontology.[22,23] Genes with TPM>1 in every sample were used for GSEA, with ranking based on sign(L2FC)*-log10(p-value), for each comparison. Highlighted pathways in visualization are top three down- and upregulated (highest and lowest NES) hallmark pathways in each comparison (**Figure 3.4E**). For testing for overlap of known FMRP targets with up- and down-regulated genes in Fmr1 KO (Comparison 1), the list of 842 genes from Darnell et al. 2011 was used,[24] and statistics by Fisher's exact test with genome size 24,252 protein-coding *M. Musculus* genes. Layer-based gene set GSEA was performed using the set of pial astrocyte-enriched genes from Hasel et al., 2023[25] and sets of L2-4 astrocyte and L5-6 astrocyte-enriched genes from Lanjakornsiripan et al., 2018.[26]

ER-TurboID Proteomics

Cloning of plasmids for viral vectors

The pAAV-TBG-Cyto-TurboID, pAAV-TBG-ER-TurboID, Sec61b-V5-TurboID, and C1(1-29)-TurboID-V5_pCDNA3 vectors were obtained from Addgene (149414, 149415, 166971, 107173.[27–29] Each were separately inserted into pZac2.1 GfaABC1D-tdTomato vector obtained from Addgene (#44332)[30] after removing tdTomato sequence. The In-Fusion HD cloning kit (Takara 638909) was used according to the manufacturer's instructions. The GfaABC1D-tdTom vector was linearized at NheI and NotI (New England Biolabs R3131S, R1089S) restriction sites for three hours at 37C and the linearized vector was purified from an agarose gel and cleaned

using Nucleospin columns (Macherey-Nagel 740609.50). The C1(1-29)-TurboID, Cyto-TurboID, ER-TurboID, and Sec61b-V5-TurboID cDNA were PCR amplified.

For the Cyto-TurboID, a cytosine was added before the start codon, and an HA tag and Ala Ser linker were added before the TurboID sequence, using the below primer sequences with 15-18bp overlapping sequences to the linearized vector:

Forward (5' to 3'): CTC ACT ATA GGC TAG CGC CGC CAT GTA TCC GTA TGA TGT TCC GGA TTA TGC AGC TAG CAA AGA CAA TAC TGT GCC T

Reverse (5' to 3'): GCT CGA AGC GGC CGC TTA GTC CAG GGT CAG GCG CTC CAG GG

For the ER-TurboID, the below primer sequences with 17bp overlapping sequences to the linearized vector were used:

Forward (5' to 3'): ACT CAC TAT AGG CTA GCG CCA CCA TGG AGA CAG AC

Reverse (5' to 3'): CTG CTC GAA GCG GCC GCT TAG AGT TCA TCT TTG GTG CTG TCC AG

For Sec61-V5-TurboID, GCCACC was added before the Sec61b sequence and Ala Ser and an HA tag were added before the stop codon, using the below primer sequences with 15-18bp overlapping sequences to the linearized vector:

Forward (5' to 3'): TCA CTA TAG GCT AGC GCC ACC ATG CCT GGT CCG ACC CC

Reverse (5' to 3'): CTC GAA GCG GCC GCT TAT GCA TAA TCC GGA ACA TCA TAC GGA TAG CTA GCC TTT TCG GCA GAC CGC A

The PCR product was subsequently gel purified and cleaned with the Nucleospin columns. The In-Fusion HD cloning enzyme premix was used to insert the above four amplified sequences into the vector.

The C1(1-29)-TurboID was cloned into the GfaABC1D-tdTom vector using the same procedure, but with KpnI HF and XhoI restriction enzymes (R3142S, R0146S). The primer sequences used are as follows:

Forward (5' to 3'): ctcactataggctagcgccaccatgga

Reverse (5' to 3'): ctcgaagcggccgcctatgcataatc

Stellar competent E. Coli cells (Takara 636763) were then transformed with the plasmids via heat-shock according to the manufacturer's instructions. Bacteria were screened using carbenicillin resistance (100 ug/mL; Teknova C2130). The colonies were expanded in an overnight LB culture. The DNA was purified using an endotoxin-free plasmid MaxiPrep kit according to the manufacturer's instructions (Qiagen 12362). Newly created constructs were sequenced with Eton sequencing (all constructs) as well as Primordium labs (ER-TurboID) to confirm desired product prior to following experiments.

Immunocytochemistry to assay subcellular localization via morphology

Two days after passaging into a 24-well plate, when the cultured rat astrocytes appeared 95% confluent, they were transfected with plasmid: either control CAG-GFP, GfaABC1D-C1(1-29)-TurboID, GfaABC1D-cyto-TurboID, GfaABC1D-ER-TurboID, or GfaABC1D-sec61b-TurboID. Three hours following initiation of transfection, astrocytes were switched to low protein conditioning media without biotin (components: 50% Neurobasal Thermo 12348017, 50% DMEM LifeTech 11960044, supplemented with Penicillin-Streptomycin (Thermo Fisher Scientific 15140-122), glutamax (Thermo Fisher Scientific 35050-061), and sodium pyruvate (Thermo Fisher Scientific 11360-070). After 48hr, astrocytes were incubated with 500uM biotin (Sigma B4639) for 10min, fixed with 4% PFA for 10 min (warmed to 34°C), washed 3 times with DPBS, then blocked and permeabilized in 50% antibody buffer (list components)/50% goat serum and 0.3% Triton X-100 for 30 min at room temperature. Cells were washed 1x with DPBS and

incubated with primary antibody rat HA (Roche Clone 3F10) at 1:1000 dilution, overnight at 4°C in antibody buffer and 10% goat serum. Cells were washed 3 times with DPBS and incubated with secondary antibody, goat anti-rat Alexa 647 (Invitrogen A48265) at 1:1000 dilution in antibody buffer and 10% goat serum for 2 hr at room temperature. Cells were washed 3 times with DPBS and mounted on microscope slides with SlowFade gold antifade mountant with DAPI (Thermo S36939). Cells were imaged using a Zeiss LSM880 Airyscan superrresolution with 63x objective (numerical aperture: 1.4) at 1.8x zoom, as 16-bit images at 2024 x 2024 pixels, 0.04um x 0.04 um pixel size, with Z-stack of 5 slices with step size 0.18um and total thickness 0.72um. Images in **Figure 4.1B** are maximum intensity projections.

Testing ER-TurboID constructs in astrocyte cultures

Five days after passaging into a 10cm plate, the mouse astrocytes were transfected with 15ug plasmid: either control CAG-GFP, GfaABC1D-C1(1-29)-TurboID, GfaABC1D-cyto-TurboID, GfaABC1D-ER-TurboID, or GfaABC1D-sec61b-TurboID; with OptiMEM (Thermo 31985062, 1800ul) and lipofectamine 2000 (Thermo 11668-019, 45ul). Three hours after the start of transfection, astrocytes were switched to high protein conditioning media without biotin (components 50% Neurobasal Thermo 12348017, 50% DMEM LifeTech 11960044, supplemented with Penicillin-Streptomycin (Thermo Fisher Scientific 15140-122), glutamax (Thermo Fisher Scientific 35050-061), sodium pyruvate (Thermo Fisher Scientific 11360-070), insulin (Sigma I6634), N-acetyl cysteine (Sigma A8199), transferrin (Sigma T-1147), BSA (sigma A4161), progesterone (Sigma P8783), putrescine (Sigma P5780), sodium selenite (Sigma S9133), and T3 (Sigma T6397)). 24hr after transfection, biotin (Sigma B4639) was added to 50uM in the media. After 17hr, the media was changed to low protein conditioning media without biotin for 21hr, after which lysates were collected by adding 200ul RIPA lysis buffer (Thermo 89901) with 1:100 protease (Thermo 78429) and phosphatase (Thermo 1862495) inhibitors directly to the cells and applying a cell scraper (Thermo 179693) to ensure lysis. Protein concentration was

quantified with BCA kit (Thermo 23227), then 75ug protein from each lysate sample was added to 15ul streptavidin beads (Thermo 88817), incubated for 1hr RT and 16hr 4C rotating, washed at RT with 250ul each of RIPA lysis buffer (2x2min), 1M KCl (Sigma P9591) (1x2min), 0.1M sodium carbonate (Sigma 222321) (1x10s), 2M urea (Invitrogen 15505-035) in 10mM Tris-HCl pH 8 (1x10s), RIPA lysis buffer (2x2min, moving to a new tube), and eluted in 30ul elution buffer (protein loading buffer (Thermo 39001) diluted to 1x, 20mM DTT (MilliporeSigma D9779), and 2mM biotin (Sigma B4639)) at 95C for 10min. Streptavidin western blots were performed as described in the Western Blot section above.

Label free mass spectrometry

Eluates from the streptavidin pulldown on cultured astrocyte lysates were precipitated by methanol/chloroform and redissolved in 8 M urea/100 mM TEAB, pH 8.5. Proteins were reduced with 5 mM tris(2-carboxyethyl)phosphine hydrochloride (TCEP, Sigma-Aldrich) and alkylated with 10 mM chloroacetamide (Sigma-Aldrich). Proteins were digested overnight at 37 ^{o}C in 2 M urea/100 mM TEAB, pH 8.5, with trypsin (Promega).

The samples were analyzed on a Orbitrap Eclipse Tribrid mass spectrometer (Thermo). Samples were injected directly onto a 25 cm, 100 μm ID column packed with BEH 1.7 μm C18 resin (Waters). Samples were separated at a flow rate of 300 nL/min on an EasynLC 1200 (Thermo). Buffer A and B were 0.1% formic acid in water and 90% acetonitrile, respectively. A gradient of 1–25% B over 100 min, an increase to 40% B over 20 min, an increase to 90% B over 10 min and held at 90% B for a 10 min was used for a 140 min total run time.

Peptides were eluted directly from the tip of the column and nanosprayed directly into the mass spectrometer by application of 2.5 kV voltage at the back of the column. The Eclipse was operated in a data dependent mode. Full MS1 scans were collected in the Orbitrap at 120k resolution. The cycle time was set to 3 s, and within this 3 s the most abundant ions per scan

were selected for CID MS/MS in the ion trap. Monoisotopic precursor selection was enabled and dynamic exclusion was used with exclusion duration of 60 s.

Protein and peptide identification were done with Integrated Proteomics Pipeline – IP2 (Integrated Proteomics Applications). Tandem mass spectra were extracted from raw files using RawConverter[31] and searched with ProLuCID[32] against Uniprot mouse database. The search space included all fully-tryptic and half-tryptic peptide candidates. Carbamidomethylation on cysteine was considered as static modifications. Data was searched with 50 ppm precursor ion tolerance and 600 ppm fragment ion tolerance. Identified proteins were filtered to using DTASelect[33] and utilizing a target-decoy database search strategy to control the false discovery rate to 1% at the protein level.[34]

Viral vector generation

Plasmids were sequenced for accuracy using Eton Sequencing and/or Primordium Labs before packaging into AAV at the Salk Institute Viral Vector (GT3) core facility. Viruses were packaged as AAV PHP.eB serotype with titer of approximately 5.6E14 genome copies (gc)/mL (GfaABC1D-ER-TurboID, plasmid for biotinylating enzyme) and 2.38E14 gc/mL (GfaABC1D-smFP, plasmid for control protein, subcloned as described in Brandebura et al. 2023,[7] based on construct from Viswanathan et al., 2015[35]).

Retroorbital virus injections and biotin supplementation

Mice at P12 were anesthetized with 2-3% isofluorane in oxygen by constant flow through a nose cone. Virus was injected via retroorbital administration at a dose of 1.0E12 viral genome copies in a total injection volume of 90 ul with either AAV-PHP.eB-GfaABC1D-ER-TurboID or AAV-PHP.eB-GfaABC1D-smFP. The virus was diluted in DPBS just prior to injection. Mice were injected with subcutaneous biotin (24mg/kg, 5mM biotin in PBS) daily from P21 to P26, with the last dose occurring 24h prior to collection.

Tissue collection and enrichment for biotinylated proteins

For all steps below, low adhesion Eppendorf tubes (USA Scientific 1415-2600) and HPLC grade water (Fisher W71) were used. Cortices were collected at P27 as described previously for fresh tissue, then frozen at -80C. Each sample consisted of two cortices from one mouse. All 16 samples (12 experimental ER-TurboID, 3 mice per genotype; 4 control smFP, 1 mouse per genotype; samples were from the four genotypes WT, WT;Smad4 cKO, FXS, FXS;Smad4 cKO) were then thawed on ice and processed in parallel. Each sample was added to 1mL of NP40 lysis buffer (50mM Tris pH 7.5, 150mM NaCl, 5mM EDTA, 0.5% NP40) with 1:100 protease and phosphatase inhibitors and 1mM DTT in a Precellys homogenization tube (Bertin P000973-LYSK0-A.0), then lysed with a Cryolys Evolution/Precellys Evolution tissue homogenizer (Bertin K002198-PEVO0-A.0; 5800rpm, 10C, 2x30s, 15s rest, cryolyse ON) and centrifuged at 20000g for 15min at 4C. The supernatant was decanted and protein concentration measured with BCA. 5mg per sample of lysate was added to 50ul Protein G beads pre-bound with 10ul anti-PCB (Abcam 110314, rotating in 500ul NP40 lysis buffer at RT for 3h then washed 1x with 500ul 50mM Tris, 150mM NaCl pH 7.5). For one sample (WT;Smad4cKO1), 3 mg lysate was used as input and all reagents were adjusted proportionally. Each tube was leveled to 1mL total volume with NP40 lysis buffer with 1:100 protease and phosphatase inhibitors, then rotated at 4C for 24h. The solution supernatant was separated from Protein G beads with a magnetic stand, and the supernatant was added to 200ul of washed streptavidin magnetic beads (88817). DTT was added to 0.5mM, and the solution was rotated for 1hr at RT, then 16hr at 4C. The magnetic beads were isolated with a magnetic rack, then washed at RT and eluted. Specifically, samples were washed with 200ul NP40 lysis solution (2min), transferred to a new tube, washed with 1mL NP40 lysis solution with 1mM DTT (2min), 1mL 1M KCl (2 min), 1mL 2M urea in 10mM Tris-HCl (10s), 1mL NP40 lysis solution (2min, transfer to a new tube), and 1mL NP40 lysis solution. Biotinylated proteins were eluted with 200ul elution buffer (1x PLB, 20mM DTT, 2mM biotin), for 5min at 95C.

Validation western blotting

Western blotting was performed as described above with modifications as below. 15-well gels were used, and both pre-enrichment lysates (10ug/sample) and eluted biotinylated proteins were analyzed. Lysates were blotted for Streptavidin 680 (no primary antibody overnight incubation, 1:5000 in blocking buffer + 0.1% Tween, 1hr RT), as further described in the Western Blot section.

Immunohistochemistry and Analysis: virus validation

The penetrance and specificity of the GfaABC1D-ER-TurboID and GfaABC1D-smFP viruses were quantified. For GfaABC1D-ER-TurboID, viruses were injected and biotin administered as described above, for three mice total, with tissue collected at P20 prior to biotin administration as well as P27 after six days of biotin. For GfaABC1D-smFP, two mice were injected with virus at P12, treated with biotin from P21-25, and collected at P26; one mouse was injected with virus at P15 and collected at P28. Sagittal brain sections of 16 um were obtained from mice injected with each virus (1.8mm lateral from midline). Slices were blocked and permeabilized in blocking buffer (10% goat serum in PBS with 0.3% Triton and 100mM L-lysine) for one hour at room temperature. Primary antibodies were diluted in antibody dilution solution (5% goat serum in PBS with 0.3% Triton and 100mM lysine) and stained overnight in a humidified chamber at 4C. Antibodies for the astrocyte marker SOX9 (1:1000, rabbit, Abcam ab185966), HA antibody (1:500, rat, Roche Clone 3F10) were used. The next day slices were washed three times in PBS with 0.2% Triton for 5, 10 and 15 minutes. Secondary antibody labeling was performed in antibody solution (5% goat serum in PBS with 0.3% Triton and 100mM lysine) and for two hours at room temperature. Appropriate secondary antibodies were used (1:500, goat anti-rat Alex 488 Invitrogen A11006; 1:500, goat anti-rabbit Alexa 555 Invitrogen A21429; 1:500 streptavidin Alexa 647 Invitrogen S32357). Washes in PBS with 0.2% Triton were performed three times for 5, 10 and 15 minutes. DAPI was applied (1:1000) for 5 minutes followed by a PBS wash. Coverslips were mounted with DAPI slowfade (Thermo S36939). Images were obtained on an AxioImager.Z2

using a 20x objective (numerical aperture = 0.8) as 14-bit images. Tiled (2x2) z-stacks (2637 x 2637 pixels, pixel size 0.323um x 0.323um) spanning all layers of visual cortex were acquired with 6 z-steps of 1um each totaling a width of 5um. Three slices/mouse were imaged with three mice total. The images were stitched and maximum intensity projections were created in Zen software. The images were then imported into ImageJ for cell counting analysis using the cell counter plug-in. The number of SOX9+ cells were counted in each image to obtain the total number of astrocytes, respectively. Then the number of HA+/SOX9+ cells were counted. The viral penetrance was quantified as the percentage of SOX9+ cells that were also HA+ for each virus. The viral specificity was quantified as the percentage of HA+ cells that were also SOX9+ for each virus. Images shown in **Figures 4.2B** and **Figure 4.3A,B** are maximum intensity projections.

Tandem Mass Tagging Mass Spectrometry

Samples were precipitated by methanol/chloroform and redissolved in 8 M urea/100 mM TEAB, pH 8.5. Proteins were reduced with 5 mM tris(2-carboxyethyl)phosphine hydrochloride (TCEP, Sigma-Aldrich) and alkylated with 10 mM chloroacetamide (Sigma-Aldrich). Proteins were digested overnight at 37 ^{o}C in 2 M urea/100 mM TEAB, pH 8.5, with trypsin (Promega). The digested peptides were labeled with 16-plex TMT (Thermo product A44522, lot YB368939), pooled samples were fractionated by basic reversed phase (Thermo 84868). Each of the 16 channels in the 16-plex was used to label a separate sample. The 16 samples consisted of 12 experimental samples (3 mice per genotype) injected with virus expressing ER-TurboID, and 4 control samplesn (1 mouse per genotype) injected with virus expressing control protein smFP. Samples were from the four genotypes WT, WT;Smad4 cKO, FXS, FXS;Smad4 cKO.

The TMT labeled samples were analyzed on a Orbitrap Eclipse Tribrid mass spectrometer (Thermo). Samples were injected directly onto a 25 cm, 100 μm ID column packed with BEH 1.7 μm C18 resin (Waters). Samples were separated at a flow rate of 300 nL/min on an EasynLC 1200 (Thermo). Buffer A and B were 0.1% formic acid in water and 90% acetonitrile, respectively.

A gradient of 1–15% B over 30 min, an increase to 45% B over 120 min, an increase to 100% B over 20 min and held at 100% B for a 10 min was used for a 180 min total run time.

Peptides were eluted directly from the tip of the column and nanosprayed directly into the mass spectrometer by application of 2.5 kV voltage at the back of the column. The Eclipse was operated in a data dependent mode. Full MS1 scans were collected in the Orbitrap at 120k resolution. The cycle time was set to 3 s, and within this 3 s the most abundant ions per scan were selected for CID MS/MS in the ion trap. The TMT samples were analyzed by MS3 analysis with multinotch isolation (SPS3) was utilized for detection of TMT reporter ions at 60k resolution.[36] Monoisotopic precursor selection was enabled and dynamic exclusion was used with exclusion duration of 60 s.

Protein and peptide identification were done with Integrated Proteomics Pipeline – IP2 (Integrated Proteomics Applications). Tandem mass spectra were extracted from raw files using RawConverter[31] and searched with ProLuCID[32] against Uniprot mouse database. The search space included all fully-tryptic and half-tryptic peptide candidates. Carbamidomethylation on cysteine and TMT on lysine and peptide N-term were considered as static modifications. Data was searched with 50 ppm precursor ion tolerance and 600 ppm fragment ion tolerance. Identified proteins were filtered to using DTASelect[33] and utilizing a target-decoy database search strategy to control the false discovery rate to 1% at the protein level.[34] Quantitative analysis of TMT was done with Census[37] filtering reporter ions with 10 ppm mass tolerance and 0.6 isobaric purity filter.

Proteomic Analysis

Proteins were filtered for contaminants and duplicates as follows: proteins with identical gene names were removed, proteins annotated as “contaminant” were removed, and streptavidin was removed. For the one sample (WT;Smad4cKO1) for which a different amount of input was used, the TMT signal was normalized for the input amount (multiplication by a factor of 1.71, after

accounting for aliquots used for QC testing). Proteomic data was analyzed with differentially expressed protein criteria as follows: p-value < 0.05, unpaired t-test. Heatmaps were created using R (v4.2.2) via RStudio (2022.12.0) using the Pheatmap package and Graphpad Prism (v8.0). Comparison to FMRP targets used reference database in Darnell et al., 2011.[24] Volcano plots were created with package ggplot2 (v3.4.0). Gene set enrichment analysis (GSEA) was performed to detect which pathways and gene sets were enriched in Fmr1 KO and Smad4 cKO using the package ClusterProfiler (v4.6.0).[16] The following gene sets from mouse MSigDB[17] were used: hallmark pathways, canonical pathways (including Reactome,[18] KEGG,[19] Wikipathways,[20] and BioCarta[21]), and gene ontology.[22,23] Proteins with Turbo/smFP ratio > 1.75 were used for GSEA, with ranking based on sign(L2FC)*-log10(p-value), for each comparison. For GSEA pathway analysis only, peptides mapped to multiple protein isoforms were only counted once as the alphanumerically first protein isoform, in order to avoid overweighting single peptides. Highlighted pathways in visualization are top three down- and upregulated (highest and lowest NES) hallmark pathways in each comparison (**Figure 4.10D**). Cellular compartment of differentially expressed proteins was determined via UniProt annotations. Rank-rank hypergeometric plot was generated using the package RRHO v1.38.0.[38]

The ER-TurboID proteome was visualized with Cytoscape v3.10.1, with nodes corresponding to the gene name for the top 200 enriched proteins (Turbo/smFP ratio). Node size for detected proteins was set as proportional to log10(TMT intensity). Clustergrams were created via Uniprot, STRING, and GeneCards database annotations. For neurologic disease association, only proteins classified as “causative mutation” in GeneCards were included.[39] Astrocyte enrichment was determined referencing the external database in Zhang et al., 2014.[40] Cellular compartment gene ontology[22,23] on the ER-TurboID proteome was conducted via overrepresentation analysis with the package ClusterProfiler (v4.6.0).[16]

For testing for overlap of known FMRP targets with up- and down-regulated proteins in Fmr1 KO (Comparison 1), the list of 842 genes from Darnell et al. 2011 was used,[24] and statistics by Fisher's exact test with genome size 24,252 protein-coding *M. Musculus* genes.

Single cell RNAseq analysis

The P14 neuron-depleted visual cortex nuclear single-cell RNAseq 10X Chromium dataset from Farhy-Tselnicker et al., 2021 was used.[41] Data were demultipliexed and mapped onto the mouse genome (mm10) using 10X Cellranger (v7.0.1) with default parameters. Data were processed with Seurat (v4.4.0)[42] to remove cells with <200 genes (low coverage), with >5000 genes (likely doublets), and mitochondrial counts >5%. Counts were log-normalized, and the top 2000 variable features were used for subsequent dimension reduction. Each cell's 40 closets neighbors were identified, clusters were identified at resolution 0.2 (18 resultant clusters), and UMAP embedding was performed with the top 40 features. Clusters were annotated by cell type as in Farhy-Tselnicker et al., 2021.[41] Individual gene expression across cells was plotted using the UMAP embedding and the FeaturePlot function.

Immunohistochemistry and Analysis: Sparc and AQP4

Immunohistochemistry for Sparc and AQP4 was performed on sagittally-sectioned PFA-fixed tissue. Immunohistochemistry proceeded as described in the above sections with the following modifications. Primary antibodies for Sparc (1:200, goat, R&D AF9424) and S100B (1:500, rabbit, abcam AB52642) were used together with the secondaries donkey anti-goat 488 (1:500, Jackson 705-545-147) and donkey anti-rabbit 568 (1:500, Invitrogen A10042). Primary antibody for AQP4 (1:500, rabbit, Sigma A5971) was used together with goat anti-rabbit 555 (1:500, A21429).

For Sparc and AQP4, visual cortex was imaged on an LSM700 confocal with 40x oil-immersion objective (numerical aperture: 1.3) as 16-bit images, as a z-stack of 8 slices with steps of 0.4um spanning 2.8um. Images were collected as 12 tiles, a total of 6143 x 2047 pixels. For Sparc, S100B surfaces were created by automated thresholding in Imaris, and Sparc fluorescence intensity was analyzed within S100B surfaces, categorized by layer using DAPI. For AQP4, fluorescence intensity was analyzed by layer using DAPI. Additionally, Imaris automatic thresholding was used to detect AQP4 at blood vessel surfaces and create separate objects for blood vessel AQP4 and background parenchymal AQP4. These Imaris objects were used to obtain the volume of AQP4 around blood vessels, as well as the intensity of AQP4 at blood vessels compared to in surrounding parenchyma. Images shown in **Figure 5.6A,5.8A** are maximum intensity projections.

Single molecule fluorescent *in situ* hybridization (smFISH): *Myoc, Tnc, Chrdl1*

smFISH for *Myoc, Tnc, and Chrdl1* was performed with RNAscope V2 (ACDBio: 323100) on sagitally-sectioned PFA-fixed tissue with details as described in the smFISH section above with the following modifications. Slides were baked for 30min at 60C prior to fixation, slides were fixed by immersion in 4% chilled PFA in PBS for 15min at 4C, and protease IV was applied for 30min at 40C. Probes for *Myoc* (ACDBio: #460981) and *Slc1a3* (encoding for glutamate aspartate transporter GLAST, ACDBio: 430781-C2) were used together with Opal 570 (Akoya FP1488001KT, 1:1500) and Opal 520 (Akoya FP1487001KT, 1:1500) respectively. Probe for *Tnc* (ACDBio #465021) was used with Opal 520 (FP1487001KT, 1:1500); following completion of the RNAscope protocol, slides were immunostained with anti-S100B-568 conjugate (1:500, rabbit, Abcam Ab201837) as in the immunostaining protocols above. Probe for *Chrdl1* (ACDBio #442811) was used with Opal 520 (FP1487001KT, 1:1500); following completion of the RNAscope protocol, slides were immunostained with anti-S100B-568 conjugate (1:500, rabbit, Abcam Ab201837) as in the immunostaining protocols above.

Visual cortex was imaged on an LSM700 confocal with 40x oil-immersion objective (numerical aperture: 1.3) as 16-bit images, as a z-stack of 8 slices of 0.4um each, spanning 2.8um. Images were collected as 12 tiles, a total of 6143 x 2047 pixels. For *Tnc*, S100B surfaces were created by automated thresholding in Imaris, and Sparc fluorescence intensity was analyzed within S100B surfaces, categorized by layer using DAPI. For *Myoc*, the whole brain sections were also imaged on an AxioImager Z.2 with Apotome module with 10x objective as a single z-plane tiled image. Images shown in **Figures 5.4A, 5.5A, 5.7A, and 5.9C** are maximum intensity projections. Quantification was performed as: visual cortex image was cropped to a height of 64um spanning the entire imaged length of pia. The thresholded *Myoc*+ area was defined as the percentage area above intensity 1000.

Quantification and statistical analysis

Statistical analysis and data visualization was performed in GraphPad Prism 8. All tests were two-tailed. Data was tested for normality using either Shapiro-Wilk or Kolmogorov-Smirnov tests. For normally distributed data, T-tests were used to compare two groups and one-way and two-way ANOVAs were used to compare multiple groups and treatments, with post-hoc comparison testing pre-determined by the experimental design; Sidak's multiple comparison test was used to assess genotype changes across multiple cortical layers, while Tukey's multiple comparison test was used in all other instances to compare each group to each other group. Comparisons of categorical data were performed with Chi-Squared test (more than two categories) and Fisher's Exact test (two categories). Least-squares linear regression was used to calculate Pearson's correlation coefficients. Comparisons of L2FC distributions of large gene sets were performed with z-tests. All bar graphs and line graphs represent mean ± standard error of the mean (SEM), with individual data points representing mice unless otherwise indicated.

Figures were generated using Adobe Illustrator 2022 and BioRender. Exact p values reported on graphs.

Data availability

RNA sequencing data have been deposited at GEO (GSE263517). Proteomics data have been deposited at MassIVE (MSV000094549). The data that support the findings of this study are available upon reasonable request.

References

1. Keysor, C. S. & Mazzocco, M. M. M. A developmental approach to understanding Fragile X syndrome in females. *Microscopy Research and Technique* **57**, 179–186 (2002).

2. Yang, X., Li, C., Herrera, P.-L. & Deng, C.-X. Generation of Smad4/Dpc4 conditional knockout mice. *genesis* **32**, 80–81 (2002).

3. Garcia, A. D. R., Doan, N. B., Imura, T., Bush, T. G. & Sofroniew, M. V. GFAP-expressing progenitors are the principal source of constitutive neurogenesis in adult mouse forebrain. *Nat Neurosci* **7**, 1233–1241 (2004).

4. Blanco-Suarez, E., Liu, T.-F., Kopelevich, A. & Allen, N. J. Astrocyte-Secreted Chordin-like 1 Drives Synapse Maturation and Limits Plasticity by Increasing Synaptic GluA2 AMPA Receptors. *Neuron* **100**, 1116-1132.e13 (2018).

5. Allen, N. J. *et al.* Astrocyte glypicans 4 and 6 promote formation of excitatory synapses via GluA1 AMPA receptors. *Nature* **486**, 410–414 (2012).

6. McCarthy, K. D. & de Vellis, J. Preparation of separate astroglial and oligodendroglial cell cultures from rat cerebral tissue. *Journal of Cell Biology* **85**, 890–902 (1980).

7. Brandebura, A. N., Asbell, Q. N., Micael, M. K. B. & Allen, N. J. *Dysregulation of Astrocyte-Secreted Pleiotrophin Contributes to Neuronal Structural and Functional Deficits in Down Syndrome*. http://biorxiv.org/lookup/doi/10.1101/2023.09.26.559633 (2023) doi:10.1101/2023.09.26.559633.

8. Musumeci, S. A. *et al.* Audiogenic Seizures Susceptibility in Transgenic Mice with Fragile X Syndrome. *Epilepsia* **41**, 19–23 (2000).

9. Louros, S. R. *et al.* Excessive proteostasis contributes to pathology in fragile X syndrome. *Neuron* **111**, 508-525.e7 (2023).

10. Prusky, G. T., Alam, N. M., Beekman, S. & Douglas, R. M. Rapid Quantification of Adult and Developing Mouse Spatial Vision Using a Virtual Optomotor System. *Invest. Ophthalmol. Vis. Sci.* **45**, 4611 (2004).

11. Fernandez, L. S. Astrocyte CCN1 stabilizes neural circuits in the adult brain.

12. Labarta-Bajo, L., Deng, J., Contreras, M. & Allen, N. J. Protocol for the purification and transcriptomic analysis of mouse astrocytes using GFAT. *STAR Protocols* **4**, 102599 (2023).

13. Ewels, P., Magnusson, M., Lundin, S. & Käller, M. MultiQC: summarize analysis results for multiple tools and samples in a single report. *Bioinformatics* **32**, 3047–3048 (2016).

14. Heinz, S. *et al.* Simple Combinations of Lineage-Determining Transcription Factors Prime cis-Regulatory Elements Required for Macrophage and B Cell Identities. *Molecular Cell* **38**, 576–589 (2010).

15. Love, M. I., Huber, W. & Anders, S. Moderated estimation of fold change and dispersion for RNA-seq data with DESeq2. *Genome Biol* **15**, 550 (2014).

16. Yu, G., Wang, L.-G., Han, Y. & He, Q.-Y. clusterProfiler: an R Package for Comparing Biological Themes Among Gene Clusters. *OMICS: A Journal of Integrative Biology* **16**, 284–287 (2012).

17. Liberzon, A. *et al.* The Molecular Signatures Database Hallmark Gene Set Collection. *Cell Systems* **1**, 417–425 (2015).

18. Milacic, M. *et al.* The Reactome Pathway Knowledgebase 2024. *Nucleic Acids Research* **52**, D672–D678 (2024).

19. Kanehisa, M., Furumichi, M., Sato, Y., Kawashima, M. & Ishiguro-Watanabe, M. KEGG for taxonomy-based analysis of pathways and genomes. *Nucleic Acids Research* **51**, D587–D592 (2023).

20. Agrawal, A. *et al.* WikiPathways 2024: next generation pathway database. *Nucleic Acids Research* **52**, D679–D689 (2024).

21. Nishimura, D. BioCarta. *Biotech Software & Internet Report* **2**, 117–120 (2001).

22. Ashburner, M. *et al.* Gene Ontology: tool for the unification of biology. *Nat Genet* **25**, 25–29 (2000).

23. Ebert, D. *et al.* The Gene Ontology knowledgebase in 2023.

24. Darnell, J. C. *et al.* FMRP Stalls Ribosomal Translocation on mRNAs Linked to Synaptic Function and Autism. *Cell* **146**, 247–261 (2011).

25. Hasel, P. *et al. Defining the Molecular Identity and Morphology of* Glia Limitans Superficialis *Astrocytes in Mouse and Human*. http://biorxiv.org/lookup/doi/10.1101/2023.04.06.535893 (2023) doi:10.1101/2023.04.06.535893.

26. Lanjakornsiripan, D. *et al.* Layer-specific morphological and molecular differences in neocortical astrocytes and their dependence on neuronal layers. *Nat Commun* **9**, 1623 (2018).

27. Wei, W. *et al.* Cell type-selective secretome profiling in vivo. *Nature Chemical Biology* **17**, 326–334 (2021).

28. Kim, K. *et al.* Dynamic tracking and identification of tissue-specific secretory proteins in the circulation of live mice. *Nat Commun* **12**, 5204 (2021).

29. Branon, T. C. *et al.* Efficient proximity labeling in living cells and organisms with TurboID. *Nature Biotechnology* **36**, 880–887 (2018).

30. Shigetomi, E. *et al.* Imaging calcium microdomains within entire astrocyte territories and endfeet with GCaMPs expressed using adeno-associated viruses. *Journal of General Physiology* **141**, 633–647 (2013).

31. He, L., Diedrich, J., Chu, Y.-Y. & Yates, J. R. Extracting Accurate Precursor Information for Tandem Mass Spectra by RawConverter. *Anal. Chem.* **87**, 11361–11367 (2015).

32. Xu, T. *et al.* ProLuCID: An improved SEQUEST-like algorithm with enhanced sensitivity and specificity. *Journal of Proteomics* **129**, 16–24 (2015).

33. Tabb, D. L., McDonald, W. H. & Yates, J. R. DTASelect and Contrast: Tools for Assembling and Comparing Protein Identifications from Shotgun Proteomics. *J. Proteome Res.* **1**, 21–26 (2002).

34. Peng, J., Elias, J. E., Thoreen, C. C., Licklider, L. J. & Gygi, S. P. Evaluation of Multidimensional Chromatography Coupled with Tandem Mass Spectrometry

(LC/LC−MS/MS) for Large-Scale Protein Analysis: The Yeast Proteome. *J. Proteome Res.* **2**, 43–50 (2003).

35. Viswanathan, S. *et al.* High-performance probes for light and electron microscopy. *Nat Methods* **12**, 568–576 (2015).
36. McAlister, G. C. *et al.* MultiNotch MS3 Enables Accurate, Sensitive, and Multiplexed Detection of Differential Expression across Cancer Cell Line Proteomes. *Anal. Chem.* **86**, 7150–7158 (2014).
37. Park, S. K. R. *et al.* Census 2: isobaric labeling data analysis. *Bioinformatics* **30**, 2208–2209 (2014).
38. Plaisier, S. B., Taschereau, R., Wong, J. A. & Graeber, T. G. Rank–rank hypergeometric overlap: identification of statistically significant overlap between gene-expression signatures. *Nucleic Acids Research* **38**, e169–e169 (2010).
39. Ben-Ari Fuchs, S. *et al.* GeneAnalytics: An Integrative Gene Set Analysis Tool for Next Generation Sequencing, RNAseq and Microarray Data. *OMICS: A Journal of Integrative Biology* **20**, 139–151 (2016).
40. Zhang, Y. *et al.* An RNA-Sequencing Transcriptome and Splicing Database of Glia, Neurons, and Vascular Cells of the Cerebral Cortex. *Journal of Neuroscience* **34**, 11929–11947 (2014).
41. Farhy-Tselnicker, I. *et al.* Activity-dependent modulation of synapse-regulating genes in astrocytes. *eLife* **10**, e70514 (2021).
42. Butler, A., Hoffman, P., Smibert, P., Papalexi, E. & Satija, R. Integrating single-cell transcriptomic data across different conditions, technologies, and species. *Nat Biotechnol* **36**, 411–420 (2018).

Chapters 1-7, in part, have been submitted for publication. Deng J**,** Labarta-Bajo L, Brandebura AN, Kahn SB, Pinto AFM, Diedrich JK, Allen NJ (2024). Suppression of astrocyte BMP signaling improves fragile X syndrome molecular signatures and functional deficits. The dissertation author will be the first author of this publication, and Dr. Nicola Allen will be the senior author and principal investigator.